Relaxed Optics: Modeling and Discussions 3

Author

Trokhimchuck Petro P.

Bright Sky Publications ™

New Delhi

Published By: *Bright Sky Publications*

Bright Sky Publication
Office No. 3, 1st Floor,
Pocket - H34, SEC-3,
Rohini, Delhi, 110085, India

Author: *Trokhimchuck Petro P.*

Edition: *1st*

Publication Year: *2024*

Pages: *239*

ISBN:

Price: *₹ 1,062/-*

Dedication

In memory of my brother Valentyn P. Trofimchuck

(October 2, 1956 - August 5, 2021)

Preface

The last author book “Relaxed Optics: Modeling and Discussions 2” was published in Lambert Academic Publishing in 2022.

However, author active scientific researches in this area of modern physics for last years allow opening and resolving some interesting problems of Relaxed Optics. Among them are problems of Cherenkov and supercontinuum radiation; thermodynamical and electrodynamical theories and models of nucleation and crystallization; shork processes in Nonlinear and Relaxed Optics, including acoustic and electrodynamical models; etc.

The necessity of print this book is caused of author researches in last two years. Results there received in the area of interference the Nonlinear Optical and Relaxed Optical processes and phenomena or correlation between radiated and nonradiated second-order processes of interaction laser radiation and matter.

The problem of Cherenkov and supercontinuum radiation have similar nature as generation heterogeneous shock nonlinear polarization in irradiated matter with various methods of excitation.

The problem of nucleation and crystallization is very important in the problem of creation laser-induced nano and microstructures. Development of electromagnetic methods of modeling added thermodynamical methods because it allow receiving the nucleation and crystallization in both direction: first, from structures with more low symmetry to structures with more high symmetry and second, from structures with more high symmetry to structures with more low symmetry.

The problem of shock processes has few aspects: acoustic and optical; macro and microscopic aspects. Comparative analysis of these aspects is representing. It was shown that only cascade model may be used for the explanation of these results.

Main peculiarities of chemical-physical processes and its influence on the corresponding Relaxed Optical processes and phenomena are represented too.

Two International conference 11-th “Relaxed, Nonlinear and Acoustic Processes and Materials” (2022) and Vth “Actual Problems of Fundamental Science” (2023) were organized in Lesya Ukrayinka Volyn’ National University. These conferences were organized for the consolidation and resolutions problems of Relaxed and Nonlinear Optics.

Author wishes to thank by V. Peretyatko, V. Antonov-Romanovskiy, I. Frank, P. Cherenkov, V. Makin, A. Medvid', I. Stoyanova, P. Eliseev, I. Khaibullin, V. Bonch-Bruyevich, Yu. Klimontovich, G. Kachurin, V. Stafeev, M. Makoviychuck, S. Vorobyov, F. Zaitov, M. Avdekovich, V. Vinetskiy, V. Shyrokovskiy, A. Svidzinskiy, P. Danyl'chenko, A. Frimer, V. Heyfets, V. Cheltsov, V. Yukhymchuk and V. Holovatskiy for the discussion of basic idea of my research and L. Maidanovych-Sörensen, D. Shvalikovskiy and M. Shevchuk (Maidanovych), for help in the preparation of this book.

Contents

Introduction

Art is man's nature; nature is God's art

Philip James Bailey

Some problems of modeling Relaxed Optical processes are represented and discussed.

Experimental data of Cherenkov [13, 20, 26, 33, 35, 43, 52, 60, 62, 67, 69, 96, 105, 109, 117, 125, 127, 133, 149, 188, 197, 198, 211, 214, 214, 217, 219, 230, 232, 233, 239, 241, 246-248, 279, 280] and supercontinuation [5, 9, 10, 15, 16, 23, 27, 36, 38-40, 46, 49, 50, 53, 54, 58, 61, 68, 71, 72, 75-78, 91-93, 112, 123, 126, 129, 130, 141-146, 150, 154, 157-159, 174, 180, 183, 186, 187, 190, 194, 199, 203-205, 209, 210, 212, 249, 256, 261, 265, 270, 272, 275, 276] radiation are discussing in Chapter I. Peculiarities of receiving these types of radiation are observing. We show that conical continuation supercontinuation radiation is connected with creation interference (diffraction) rings and has surface nature. Classic Cherenkov radiation has volume nature and small foton efficiency. Continuation supercontinuation radiation has large photon efficiency. However, both types of irradiation has similar nature – shock heterogeneous polarization of matter. The problem of Cherenkov radiation of tachyons [246, 247] is represented too.

Main theories and models of Cherenkov and supercontinuation radiation are analyzed in Chapter II. Detail analysis of main models and theories of Cherenkov radiation is represented. Among them: Frank-Tamm theory of Cherenkov radiation [35, 69, 96, 211, 279, 280]; E. Fermi theory of the ionization loss of energy in condensed matter [67]; A. Bohr theory of the influence of atoms interactions on the penetration of particles through matter [33]; I. Golub model of the similarity Descartes-Snell law and Cherenkov radiation [77] and synthetic model, which allows to combine the Fermi-Bohr microscopic concept of and the Golub macroscopic concept into a single system [232, 233]. Theory of Cherenkov radiation of tachyons [24, 35, 63, 65, 263] is discussed too.

The main problems of thermodymical modelling the nucleation and crystallization are discussed in Chapter III. Some questions of crystal nucleation and crystallization [57, 70, 73, 74, 82, 87, 99-101, 103, 115, 116, 119, 132, 134-136, 152, 163, 167, 171, 173, 189, 192, 195, 250, 252, 273] are observed. Among them: macroscopic theory of homogeneous nucleation [1, 2, 22, 41, 42, 56, 195, 264]; thermodynamics electrochemical nucleation [31, 34, 37, 56, 139, 194, 201, 264]; Stranski-Krastanov theory

[19, 205, 206]; Walton's microscopic theory of nucleation [194, 257] and advantages and minuses of thermodynamically methods of nucleation and crystallization.

The main problems of electrodymical modelling the nucleation and crystallization are analysed in Chapter IV. Among them Vitaliy Stafeev phasons theory [200, 219, 231]; cascade models of step-on-step excitation of proper chemical bonds in the regime of saturation the excitation [217-219, 224, 225-227, 229, 232, 233, 235-238] and temperature rise induced by a laser beam. Stafeev theory has universal character and may be using for various media. Cascade models were used for two-dimensional scheme of crystal lattice sphalerite (indium antimonite and indium arsenide) and for phase diagram of silicon and germanium. Problems of laser-induced crystallization [7, 14, 25, 29, 30, 32, 48, 51, 81, 84-86, 89, 104, 110, 118, 121, 128, 137, 164-165, 169, 184, 192, 208, 218-244, 251, 255, 259, 274, 277, 278] in more widely sense are discussing too.

Chapter V is devoted to the study of the problem of laser-induced shock processes in Nonlinear and Relaxed Optics [12, 29, 30, 44, 47, 64, 106, 139- 141, 154, 160-161, 168, 172, 176-179, 1901, 251, 265-269]. Experimental results are presented for various regimes of laser radiation and various matter. Next concepts, theories and models were analyzed: main peculiarities of classic theories of shock processes [18, 45, 107, 162, 216]; Rayleygh concept on the pressure developed in a liquid during the collapse of a spherical cavity [175, 176]; the main extensions of Rayleigh's theory for liquids as Rayleigh–Plesset, Gilmore and Keller–Miksis models [120] and modified Rayleygh theory [232, 233] for the case of solid. Elements of cascade theory of laser-induced optical breakdown are analyzed. Comparative analysis of acoustic and electromagnetic nature of generation cavity bubbles and nanovoids is represented too.

Chapter - 1

Cherenkov and Supercontinuum Radiation: Experimental Data

Be a friend of truth to the point of martyrdom, but do not be its defender to the point of intolerance

Pythagor

1.1 Introduction

Main experimental data and its peculiarities of Cherenkov [11, 13, 20, 26, 33, 35, 43, 52, 60, 62, 67, 69, 96, 105, 109, 117, 125, 127, 133, 149, 188, 197, 198, 211, 214, 215, 217, 219, 230, 232, 233, 239, 241, 246-248, 279, 280] and supercontinuum [5, 9, 10, 15, 16, 23, 27, 36, 38-40, 46, 49, 50, 53, 54, 58, 61, 68, 71, 72, 75-78, 91-93, 112, 123, 126, 129, 130, 142-147, 150, 154, 157-159, 174, 180, 183, 186, 187, 190, 194, 199, 203-205, 209, 210, 212, 249, 256, 261, 265, 270, 272, 275, 276] radiation are discussed. Comparative analysis of these processes are represented. Roughly speaking difference between these two processes is methods of creation and generation of nonlinear polarization, which is source of corresponding radiation. This problem has next peculiarities. First is connected with processes of scattering (absorption) of initial radiation. Second is connected with second-order processes of relaxation the first-order excitation discussed. As rule it is chain processes. The relaxation processes is next: reirradiation and reabsorption, electromagnetic wave processes, thermal processes.

These features can be analyzed in the most detail on the example of Cherenkov and supercontinuum radiation. It is these processes that have a more "pure" electromagnetic nature. But this nature is expressed here through radiation. Since radiative processes are caused by a change in the polarization of the medium, these processes also differ only in the method of excitation of this polarization.

Cherenkov radiation is the emission of electromagnetic waves by a charged particle moving in a medium at a speed greater than the phase speed of light propagation in this medium [69, 96]. The radiation forms a cone with the apex directed in the direction of the particle's movement. The angle at the top of the cone depends on the speed of the particle and the speed of light in the medium. This is precisely what makes Cherenkov radiation extremely useful

from the point of view of elementary particle physics, since, having determined the angle at the top of the cone, it is possible to calculate the particle's speed from it.

Cherenkov radiation is due to shock polarization of the medium [77, 232, 233]. At the same time, only a small part of the energy of the incoming particle is used. At the same time, the particle itself does not necessarily have to pass through the medium, it is enough that it flies near the medium.

Cherenkov radiation itself can be considered as a braking medium. It is from this point of view that Cherenkov radiation was considered by E. Fermi [67] and A. Bohr [33]. The phase speed of light in the medium is a characteristic of the medium, it shows how much the medium "slows down" the speed of light in a vacuum. This is a macroscopic electrodynamic characteristic of the medium. Cherenkov radiation itself is characterized by low photon efficiency [233].

Roughly speaking, supercontinuum (supercontinuum cone) radiation is laser-induced Cherenkov radiation [77, 233].

Supercontinuum radiation was observing in all media when irradiated with pulsed laser radiation [58]. At the same time, as a rule, these processes have a high photon efficiency, while classical Cherenkov radiation has a low photon efficiency [233].

Classical Cherenkov radiation is using to create various Cherenkov detectors for problems in nuclear physics, ecology, astrophysics, etc.

Supercontinuum radiation is using in the creation of white lasers [209], that is, lasers with a wide spectrum of radiation.

A promising direction of application of supercontinuum (laser-induced Cherenkov) radiation is optoelectronic micro and nano technologies [233]. Classical Cherenkov radiation cannot be using for these problems, as it has a relatively low intensity.

1.2 Cherenkov radiation

Cherenkov radiation is electromagnetic radiation emitted when a charged particle (such as an electron) passes through a dielectric medium at a speed greater than the phase velocity (speed of propagation of a wavefront in a medium) of light in that medium. A classic example of Cherenkov radiation is the characteristic blue glow of an underwater nuclear reactor. Its cause is similar to the cause of a sonic boom, the sharp sound heard when faster-than-sound movement occurs. The phenomenon is named after Soviet physicist

Pavel Cherenkov [69, 96], who was the first to detect it experimentally under the supervision of Sergey Vavilov at the Lebedev Institute in 1934. Therefore, it is also known as Vavilov–Cherenkov radiation. Cherenkov saw a faint bluish light around a radioactive preparation in water during experiments. His doctorate thesis was on luminescence of uranium salt solutions that were excited by gamma rays instead of less energetic visible light, as done commonly. He discovered the anisotropy of the radiation and concluded that the bluish glow was not a fluorescent phenomenon.

A theory of this effect was later developed in 1937 within the framework of Einstein's special relativity theory by Cherenkov's colleagues Igor Tamm and Ilya Frank [69, 211], who also shared the 1958 Nobel Prize.

Cherenkov radiation as conical wavefronts had been theoretically predicted by the English scientist Oliver Heaviside in papers published between 1888 and 1889 [151] and by Arnold Sommerfeld in 1904 [69, 96], but both had been quickly dismissed following the relativity theory's restriction of superluminal particles until the 1970s. Marie Curie observed a pale blue light in a highly concentrated radium solution in 1910 [188], but did not investigate its source. In 1926, the French radiotherapist Lucien Mallet described the luminous radiation of radium irradiating water having a continuous spectrum [69, 96].

In 2019, a team of researchers from Dartmouth's and Dartmouth-Hitchcock's Norris Cotton Cancer Center discovered Cherenkov light being generated in the vitreous humor of patients undergoing radiotherapy. The light was observed using a camera imaging system called a CDose, which is specially designed to view light emissions from biological systems. For decades, patients had reported phenomena such as "flashes of bright or blue light"[28] when receiving radiation treatments for brain cancer, but the effects had never been experimentally observed.

A reverse Cherenkov effect [60] can be experienced using materials called negative-index metamaterials (materials with a subwavelength microstructure that gives them an effective "average" property very different from their constituent materials, in this case having negative permittivity and negative permeability). This means that, when a charged particle (usually electrons) passes through a medium at a speed greater than the phase velocity of light in that medium, that particle emits trailing radiation from its progress through the medium rather than in front of it (as is the case in normal materials with, both permittivity and permeability positive). One can also obtain such reverse-cone Cherenkov radiation in non-metamaterial periodic media where

the periodic structure is on the same scale as the wavelength, so it cannot be treated as an effectively homogeneous metamaterial [60].

While the speed of light *in vacuum* is a universal constant (c = 299792458 m/s), the speed in a material may be significantly less, as it is perceived to be slowed by the medium. For example, in water it is only $0.75c$. Matter can accelerate to a velocity higher than this (although still less than c, the speed of light in vacuum) during nuclear reactions and in particle accelerators. Cherenkov radiation results when a charged particle, most commonly an electron, travels through a dielectric (can be polarized electrically) medium with a speed greater than light's speed in that medium [60, 69, 96].

The effect can be intuitively described in the following way. From classical physics, it is known that accelerating charged particles emit electromagnetic waves and via Huygens' principle these waves will form spherical wavefronts which propagate with the phase velocity of that medium (i.e. the speed of light in that medium given by c/n, for n, the refractive index). When any charged particle passes through a medium, the particles of the medium will polarize around it in response. The charged particle excites the molecules in the polarizable medium and on returning to their ground state, the molecules reemit the energy given to them to achieve excitation as photons. These photons form the spherical wavefronts which can be seen originating from the moving particle. If $v_p < c/n$, that is the velocity of the charged particle is less than that of the speed of light in the medium, then the polarization field which forms around the moving particle is usually symmetric. The corresponding emitted wavefronts may be bunched up but they do not coincide or cross and there are no interference effects to worry about. In the reverse situation, i.e. $v_p > c/n$, the polarization field is asymmetric along the direction of motion of the particle, as the particles of the medium do not have enough time to recover to their "normal" randomized states. These results in overlapping waveforms (as in the animation) and constructive interference leads to an observed cone-like light signal at a characteristic angle: Cherenkov light.

A common analogy is the sonic boom of a supersonic aircraft [60]. The sound waves generated by the aircraft travel at the speed of sound, which is slower than the aircraft, and cannot propagate forward from the aircraft, instead forming a conical shock front. In a similar way, a charged particle can generate a "shock wave" of visible light as it travels through an insulator.

The velocity that must be exceeded is the phase velocity of light rather

than the group velocity of light. The phase velocity can be altered dramatically by using a periodic medium, and in that case one can even achieve Cherenkov radiation with v_0 minimum particle velocity, a phenomenon known as the Smith–Purcell effect [60]. In a more complex periodic medium, such as a photonic crystal, one can also obtain a variety of other anomalous Cherenkov effects, such as radiation in a backwards direction (see below) whereas ordinary Cherenkov radiation forms an acute angle with the particle velocity.

Typical picture of Cherenkov radiation is represented in Fig. 1.1. [60].

Fig 1.1: Cherenkov radiation in the University of Massachusetts Lowell Radiation Laboratory [60]

In their original work on the theoretical foundations of Cherenkov radiation, Tamm and Frank wrote, "This peculiar radiation can evidently not be explained by any common mechanism such as the interaction of the fast electron with individual atom or as radiative scattering of electrons on atomic nuclei. On the other hand, the phenomenon can be explained both qualitatively and quantitatively if one takes into account the fact that an electron moving in a medium does radiate light even if it is moving uniformly provided that its velocity is greater than the velocity of light in the medium" [211].

Wyckoff and Henderson (1943) carried out an experiment to check the relation between θ (angle of light emission) and β. They used mica foils (in the thickness range 0.00013-0.0025 cm) which they bombarded with ~ 1 μA

of electrons in the energy range 240-815 *keV*, obtaining the results shown in Fig. 1.2, in which the solid curve is that calculated from the Cherenkov relation. They realized that since mica has a crystalline structure there should be two cones of radiation; these could not be resolved however with the existing resolution.

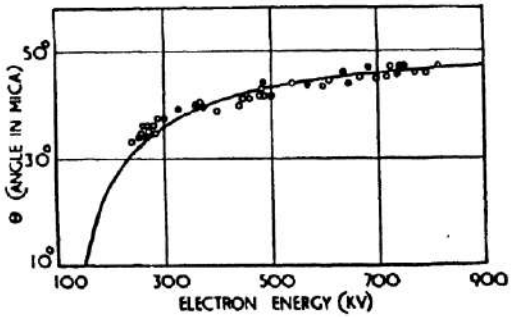

Fig 1.2: The dependence of θ on E. (After Wyckoff and Henderson, 1943.) [96]

Experiments of the same general type were also carried out by Harding and Henderson (1948), who investigated the variations of intensity and polarization of the light in the neighbourhood of the threshold, and arrived at the conclusion that the light was unpolarized at the threshold and rapidly became polarized as the energy of the electrons was increased. A study has been made of Cerenkov radiation from mica in the vicinity of the threshold predicted classically when the incident electron travels with a velocity equal to the velocity of the light which it produces in the medium. The electrons were directly accelerated by means of a Van de Graaff generator and passed through a transverse magnetic field. The magnetic field served not only to provide velocity selection and focusing, but also eliminated the direct light from the filament of the tube from confusing the interpretation of the light from the mica. It is found that:

1) A threshold does exist very close to the conditions predicted by simple theory.
2) The light at the threshold is unpoiarized and rapidly becomes polarized as the electron energy exceeds the threshold and the cone of radiation expands.
3) The total radiation increases approximately linearly with energy above the threshold energy over the region investigated, which is about twice the threshold.

This information at the larger values of electron energy becomes

increasingly uncertain due to larger angles of emission, introducing internal reflection problems within the mica.

To reduce the effective noise from the photomultiplier, Marshall found it better to split the beam by small mirrors *D* and then use two phototubes E run in coincidence; in addition, this arrangement had the advantage that the beam of electrons did not pass through the multipliers themselves. By varying the position of the phototubes, different angles could be selected; the variation of output with angle is shown in Fig. 1.3 [96]. The Cerenkov angle θ calculated for n = 1.50 and $\beta = 1$, is 48°, quite close to the observed maximumat 49.5°. Shortly after these experiments, Marshall (1952) developed a whole range of instruments of the focusing type.

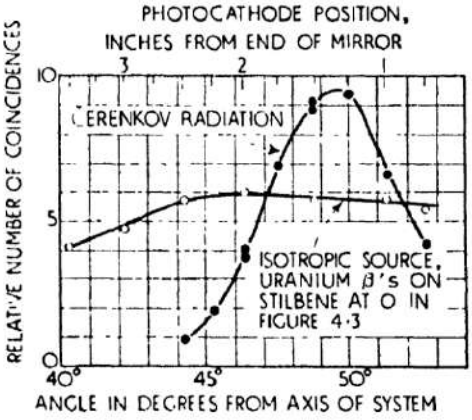

Fig 1.3: Results obtained by Marshall, using fast electrons [96]

Dicke (1947) attempted to detect cosmic-rays with a device similar to that proposed by Getting, mounting the instrument above a Geiger counter in a coincidence arrangement. This experiment gave a negative result, the reason for which has not been explained.

Shortly after this, Weisz and Anderson (1947) tried to detect cosmic rays using the very simple apparatus [96]. They used light-sensitive Geiger counters of special construction which operated in the ultra-violet region of the spectrum, 2000-3000 A, and which had quantum conversion efficiencies in the range $2 \cdot 10^{-4} - 60 \cdot 10^{-4}$ counts/quantum.

The first clear evidence that single fast particles could be detected at high efficiency with a photomultiplier, was obtained by Jelley (1951) who used the simple water detector [96].

Jelley later found that at higher values of bias, at which the counting of

dark-current pulses from the phototube was sufficiently reduced, the detector was sensitive to its orientation. It was then possible to detect particles with a good discrimination against background, without the necessity for the coincidence system, as revealed in the bias curves shown in Fig. 1.4 [96].

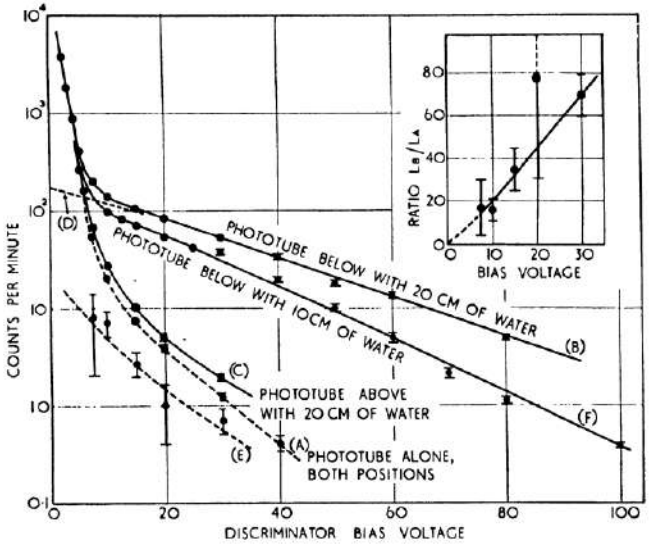

Fig 1.4: Bias curves obtained by Jelley with the counter of his detector [96]

The directional characteristic of this simple cylindrical form of detector is shown in Fig 1.5 [96].

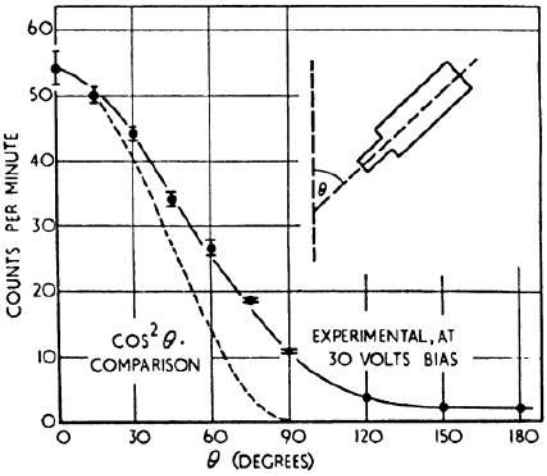

Fig 1.5: The variation of counting rate with zenith angle, obtained by Jelley with his water detector [96]

In a later series of experiments Bassi *et al* (1952) investigated the light output of Cherenkov radiation produced in a Plexiglas converter, as a function of particle energy, using an anticoincidence system with lead absorbers. These results, which appeared to disagree with the theory of Frank and Tamm, were, however, not inconsistent with the predictions of Budini (1953) [96]; nevertheless it must be admitted that their statistics were poor.

A very thorough examination into this question of the possible deviation of the Cherenkov yield from the Frank and Tamm theory, has recently been made by Millar and Hincks (1957) [96]. For this, they used cosmic-ray ft-mesons, the energies of which were selected by lead absorbers in a scintillator telescope arrangement. Their results, which are shown in Fig. 6, reveal that with μ-mesons passing through their Plexiglas radiator, there is no high-energy anomaly up to energies of 4.2 *GeV* for which β = 0.99970 c. The results of other investigators are also reproduced in Fig. 1.6 in which the relative intensity I is plotted against $(\gamma - 1)$, where I is the ratio of the intensity at a velocity βc to the plateau intensity, i.e. $\left(1 - {}^{1}/_{\beta^2 n^2}\right)/(1 - n^2)$, and $\gamma = (1 - \beta^2)^{-1/2}$.

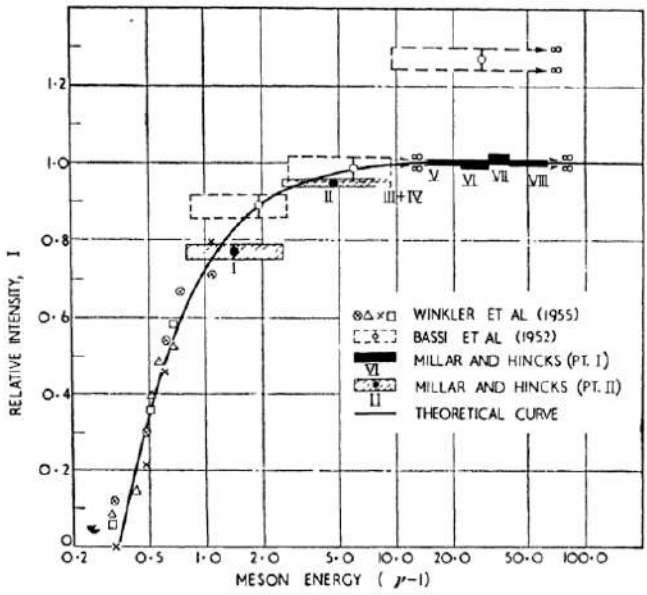

Fig 1.6: The results of experiments by Millar and Hincks (1957) carried out to search for deviations of the Frank and Tamm theory at high energies [96]

A quite different approach to the study of Cherenkov radiation was made

by Belcher in 1953, who carried out a thorough investigation into the faint luminescence observed from aqueous solutions of radioactive isotopes. The results of these experiments are shown in Fig. 1.7 [96] where the average intensity of the radiation, from each sample solution, is plotted against the corresponding maximum energy of the β-particles, in *MeV*.

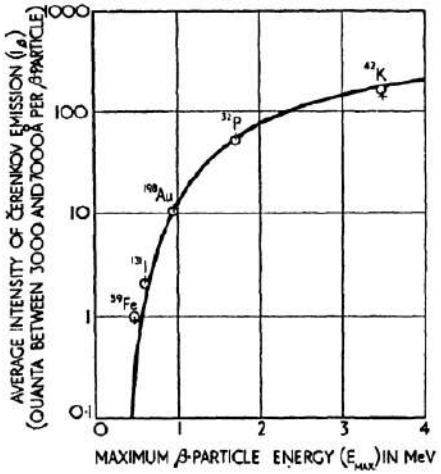

Fig 1.7: Results of Belcher's experiment. (The continuous curve is constructed from the theory of Frank and Tamm) [96]

The isotopes used in this work are indicated beside the experimental points. The full line is that calculated from the theory of Frank and Tamm, taking into account the following factors for which corrections had to be applied: (a) the variation β of along the track of the particle, as it slows down, until its velocity is below the Cherenkov threshold, (b) the energy distribution of the β-particles, (c) the wall-effects, i.e. loss of particles emitted near the boundaries of the container, and (d) effects due to self-absorption of γ-rays when present. A value was obtained for the absolute intensity, which corresponded to an emission of ~90 photons between 300-700 *nm* for a 1 *MeV* electron brought to rest in the solutions. This represents an energy loss, in this wavelength region, of ~ 0-20% of the total energy dissipated by the particle in the medium [96].

Two α-emitting species were also used, polonium 210 and natural uranium. The radiations from these were of course far below the Cherenkov threshold, though a weak visible radiation was nevertheless observed. For instance, in the case of ^{210}Po, which is entirely free from β -radiation, this residual light emission amounted to ~0.5 photon for each α-particle brought to rest (for the same range of wavelengths).

The work described so far has been exclusively concerned with generation of Cerenkov radiation in solids and liquids. Blacken (1948) was the first to point out that the Cerenkov effect should be observable in gases, though it was not until five years later that the radiation from single particles passing through gases was detected [96]. In a gas the refractive index is so close to unity that the general features of the radiation appear rather different from those in solids and liquids. The light intensity is much lower, the threshold energy higher and the maximum angle of light emission smaller. For instance, in air at atmospheric pressure, n = 1.00029, from which it is calculated through the usual relations, that (for electrons) $\theta_{\max} = 1.3°$, $E_{min} = 21\ MeV$ and $(dW/dl)_{\beta=1}$ = 0.3 photons/cm (400-500 nm). For comparison, the corresponding figures for electrons in water are: n = 1.33, $\theta_{\max} = 41°$, $E_{min} = 0.26\ MeV$ and $(dW/dl)_{\beta=1}$= 250 photons/cm.

The first experimental investigations of generating microwaves using the Cherenkov effect were carried out by Danos et al (1953) who used the apparatus shown in Fig. 1.8 [96].

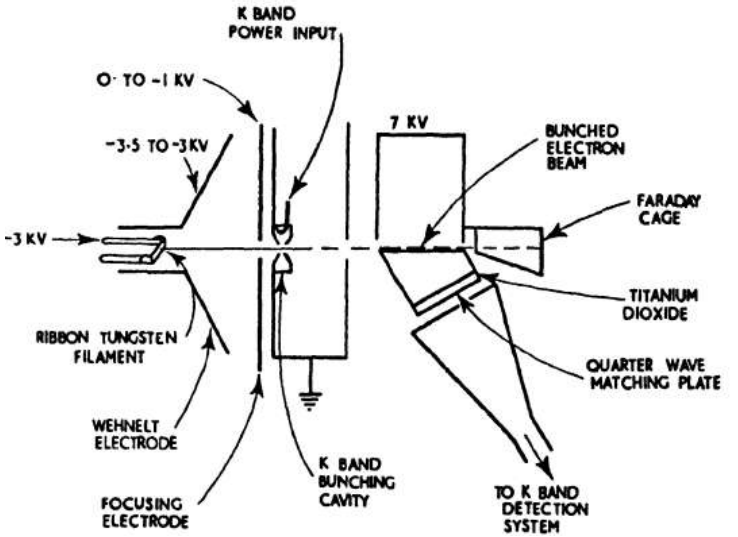

Fig 1.8: Equipment used by Danos *et al*. (1953) in the first detection of Cherenkov radiation at microwave frequencies [96]

A current of 0.2 *mA* of electrons at an energy of 10 *keV* were "bunched" by a cavity driven from an oscillator at a frequency of 24 *kMc/s* (A = 1-25 *c*m). The electron beam, of width 4 *mm* and thickness 0.3 *mm*, was directed over the face of a block of dielectric composed of polycrystalline TiO_2 having a dielectric constant of 105 at the above frequency. The Cherenkov radiation

generated in the TiO_2 at the appropriate angle, was received by an electromagnetic horn coupled to a crystal and meter. In order to facilitate amplification, the electron beam was modulated by switching the cavity on and off at a rate of 6 *kc*/*s*. Discrimination against possible direct interaction between the R.F. oscillator and the receiver was assured by "chopping" the electron beam at 20 *c*/*s*. With this apparatus in its earliest form, 10^{-7} *W* of radiation at this frequency was obtained, which is to be compared with a calculated figure of 10^{-6} W, the maximum possible output from this arrangement. As the distance between the electron beam and the dielectric was increased, the radiation output decreased rapidly, as predicted by theory [96].

The angular distributions of the radiation intensity for liquids with different refractive indices are shown in Fig. 1.9.

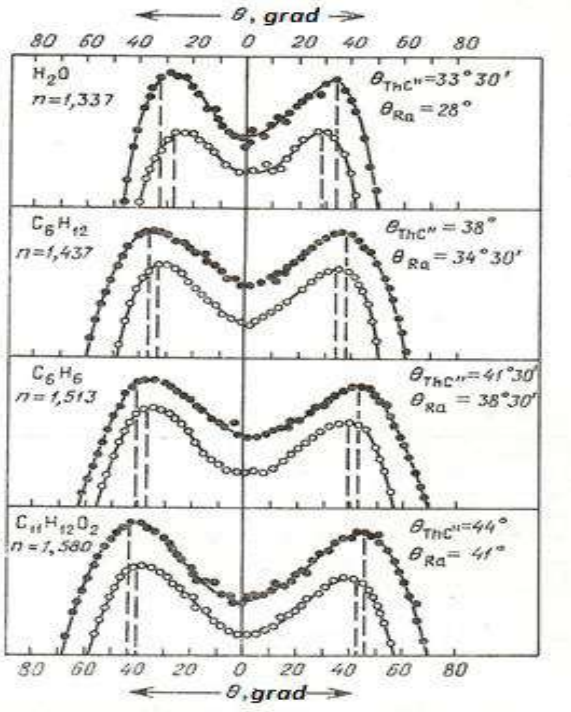

Fig 1.9: The angular distributions of the radiation intensity for liquids with different *n* [96]

The spectral distribution of Cherenkov radiation has a continuous spectrum, the maximum of which is shifted to the short-wavelength region.

As an example, we present the spectra of Cherenkov radiation from the ^{60}Co (Fig. 1.10) [96].

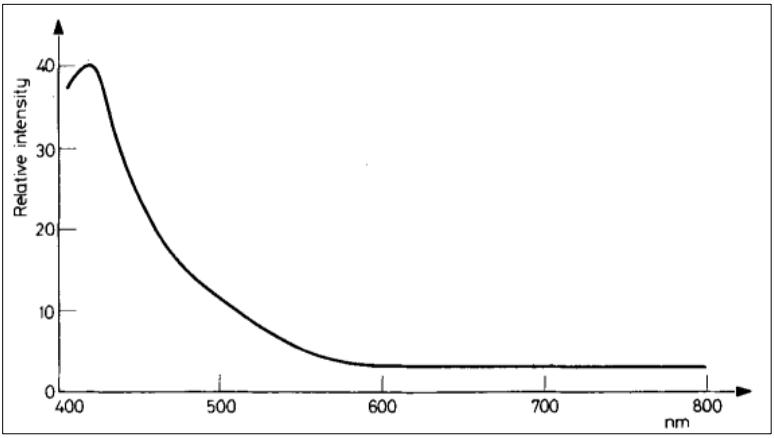

Fig 10: Cherenkov spectrum of ^{60}Co [96]

The spectrum of Cherenkov photons which have travelled 10 *m* in water (Fig. 1.11) [96].

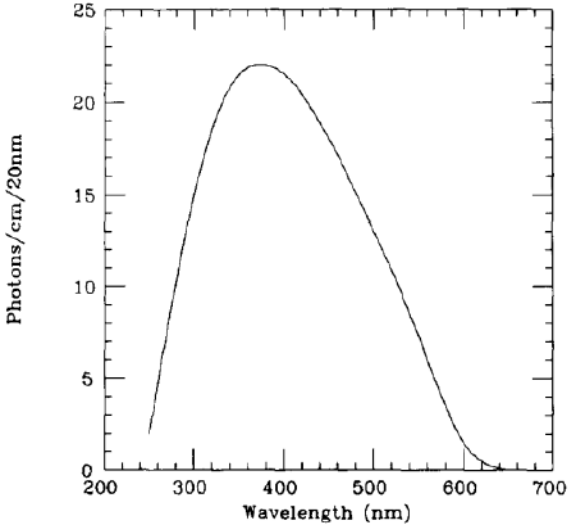

Fig 1.11: The spectrum of Cherenkov photons which have travelled 10 *m* in water [96]

Generation Cherenkov light flashes by cosmic radiation within the eyes of the Apollo astronauts was observing in [96]. The Cherenkov light yield, and the specific ionization, for the particle traversing the ocular media and retina of the eye is representing on Fig. 1.12.

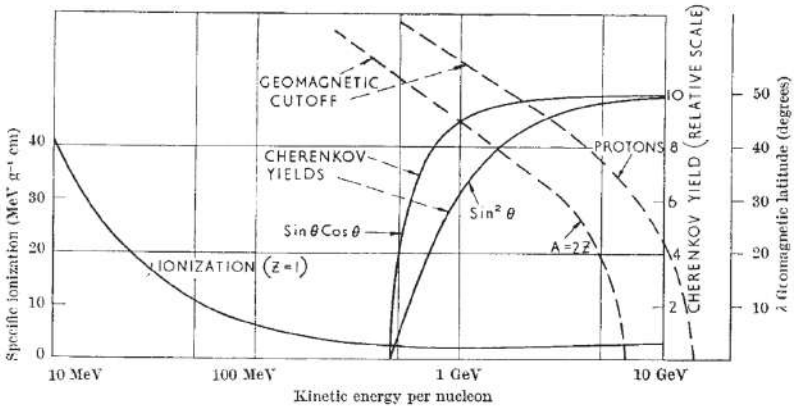

Fig 1.12: The Cherenkov light yield, and the specific ionization, for the particle traversing the ocular media and retina of the eye. Also show are lines representing the rigidity cutoff imposed by the Earth's magnetic field [96]

The experimental setup for receiving the coherent Cherenkov radiation as TERAhertz source has been developed such that the direct interaction of the electron beam and the target can be controlled, and, if necessary, excluded. Non-invasive nature of the Cherenkov radiation gives an additional advantage as the beam parameters are kept almost the same as the initial ones. Therefore, the beam can later be used by other experimental groups during the entire beam time. To realise the plan, we created an experimental setup schematically illustrated in the Fig. 1.13 [26]. Together with Cherenkov radiation the electron beam will generate forward diffraction radiation, which will propagate along the electron beam trajectory but not in the direction of Cherenkov radiation.

In the experiment we plan to use four different target with different AC side lengths to be able to compare the quadratic dependence of the Cherenkov radiation photon yield as a function of the interaction area with the theoretical predictions shown in the figure 1.13b [26]. Geometrically all targets are the same, just the base length is 20, 30, 40, and 50 *mm*. The targets are mounted on a rotation/translation stage (see figure 1.13b) enabling to change the targets with respect to the beam. Horizontal translation also enables optimal impact parameter adjustment. A YAG screen placed downstream the target on a linear translation stage enables us to observe and optimise the electron beam shape and position. The image of the beam is observed in real time by the CCD camera installed outside the vacuum chamber. It shows the target position with respect to the beam.

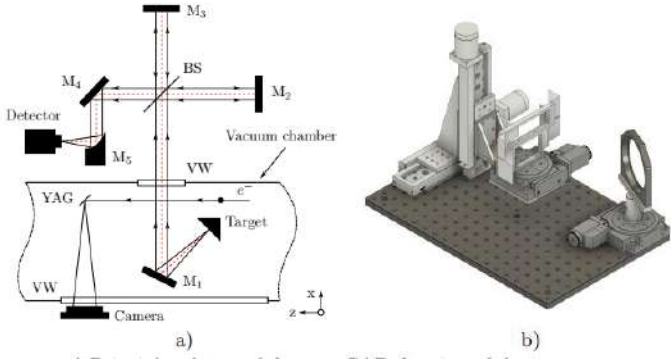

Fig 1.13: a) Principle scheme of the experiment; b) CAD drawing of the in-vacuum target and mirror M1 manipulation system [26]

The Cherenkov radiation induced by the electron beam Coulomb field propagates towards the rotating mirror M1 and, then, which reflects the radiation out of the vacuum chamber through the fused silica vacuum window with the diameter of 150 *mm*. The mirror M1 is mounted on the rotation stage allowing the angular distribution of the radiation to be scanned. In order to measure the spectrum of the generated radiation the Michelson interferometer will be used. The interferometer consists of a stationary mirror M2, movable mirror M3 and a beam splitter BS. After the interferometer the radiation is directed by the mirror M4 to the off-axis parabolic mirror M5 which focuses the beam of radiation into the detector [26]. A pyroelectric and Golay Cell detectors are used to detect the power of the radiation.

Under the influence of a strong electromagnetic field, quantum fluctuations can become polarized, imbuing the vacuum with an effective anisotropic refractive index and allowing the possibility of Cherenkov radiation from the quantum vacuum. We analyze the properties of this vacuum Cherenkov radiation in strong laser pulses and the magnetic field around a pulsar, finding regimes in which it is the dominant radiation mechanism. This radiation process may be relevant to the excess signals of high energy photons in astrophysical observations [MacLeod 2019]. Radiated power from the interaction of an electron with $\gamma = 10^5$ and a crossed field with field strength $E = E_S \times 10^{-3}$, due to various type of radiation is represented in Fig. 1.14 [127].

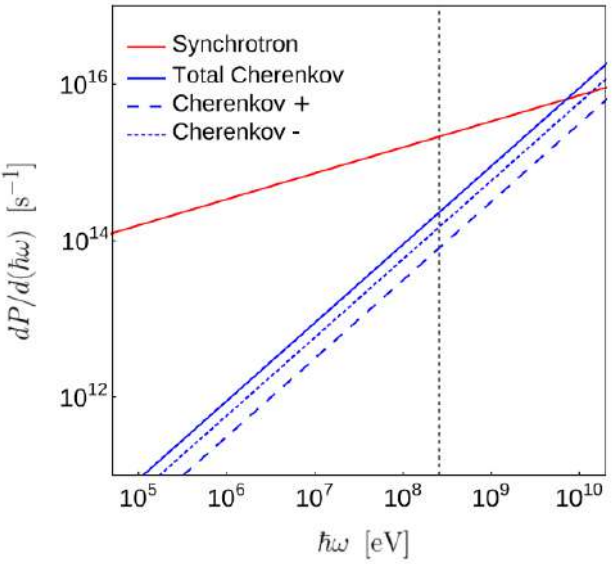

Fig 1.14: Radiated power from the interaction of an electron with $\gamma = 10^5$ and a crossed field with field strength $E = E_S \times 10^{-3}$, due to: synchrotron radiation (red line); total Cherenkov radiation (blue, total line); Cherenkov + mode (blue, dashed line); Cherenkov – mode (blue, dotted line). The cutoff energy (black, dashed line) is $\hbar\omega_{max} \cong 0.25\ GeV$ [127]

Power radiated via synchrotron, pion, and Cherenkov emission, by protons in a magnetic field B = 10^4 T, with Lorentz factor $\gamma = 5\times10^7$ (upper panel) and $\gamma = 5\times10^9$ (lower panel). The cutoff energy is $\hbar\omega_{max} \simeq 225\ GeV$ is represented in Fig. 1.15 [127]. For clarity, we include only the total Cherenkov contribution. For $\gamma = 5\times10^7$, the Cherenkov radiation exceeds synchrotron emission for photon energies above 8.5 GeV but remains below the pion emission up to $\hbar\omega_{max}$. For $\gamma = 5\times10^9$, however, Cherenkov radiation is, by far, the dominant emission channel for photon energies from 54 *MeV* up to the cutoff. So for the highest energy proton cosmic rays, the highest energy radiation is completely dominated by the Cherenkov process.

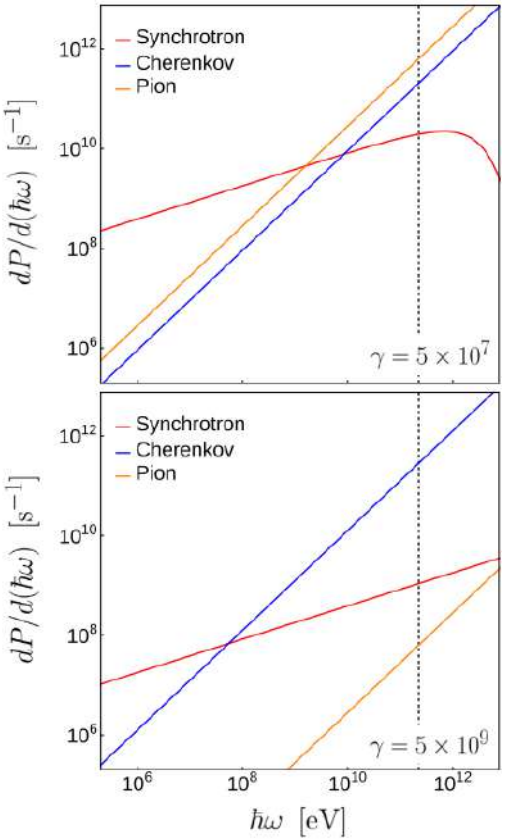

Fig 1.15: Power radiated via synchrotron, pion, and Cherenkov emission, by protons in a magnetic field B = 10^4 *T*, with Lorentz factor $\gamma = 5\times10^7$ (upper panel) and $\gamma = 5\times10^9$ (lower panel). The cutoff energy is $\hbar\omega_{max} \simeq 225\ GeV$ [127]

To summarize, according [127], we have provided a comprehensive, quantitative study of the Cherenkov effect in nonlinear theories of vacuum electrodynamics. This effect – expected due to the reduced phase velocity of light predicted by these theories in regions of strong fields – may provide an alternate radiation mechanism for very high energy particles. We considered two examples of background field with relevance to future experimental or observational campaigns, and determined the possibility of observing Cherenkov radiation in each case. When the background field is a constant crossed field (approximating a laser pulse), the availability of high energy particles appears to put observation of Cherenkov radiation out of reach. In contrast, astrophysics provides environments in which the vacuum Cherenkov effect may be observed due to the presence of very high energy cosmic rays

and strong magnetic fields. We have demonstrated regimes in which radiation due to the nonlinear Cherenkov effect dominates over radiation produced through synchrotron and pion emission, generating very high energy photons. A notable excess of gamma rays with energies in the *GeV–TeV* range has been observed in various astrophysical contexts, and the vacuum Cherenkov process could provide an alternate explanation for their origin, not previously considered in the literature.

In [133] was shown an optical analog of Cherenkov radiation (dispersive wave) is observable in a nonlinear microring resonator generating Kerr frequency comb and containing linearly interacting families of equidistant modes. The radiation results from disruptions in the frequency dependent group velocity dispersion of the pumped cavity modes and is emitted into different mode families of the resonator. This effect reveals itself as a dispersive shaped structure in the spectral envelope of the frequency comb. We found that the dips in the comb spectrum correspond to peaks of the emission of the power in the other mode families of the resonator. The spectrum of the combs that includes both mode families does not have any dips, but peaks and resembles the Cherenkov radiation spectra frequently observed in Kerr comb systems. This Letter shows that a correct description of the Kerr comb in presence of mode anti-crossings should take into account not only the pumped mode family with modified dispersion parameter, but also the modes of the interacting families.

The propagation of the pulse is the analog of the charged particle, and the produced radiation is a dispersive wave. This phenomenon was predicted for optical fiber solitons [133] and was later observed in optical resonators [133].

Optical ring resonators pumped with continuous wave (cw) radiation can produce what is known as Kerr frequency combs [133], which emerge as a result of a symmetry braking phenomenon mediated by the effect of modulation instability [133]. Under favorable conditions, the resonator can support a mode-locked Kerr frequency comb corresponding to a train of short optical pulses [133]. The generation of spectrally broad Kerr frequency combs is essential for their multiple applications, and the involvement of soliton Cherenkov radiation is found to be instrumental for generation of the broadband mode-locked Kerr combs [133]. Cherenkov radiation can occur in presence of high-order dispersion in the resonator when the optical pulses and the dispersive waves are phase matched.

Cherenkov radiation that involves not a single-, but multiple-mode families of a nonlinear optical ring resonator was introducing and,

theoretically and numerically studying [133]. We show that emission of this radiation is associated with the frequently observed cutoff in the spectrum of Kerr combs due to mode anti-crossing. We discovered that in this case a strong dispersive wave is emitted in a mode family interacting with the pumped mode family, facilitating the mode anticrossing and not impacted by the cw optical pump.

The numerical model describes qualitatively the experimental spectra of Kerr frequency combs impacted by mode interaction (Fig. 1.16) [133]. We are able to reproduce the observed interruptions in the comb envelope by modifying the frequency of interacting mode families. Depending on the relative frequency of the crossing mode family, mode anti-crossing can either suppress further spreading of the frequency comb rather significantly, or cause negligible envelope change.

In experiments investigating Kerr combs, only the light exiting the pumped mode family is collected. The high-order mode families interacting with the pumped one are invisible to the observer because of the mode mismatch between them and the coupler. It is possible to observe some of the modes if the pumped mode is significantly overloaded [see Fig. 1.16 (a)] [133].

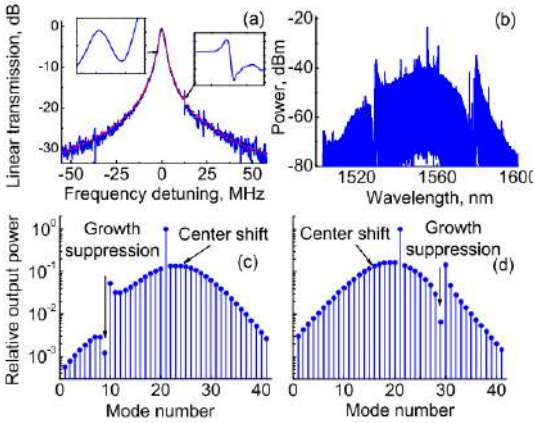

Fig 1.16: (a) Transmission spectrum of a loaded WGM. The red dashed curve stands for the Loretzian fit. High-Q high-order WGMs are coupled through the loaded mode. These modes introduce GVD variations in the resonator. (b) Kerr frequency comb generated in a magnesium fluoride whispering gallery mode resonator with 26 GHz FSR pumped with cw light. The comb envelope is rather irregular due to the interaction among resonator modes, and two significant disruptions of the spectrum having approximately 20 dB contrast are clearly visible at both sides of the pump. Using the numerical model described in this Letter, the disruptions of the spectrum are qualitatively reproduced [panels (c) and (d)] [133].

The first experimental indication of the Cherenkov radiation caused by superluminal particles - tachyons - is informed in [246, 247]. This conclusion has been made on the basis of the analysis of the anomalous Cherenkov radiation when the beam of relativistic lead ions of SPS accelerator at CERN was passing through a gas radiator.

The results presented in [246, 247] based on the analysis of three photoshots which were made with the Cherenkov detector filled with air at the atmospheric pressure. In each case the accumulated statistics was about 10^7 lead ions passed through the detector. One of these pictures is shown in Fig. 1.17. A bright narrow ring of the Cherenkov radiation seen on the picture is caused by relativistic lead ions. Two other narrow rings located inside and outside the ring caused by the beam have the other origin that will be discussed in another paper. Besides, in this picture we have found hardly noticeable narrow Cherenkov radiation rings of the particles flying out under small angles to the direction of the beam. The calculation of the velocity of these particles has shown that it corresponds to those of particles moving faster than the light velocity in the vacuum. The large Cherenkov radiation ring shown with an arrow in Fig. 1.17a corresponds to the particle velocity approximately equal to $\beta = 1.008$. The ring diameter of its radiation is approximately two times larger than the ring diameter of the proton radiation at the velocity of motion $\beta \to 1$. For the better visual representation of this photoshot (Fig. 1.17a), it was scanned by means of a specialized technique of image transformation which provides extraction of 3 rings more in the same photoshot (Fig. 1.17b).

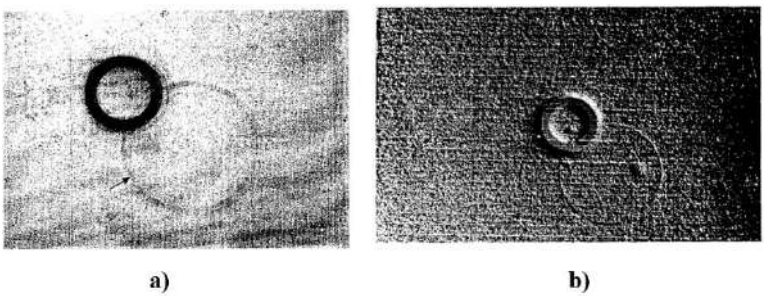

Fig 1.17: a) Example of the observed anomalous Cherenkov radiation ring (indicated by pointer); b) The image of the photoshot of Fig. 1.17 a) obtained by means of a specialized technique of image transformation [246, 247]

It was shown if an electron passes close to the surface of a metal diffraction grating, moving at right angles to the rulings, the periodic motion of the charge induced on the surface of the grating should give rise to radiation. A simple Huygens construction shows the fundamental wavelength to be

$d\ (\beta^{-1} - \cos\theta)$, in which d is the distance between rulings, β stands for $^{v}/_{c}$ as usual, and 6 is the angle between the direction of motion of the electron and the light ray. If d =1.67 microns, as in a typical optical grating, and if electrons of energy around 300 *keV* are used, the light emitted forward should lie in the visible spectrum. As for intensity, if we assume that the surface charge traversing the hills and dales is equivalent to a point charge e oscillating with an amplitude d/10, we find that in the forward direction the radiation (in laboratory coordinates) should amount to 40×10^{-12} *erg* (about ten photons) per *sterad* per *millimeter* of electron path. Only if the electron path lies within perhaps d/2 of the grating will the surface charge be so well localized. Nevertheless, with a reasonable electron current density over the surface an easily detectable amount of light should be produced. In fact, under the assumed conditions, the total radiation per cm^2 of grating surface, in milliwatts, should be about four times the electron current density parallel to the surface in amp/cm^2.

Results on the generation of X-ray Cherenkov radiation [20] were also obtained and a conclusion was made about compact X-ray radiation sources.

1.3 Supercontinuation radiation

We will now give typical examples of the generation of supercontinuum radiation in three media: gases, liquids, and solids.

Spectral broadening and the generation of new frequency components are inherent features of nonlinear optics, and have been studied intensively since the early 1960s. A fascinating perspective on the history of this subject has been given by Bloembergen [27]. The particular process known as supercontinuum (SC) generation occurs when narrow-band incident pulses undergo extreme nonlinear spectral broadening to yield a broadband very often a white light spectrally continuous output. Supercontinuum generation was first reported by Alfano and Shapiro [9, 10] in bulk glass, and has since been the subject of numerous investigations in a wide variety of nonlinear media, including solids, organic and inorganic liquids, gases, and various types of waveguide. Supercontinuum generation has found numerous applications in such diverse fields as spectroscopy, pulse compression, and the design of tunable ultrafast femtosecond laser sources. In a telecommunications context, the spectral slicing of broadband SC spectra has also been proposed as a simple way to create multiwavelength optical sources for dense wavelength division multiplexing applications. An extensive review of the research into SC generation and its applications before 1990 is given in Part I of the [9]. The advent of a new class of optical waveguides in the form of the photonic crystal

fiber (PCF) in the late 1990s attracted widespread interest throughout the scientific community, and has led to a revolution in the generation of ultrabroadband high brightness spectra through SC generation Ranka *et al*. [174]; Knight [108]; Russell [181]. The characteristics of PCFs that have led to such interest relate to their guidance properties that yield single-mode propagation over broad wavelength ranges, their enhanced modal confinement and therefore elevated nonlinearity, and the ability to engineer their group velocity dispersion Reeves *et al*. [180]. The design freedom of PCFs has allowed SC generation to be observed over a much wider range of source parameters than has been possible with bulk media or conventional fibers. For example, experiments have reported SC generation using unamplified input pulses of durations ranging from tens of femtoseconds to several nanoseconds, and even using high-power continuous wave CW sources. Supercontinuum generation in PCFs has subsequently been widely applied in interdisciplinary fields such as optical coherence tomography, spectroscopy, and, particularly, in optical frequency metrology. In this field it has led to the development of a new generation of optical clocks, and has opened up new perspectives to study limits on the drift of fundamental physical constants Jones *et al*. [97, 98]; Holzwarth *et al*. [88]; Udem *et al*. [254]. The award of one-half of the 2005 Nobel Prize in Physics to Hall and Hänsch is of course a measure of the tremendous significance and impact of this work in precision frequency metrology [58].

Because of the evident significance of PCF-generated supercontinua, a complete understanding of the various underlying physical mechanisms is of prime importance [58]. Somewhat paradoxically, however, the ease with which SC generation in PCF has been observed experimentally has actually made it relatively difficult to understand in clear physical terms. In particular, the wide range of fiber types, pulse durations, and pulse energies that have been used in experiments has led to confusion in isolating the relative contributions of processes such as selfand cross-phase modulation, four-wave mixing, modulation instability, soliton fission, dispersive wave generation, and Raman scattering. As a result, significant misunderstanding has developed in the existing literature, and incorrect identification of the underlying physical processes corresponding to particular experimental conditions is not unusual. This naturally represents a disadvantage for researchers who are not specialists in nonlinear ultrafast optics, because it appears that there is no straightforward way in which to interpret the physics of what is clearly a phenomenon of much interest. Our objective here is to address this problem, and to present a unified discussion of the various nonlinear SC spectral broadening processes. We structure our review around numerical simulations that illustrate the SC generation characteristics for conditions covering the typical experimental

parameter range. We focus on the underlying physics of the nonlinear spectral broadening processes and aim to complement existing, more general, descriptions of PCF nonlinearities that have been given by Knight [58], Russell [58], and Zheltikov [58]. In this way, we hope that the reader will be well prepared to study in detail more specific discussions of SC applications such as those by Hansen and Smirnov [58].

In the first observation of SC generation, Alfano and Shapiro [10] reported the generation of a white light spectrum covering the entire visible range from 400 to 700 nm after propagating 5 mJ picosecond pulses at 530 nm in bulk BK7 glass. Shortly afterward, similar results were reported independently by Bondarenko *et al*. [36]. It is important to note that the nonlinear spectral broadening of laser light was not completely new at the time, having been observed earlier by Stoicheff [203]. Indeed, Jones and Stoicheff [97] had even applied a relatively narrow "continuum" of light in what was the first inverse Raman spectroscopy measurement. Spectral broadening had also been reported in CS2 Brewer [39], and correctly interpreted in terms of the nonlinear process of self-phase modulation SPM Shimizu [194]. What made the experiment of Alfano and Shapiro [10] so exciting was the sheer extent of the spectral width of the generated light, more than 10 times wider than anything previously reported. Interestingly, the authors do not particularly emphasize this aspect in their publication. Their work is actually dedicated to the first identification of nonresonant four-photon coupling, i.e., four-wave mixing. The term "supercontinuum" was not even used in Alfano and Shapiro's paper [10], and was only introduced later Manassah *et al*. [128, 129]. In the meantime, the phenomenon of SC generation was referred to as superbroadening Bondarenko *et al*. [36]; Il'ichev *et al*. [91], anomalous frequency broadening Werncke *et al*. [261]; Bloembergen [27], or white-light continuum Fork *et al*. [68]. From the start, it was clear that self-focusing was a key ingredient to SC generation in bulk media, as it was commonly observed that the SC threshold coincided with the critical power for catastrophic collapse, usually associated with the formation of self-trapped filaments Chiao *et al*. [48]; Alfano and Shapiro [10]; Bondarenko *et al*. [36]; Il'ichev *et al*. [91]; Werncke *et al*. [261]. Beam collapse leads to an explosive increase in the peak intensity, which enhances SPM, but which also gives rise to a range of higher-order nonlinear effects, including self-steepening, space-time focusing Rothenberg [58], multiphoton absorption, avalanche ionization, and the formation of a free-electron plasma Bloembergen [58]. In particular, Werncke *et al*. [261] postulated that SC generation corresponded to "an essential deformation of light pulses within the filaments which should lead to a steepening of the backside of the pulse." Self-phase modulation associated with this very steep negative intensity slope then explains the broad extent of bulk SC spectra on the blue side of the pump.

Bloembergen [27] also pointed out that the defocusing effect of the electron plasma could lead to similar behavior. It was not until the work by Gaeta [58], however, that a consistent explanation emerged based on full three-dimensional simulations of light propagation. It is now accepted that white-light continuum generation in bulk material is due to the formation of an optical shock at the back of the pump pulses due to space-time focusing and self-steepening, confirming the early ideas of Werncke *et al.* [261]. The role of multiphoton absorption and plasma formation is simply to arrest the collapse of the beam and to prevent the optical breakdown of the material. Self-trapped filaments may or may not form in the process depending on the pulse duration and on the relative strength of chromatic dispersion, self-focusing, and plasma defocusing Aközbek *et al.* [5]. This scenario is in agreement with all known observations, including the dependence of SC generation on the band gap of the material Brodeur and Chin [40]. In material with a small band gap, self-focusing is stopped at lower intensities by free-electron defocusing, preventing the formation of a shock. From this summary, it is clear that SC generation in bulk material is a highly complex process involving an intricate coupling between spatial and temporal effects. In contrast, SC generation in optical fibers involves purely temporal dynamical processes, with the transverse mode characteristics determined only by linear waveguide properties. In fact, this suggests that a further motivation to study SC generation in PCFs is to clarify the nature of temporal nonlinear propagation effects in order to improve the understanding of the more complex spatiotemporal bulk case.

The first SC generation experiments in optical fiber injected high-power pulses in the visible spectral region into standard silica-based optical fiber with zero group velocity dispersion GVD wavelength around 1.3 μm. In particular, Lin and Stolen [123] used visible kW peak power pulses from a nanosecond dye laser to generate a SC over a spectral range of 200 THz on the long-wavelength side of the pump. The observed spectral broadening was attributed to cascaded stimulated Raman scattering and SPM. Subsequent experiments using visible pump pulses in the 10 ps– 10 ns range produced similar results. These studies also clarified the im portance of the mutual interaction between Raman scattering and SPM, as well as the role of cross-phase modulation XPM and various four-wave-mixing processes in providing additional broadening, and in merging discrete generated frequency components to produce a spectrally smooth output Stolen *et al.* [204]; Baldeck and Alfano [16]; Ilev *et al.* [90]. The Raman and SPM-dominated broadening in the experiments above was observed for the case of normal GVD pumping. When pumping in the anomalous GVD regime, however, spectral broadening arises from soliton-related dynamics. The possibility of soliton propagation in the anomalous

GVD regime of optical fibers was first suggested from theoretical analysis of the nonlinear Schrödinger equation NLSE by Hasegawa and Tappert [83], but the lack of ultrashort pulse sources at wavelengths 1.3 m delayed experimental observation until the work of Mollenauer *et al*. [145]. In these experiments, 7 ps pulses around 1.55 μm were used to excite not only a nonbroadening stable fundamental soliton, but also higher-order solitons that were observed at increased power levels. A higher-order soliton1 is a particular class of solution of the NLSE representing a bound state of N fundamental solitons Zakharov and Shabat [272]; Satsuma and Yajima [186]. Such solutions propagate in a complex manner consisting of both spectral and temporal compression and splitting, followed by subsequent recovery to the original pulse shape after a characteristic propagation distance known as the soliton period. Experiments using picosecond pulses at 1.55 μm have studied different aspects of higher-order soliton propagation, including explicit measurements of pulse restoration over a soliton period Stolen *et al*. [205] and application to pulse compression Mollenauer *et al*. [144]. These latter experiments are of particular significance because they show that, although higher-order soliton evolution can be very complex, the initial phase of propagation is always associated with relatively simple SPM-induced spectral broadening and temporal compression due to the fiber-anomalous GVD. Also of much importance in this context are a number of early studies on the sensitivity of soliton propagation to perturbations such as Raman scattering and higherorder dispersion. For the case of a fundamental soliton, intrapulse stimulated Raman scattering i.e., Raman scattering within the soliton bandwidth was found to lead to a continuous downshift of the mean frequency known as the soliton self-frequency shift Gordon [79]; Mitschke and Mollenauer [143]. In a study of solitons propagating close to the fiber zero-dispersion wavelength ZDW, Wai *et al*. [256] numerically studied the effect of third-order dispersion on soliton stability and found significantly different consequences for fundamental and higher-order solitons. For fundamental soli tons, although the shape of the soliton was only slightly affected, third-order dispersion was found to stimulate the resonant transfer of energy from the soliton to a low-amplitude nonsolitonic narrow-band dispersive wave background with frequency in the normal GVD regime. In contrast, higher-order soliton evolution was found to be more seriously perturbed by higher-order dispersion, with the soliton temporally breaking up and separating into its constituent fundamental soliton components. This process is now generally referred to as soliton fission. Soliton fission is an important example of symmetry breaking in a nonlinear optical system, and has been studied extensively. Kodama and Hasegawa [111] derived explicit expressions for the amplitudes and widths of the constituent fundamental soliton components, and showed that the energy of the higher-

order soliton was equal to the sum of the energies of its components. In fact, while seemingly a trivial observation, this result highlights the intrinsic instability of higher-order soliton propagation that arises from an absence of any binding energy. Indeed, numerical studies by Golovchenko *et al.* [58] noted the instability of higher-order soliton propagation in the presence of self-steepening, and other theoretical and experimental studies have shown that it can be induced by Raman effects Dianov *et al.* [53]; Tai *et al.* [210], two-photon absorption Silberberg [196], and input pulse chirp perturbations Friberg and DeLong [71]; Krylov *et al.* [113]. Experiments on soliton fission around 1.3 μm were performed by Beaud *et al.* [23] and Schütz *et al.* [190] using 1 – 3 ps pulses, Gouveia-Neto *et al.* [80] using 90 ps pulses, and around 1.55 μm by Islam *et al.* [92, 93] using 14 ps pulses. These results showed that soliton fission leads to an equivalent form of SC generation, allowing broadband spectral generation over the telecommunications wavelength range. Moreover, numerical simulations clarified that the SC generation process occurred broadly in three phases: i an initial period of spectral broadening and temporal compression, ii fission into a series of distinct fundamental soliton components, and iii the continued propagation of these solitons. This last phase was shown to be associated with a continuous shift to longer wavelengths through the Raman soliton self-frequency shift and the generation of corresponding dispersive waves on the short-wavelength side of the ZDW. This detailed physical interpretation was present in the literature by 1989, and the same mechanisms continue to play dominant roles, even in the different parameter regime associated with PCF [58]. Islam *et al.* [92, 93] and Nakazawa *et al.* [153] interpreted the soliton fission process in terms of a modulation instability process on the input pulse envelope. Modulation instability is a phenomenon exhibited by waves propagating in nonlinear dispersive media, in which weak amplitude perturbations at different frequencies are subject to gain. In whole, the development of a temporal modulation on the input field is associated with the growth of sidebands at characteristic frequencies and can equivalently be interpreted in terms of a four-wave-mixing process. These studies were significant in highlighting the sensitivity of soliton fission to input pulse noise. Because the nonlinear pulse propagation depends on input power, fluctuations on the input pulse can lead to jitter in both the spectral and temporal characteristics. This has practical consequences in that the actual spectral characteristics observed are an ensemble average of constituent fundamental solitons that have undergone different frequency shifts. The fact that such jitter could introduce an effective smoothing of spectral characteristics had, in fact, been previously noted by Beaud *et al.* [23] and by Islam *et al.* [92, 93]. This latter work also reported experimental characterization of spectral instabilities using cross-correlation between different SC spectral bands to demonstrate that

different output wavelengths were not necessarily simultaneously present in each individual pulse. The possibility of generating broadband SC spectra around 1.3 μm and 1.55 μm motivated research aimed at developing multiwavelength sources for wavelength division multiplexing transmission Morioka *et al*. [146, 147]. For such applications, the absolute bandwidth required is relatively low around 20– 40 THz, but it is important that the SC source is generated at GHz repetition rates with low noise and with a flat spectrum. A number of experiments were therefore carried out to study the instabilities observed during soliton fission in more detail. Nakazawa *et al*. [153] characterized what they termed coherence degradation by observing the noise level between longitudinal modes of the broadened spectrum see also Kubota *et al*. [114]. The timing jitter of SC pulses was analyzed by Nowak *et al*. 1999 using the standard technique of measuring the energy of a high harmonic of the rf spectrum von der Linde [58], and directly using a sampling oscilloscope by Tamura *et al*. [211]. Boyraz *et al*. [38] used a different approach by checking that pulse trains carved out of the SC exhibited the correct behavior with regard to SPM-induced spectral broadening and mode-beating induced repetition rate multiplication after dispersive propagation. Although the majority of SC generation studies in conventional fiber focused on the regime where pumping used ultrafast pump pulses, the detailed physics underlying SC generation using longer pump pulses or CW excitation remained a subject of active research. Particularly important work was reported by Golovchenko *et al*. [75, 76] where numerical simulations were used to elucidate the relationship between modulation instability, soliton dynamics, and Raman scattering under CW pump conditions. This work highlighted the fact that the SC generation in the anomalous GVD regime using CW pumps also involved soliton dynamics as in the case of pulsed excitation. Although an important physical insight, the lack of suitable high-power CW sources somewhat limited follow-up experimental studies in this field.

On Fig. 1.18 experimental data, which are received for sodium containing heat-pipe with 20 *cm* active length and a Hänsh-type 10 *kW* peak dye laser, are represented. The sodium density was $10^{14} – 10^{16}$ cm^{-3}. The beam of 0,5 cm^{-1} bandwigth laser was focused by a lens into the sodium cell after special filtering. The laser intensity at the focus was 10 MW/cm^2 and is sufficient for the formation of self-trapped filaments. The forward emission was photographed by an Alphax B216 camera with f/number of 1,9, placed after the sodium cell without any imaging optics [71]. The laser beam was blocked with small on axis disc to prevent over-expose.

The spectral and angular properties of the conical radiation are well-known [71]. The cone angle is 1º – 3º and increases as the laser frequency

approaches the atomic transition and with increasing sodium density. The cone spectrum is broad (5 – 10 cm^{-1}) and is to the red of the transition. For small laser detuning (5 – 10 cm^{-1}) the peak of conic emission is detuning. For large laser detuning (6 – 20 cm^{-1}) the peak detuning exhibits saturation behavior; the limiting value is at the dispersionless point – 589,4 *nm* [71].

Two kinds of experiments were performed to establish the surface character of the conical emission. The light changes polarization of initial beam in a linear case, with a direction determines the difference of right and left polarizations. Self-trapping of laser light close to the transition is due to saturation effects, and this change in polarization is expected to occur inside the filaments, where saturation degree is maximum. In [71] next conclusion was made: conical radiation is generated at a nonsaturated region such as self-trapped filament surface.

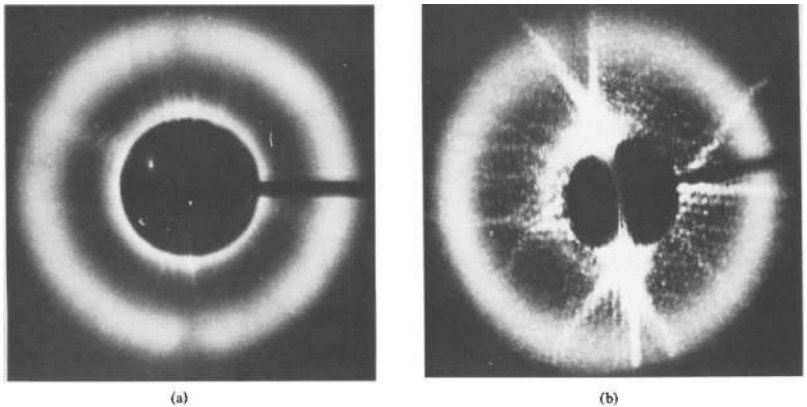

Fig 1.18: The pattern of the conical radiation at sodium density $1{,}8 \cdot 10^{15}$ cm^{-3} and laser detuning of 0,2 *nm* to the blue of the D_2 transition. The laser radiation is focused into the sodium cell bay a spherical lens (a) and by a cylindrical lens (b). The laser beam is blocked with a small of on-axis disc. The focal line of the cylindrical lens (b) is the long of horizontal line [78]

Two kinds of experiments were performed to establish the surface character of the conical emission. The light changes polarization of initial beam in a linear case, with a direction determines the difference of right and left polarizations. Self-trapping of laser light close to the transition is due to saturation effects, and this change in polarization is expected to occur inside the filaments, where saturation degree is maximum. In [78] next conclusion was made: conical radiation is generated at a nonsaturated region such as self-trapped filament surface.

The question about spatial coherence of conical radiation was observed

in [78]. It was found that the angular and spectral distribution of the conical radiation is independent of lens type. The next conclusion was made the conical radiation from various filaments add upp incoherently and display no interference pattern.

The data of laser irradiated different 1 – 10 *cm* – long cells containing H_2O or D_2O are represented in Fig. 1.19 [78]. In these experiments a Quantel YG-471 mode-locked laser was used, which produced 22-psec-duration pulses at 1,06 μm of aup to 35 *mJ* energy or its second harmonic 15-psec-duration pulses of 12 *mJ* energy. A variefy of lenses with focal lengths from 2 to 25 *cm*, capable of producing intensities in the focal spot of up to 10^{12} W/cm^2. Several (usually 5 to 10) filaments were produced by each pulse/ It was easier to produce supercontinuum by focusing the laser beam with long-focal-length lenses into the long cells, and the threshold for supercontinuum in D_2O was lower than that in H_2O. The supercontinuum was spread in a circular reinbow, and for 1,06-μm excitation the generated photon energy increases with the off-axis angle, while for 0,53-μm excitation the pattern is more complicated.

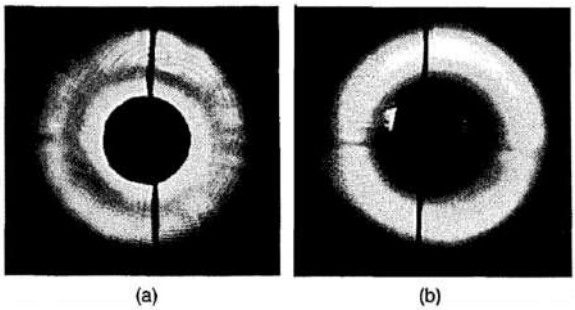

Fig 1.19: Supercontinuum generated in D_2O by 0,53-μm laser excitation. The laser is focused into the cell (a) by a spherical lens or (b) by a combination the spherical and cylindrical lenses. The laser beam is blocked with a small of on-axis disc. The focal line of the cylindrical lens (b) is the long of vertical line [77]

Data of Fig. 1.19 shown that spatial pattern of the supercontinuum conic radiation is independent of the focusing mode, leading one to conclude that the origin of this emission is at the surface of the filaments.

Supercontinuum spectra, which are received a Raman fibre laser emitting around 1455 *nm* was used, i.e. in the vicinity of the zero dispersion wavelength (λ_0) of a nonzero dispersion wavelength fibre (1453 nm) [249] (see Fig. 1.20). Note that all the pump power levels we quote in this paper represent the power that is effectively launched into the NZDSF, taking into account an 80 %

coupling efficiency. For low pump power levels ($P_p \neq 0.24$ *W*), the output spectrum exhibits a clear signature of the influence of FWM through the generation of two nearly symmetric modulational instability (MI) sidebands around the pump frequency. The asymmetry in the intensity of those sidebands is caused by SRS amplification of the longer wavelengths and attenuation of the shorter ones. For higher pump powers, the effective FWM and Raman gains increase, which leads to a continuous broadening of the generated spectrum. Note that this broadening mainly occurs on the long wavelength side of the pump wave but that short wavelength components are also significantly generated. Beyond a pump power $P_p \approx 1.2$ *W*, all the pump energy has been transfered to the SC and nearly complete pump depletion is achieved (see the inset of Fig. 1.20). At this point, our SC has a 20-*dB* bandwidth of over 200 *nm* and a peak power spectral density > 8 *dBm*/*nm*.

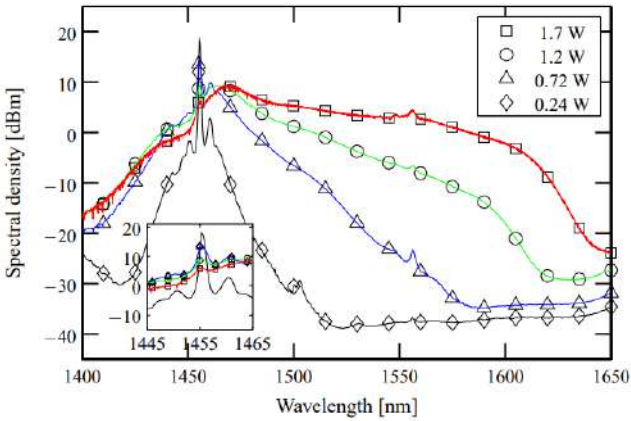

Fig 1.20: Supercontinuum spectra with different pump powers at room temperature (≅ 20°C). All the curves have been normalized to the same peak value. Inset shows how increasing pump power leads to a stronger pump depletion [249]

A Q-switched ruby laser beam with diameter 3 *mm* was used to produce filaments in a carbon disulfide liquid cell of 7.5 *cm* length [194]. The intensity distribution of the light at the end of the cell was projected on the entrance slit of a spectrometer using a 5.2-*cm* focal length lens with magnification of 17. In order to eliminate the nonscattered part of the laser beam from that in filaments, a wire with diameter of 1 *mm* was placed at the focusing point of the lens perpendicularly to the slit of the spectrometer. The entrance slit was wide open (about 2 *mm*). The resolution of the spectrum was determined from the magnitude of the image of the filament. The laser beam was composed of four or five groups of axial modes, the separation of the groups being approximately 0.45 cm^{-1}. With this mode structure the intensity of the laser

beam changes considerably within the time interval $1/\Delta\nu$, where $\Delta\nu$ is the total spectral width. Therefore, at relatively low laser power the duration time of the filament is expected to be 10^{-11} *sec* or less. (In the present experiments the laser power was kept lower than 50% above threshold for observations of optical trapping.) The total energy of a filament estimated from the photographic emulsion sensitivity is less than 10^{-7} *J*. Since the threshold for optical trapping in carbon disulfide is approximately 2 to 20 *kW*, this energy also leads to a duration time of the order of 10^{-11} *sec*. Typical spectra of the individual filaments in carbon disulfide are shown in Fig. 1.21 [194].

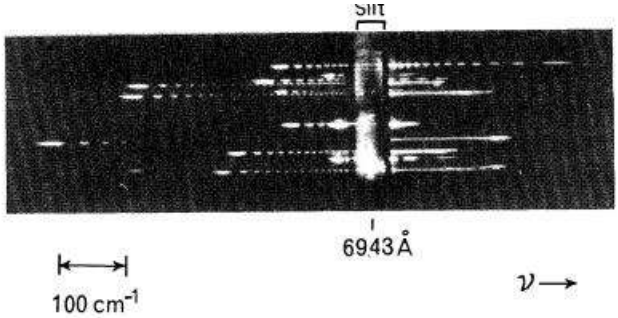

Fig 1.21: Spectra of filaments in CS_2 excited with a single laser pulse. The vertical structure is produced by individual filaments occurring during the pulse. The frequency broadening (and periodic structure) is displayed in the horizontal direction and is evidently different for each filament. The image of the slit and the low-frequency side of the spectrum (at left) are attenuated by factors of 41 and 13, respectively, in comparison with the high-frequency side of the spectrum. (Some of the vertical fine structure within each filament is caused by diffraction by the masking wire placed at the focus of the objective lens.) [194]

A regular periodic structure is observed in the low-frequency side of the broadening in every filament, when the broadening is smaller than the Raman shift. The period in a filament increases linearly with the amount of the broadening from the center. The average period for most filaments is 10±3 cm^{-1} irrespective of the total magnitude of the broadening. The ratio between the intensity maxima and minima is at least 10. Most of the energy (about 90%) lies in the low-frequency side. The overall intensity is fairly uniform throughout the low-frequency side with an intensity maximum at the low-frequency extremity. In most cases an intensity peak is also observed at the laser frequency itself. A periodic structure but with larger spacing is also observed in the high-frequency side. The structure is smeared out when the low-frequency broadening is relatively large.

Self-focusing of few-cycle pulses in atmospheric-pressure argon results in a supercontinuum which differs remarkably from the case of longer pulses: under single-filament conditions it extends to 200 *nm* and 250 *nm* with 6 *fs* and 10 *fs* pulses, respectively; the radiation, including the shortest wavelengths, is collimated and shows no conical emission. The short-wavelength part is intrinsically at least as short as the incoming fundamental pulse. These features make the few-cycle supercontinuum attractive as a source of widely tunable 10 *fs* pump pulses for spectroscopic applications [112].

Two different Ti-sapphire laser systems were used in [112]. Most experiments were performed with a commercial system (Spectra-Physics Tsunami and Spitfire). It emits pulses at 805 *nm* with energy of 2 *mJ*, pulse duration of 45 *fs* (FWHM), spectral half-width of 35 nm (16 *THz*) at a repetition frequency of 1 *kHz*. To obtain shorter pulses, the beam (initial diameter of 3w = 16 *mm*) was attenuated to 0.7–1 *mJ* (to avoid multiple filamentation) and was focused by a mirror with a focal length of f = 2 m into a glass cell, which was typically windowless and 150 *cm* long, containing slowly flowing argon at ambient pressure (950 mbar). The emerging radiation was recollimated and then three times reflected from chirped mirrors (Layertec, group delay dispersion 120 fs^2). The resulting pulses have a duration of 10–11 *fs*, measured by an interferometric autocorrelator, and a spectral half-width of 100–110 *nm* (47–52 *THz*). Using air instead of Ar results in pulses of 14 *fs*. After the compression, the pulses were refocused to a second windowless cell with Ar flow, this time by a mirror with $f = 1$ *m* (sometimes 1.5 *m*) and a variable diaphragm ('input iris') before the focusing mirror (Fig. 1.22) [112].

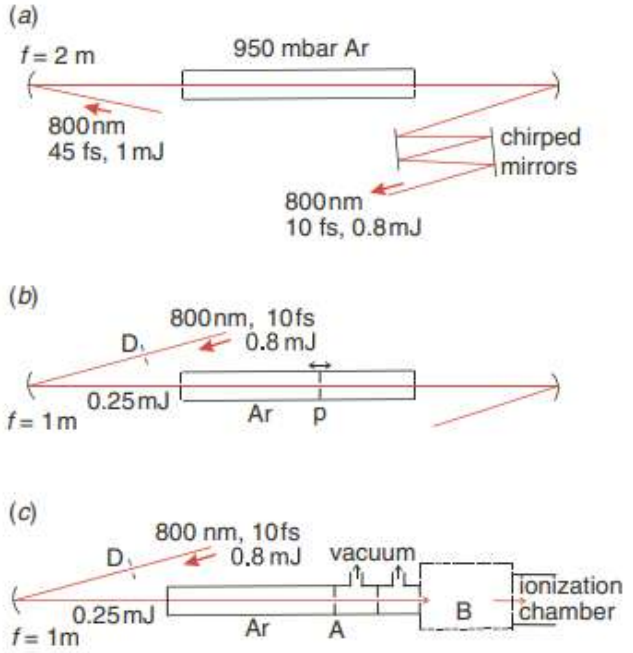

Fig 1.22: Setup for generation of (a) the 10 fs pulses and (b) the supercontinuum with atmospheric beam path; the geometrical focus is in the center of the Ar cells; p is an optional pinhole movable along the filament. (c) Setup with termination of the filament by an aperture A near the geometrical focus and a vacuum beam path (with differential pumping and additional apertures) beyond A; in the evacuated box B the beam is collimated and focused (dielectric mirrors) to the detection setup (ionization chamber). D is a variable diaphragm (iris). Typical parameters are indicated [112]

The spectrum of the emerging radiation was measured by a calibrated broad-band spectrometer (Ocean Optics) covering the range of 1100–200 *nm*, in some cases by a UV spectrometer (520–200 *nm*). In most cases, before entering the spectrometer the full beam was spatially integrated by an Ulbricht sphere coated with PTFE. When in contrast the spectral variation over the beam cross-section was to be measured, we used a variable diaphragm before the integrating sphere. The spectra shown in the figures are typically integrated over about 1000 pulses; however, observing single-pulse spectra showed that the shape including the spectral structures are stable from pulse to pulse under conditions, when only a single filament was generated. For comparison, the spectrum after the first cell (with 45 *fs* incident pulses) was also investigated, using focal lengths of f = 1 and 2 *m*. In some experiments, the cell was equipped with windows of quartz glass (0.2 *mm*) or CaF_2 (0.5 *mm*), so that the pressure could be varied. These cells also served to investigate mixtures of Ar with He.

Fig. 1.23 [112] shows a spectrum integrated over the output beam cross-section under conditions optimized for the maximum of energy in the 300 *nm* region, i.e. with the iris diameter d = 5 *mm* and the incident E_p = 0.26 *mJ*. (A spectrum of the incident radiation is also displayed for comparison.) It is fully continuous and extends as far as 250 nm to the UV. In the near IR, it reaches to about 2 *mm* (not shown), as found by a scanning spectrometer1. The general shape of the spectrum including the cutoff and the structures [8] is stable from pulse to pulse. An independent measurement of some spectral parts, using dielectric filters, showed that the UV edge should be lifted by a factor of 2 [8]; probably the calibration curve of the spectrometer is not sufficiently accurate in this region.

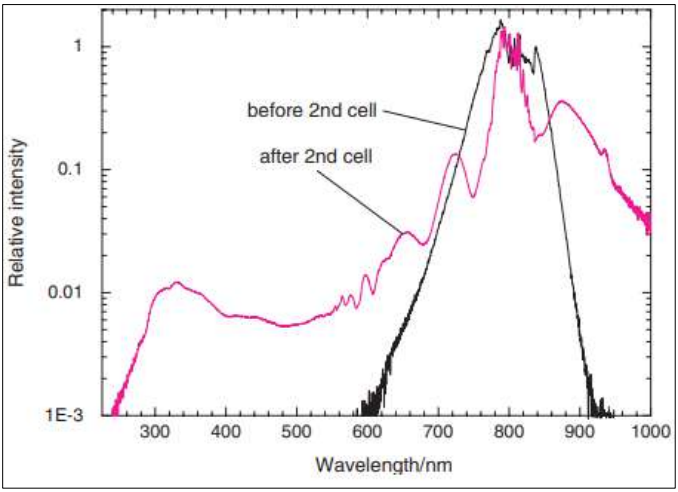

Fig 1.23: Spectrum ('after 2nd cell') integrated over the output beam under conditions optimized for the maximum of energy in the 300 *nm* region, i.e. with the iris diameter d = 5 mm and the incident E_p = 0.26 mJ (pulse duration τ_p=10 *fs*). A spectrum ('before 2nd cell') of the incident radiation is also displayed for comparison) [112]

The spectra measured with different input iris diameters d are shown in Fig. 1.24 (see also [8]). Obviously, the UV part is very sensitive to E_p and/or d. The UV fraction below 300 nm is maximal at E_p = 0.26–0.3 *mJ*; at 0.3 *mJ* it already shows some instability and decreases rapidly on increasing d (inset of Fig.24 [112]; the exact shape of the EUV(d) curve is sensitive to the iris alignment). That is, under conditions of multiple filamentation, there is not only a poor pointing stability and shorter filament (see above) but also less spectral extension to the UV. It is also remarkable that the central part of the spectrum (down to about 10% of the maximum) is not much altered by varying

E and/or *d*, despite the strong changes in the pedestal. It is worth noting that multiple filamentation with the longer pulses (45 *fs*, in the first cell) sets in at about the same power (0.7–1 *mJ*).

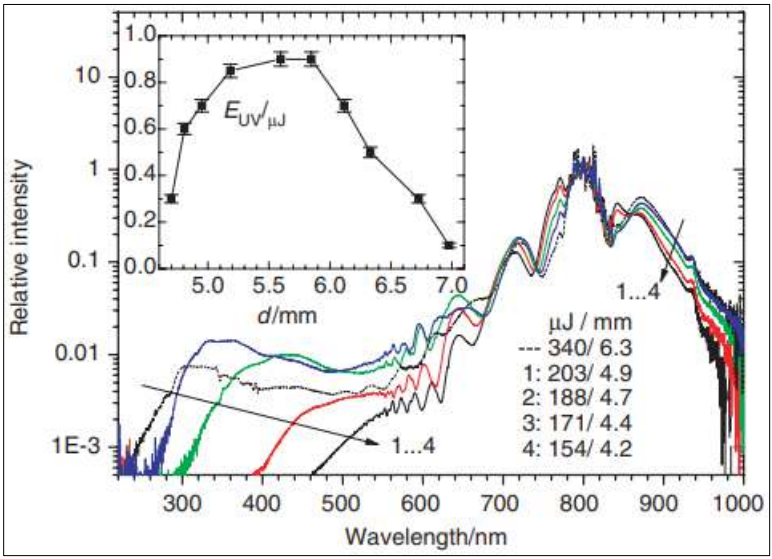

Fig 1.24: Spectra measured with different iris (diaphragm) diameters *d* (τ_p = 10 *fs*). The solid-line spectra are labeled 1 - 4. The transmitted energies corresponding to the different curves and the *d* values are compiled in the list. Inset: UV energies, measured as reflected by four dielectric mirrors at 270 *nm* (bandwidth 19 *nm*) versus *d* [112]

Using a mode-locked ruby laser, frequency broadenings by self-modulation in filaments up to 17 000 cm^{-1} have been observed in water. The large effect of this low dispersive medium is mainly due to its high threshold for stimulated Raman scattering [261].

In detail the following quantities were determined [261]:

i) The maximum anti-Stokes broadening ($\Delta\omega_{max}$) collinear to the laser radiation;

ii) The relative value of the nonlinear index of refraction (n_2) related to the value of water (obtained from measurements of self-focusing length). The achieved values are in good accordance with the values, determined by Saikan and Takuma under similar conditions [261]. The n_2-values determined by this technique do not have to be in agreement with then 2 responsible for frequency modulation especially if pulse steepening will occur. Although the values will

have a certain significance, detailed information cannot be obtained as long as the importance of the different physical mechanisms with different relaxation times remains unclear [261];

iii) The relative Raman-gain (g) related to the Raman-gain of water. To determine these values we investigated mixtures with water, by changing the ratio of the two components until the thresholds for Raman emission of both components were equal. By this procedure the effects of the short pulse duration and of the spectral broadening within the liquid are detected relatively well [261].

Main experimental results are shown in Table 1.1.

Table 1.1: Anti-Stokes broadening in different substances [261]

Substance	n_2/n_{2water}	g/g_{water}	$dn/d\lambda \Big/ (dn/d\lambda)_{water}$	$\Delta\omega_{max}$, $[cm^{-1}]^{a)}$
water	1	1	1	17000
methanol	1.3	4	3.2	8000
ethanol	4	8	3.4	6000
acetonitrile	10	25	0.9	3000
toluene	50	14	48	2000
CS_2	90	8	48	5000

a) Besides the lower extension of the spectra of methanol and ethanol they have an essentially lower intensity compared to that of water. The extension of the anti-Stokes continuum of acetonitrile, toluene and CS_2 depends on the number of broadened anti-Stokes lines. Thus, the extension of broadening by frequency modulation of the laser line only will be lower than the values given here.

Fig. 1.25 *a*) shows that under our experimental conditions the spectral broadening is mainly generated in filaments. The observed structure in these spectra corresponds to a mechanism of frequency modulation. The Stokes broadening has an extension of more than 4000 cm^{-1}. The integrated intensity at the highest laser peaks on the Stokes side is 10% including the Stokes bands of water. The overall time constant of our photoelectric detector and oscilloscope was 0.4 *ns*.

Our main result is an intense anti-Stokes broadening, extending from 694 nm up to 320 nm as shown in Fig. 1.25 *b*) [261]. Conversion efficiencies of the laser power have been achieved up to 1%. The broad absorption at 550 *nm* is due to the inverse Raman effect of water. The continuum is emitted collinearly

to the direction of the laser emission. Only near the frequency of the anti-Stokes Raman lines can a non-collinear emission be detected. This leads to the conclusion, that the continuum formation is not strongly affected by a non-resonant four photon process. This is furthermore confirmed by the fact, that contrary to experiments with spontaneous four photon scattering no further enhancement of the extension or intensity of the continuum is observed in a solution of sodium chloride in water [14].

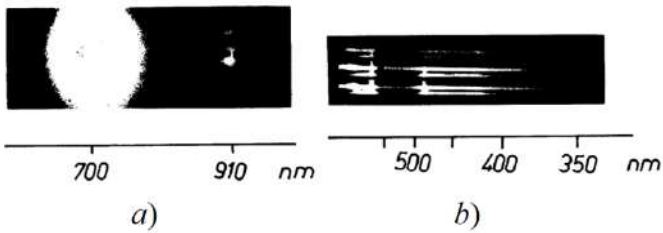

Fig 1.25: a) Stokes spectrum of water. The exit window of the cell is imaged on the slit of the spectrograph (at 3450 cm^{-1} the strongest Raman line appears); b) nti-Stokes spectrum of water [261]

Thus, there is a good correspondence between the appearance of the continuum and our conception of the mechanism responsible for frequency modulation. The extension of the continuum can at least partially be explained by taking the Raman gain into account. In liquid mixtures of water, with substances producing strong Raman scattering, the extension of the continuum quickly diminishes, if the Raman gain of the second component becomes larger than the gain of pure water (Fig. 1.26). This will be due to the extremely efficient Raman scattering from picosecond pulses in liquids with large Raman cross section and low dispersion [13]. For example, we obtained in acetonitrile up to 60% power conversion to the first Stokes frequency over the whole cross section of the laser beam. Increasing the laser power up to 10 GW/cm^2 the power of the first Stokes frequency decreases to 20% of the incident laser power, indicating that higher Stokes frequencies are excited. After the cell the laser power is depleted to 5%. Efficient SRS will therefore pump the intensity to the Stokes side, decreasing intensity and extension of the anti-Stokes continuum. In addition, SRS may act as a loss mechanism in exciting phonons and in producing Raman antiStokes emission, which will leave the filaments, thus reducing the self-modulation effect. Thus, it seems, that the appearance of a broad continuum in water is determined by the large value of its Raman threshold. This also corresponds to the fact, that a broadening effect of approximately, the same order has only been observed in glasses, until now.

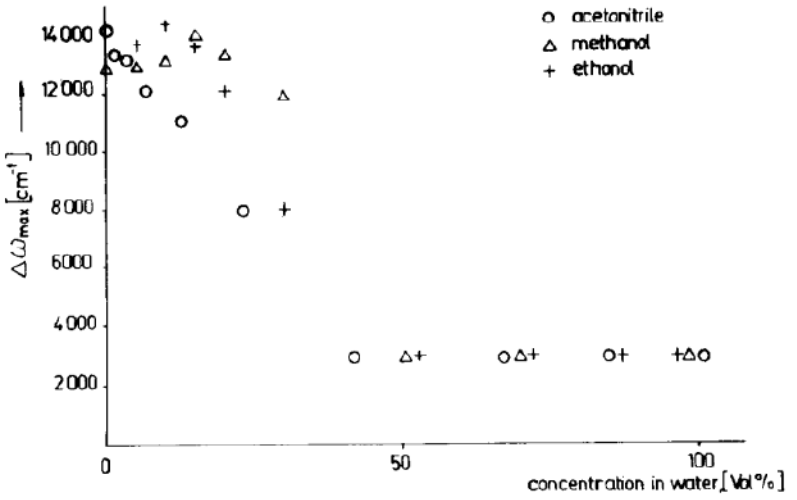

Fig 1.26: Extension of the anti-Stokes continuum versus concentration of a second component in the mixtures with water [261]

An investigation of white-light continuum generation during self-focusing in extended transparent media using 140-*fs* Ti: sapphire laser pulses is made in [40].

A band-gap threshold is found above which the width of the continuum tends to increase with increasing band gap and below which there is no continuum generation. This is, to our knowledge, the first report of a parameter predicting the width of the continuum in condensed media. Multiphoton excitation of electrons into the conduction band is proposed as the primary mechanism responsible for the observations. The media listed in Table 1.2 are investigated [40]. Let us first consider the effect of self-focusing on the diameter d (FWHM) of the beam at the geometrical focus. This is measured by first positioning lens f_1 such that the geometrical focus is at the output surface of the medium and then varying the input power. At low power d = 27 μm in all media.

Table 1.2: Anti-Stokes broadening $\Delta\omega_+$ and self-focal characteristics measured at $P = 1.1P_{th}$: minimum beam diameter d_{min} (FWHM) (± 0.5 *mm*), maximum fluence F_{max} (610%), and energy loss E_{los} ($\pm 1\%$). P_{th} is accurate within $\pm 20\%$. E_{gap} is obtained from the medium's absorption spectrum, which generally exhibits a sharp absorption edge in the UV corresponding to E_{gap} [40]

medium	E_{gap},**(eV)**	$\Delta\omega_+$, (cm^{-1})	d_{min}, (μm)	F_{max}, (J/cm^2)	E_{los}, **(%)**	P_{th}, (MW)
LiF	11.8	19 800	10.8	1.3	13	8.8
CaF_2	10.2 1.0	18 300	10.4	1.0	11	7.4
Water	7.5	14 600	9.8	0.62	4	4.4
D_2O 7.5	7.5	14 600	10.6	0.46	4	3.6
Fused silica	7.5	13 500	10.4	0.57	3	4.3
Propanol	6.2	14 200	9.1	0.57	3	3.3
Methanol	6.2	14 500	10.2	0.54	4	3.9
NaCl	6.2	9 000	9.9	0.29	3	2.0
1,4-Dioxane	6.0	10 200	9.3	0.44	3	2.7
Chloroform	5.2	11 200	10.0	0.29	1	2.2
CCl_4	4.8	10 400	8.7	0.44	2	2.5
C_2HCl_3	4.7	950	14.6	0.08	<1	1.2
Benzene	4.5	600	14.0	0.07	<1	0.90
CS_2	3.3	400	15.6	0.01	<1	0.23
SF-11 Glass	3.3	340	15.6	0.03	3	0.52

A Ti:sapphire laser system (Clark-MXR CPA-1) is used to generate 140-*fs* (FWHM) transform-limited pulses centered at $\lambda_0 = 796nm$,, with beam diameter 2.2 *mm* (1/e^2 of intensity) [40].

Self-focusing is accompanied in most media by whitelight continuum generation. This occurs at $P \geq P_{th}$, thus confirming that self-focusing triggers continuum generation. Examples of continua generated in water, NaCl, and LiF are shown in Fig. 1.27(a) [40]. Typical features are modulation near the laser wavelength and very strong Stokes/ anti-Stokes asymmetry: the extent $\Delta\omega_+$ of the anti-Stokes pedestal reaches ~10 000–20 000 cm^{-1}, depending on the medium, whil1e the extent $\Delta\omega_-$ of the Stokes pedestal is limited to a modest ~1000–2000 cm^{-1}. In some media there is no continuum generation; the spectra are comparatively much narrower and nearly symmetric. In all media there is usually an energy loss of a few percent at $P \geq P_{th}$, occurring

through the self-focus over a distance of typically 200–350 *mm*. The continuum develops concurrently with this energy loss.

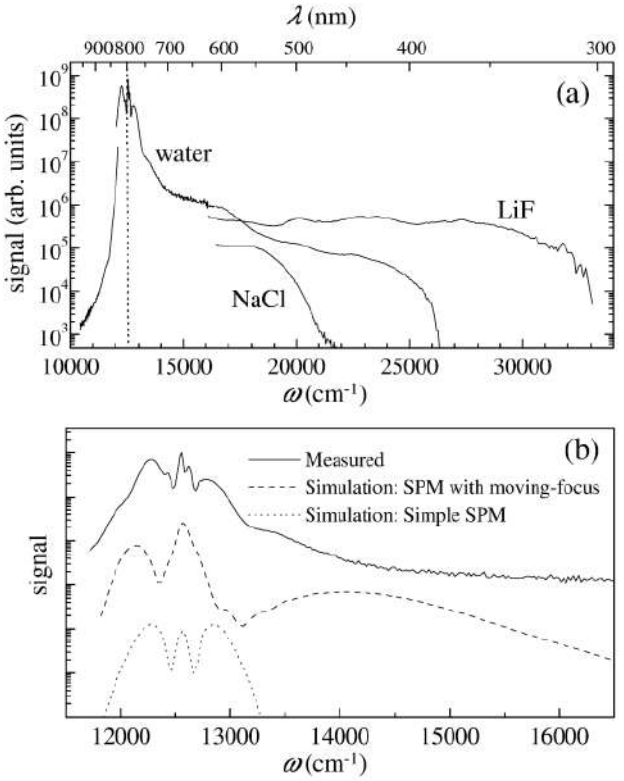

Fig 1.27: (a) White-light continuum spectrum generated in water, LiF, and NaCl at $P = 1.1P_{th}$. Only $\lambda > 630nm$ is shown for LiF and NaCl, for clarity. (b) Continuum spectra generated in water at $P = 1.1P_{th}$ in the experiment (solid line), in a 1D simulation including the moving-focus dynamics under MPE conditions (dashed line) and in simple SPM (dotted line). The simulations use $n_2 = 2 \cdot 10^{-16}\, cm^2/W$, estimated from the measured P_{th} [40]

A Ti:sapphire laser system based on the chirpedpulse amplification technique produced a 1-*mJ*, 70-*fs* pulse at a 10-Hz repetition rate [150]. The center wavelength was 785 *nm*, and the bandwidth was 20 *nm*. This fundamental pulse, which had a diameter of 7 *mm*, was converted into second- and third-harmonic pulses by doubling and tripling with two 100-μm thick β-barium borate crystals. The maximum output energies of the second- and third-harmonic pulses were 180 and 30 μJ, respectively. The temporal width of the third-harmonic pulse was estimated to be approximately 100 *fs* ($\pm$20 *fs*)

from the result of a separate experiment with a single-shot autocorrelator by the transient grating method.

Fig. 1.28 shows typical white-light continuum spectra of various materials obtained with 393-*nm* radiation focused at an intensity of 1.5 10^{12} W/cm^2 [150].

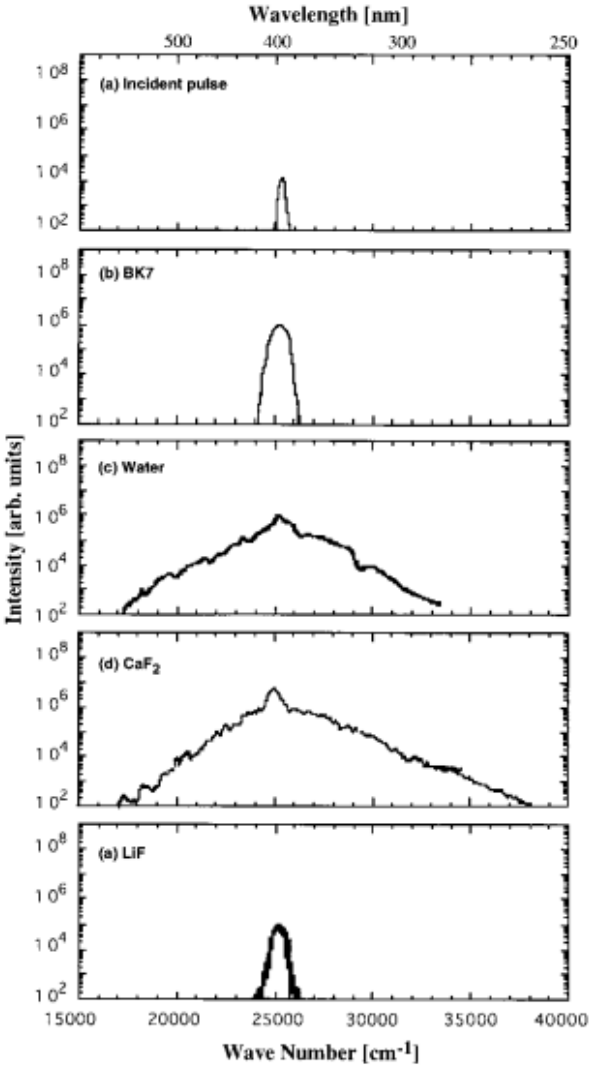

Fig 1.28: White-light continuum spectra in various condensed media. The incident pump wavelength and intensity are 393 *nm* and 1.5 10^{12} W/cm^2, respectively [150]

Spectral range of white-light continua produced in various condensed media for three incident wavelengths, 262 (3 ω), 393 (2 ω), and 785 *nm* (1 ω) at a focused intensity of the order of 10^{13} W/cm^2 are represented in Fig. 1.29 [150].

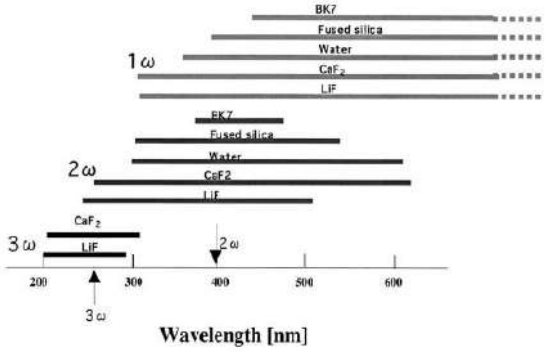

Fig 1.29: Spectral range of white-light continua produced in various condensed media for three incident wavelengths, 262 (3ω), 393 (2 ω), and 785 nm (1 ω) at a focused intensity of the order of 10^{13} W/cm^2 [150]

1.4 Some remarks

As it is easy to see from the presented material, Cherenkov and supercontinuum radiation is caused by heterogeneous, as a rule, shock polarization of the irradiated medium. This heterogeneity may be due to the irradiation regime. For the case of Cherenkov radiation, this is the envelope of the track of the incident particle, and for the supercontinuum – the focusing cone of the laser irradiation, which is analogous to the envelope of the track.

Secondly, this heterogeneity can be caused by the heterogeneity of the irradiated material (diffraction and parametric Cherenkov radiation). Thirdly, this heterogeneity can be formed as a result of irradiation (diffraction stratification of incident laser radiation - generation of conical supercontinuum (Cherenkov) radiation and interference of this radiation).

The essential difference between Cherenkov and supercontinuum irradiation lies in the methods of obtaining them. Cherenkov radiation is obtained by being irradiated by streams of high-energy particles, usually - quanta and electrons with rather high energies. This is due to the conditions for minimizing the rate of inelastic scattering. However, the probability of the formation of radiation defects remains quite high. This is what limits the intensity of both the initial radiation and the generated Cherenkov radiation: the specific emissivity for Cherenkov radiation is many orders of magnitude lower than for supercontinuum radiation.

Supercontinuum radiation has a higher specific efficiency precisely because it does not create defects in such a quantity as streams of high-energy particles. This radiation is the result of the synthesis of various nonlinear optical effects, or roughly speaking, a mixture of Compton scattering in the irradiated material.

At the same time, if for high-energy particles, only a small part of their energy goes to the nonlinear polarization of the medium, which causes radiation; then, for supercontinuum radiation, almost every photon (when choosing favorable irradiation modes) takes part in the final radiation.

Thus, the nature of these phenomena is the same, they differ only in methods of excitation. That is why I. Frank attributed Cherenkov radiation to the phenomena of Nonlinear Optics.

From this point of view, supercontinuum radiation is energetically and economically more profitable than Cherenkov radiation. However, Cherenkov radiation is often indispensable for recording high-energy particles in nuclear physics and astrophysics.

It should be noted that the above material shows that Cherenkov radiation covers a wider spectral range. So, terahertz range is mainly implemented using lasers emitting at different frequencies.

Higher frequencies can be obtained not only from above (Cherenkov emission), but also from below. In this case, it is necessary to choose either a shorter-wavelength source radiation or to calculate processes with the generation of harmonics or nonlinear optical phenomena of higher orders. Even at the early stages of the development of laser physics, experimental results were obtained on the generation of harmonics of the order of 1500 [192]. However, there may be a problem with the irradiated substance, so it is probably better to use gases for such experiments.

1.5 Conclusions

2. Main experimental data of Cherenkov and supercontinuation radiation are representing.
3. It was shown that Cherenkov radiation might be used as source of TERAhertz and X-ray radiation.
4. An influence of heterogeneity of irradiation and matter on the finished characteristics of irradiation is analyzing.
5. The problem of registration tachyons with help Cherenkov radiation is observing.

6. Main ways of receiving the laser-induced supercontinuation radiation are researching.
7. Main differences of Cherenkov and supercontinuation radiation are analyzing.

Chapter - 2

Cherenkov and Supercontinuum Radiation: Modeling and Discussions

Any action always has a consequence.

Mahabharata

2.1 Introduction

The problem of modeling Cherenkov [33, 60, 67, 69, 79, 96, 109, 210, 232, 233] and supercontinuum [58, 79, 232, 233] radiation is discussed. This problem has next peculiarities. First is connected with processes of scattering (absorption) of initial radiation. Second is connected with second-order processes of relaxation the first-order excitation. As rule it is chain processes [232, 233]. The relaxation processes is next: reirradiation and reabsorption, electromagnetic wave processes, thermal processes [217-244].

These features can be analyzed in the most detail on the example of Cherenkov and supercontinuum radiation. It is these processes that have a more "pure" electromagnetic nature. But this nature is expressed here through radiation. Since radiative processes are caused by a change in the polarization of the medium, these processes also differ only in the method of excitation of this polarization.

Cherenkov radiation is the emission of electromagnetic waves by a charged particle moving in a medium at a speed greater than the phase speed of light propagation in this medium. The radiation forms a cone with the apex directed in the direction of the particle's movement. The angle at the top of the cone depends on the speed of the particle and the speed of light in the medium. This is precisely what makes Cherenkov radiation extremely useful from the point of view of elementary particle physics, since, having determined the angle at the top of the cone, it is possible to calculate the particle's speed from it.

Cherenkov radiation is due to shock polarization of the medium [33, 60, 67, 69, 79, 96, 109, 210, 232, 233,279, 280]. At the same time, only a small part of the energy of the incoming particle is used. At the same time, the particle itself does not necessarily have to pass through the medium, it is enough that it flies near the medium.

Cherenkov radiation itself can be considered as a braking medium. It is from this point of view that Cherenkov radiation was considered by E. Fermi [67] and A. Bohr [33]. The phase speed of light in the medium is a characteristic of the medium, it shows how much the medium "slows down" the speed of light in a vacuum. This is a macroscopic electrodynamic characteristic of the medium. Cherenkov radiation itself is characterized by low photon efficiency.

Roughly speaking, supercontinuum (supercontinuum cone) radiation, according to I. Golub, is laser-induced Cherenkov radiation and has analogy with Descartes –Snell law [79, 232, 233].

Supercontinuum radiation was observed in all media when irradiated with pulsed laser radiation. At the same time, as a rule, these processes have a high photon efficiency, while classical Cherenkov radiation has a low photon efficiency [232, 233].

Classical Cherenkov radiation is using to create various Cherenkov detectors for problems in nuclear physics, ecology, astrophysics, etc. [96]

Supercontinuum radiation is used in the creation of white lasers, that is, lasers with a wide spectrum of radiation [58] and optoelectronics technology [232, 233, 251].

A promising direction of application of supercontinuum (laser-induced Cherenkov) radiation is optoelectronic micro and nano technologies. Classical Cherenkov radiation cannot be using for these problems, as it has a relatively low intensity [232, 233].

2.2 Frank-Tamm theory

The Frank–Tamm formula yields the amount of Cherenkov radiation emitted on a given frequency as a charged particle moves through a medium at superluminal velocity. It is named for Russian physicists Ilya Frank and Igor Tamm who developed the theory of the Cherenkov effect in 1937 [69, 211], for which they were awarded a Nobel Prize in Physics in 1958.

When a charged particle moves faster than the phase speed of light in a medium, electrons interacting with the particle can emit coherent photons while conserving energy and momentum.

The energy emitted per unit length travelled by the particle per unit of frequency $d\omega$ is [69, 211]:

$$\frac{\partial^2 E}{\partial x \partial \omega} = \frac{e^2}{4\pi}\mu(\omega)n(\omega)\omega\left[1 - \frac{c^2}{v^2 n^2(\omega)}\right] \qquad (2.1)$$

provided that $\beta = \frac{v}{c} > n(\omega)$. Here $\mu(\omega)$ and $n(\omega)$ are the frequency-

dependent permeability and index of refraction of the medium respectively, e is the electric charge of the particle, v is the speed of the particle, and c is the speed of light in vacuum.

Cherenkov radiation does not have characteristic spectral peaks, as typical for fluorescence or emission spectra. The relative intensity of one frequency is approximately proportional to the frequency. That is, higher frequencies (shorter wavelengths) are more intense in Cherenkov radiation. This is why visible Cherenkov radiation is observed to be brilliant blue. In fact, most Cherenkov radiation is in the ultraviolet spectrum; the sensitivity of the human eye peaks at green, and is very low in the violet portion of the spectrum.

The total amount of energy radiated per unit length is [69]:

$$\frac{e^2}{4\pi}\left\{\int \mu(\omega)\omega\left[1-\frac{c^2}{v^2n^2(\omega)}\right]d\omega\right\}_{v>\frac{c}{n(\omega)\omega}}. \qquad (2.2)$$

This integral is done over the frequencies ω for which the particle's speed v is greater than speed of light of the media c. The integral is convergent (finite) because at high frequencies the refractive index becomes less than unity and for extremely high frequencies it becomes unity.

The total energy radiated by an electron through the surface of a cylinder with length l and radius r (with the axis coinciding with the line of motion of the electron) is equal to [69].

$$W = 2\pi rl\int_{-\infty}^{+\infty}\frac{c}{4\pi}[E\times H]_r dt. \qquad (2.3)$$

After substitution of corresponding values [] we have

$$W = \frac{e^2 l}{c^2}\left\{\int \omega\left(1-\frac{1}{\beta^2n^2}\right)d\omega\right\}_{\beta n>1}. \qquad (2.4)$$

Exactly the same result is obtained when calculating the total radiation energy of an electron that was initially at rest, then suddenly acquired a speed v, and having traveled a path l, suddenly stopped. In this case, the applicability of (2.4) is limited only by the condition that the electron path l be large compared to the wavelength of the emitted light. If the electron gradually loses its speed, then equation (2.3) can be applied to individual sections of its path, it is only essential that the magnitude of these sections be large compared with the wavelength. In this case, the angle θ between v and the direction of radiation decreases as the speed is lost.

The order of magnitude for the total energy loss to radiation can be determined by replacing n^2 in (2.4) with its approximate value from the equations [69]

$$n^2 = 1 + \frac{A}{\omega_0^2 - \omega^2}, n_{\omega=0}^2 = \epsilon = 1 + \frac{A}{\omega_0^2} \quad (2.5)$$

and perform an integration from $\omega = 0$ to $\omega = \omega_0$, where ϵ is the permittivity, and ω_0 is some average natural frequency of the medium. Thus, we obtain the following approximate expression for the energy loss for radiation per unit of electron path [69]:

$$W = \frac{e^2\omega_0^2}{2c^2}(\epsilon - 1)\ln\frac{\epsilon}{\epsilon - 1}. \quad (2.6)$$

Assuming $\omega_0 \approx 6 \cdot 10^{15} s^{-1}$, for dW/dl we obtain a value of the order of several kilovolts per centimeter, i.e. a value that is vanishingly small compared to the energy loss caused by other causes.

Equation (2.4) gives the following value for the total number of photons emitted by an electron in the spectral region limited by the wavelengths λ_1 and λ_2:

$$N_{phot} = 2\pi\alpha\left(\frac{1}{\lambda_2} - \frac{1}{\lambda_1}\right)\left(1 - \frac{1}{\beta^2 n^2}\right), \quad (2.7)$$

where α – fine structure constant, $\alpha = e^2/\hbar c$, and n is average value of refractive index in this area.

Assuming n = 1.33, β = 3/4 (an electron with an energy of 500 *keV*) and $\lambda_1 = 4 \cdot 10^{-5}\ cm$ and $\lambda_2 = 6 \cdot 10^{-5}\ cm$, we find that 10 photons per electron are emitted in the visible region between cm and cm. This result coincides in order of magnitude with Cherenkov's observations.

If we take into account that most of Cherenkov's measurements were made with a strongly divergent beam of Compton electrons obtained from γ-rays and characterized by a diffuse velocity spectrum, then with respect to the totality of the experimental material, including the issues of polarization, angular asymmetry, and absolute luminescence intensity, we can claim that it is in full agreement with the theory presented here.

2.3 The ionization loss of energy in condensed matter

E. Fermi theory

The determination of the energy lost by a fast charged particle by ionization and excitation of the atoms through or near which it is passing has been the object of several theoretical investigations [67, 258, 260, 262]. The essential features of the phenomenon are explained as well know in terms of a classical theory due to Niels and Aage Bohrs [33]; the electrons near which the particle passes are treated as classical oscillators that are set in motion by the electric

field of the passing particle. The energy thus absorbed by the electrons is equal to the energy lost by the particle. This theory gives a satisfactory description of the influence of the impacts for which the minimum distance b between the electron and the passing particle is larger than the atomic dimensions. Quantum mechanical corrections have to be introduced for the very close impacts, when the particle passes through the atom. Both in the classical and in the quantum mechanical theories the action on every atom has been discussed so far by neglecting the perturbation of the field of the passing particle arising from the electric polarization of the surrounding atoms. A detailed analysis shows however that in some cases these polarization effects are very important. The influence of the polarization has been calculated in the present paper based on the classical theory. This may be expected to give correct results for at least that part of the energy loss, which is due to collisions at distances b greater than the atomic radius.

The field of a charged particle moving through a medium having dielectric properties is affected by the polarization of the medium [67]. We shall first calculate the field by applying classical electrodynamics. The amount of energy lost by the particle at distances greater than a certain minimum distance b from the path of the particle will then be calculated as flux of the Poynting vector across a cylindrical surface of radius b having the path of the particle as axis. We may reasonably hope to get in this way a correct estimate of the losses due to the atoms for which b is somewhat larger than the interatomic distances. Indeed, we might then expect the quantum mechanical correction not to be very important; moreover, a description of the dielectric properties of the medium with a continuum theory is permissible.

We write the Maxwell equations in the usual form [67]:

$$\mathrm{div}\,(E+4\pi P) = 4\pi\rho, \tag{2.8}$$

$$\mathrm{div}H = 0, \tag{2.9}$$

$$c\,\mathrm{rot}E = -\dot{H}, \tag{2.10}$$

$$c\,\mathrm{rot}H = \dot{E} + 4\pi\dot{P} + 4\pi\rho v, \tag{2.11}$$

where E, H, P, ρ, v are, respectively, the electric and magnetic field strength, the electric polarization vector, the density and velocity of the electric charges. The magnetic polarization of the medium has been neglected.

The relationship between E and P can be simply expressed on the assumption that the electrons are elastically bound to equilibrium positions and are furthermore subjected to a friction force. It is then:

$$E = \frac{m}{ne^2}\left(\ddot{P} + 2p\dot{P} + \nu_0^2 P\right), \tag{2.12}$$

where m, e, n are the mass, the charge and the number of electrons per unit volume; $\nu_0/2\pi$ is the frequency of the electronic oscillators when E=0; $2p$ is the coefficient of the friction force.

Let E_ν and P_ν be the components of frequency $\nu/2\pi$. (with the time dependence; exp (*-ivt)*) in the harmonic analysis of E and P; we have then:

$$E_\nu = \frac{m}{ne^2}(\nu_0^2 - \nu^2 - 2ip\nu)P_\nu. \tag{2.13}$$

In general we may assume between E_ν and P_νa relationship of the type:

$$E_\nu = 4\pi\gamma(\nu)P_\nu, \tag{2.14}$$

$\gamma(\nu)$ is in general a complex function of ν. In the special case (5) that the dispersion law can be described in terms of one kind of dispersion oscillators only we have:

$$\gamma(\nu) = \frac{m}{4\pi ne^2}(\nu_0^2 - \nu^2 - 2ip\nu). \tag{2.15}$$

Our problem is to find the field produced by a concentrated charge e moving with the constant velocity v. We take the path of the particle as x axis and the position occupied by the particle at t = 0 as origin of the coordinates.

If we know the field at t =0 we can obtain the field at any time by translating it with the uniform velocity v. This enables us to eliminate the time from the Maxwell equations by using the relationship [57]:

$$\frac{\partial}{\partial t} = -v\frac{\partial}{\partial x}. \tag{2.16}$$

Since at t = 0 the charge is at the origin we have further $\rho = e\delta(x)\delta(y)\delta(z)$, and the Maxwell equations become ‘57\

$$\text{div}\,(E+4\pi P) = 4\pi e\delta(x)\delta(y)\delta(z), \tag{2.17}$$

$$\text{div}H = 0, \tag{2.18}$$

$$c\text{rot}E = -vH', \tag{2.19}$$

$$c(rotH)_x = -vE_x' - 4\pi vE_x' + 4\pi ev\delta(x)\delta(y)\delta(z), \tag{2.20}$$

$$c(rotH)_y = -vE_y' - 4\pi vE_y', c(rotH)_z = -vE_z' - 4\pi vE_z', \tag{2.21}$$

where a dash means the derivative with respect to x. Since the field moves with the uniform velocity v we may develop the field vectors in Fourier components with respect to x instead of t and interpret E_ν and P_ν in (2.21) as those components whose dependence on x is represented by the factor exp(ivx/v).

The integration of the equations (2.14), (2.17), (2.18), (2.19), (2.20) and (2.21) with the boundary condition that the fields must vanish at infinite distance can be performed as follows. From (2.14) and (2.17) we first calculate div$P$ and div div$E$:

$$\text{div}P = \frac{e}{2\pi v}\delta(y)\delta(z)\int_{-\infty}^{+\infty}\frac{\exp(ivx/v)}{1+\gamma(v)}dv,$$

$$\text{div}P = \frac{2e}{v}\delta(y)\delta(z)\int_{-\infty}^{+\infty}\gamma\frac{\exp(ivx/v)}{1+\gamma(v)}dv. \qquad (2.22)$$

We can then eliminate H from (2.20) and (2.21) in the usual way and eliminate also E with (2.14). Taking ' into account (2.22) we find an equation for each component of P. Developing these components in Fourier integrals with respect to x one easily finds the solutions in terms of the Bessel functions K_0 and K_1.

$$P_x = -\frac{e}{4\pi^2v^2}\int_{-\infty}^{+\infty}\left(\frac{1}{1+\gamma}-\frac{v^2}{c^2\gamma}\right)K_0(kb)\exp\left(ivx/v\right)i\,v dv, \qquad (2.23\text{ a})$$

$$P_b = \frac{e}{4\pi^2v}\int_{-\infty}^{+\infty}\frac{kK_1(kb)}{1+\gamma}\exp\left(ivx/v\right)dv, \qquad (2.23\text{ b})$$

where P_b is the component perpendicular to the x axis and

$$k^2 = \frac{v^2}{v^2}\left(1-\frac{v^2}{c^2}\right)-\frac{v^2}{c^2\gamma(v)}. \qquad (2.24)$$

I'he sign of k is determined so as to have its real part ≥ 0. From (2.23) and (2.14) we obtain the components of the electric field [57]

$$E_x = -\frac{e}{\pi v^2}\int_{-\infty}^{+\infty}\left(\frac{\gamma}{1+\gamma}-\frac{v^2}{c^2}\right)K_0(kb)\exp\left(ivx/v\right)i\,v dv,$$
$$P_b = \frac{e}{4\pi^2v}\int_{-\infty}^{+\infty}\frac{\gamma kK_1(kb)}{1+\gamma}\exp\left(ivx/v\right)dv. \qquad (2.25)$$

From these and (2.19) we finally obtain the magnetic field. This reduces to one component only, perpendicular to the x,b-plane. Its magnitude is given by

$$P_b = \frac{e}{\pi c}\int_{-\infty}^{+\infty}kK_1(kb)\exp\left(ivx/v\right)dv. \qquad (2.26)$$

The amount. of energy lost by the particle per unit time at distances larger than b is given by the flux of the Poynting vector out of a cylinder of radius b. Dividing this flux by v we obtain the corresponding loss of energy W_b per unit path. This is

$$W_b = \frac{c}{4\pi v}\oint_\sigma [E,H]_n d\sigma = -\frac{cb}{2v}\int_{-\infty}^{+\infty}HE_x\,dx. \qquad (2.27)$$

We substitute in this expression (2.25) and (2.26) changing in the last the name of the integration variable to v'. W_b is then expressed by a triple integral

over x, ν, ν'. The integration over x gives a δ-function. This fact enables us to perform in the usual way also the integral over ν'. We find at last, taking into account $k(-\nu) = k^*(\nu)$

$$W_b = -\frac{e^2 b}{\pi v^2}\int_{-\infty}^{+\infty}\left(\frac{\gamma}{1+\gamma}-\frac{v^2}{c^2}\right) i\nu k^* K_1(k^* b)K_0(kb)\, d\nu. \tag{2.28}$$

One easily recognizes that the integrand takes complex conjugate values for the values ν and $-\nu$ of the integration variable; we have therefore:

$$W_b = -\frac{e^2 b}{\pi v^2} R\int_{-\infty}^{+\infty}\left(\frac{\gamma}{1+\gamma}-\frac{v^2}{c^2}\right) i\nu k^* K_1(k^* b)K_0(kb)\, d\nu, \tag{2.29}$$

where we have indicated the real part of a by R_a.

In order to calculate this integral we specialize our assumptions as to the dielectric properties of the medium by using (2.15). We find

$$W_b = -\frac{8ne^4}{mv^2(\epsilon-1)} R\int_{-\infty}^{+\infty}\left(\frac{1-x^2-2i\eta x}{\epsilon-x^2-2i\eta x}-\frac{v^2}{c^2}\right) ixk^* bK_1(k^* b)K_0(kb)\, dx, \tag{2.30}$$

where

$$\epsilon = 1+\frac{4\pi ne^2}{m\nu_0^2} \tag{2.31}$$

is the dielectric constant for low frequencies. We have further

$$\eta = \frac{p}{\nu_0};\ x = \frac{\nu}{\nu_0};\ k^2 = g^2 x^2\,\frac{a-x^2-2i\eta x}{1-x^2-2i\eta x} \tag{2.32}$$

with

$$g^2 = \frac{4\pi ne^2}{mc^2(\epsilon-1)}\left(\frac{c^2}{v^2}-1\right);\ a = \frac{c^2-v^2\epsilon}{c^2-v^2}. \tag{2.33}$$

The integral (2.30) can be calculated when b is very small. In this case we may use for the Bessel functions the following expression

$$K_0(kb) = \frac{1}{2}\log\frac{4}{3.17k^2b^2};\ K_1(k^* b) = \frac{1}{k^* b}, \tag{2.34}$$

in which 3.17 = exp (2×Eulers constant).

(2.30) becomes now [57]:

$$W_b = -\frac{4ne^4}{mv^2(\epsilon-1)} R\int_0^{+\infty}\left(\frac{1-x^2-2i\eta x}{\epsilon-x^2-2i\eta x}-\right)\log\frac{4(1-x^2-2i\eta x)}{3.17k^2b^2x^2(a^2-x^2-2i\eta x)}\, i\, xdx. \tag{2.35}$$

The integral can be reduced to the following integrals, that can easily be calculated by complex integration. The integration path of these integrals is along the positive real axis. They can be calculated by deforming the integration path moving first from the origin in the positive imaginary direction to a very large distance from the origin and then coming back on the

real axis along a quarter of a circle of very large radius with center in the origin and by taking proper account of the singularities. Notice further that only the real part of the above integrals is convergent. The divergence of the imaginary part has been introduced when we have used the approximate expressions (2.34) for the Bessel functions. This divergence is of course immaterial to us, since in our formulae only the real part of the integrals is used.

We obtain now [67]:

$$W_b = -\frac{2\pi e^4}{mv^2}\left\{\log\frac{mv^2(\epsilon-1)}{3.17\pi e^2b^2\epsilon\left(1-\frac{v^2}{c^2}\right)} - \frac{v^2}{c^2} - \frac{2\eta}{(\epsilon-\eta^2)^{1/2}}\operatorname{artg}\frac{(\epsilon-\eta^2)^{1/2}}{\eta}\right\} \text{ for } v < c/\sqrt{\epsilon}; \quad (2.36)$$

$$W_b = -\frac{2\pi e^4}{mv^2}\left\{\log\frac{mv^2}{3.17\pi e^2b^2} - \frac{v^2}{c^2} + \frac{1-\frac{v^2}{c^2}}{(\epsilon-1)}\left[\eta^2 + \frac{v^2\epsilon-c^2}{c^2-v^2}\right]^2 - \right.$$

$$\left. - \frac{2\eta}{(\epsilon-\eta^2)^{1/2}}\operatorname{artg}\frac{(\epsilon-\eta^2)^{1/2}}{\left(\eta^2+\frac{v^2\epsilon-c^2}{c^2-v^2}\right)^{1/2}}\right\} \text{ for } v > c/\sqrt{\epsilon}. \quad (2.37)$$

When the damping is negligible (lim η =0) the above formulae become [67]:

$$W_b = -\frac{2\pi e^4}{mv^2}\left\{\log\frac{mv^2(\epsilon-1)}{3.17\pi e^2b^2\epsilon\left(1-\frac{v^2}{c^2}\right)} - \frac{v^2}{c^2}\right\} \text{ for } v < c/\sqrt{\epsilon}; \quad (2.38)$$

$$W_b = -\frac{2\pi e^4}{mv^2}\left\{\log\frac{mv^2}{3.17\pi e^2b^2} - \frac{1-\frac{v^2}{c^2}}{(\epsilon-1)}\right\} \text{ for } v > c/\sqrt{\epsilon}. \quad (2.39)$$

These results should be compared with the corresponding energy loss calculated with the usual theory by neglecting the polarization effects:

$$W_b(\text{usual theory}) = -\frac{2\pi e^4}{mv^2}\left\{\log\frac{mW_b{}^2(\epsilon-1)}{3.17\pi e^2b^2\epsilon\left(1-\frac{v^2}{c^2}\right)} - \frac{v^2}{c^2}\right\}. \quad (2.40)$$

The comparison is shown in Fig. 2.1. The three curves represent the energy loss per unit path due to impacts at distances greater than 10^{-8} *cm*, measured taking $\frac{2\pi e^4}{mv^2}$ as unit, according to the ordinary formula (2.40) and according to the present theory with formulae (2.38) and (2.39) for standard air and for water. In both cases the difference from the ordinary result is very small at low energies. For high energies, instead, the loss calculated with the ordinary theory keeps increasing logarithmically with increasing energy, whereas the effect of the polarization produces a Qattening out of the curves for air and water. in such a way that W_b remains finite even when the energy of the particle becomes infinite.

It can easily be seen from (2.36) and (2.37) that the limiting value of W_b for $v = c$ is independent on both the binding frequency ν_0 of the dispersion oscillators and the damping constant η. It depends only on the number *n* of electrons per unit volume, and is given by [67]:

$$W_b(v = c) = -\frac{2\pi e^4}{mc^2}\log\frac{mc^2}{3.17\pi e^2 b^2}. \tag{2.41}$$

This shows that the energy loss of very high energy particles due to various materials in layers of such thicknesses as to contain always the same number of electrons per cm^2, is smaller for larger electronic densities *n* of the material (see on Fig. 2.1 the difference between air and water).

When the damping η of the dispersion oscillators is very small it is possible to calculate the integral (2.30) for arbitrary values of *b* by using the exact expressions for the Bessel functions instead of the approximate expressions (2.34). One finds [67]:

$$W_b = \frac{2\pi e^4}{mv^2}\left\{\frac{2b\nu_0\sqrt{\epsilon}}{v}K_0\left(\frac{b\nu_0\sqrt{\epsilon}}{v}\right)K_1\left(\frac{b\nu_0\sqrt{\epsilon}}{v}\right) - \frac{v^2}{c^2} - \log\left(1 - \frac{v^2}{c^2}\right)\right\}$$

for $v < {}^{c}/_{\sqrt{\epsilon}}$; (2.42)

$$W_b = \frac{2\pi e^4}{mv^2}\left\{\frac{2b\nu_0\sqrt{\epsilon}}{v}K_0\left(\frac{b\nu_0\sqrt{\epsilon}}{v}\right)K_1\left(\frac{b\nu_0\sqrt{\epsilon}}{v}\right) - \frac{1-{}^{v^2}/_{c^2}}{\epsilon-1} - \log\frac{\epsilon}{\epsilon-1}\right\}$$

for $v > {}^{c}/_{\sqrt{\epsilon}}$. (2.43)

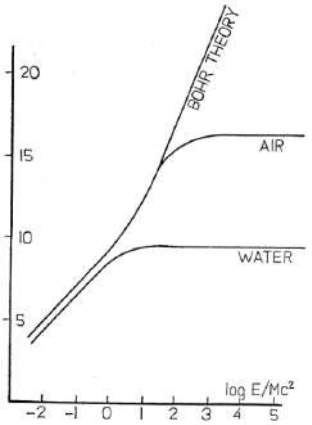

Fig 2.1: Energy loss per unit path due to impacts at distances greater than 10^{-8} *cm*. The curves marked air and water are calculated according to the present theory with formula (2.38) and (2.39) [67]

For very small b these expressions go over into (2.38) and (2.39). It is interesting to note, however, that W_b in this case does not vanish, as one might

expect, for very large b. Indeed it follows from (2.42) and (2.43) that for $b = \infty$ it is:

$$W_\infty = \frac{2\pi e^4}{mv^2}\left\{-\frac{v^2}{c^2} - \log\left(1 - \frac{v^2}{c^2}\right)\right\} \text{ for } v < {}^{c}/_{\sqrt{\epsilon}}; \tag{2.44}$$

$$W_\infty = \frac{2\pi e^4}{mv^2}\left\{-\frac{1-{}^{v^2}/_{c^2}}{\epsilon-1} - \log\frac{\epsilon}{\epsilon-1}\right\} \text{ for } v > {}^{c}/_{\sqrt{\epsilon}}. \tag{2.45}$$

W_∞ represents that part of the energy lost by the particle that is emitted in the form of radiation. Such an emission of radiation has actually been observed by Cherenkov, and can easily be seen to occur in those ranges of frequency for which the phase velocity of light in the given medium is smaller than the velocity of the particle. Its theory has been developed by Frank and Tamm' with methods very similar to those used here and with similar results. It is noteworthy that the Cherenkov radiation, as results from the preceding formulae, does not represent a loss of energy to be added to that calculated with the Bohr theory [33]; but it forms instead part of the loss of the Bohr theory, as is seen from the fact that (2.38) (2.39), which include the Cherenkov radiation, give the same result (2.40) as the Bohr theory in the limit of very low densities ($\epsilon = 1$) when the polarization effects become negligible.

We have considered so far only the phenomena occurring at distances greater than the interatomic distance, for which it is legitimate to apply the continuum electrodynamics. A description of the effects of impacts at close distances requires a quantum mechanical description of the impact process as well as of the field of the passing particle and of its change due to the polarization of the other atoms. If we assume, however, that the effect of the polarization on the close distance impacts is not large we may use the ordinary theory, as developed by Bethe and Bloch for the calculation of the energy loss due to such impacts [67].

Under this assumption we may take the difference between the formulae (2,37), (2.38) of the present theory and formula (2.39) giving the result of the Bohr theory as the correction representing the polarization effects. We find thus that. the energy loss per unit path is less than that given by the ordinary formulae by the following amount [67]:

$$\frac{2\pi e^4}{mv^2}\log\epsilon \text{ for } v < {}^{c}/_{\sqrt{\epsilon}}; \tag{2.46}$$

$$\frac{2\pi e^4}{mv^2}\left\{\log\frac{\epsilon-1}{1-{}^{v^2}/_{c^2}} - \frac{1-\epsilon{}^{v^2}/_{c^2}}{\epsilon-1}\right\} \text{ for } v > {}^{c}/_{\sqrt{\epsilon}}. \tag{2.47}$$

The correction is negligible for low velocities; for very large energies instead it reduces the energy loss to less than 50 percent of the loss calculated

with the ordinary theory. For very large energies we have from the ordinary theory the following energy loss [67]:

$$\frac{2\pi e^4}{mc^2}\log\frac{mc^2W}{\left(1-v^2/c^2\right)\hbar^2\nu_0^2}. \tag{2.48}$$

We obtain thus from (2.47) the following formula valid asymptotically for very large energies:

$$\frac{2\pi e^4}{mc^2}\left[\log\frac{\pi m^2c^2W}{ne^2h^2}-1\right]. \tag{2.49}$$

We note that this asymptotic formula does not. contain the binding frequency of the electrons but only their number per unit volume.

Only a very small polarization effect should be expected according to the present theory in the stopping power of different materials for α-particles, protons or deuterons having energies up to the order of magnitude of some *MeV*. In all these cases the velocity is rather small compared with *c*, so that we must use (2.46). This formula gives an entirely negligible correction in the case of air, since in this case e is very close to unity. Corrections of the order of several percent might be expected in the case of the stopping power in solid or liquids. It is doubtful whether such differences are large enough to be observable. Moreover, when the velocity of the particle is small, as in the present case, the ionization produced by the particle does not reach far enough from the trajectory as to make the description of the field in terms of continuum electrodynamics a good approximation.

Greater effects are to be expected in the case of *β*-particles and especially for particles of several millions of *eV*. The correction for air is again negligible but an appreciable correction is found for condensed substances especially for high energy *β*-particles. The energy loss per *cm* of water calculated with the usual theories for *β* -particles of 10^6, 10^7, 10^8 *eV* is, respectively, 1.93, 2.15, 2.72 *MeV*. The correction (2.46) and (2.47) reduces these losses to 1.83, 1.75, 1.94 *MeV* if we take $\epsilon = 1.7$; since, however, the effective ϵ may be as low as 1.1, the corrected energy losses may be 1.92, 1.91, 2.09 *MeV*. In spite of the fact that the differences are in some cases rather large, it is very difficult to compare these results with the available expermental material. Indeed the data for relatively low energies are largely affected by the scattering while those for large energies are perturbed by the radiation losses of energy.

The results for mesotrons are represented in Fig. 2.2. The diagrams have been calculated for a rest energy of the mesotron of 80 *MeV*. The energy of the mesotron is plotted in a logarithmic scale on the abscissae; and the energy loss in units $\frac{2\pi e^4}{mv^2}$ is plotted on the ordinates for standard air, water and lead. The curves A are calculated with Bloch's formula; the curves *B* are corrected

for the polarization effects according to the present theory. It should be noticed that the incomplete knowledge of the dispersion law makes the shape of the curves *B* in the neighborhood of the point at which they begin to deviate appreciably from the corresponding curves A rather uncertain. For somewhat greater energies instead the curves B become practically independent of the dispersion law, being given by (2.49).

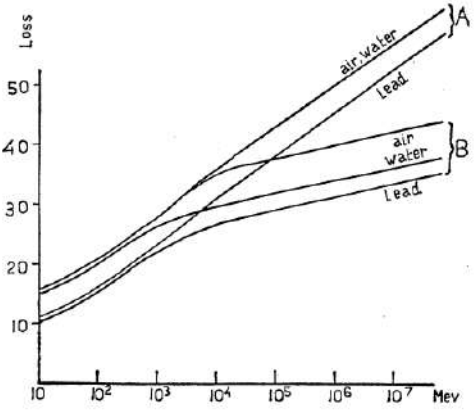

Fig 2.2: Energy loss in units of $\frac{2\pi e^4}{mv^2}$ for mesotrons of various energies in air, water, and lead. Curves *A* are calculated with Bloch's formula and curves *B* are corrected for the polarization effects according to the present theory [67]

According to (2.49) the loss of energy in a layer containing *N* electrons per cm^2 depends on the electronic density *n* in the layer. For two layers having the same *N* and different electronic densities n_1 and n_2 the difference in energy loss is:

$$W_1 - W_2 = \frac{2\pi Ne^4}{mc^2}\log\frac{n_2}{n_1}, \tag{2.50}$$

the energy loss being smaller for the substance of greater density. (2.50) is valid only for rather large energies of the mesotron; for smaller energies the difference is considerably less, as can be seen on the curves of Fig. 2.2, and it depends on the difference in atomic number between the different substances and not so much on the differences in density.

A difference in the absorption of mesotrons by air and by condensed substances in the sense that condensed substances have a smaller massabsorption than air has been reported by several experimenters. This difference is usually considered as evidence for a spontaneous decay of the mesotron. As the difference (2.50) is in the same sense as the experimentally observed differences, it is interesting to compare them quantitatively. Indeed

if it were possible to prove that (2.50) accounts for all the difference observed experimentally, this would eliminate the strongest argument in favor of the decay of the mesotron.

2.4 A. Bohr theory of the influence of atoms interactions on the penetration of particles through matter

Now we receive an estimation of interaction of electron, which is placed in point Q and collided with particle Z that is transmitted on distance *p* (Fig. 2.3) [33].

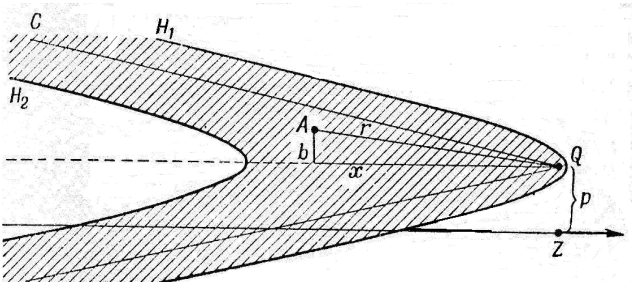

Fig 2.3: To explanation of a deceleration of particle in matter (Bohr hyperboloid) [33]

Simultaneously other accelerated electrons mainly in time $t' = t - \frac{r}{c}$ after a collision from this particle. An electron in point *A* in moment t' was placed in phase of co-collision, which is advanced on time τ the phase of co-collision in point Q. A time τ is equalled

$$\tau = \frac{r}{c} - \frac{x}{v} \tag{2.51}$$

where v – a velocity of particle, *x* – a projection of distance *QA* on the direction of motion.

Introductive $r^2 = x^2 + b^2$ we received from formula (2.51) next correlation [33]

$$\frac{(x+v\tau\gamma^2)^2}{v^2\tau^2\gamma^2(\gamma^2-1)} - \frac{b^2}{c^2\tau^2(\gamma^2-1)}. \tag{2.52}$$

Where $\gamma = \left(1 - \frac{v^2}{c^2}\right)^{-1/2}$.

Points $\tau = const$ in (2.52) are placed on hyperboloid.

Thus electrons, which in moment of time t' were had a phases equalled of phase of electron in point *Q*, will be placed on conical surface that propagate

to back direction with θ. Last angle are determined from equation $sin\frac{\theta}{2}=\frac{1}{\gamma}$. This surface is crossed the way of particle on distance $x=\frac{v}{c}\gamma p$.

On Fig.2.3 an electron, in point *Q* is placed on minimal distance p to particle. Electrons, which in moment of time t' are begun and ended collision will be placed on hyperboloids H_1 and H_2 approximately. Surfaces H_1 and H_2 are corresponded $\frac{\tau}{2\gamma v}$ and $-\frac{\tau}{2\gamma v}$. A value $\frac{\tau}{\gamma v}$ is equalled of collision time approximately. Therefore, basic part of force of action matter on electron is generated by electrons, which are placed in shaded region between H_1 and H_2 hyperboloids. For $\gamma \gg 1$ main part of this region is placed behind of electron on distance $\leq p\gamma$. Intensity of electrical field for this case may be determined as [33]

$$E(t)=\frac{e\ddot{\eta}(t')}{c^2 r}\sin\varphi, \tag{2.53}$$

where φ – an angle between an acceleration and a radius-vector, η – a displacement; $\ddot{\eta}$ – an acceleration.

This field is transverse (perpendicular to *r*). Therefore force, which act on particle in back direction relatively to direction of particle motion, is equalled [33]

$$\delta K(t)=\frac{z_1 e^2 \ddot{\eta}(t')}{c^2 r}\sin\varphi\cos\varphi. \tag{2.54}$$

For the case of Fig. 2.3 $\sin\varphi\sim 1$ and majority of represented electrons have acceleration near to the acceleration of electrons in point *Q*. Resulting polarized force has value

$$K\sim\frac{e^2}{c^2}\ddot{\eta}p^2 n \tag{2.55}$$

and back direction relatively to direction of $\ddot{\eta}$. This force is less as force $\mu\ddot{\eta}$ if

$$p\ll\frac{c}{\nu}, \tag{2.56}$$

where

$$\nu^2=\frac{4\pi n e^2}{\mu}. \tag{2.57}$$

Where μ – a mass of electron, n – a density of electron flow.

For the estimation of slowing-down power of matter we must compare a distance d_ν and adiabatic distance d_a. Last distance is determined as [33]

$$p \ll d_a = \frac{v}{\omega_a}\gamma,\ d_v = \frac{v}{\nu}, \tag{2.58}$$

where ω_a is adiabatic frequency.

Now we used this model for the explanation of microscopic mechanism of Cherenkov radiation. A condition of Cherenkov radiation is determined as

$$\sqrt{\varepsilon} = \frac{c}{v}. \tag{2.59}$$

In addition, according to condition of wave's stationarity relatively to moving particle, the angle of radiation is equalled

$$\cos\theta = \frac{c}{v\sqrt{\varepsilon}}, \tag{2.60}$$

where θ is measured from direction of particle motion.

With microscopic point of view Cherenkov radiation is caused of radiation of part of energy, which was transferred to electron from incident particle.

An influence of interatomic interactions on spectrum of Cherenkov radiation may be represented for two extremely cases: $d_\nu \gg d_a$ and $d_\nu \ll d_a$ Forces of interactions are weak for first case and are strong for second case comparatively to a force of electron bond in atom. Atoms will can realize many oscillations before an radiation for $d_\nu \gg d_a$. Therefore, radiation spectrum has narrowband nature near eigenfrequency. In case $d_\nu \ll d_a$ atoms can't be oscillated and spectral distribution don't be simple on narrowband spectrum. These properties of radiation are corresponded to condition (2.59). Dispersion law for one eigenfrequency has form [33]

$$\varepsilon = 1 + \frac{\nu^2}{\omega_a^2 - \omega^2}, \tag{2.61}$$

where frequency of oscillations of a "free" electron in the matter ν is determined from formula (2.60). Further according to formula (2.61) our two cases may be written as $\nu\gamma \ll \omega_a$ and $\nu\gamma \gg \omega_a$. It is certificated our conclusions about forms of spectra.

These explanations may be continued on processes of radiationless relaxation. For the case of ionization in the field of strong electromagnetic wave [33] we can have two possible ways of relaxation: radiation and radiationless. First way is generated the laser radiation, second may be caused the optical breakdown and destruction of irradiated material.

2.5 I. Golub model

Intense picosecond pulses propagating in nonlinear media can produce

frequency-broadened output beams with a nearly white spectrum, called the supercontinuum (SC) [77]. The observed SC generation is correlated with self-focusing and self-trapped filament formation, which are associated with saturation of nonlinearity and laser beam intensity stabilization. The effect was demonstrated in a variety of media, including solids, liquids and gases. Although SC and accompanying ring emission have been extensively studied and used as a white-light source of short pulses, the basic understanding of the phenomenon is far from being complete Self-phase modulation" (SPM), four-wave mixing (FWM), and SPM accompanied by FWM and Raman processes have been proposed to explain the SC. All these models have difficulties in explaining this effect; moreover, none of them is universal enough to explain the common characteristics observed in such a variety of media. For example, the FWM process is inconsistent with the observed spatial order of the colored rings and the spectral asymmetry of SC, the Raman effect cannot explain SC in liquid Ar or Xe gas and SPM as a source of the SC predicts a spectral broadening smaller than the observed one6 and does not explain the spatial properties of SC and ring emission. (Under the conditions that SPM plays a more prominent role than self-focusing and propagation effects, such as a white-light continuum generated in a short interaction length by femtosecond pulses, the observed spectrum is independent of emission angle and retains the directional properties of the pump beam. The model of the SC should not depend on spectroscopic details of the media; it must explain the spatial properties of SC [77].

While most of the studies were centered on the spectral characteristics of the SC, practically no attention was paid to its spatial properties. This is surprising, since the spatial properties are among the most salient features of the SC: In many experiments the SC generation is either accompanied by a ring emission" or itself evolves in the form of a divergent cone/ring emission in the forward direction. In the following this emission is referred to as SC cone emission (SCCE). The aim of [77] is to present new results on the spatial and polarization properties of the SC generated in H_20 or D_20 and to point out the similarity among the optical properties of the SCCE, the conical emission observed in alkali metal vapors and class II Raman radiation produced in liquids in the form of cones. These properties are characteristic of an emission formed at the surface of self-trapped filaments. As a surface phenomenon the SCCE obeys the condition of the Cherenkov-type emission process, where the transverse component of the linear momentum is not conserved. Surface radiation is expected at an angle that satisfies the Cerenkov relation when the laser-induced nonlinear polarization travels with an apparent velocity faster

than the phase velocity of light. By apparent velocity the propagation velocity of the induced perturbation of the medium is meant. This velocity can have both signs and can be larger than c, as in the case of a moving foci or a point of intersection of an obliquely impinging light wave with an interface between two media.

In these experiments a Quantel YG-471 mode locked laser was used, which produced 22-*ps*-duration pulses at 1.06, μm of up to 35-*mJ* energy or its second-harmonic 15-*ps*-duration pulses of 12-*mJ* energy. The laser radiation was focused into different 1-10-*cm*-long cells containing H_20 or D_20. A variety of lenses with focal lengths of 2 to 25 *cm*, capable of producing intensities in the focal spot of up to 10^{12} W/cm^2, were used. Several (usually 5 to 10) filaments were produced by each pulse. It was easier to produce SC by focusing the laser beam with long-focal-length lenses into the long cells, and the threshold for SC in D_20 was lower than that in H_20. The SC was spread in a circular rainbow, and for 1.06-μm excitation the generated photon energy increases with the off-axis angle, while for 0.53- μm excitation the pattern was more complicated. The surface character of the SC generated in H_20/D_20 is deduced from experiments similar to those used in [78] to show that the conical emission in sodium vapor is a surface emission of a Cherenkov-type process.

First, it was found that the SCCE emission had the same circular or linear polarization as that of the 1.06-μm input laser beam. The SCCE polarization, either linear or circular, is as pure as that of the input beam to a degree of 100:1, limited by the resolution [77]. Any light of circular polarization contains a small portion of counter rotating circular-polarization radiation. Owing to a difference in nonlinear refractive indices for the two polarizations, the weaker polarization should be self-trapped before the stronger one. The tendency of the weaker circular component to increase in intensity owing to self-focusing faster than the strong oppositely polarized component will result in intensities of both circular polarizations being equal inside the filaments, where the saturation degree is maximal. Thus, the light emitted from the filaments should have a linear polarization. This change was experimentally observed for Raman Stokes emission that originated in the self-trapped filaments. Since SCCE preserves the circular polarization of the input laser, we conclude that it is generated in a non-saturated region, i.e., at the surface of the self-trapped filaments. The absence of a change of a linear input polarization is due to its stability as a self-trapped component.

Next the spatial coherence of the SCCE was studied. The laser light was focused into the D_2O by either a spherical lens or a combination of cylindrical and spherical lenses (to produce the threshold intensity required for SC

generation). For the cylindrical focusing mode the laser beam's transverse cross section in the cell was elliptical, with an ellipticity of approximately 4:1. For both focusing modes the SCCE has a ring form (Fig. 1.18 and Fig. 1.29). The spherical or elliptical nature of the laser beam's cross section is evident in these photographs. Neutral-density filters, Corning color filters, and an on-axis disk were used to avoid overexposure by the laser beam. As in [77, 78], one should reason that the emission from the interior saturated parts of different filaments should be spatially coherent. This happens because the saturated refractive indices in different self-trapped filaments have the same value, resulting in the absence of dispersion and phase shifts between the light emitted from different filaments. In other words, the emission from the interior of the filaments should preserve the spatial coherence of the pump light. On the other hand, emission from the surface of different stochastically formed filaments does not preserve the coherence because of varying local conditions such as the laser intensity and the degree of saturation at the surfaces of the filaments. Thus, the emission from the interior of the filaments should interfere to form an ellipse for the cylindrical focusing mode that corresponds to the spatial distribution of the filaments, as observed for usual (or class I) Raman radiation. The uncorrelated emissions from the surfaces of the filaments sum incoherently, which results in a ring halo around the laser beam, independently of the excitation region pattern. The experiment (Fig. 1.18) shows that the SCCE spatial pattern is independent of the focusing mode, leading one to conclude that the origin of this emission is at the surface of the filaments. It was also found that the cone emission angle is independent of the lens focal length in the range 5-20 *cm*. The same effect was observed for class II Raman radiation. In contrast, the usual Raman emission cone angles are inversely proportional to the lens focal length. All these observations support the conclusion that the SCCE, similar to conical emission is alkali metal vapors and class II radiation, is a radiation formed on the surface of the self-trapped filaments-a process involving longitudinal momentum conservation only.

Kinematically the far-field pattern of the whiskers observed during SC generation in glasses is similar to the picture of Doppler effect or Cherenkov radiation produced by a moving source-polarization, for example. Recently conical emission of a 780-cm^{-1} bandwidth was observed in Na vapor irradiated with picosecond pulses, and it was explained in terms of Cherenkov emission. The observation of such a spectrally broad conical emission is seen as a strong argument in favor of a common mechanism for SCCE and conical emission in alkali vapors. The generality of the widely occurring phenomenon of

conical emission points to the need for a unifying model. Golub propose a Cherenkov type process to explain the SCCE. In the case of an electron-generated Cherenkov emission the polarization induced in the medium is radiating at frequencies that satisfy the Cherenkov relation

$$\cos\theta = {}^{c}/_{n(\omega)v},$$

even if they are far away from the resonant transitions. Similarly, the polarization (medium excitation) generated by a laser in a nonlinear medium contains Fourier components oscillating at frequencies of the light-induced response of the medium. This polarization, progagating with the laser pulse group velocity v_{gr}, will result in an emission at frequencies fulfilling the same Cherenkov condition at conical angle θ given by

$$\cos\theta = v_{ph} \,/\, v_{gr}.$$

Here v_{ph} is the phase velocity of the emitted light. Thus, it is the properties of the medium that, through conditions satisfying the Cherenkov relation, choose each Fourier-frequency component of the nonlinear polarization to emit at a specified angle.

To elucidate the similarity between the charged particle and light-induced Cherenkov emission one can invoke the analogy between Snell's law and Cherenkov emission. This is natural since both effects can be derived in the same way from the Huygens interference principle [77]. In Fig. 2.4(a) the point of intersection of a light pulse impinging at an angle φ on a boundary between two media moves with a velocity

$$v = {}^{c}/_{n_1\cos\varphi}$$

This relation, in conjunction with Snell's law, gives the Cherenkov relation $\cos\theta = {}^{c}/_{n_2(\omega)v}$ (Fig. 2.4(a)). Thus, the refraction law of light at the boundary between two media is the same as the condition for Cherenkov emission by a source moving along the boundary. In a nonlinear medium the emitted frequencies may differ from the excitation frequency. The Cherenkov relation is still valid since the constructive interference occurs at a given Cherenkov angle for each Fourier-frequency component of the light-induced nonlinear polarization. In a sense, one can speak about a nonlinear Snell-Cherenkov effect [77].

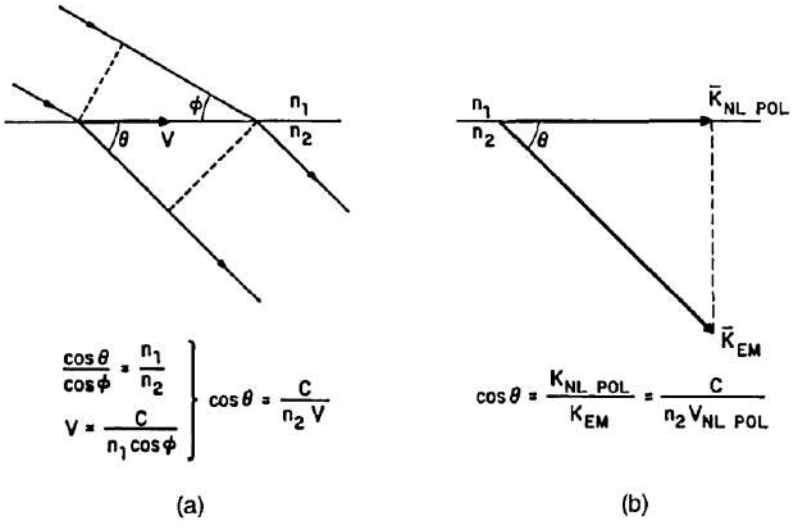

Fig 2.4: (a) Analogy between Snell's law and the Cherenkov effect. The point of intersection of a light pulse impinging upon a boundary between two media moves with velocity $v = {}^{c}/_{n_1 \cos\varphi}$. Combining this relation with Snell's law one obtains the Cherenkov relation, $\cos\theta = {}^{c}/_{n_2(\omega)v}$. (b) The Cherenkov angle relation can be obtained from the conservation of the longitudinal component of the linear momentum at a boundary between two media along which a nonlinear polarization is propagating [77]

The Cherenkov emission angle can also be derived from the conservation of the longitudinal component of the linear momentum at a boundary between two media along which a nonlinear polarization is propagating [Fig. 2.4(b)]. Using $k = {}^{\omega}/_{v}$, one obtains [77]

$$\cos\theta = {k_{nl\,pol}(\omega)}\Big/{k_{em}(\omega)} = {V_{em}}\Big/{V_{nl\,pol}} = {}^{c}/_{n_2(\omega)V_{nl\,pol}} \qquad (2.62)$$

The role of the boundary can be played by the surface of a self-trapped filament. The nonlinear polarization propagating along this surface will result in a light-induced Cherenkov emission. The non-conservation of the transverse component of the linear momentum can be related to the uncertainty principle, $\Delta x \Delta k > 1$, where Δx is the thickness of the boundary. Far from transitions in a region of normal dispersion from Eq. (2.62),

$$\cos\theta = \frac{n_l}{n_c(\omega)},$$

where n_l and $n_c(\omega)$ are the refractive indexes at the laser and the emitted radiation frequencies, respectively. This relation holds also for a two-level

system for laser intensities of the order of the saturation intensity." The Cherenkov condition, $v_{ph} < v_{gr}$ or $n_l < n_c(\omega)$, is satisfied for excitation by a laser at 1.06 μm and light emitted in the visible. It predicts light of higher frequencies to be emitted at higher angles-exactly as observed experimentally in [77, 78]. A similar frequency distribution that obeys the Cherenkov relation, i.e., the highest frequencies being emitted farther from the center of the beam, was observed for conical emission in Na. Note that for a parametrical FWM process the phase-matching condition $2k_L = k_{blue} + k_{red}$ predicts an inverse spatial order of the emitted photons k_{blue} and k_{red} ($|k| = {\omega n}/{c}$). The pattern of SCCE for 0.53-μm excitation is more complex. One may speculate that this is a result of an alternation of the normal dispersion in the visible owing to an induced Fano-type structure in the laser dressed continuum of the ionization levels. Note that the Fano profile is asymmetric and will result in an asymmetrical spectral emission, as observed for SC [77].

In summary, it has been shown that the SCCE is generated at the surface of self-trapped filaments. As a surface phenomenon, the SCCE shares its optical characteristics with other Cherenkov-type processes of conical emission in alkali metal vapors and class II Raman radiation. A model in which the surface radiation is emitted at angles that satisfy the Cherenkov relation explains qualitatively the spectrospatial properties of SCCE [77].

2.6 Supercontinuum radiation

The picture of Fig. 2.3 [33] may be used for the explanation of the processes of polarization under short-pulse laser irradiation too. Roughly speaking angle condition of Cherenkov radiation is simple to conditions of phase synchronism of basic nonlinear optical phenomena [59, 106, 140, 192]. Therefore, the process of laser destruction of dielectrics has oriental character. It may be represented as "nonadiabatic" process of the optical breakdown too. Large value for summary effect has problem of the saturation of excitation. For optical case it is determined as condition of multiphoton absorption.

The focusing (α_f) and Cherenkov (θ_{ch}) angles are connected with help formula [232, 233]

$$\alpha_f + \theta_{ch} = {\pi}/{2}. \tag{2.63}$$

This theory is universal and can be used for all cases of particle scattering and corresponding types of radiation, including Cherenkov radiation. Optically induced Cherenkov radiation, also known as cone continuous radiation, is of particular interest [58, 77, 232, 233].

Ionization losses due to a change in the polarization of the medium when ionizing particles pass through it are greater for the optical range of irradiation

than for high-energy particles. Optical radiation is too soft for high-energy particles, while the mode of irradiation by high-energy particles is too harsh for optical radiation.

Here we have two complementary processes. For high-energy particles, ionization losses are the inelastic part of the collision of the incoming particle with the particles of the medium, which leads to a change in its polarization and, accordingly, radiation. Roughly speaking, this is the radiative reaction of the medium to the passing of a particle. It should be noted that at the same time, elastic processes associated with the displacement of atoms under the action of an incoming particle can also occur.

In the optical case, nonuniform polarization is caused by nonuniformity of optical radiation absorption, which leads to the generation of a mixture of nonlinear optical effects, the spectrum of which is the spectrum of total radiation, including Cherenkov. Thus, for focused laser radiation, this inhomogeneity is due to the focused cone, and the generators of the cone of Cherenkov radiation are perpendicular to the focusing cone [232, 233].

Thus, in both cases we have radiation caused by non-uniform non-equilibrium polarization. From this point of view, Cherenkov radiation can also be attributed to the phenomenon of nonlinear optics. The classical phenomena of nonlinear optics are caused by a change in uniform non-equilibrium polarization.

According to A. Bohr, the generators of the cone of Cherenkov radiation are perpendicular to the enveloping line of the track of a high-energy particle [33]. In the optical case, instead of a track, we have a focused area [232, 233].

Different nature and appearance of the Mach cone for the case of high-energy particles and laser irradiation. For particles, the condition for the formation of a cone is that the speed of the incoming particle is greater than the phase speed of light in the medium. For the optical case, the main role is played by the excitation intensity, multiphoton processes must be mutually coherent, in other words, the processes have cascade nature.

The frequency spectrum of Cherenkov radiation by a particle is given by the Frank–Tamm formula [69, 211]:

$$\frac{d^2E}{dxd\omega} = \frac{e^2}{4\pi}\mu(\omega)\omega\left(1 - \frac{c^2}{v^2n^2(\omega)}\right), \tag{2.64}$$

The Frank–Tamm formula describes the amount of energy E emitted from Cherenkov radiation, per unit length traveled x and per frequency ω, $\mu(\omega)$ is the permeability and $n(\omega)$ is the index of refraction of the material

the charged particle moves through, q is the electric charge of the particle, v is the speed of the particle, and c is the speed of light in vacuum.

Let us now analyze the radiation spectrum [69]. Consider a system that has its own frequencies, for simplicity we will take one ω_0 (ω_0 – the frequency is measured in the laboratory frame of reference, i.e. $\omega_0 = \omega_0'\sqrt{1-\beta^2}$). It can be considered one of the components of a complex spectrum, and it is permissible to consider the radiation associated with it.

If the momentum of a photon in the medium $\frac{n\hbar\omega}{c}$ is small compared to the momentum of the emitter, then the law of conservation of momentum during radiation can be written as follows:

$$\frac{n\hbar\omega}{c}\cos\theta = \frac{\Delta E}{v}. \tag{2.65}$$

Where ΔE is change of kinetic energy the radiator, v its velocity.

The change in kinetic energy is determined by the energy of the emitted photon $\hbar\omega$ and the change in the internal energy of the system $\hbar\omega_0$:

$$\Delta E = \hbar\omega \pm \hbar\omega_0. \tag{2.66}$$

The value $\hbar\omega_0$ should be taken with a minus sign if the system passes from a higher state to a lower state during radiation. A plus sign should be taken if the system is excited during radiation.

Combining equations (2.65) and (2.66) we get [69]:

$$\frac{n(\omega)\omega}{c}\cos\theta = \frac{\omega\pm\omega_0}{v}. \tag{2.67}$$

Equation (2.67) describes three cases [69]:

1. Let

$$\frac{n(\omega)v}{c}\cos\theta = 1. \tag{2.68}$$

Then equation (2.67) is fulfilled only under condition ω_0 =0. This is precisely the condition of Cherenkov radiation.

2. Let us now assume that in equation (2.68) there is a value less than unity on the left, then (2.67) can be valid only in the case of a minus sign in front ω_0, i.e.

$$\frac{n(\omega)\omega}{c}\cos\theta = \frac{\omega-\omega_0}{v} \text{ for } \frac{n(\omega)v}{c}\cos\theta < 1. \tag{2.69}$$

This is nothing but the Doppler condition for a light source moving in a medium.

3. The third case occurs when the left side of equation (2.68) contains a value greater than unity. Then in (2.67) there should be a plus sign before; so,

$$\frac{n(\omega)\omega}{c}\cos\theta = \frac{\omega+\omega_0}{v} \text{ for } \frac{n(\omega)v}{c}\cos\theta > 1. \quad (2.70)$$

This is a case of the relativistic Doppler effect.

Thus, as in the case of Cherenkov radiation, a system with its own oscillation frequency will spend its kinetic energy on radiation at superluminal speed.

It can be formulated as follows: it is known that in classical electrodynamics, a ruse with superluminal speed in a vacuum is impossible. It is possible in the environment, but nature does not completely remove this prohibition. Any system that interacts with radiation at superluminal speeds will slow itself down by emitting light.

Let us now consider the spatial distribution of the spectrum by the frequencies of Cherenkov radiation [69].

For the classical case, the shorter-wavelength radiation is closer to the trajectory of the incident particle. A similar frequency distribution is typical for the optical case (Fig. 2.5) [160, 161, 232, 233].

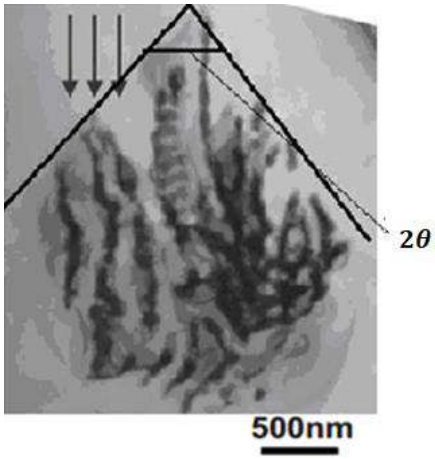

Fig 2.5: Schematic representation of the first stage of the destruction cascade during laser-induced optical breakdown of silicon carbide [160, 161, 232, 233]

Focused laser irradiation with wavelength 800 *nm* and pulse duration 130 *fs* was used for the irradiation hexagonal silicon carbide 4H-SiC [160, 161]. Sectional area of these structures was ~ 22 μm, the depth of ~ 50 μm. As seen

from [160, 161] we have five stages disordered regions, which are located at a distance from 2 to 4 μm apart vertically [160, 161]. Branches themselves in this case have a thickness from 150 to 300 *nm*. In this case there are lines in the irradiated nanocavity spherical diameter of from 10 *nm* to 20 *nm*. In this case irradiated structures have crystallographic symmetry of the initial structure. The first three stages of the cascade have a clearly defined conical structure [160, 161, 232, 233].

As can be seen from the figure, traces of laser-induced optical breakdown, which correspond to the short-wavelength part, are larger near the axis of the cone. More detail information of all processes, which are generated in silicon carbide will be represented in Chapter V.

Critical value of power for self-focusing may be estimate in next way. If the beam diameter is *D*, the beam might be expected to expand by diffraction with an angular divergence of $\theta = {1.22\lambda}/{n_0 D}$, where n_0 – linear refractive index of medium, λ – laser wavelength. Therefore, Kerr media critical power may be determined as [193, 232]

$$P_{cr} = (1.22\lambda)^2 \frac{c}{64 n_2}. \tag{2.71}$$

Where n_2 is nonlinear refractive index of the medium.

The self-focusing length determined with help next formula [193, 232]

$$Z_{sf} = \frac{0.367 k \omega_0^2}{\left[\left(\sqrt{{P}/{P_{cr}}} - 0.852\right)^2 - 0.0219\right]}, \tag{2.72}$$

Where $k = {2\pi}/{\lambda}$ is the wave number, ω_0 – is the spot side of the pump beam, *P* – pump power.

This formula are using as basic for the determination of threshold self-focusing and self-trapping generation. But this formula can't be use for the determination threshold of power the optical breakdown. For example, the power of creation the laser filaments in irradiated matter may be ~700 P_{cr} [193]

In [193, 232] formula for the determination P_{cr}, as threshold power of self-focusing, is represented in next form

$$P_{cr} = \frac{3.77\lambda^2}{8\pi n_0 n_2} \tag{2.73}$$

Therefore, first model were connected with self-focusing and self-trapping and liquid and other isotropic matter.

For Kerr media the change of refractive index is represented as $\delta n = K|E|^2$, where E is peak amplitude of linearly polarized field. According to [113] coefficient K have 12 presentations [193].

But Kerr media are represented liquids basically. For solid state basic phenomena are laser-induced electrostriction [191]. In the gas case we can have other nonlinear optical phenomena. Therefore, we must select more universal concept for the determination P_{cr}. It may be physical-chemical method. In this case we must have concentration of proper centers of scattering (absorption) of laser radiation, which are generated proper nonlinear optical phenomenon, and its activation energy. The self-focusing is nonlinear optical process; therefore, P_{cr} or the critical value of energy may be determined in next way [232, 233]. Volume density of energy of the creation self-focusing process may be determined with help next formula W_{crvol}

$$W_{crvol} = E_a N_{nc}, \tag{2.74}$$

where E_a – energy of activation proper "nonlinear" centers; N_{nc} – their concentration.

Surface density for optical thin may be determined as

$$W_{crsur} = {}^{W_{crvol}}/_{\alpha}, \tag{2.76}$$

where α – absorbance index. Integral value of energy may be determined as

$$W_{crin} = W_{crsur} \cdot S, \tag{2.77}$$

where S – the square of irradiation.

In this case

$$P_{cr} = {}^{W_{crin}}/_{\tau_{ir}}, \tag{2.78}$$

where τ_{ir} is duration of laser irradiation.

Optically induced Cherenkov radiation compared to the classical case (irradiation by γ-quanta, electrons, ions) has the following features [232, 233]:

1. Has significantly higher photon efficiency, both differential and integral;
2. Optical radiation, in contrast to the classical case, does not create additional radiation defects by itself, unless the transition to optical breakdown modes occurs;

3. The specific quantum yield (photon efficiency) is much higher than for the classical case, which makes it promising for micro and nanophotonics.

The energy of a particle converted into Cherenkov radiation is small compared to the energy it spends on ionization and excitation of the atoms of the medium. The number of photons emitted per 1 *cm* path, depending on the medium (radiator), varies from several units to several hundreds. This radiation can be observed visually and recorded using photographic film or a photomultiplier tube (PMT), which converts the radiation energy into an electrical signal. On a color photographic film placed perpendicular to the direction of motion of the particle, the radiation coming out of the radiator has the form of a ring of blue-violet color.

The Cherenkov detector consists of a transparent radiator (it can be solid, liquid or gaseous), an optical system that ensures the "collection and delivery" of Cherenkov photons to the PMT, and the PMT themselves. The duration of the signal of the Cherenkov counter is $\approx 10^{-9}\ s$ [96, 279, 280].

The dependence of the radiation angle θ on $\beta = {}^{v}/_{c}$ makes it possible, by determining this angle, to find the velocity and energy of the particle. The Cherenkov detector can detect particles with energies up to 100 *GeV*.

There are three types of Cherenkov detectors [60]:

- Threshold Cherenkov counters.
- Differential Cherenkov counters.
- Differential counters with total internal reflection.
- Differential counters with an annular diaphragm.
- Cherenkov detectors of the ring image or RICH detectors (RICH - Ring Imajing CHerenkov).
- RICH detectors with quasi-focusing (direct focusing) (Proximity focusing RICH).
- RICH detectors with a spherical mirror.
- RICH detector with total internal reflection. DIRC detectors (DIRC - Detection of Internally Reflected Cherenkov light).

The use of optically induced optical radiation is the creation of lasers with a wide spectrum of radiation.

As we can see, the difference between the use of optically induced and classical Cherenkov radiation is different: optically induced is used to obtain

powerful fluxes of supercontinuum radiation, while classical is used to detect rather weak fluxes.

The relationship between Cherenkov radiation and supercontinuum radiation can be demonstrated with the help of formula (2.50). For a homogeneous environment different electronic densities n_1 and n_2 are determined by light absorption and may be represent as

$$n_i = n_{i0}e^{-\alpha x}, i \in (1,2), \tag{2.79}$$

where α is corresponding absorption index.

Therefore, formula for one type of excitation the electronic states after substitution (62) may be represented as

$$W_1 - W_2 = \frac{2\pi Ne^4}{mc^2}\log\frac{n_2}{n_1} = \frac{2\pi Ne^4}{mc^2}\alpha(x_1 - x_2). \tag{2.80}$$

In other words, the energy losses of radiation in the environment are determined by the effective absorbed energy. Having the spectral distribution of radiation, we can determine the contribution of a certain spectral region to the integral effect. For example, this calculation can be compared with the physical-chemical energy calculation of the energy required for the optical breakdown of silicon carbide or potassium chloride.

For optical case

$$N = kN_{phot}, \tag{2.81}$$

where N_{phot} is the number of photons emitted by the laser, k is the conversion factor of the incident radiation, usually, k may be change from 0,01 for case of CO_2-laser irradiation of potassium chloride to 0,2 for case femtosecond laser irradiation with wavelength 800 *nm* of silicon carbide.

2.7 Cherenkov radiation of tachyons

A tachyon or tachyonic particle is a hypothetical particle that always travels faster than light [63]. Physicists believe that faster-than-light particles cannot exist because they are not consistent with the known laws of physics. If such particles did exist they could be used to send signals faster than light. According to the theory of relativity this would violate causality, leading to logical paradoxes such as the grandfather paradox. Tachyons would exhibit the unusual property of increasing in speed as their energy decreases, and would require infinite energy to slow down to the speed of light [35, 65]. No verifiable experimental evidence for the existence of such particles has been found.

Particles moving at speeds greater than the speed of light were theoretically predicted by Sudarshan, Bilanyuk and Deshpande in 1962 [24].

In the 1967 paper that coined the term, Gerald Feinberg proposed that tachyonic particles could be made from excitations of a quantum field with imaginary mass [65]. However, it was soon realized that Feinberg's model did not in fact allow for superluminal (faster-than-light) particles or signals and that tachyonic fields merely give rise to instabilities, not causality violations. Nevertheless, in modern physics the term *tachyon* often refers to imaginary mass fields rather than to faster-than-light particles. Such fields play a significant role in modern physics.

The term comes from the Greek: ταχύ, *tachy*, meaning *swift*. The complementary particle types are called luxons (which always move at the speed of light) and bradyons (which always move slower than light); both of these particle types are known to exist [63, 65].

It is shown that, in the general case, tachyon Cherenkov radiation cannot have axial symmetry with respect to the tachyon velocity v.

Hence the conclusion about the “vector nature” of the tachyon is made. An electric dipole is considered as a vector characterizing the tachyon [63]. Expressions are obtained for the tachyon Cherenkov radiation spectrum, taking into account the asymmetry, for the case of a charged tachyon without a dipole moment and for a neutral tachyon dipole arbitrarily oriented with respect to v. Installed the identity of the integral characteristics of both types of tachyon Cherenkov radiation, which indicates the universal nature of the "vector" of tachyons. A new tachyon-specific integral of motion is indicated.

The application of known physical principles to charged tachyons leads to the conclusion that they have Cherenkov radiation in vacuum [63]. However, attempts to detect tachyons by such radiation gave a negative result [63]. But attempt of measurement the Cherenkov radiation of tachyon was made by Tyapkin [246, 247]. This prompted a number of authors to introduce a kind of "rule of prohibition" on the emission of photons by charged tachyon [35, 63]. Such rules seem unsatisfactory, because:

1) They do not follow from known conservation laws;
2) Them the conclusion suggests the possibility of implementing reference systems rigidly connected with tachyons;
3) They contradict Maxwell's equations, which are valid for any source velocity [63].

On the other hand, from the negative results of [63], in general, there is no need to revise the physical principles. These results can be explained simply by the absence of tachyons in nature, the small the cross section for their

photoproduction or the presence of features in the Cherenkov radiation of tachyons that were not taken into account in the experiment. One of these features is indicated in [63, 263]: this is the constancy of the radiation reaction force, due to which the tachyon practically cannot achieve a stable mode of motion in an external electric field.

In [63], we consider another feature of Cherenkov radiation of tachyons, not taken into account in previous studies and associated with an important property of the tachyon – "vector". Namely, as shown below, the Cherenkov radiation of tachyons spectrum, generally speaking, has no axial symmetry with respect to the velocity vector ω. As a result, in addition to the frequency ω, the spectrum depends on two more parameters: azimuth angle φ and "mismatch" angle χ.

The absence in the general case of axial symmetry of the Cherenkov radiation of tachyons follows directly from the transformation properties of the 4-vector $(\omega/c, \mathrm{k})$, where k is the wave vector of radiation with frequency ω. Due to these properties (or, which is the same, due to the Doppler effect) radiation symmetric with respect to the tachyon velocity v_0 in some inertial frame L_0 is not such in another inertial frame L moving with the speed $V \perp v_0$. This effect manifests itself most clearly when in L_0 velocity $v_0 = \infty$ and PIT is a diverging cylindrical wave [63].

Then in L (at $V \perp v_0$) the speed is $v = v_0 = \infty$, and the Cherenkov radiation of tachyons front is also cylindrical. However, due to the Doppler frequency shift, the stiffness ratio radiation emitted along and against the direction V is equal to (c – V)/(c + V) and becomes arbitrarily small as V→c.

In the general case (for $v_0 \neq \infty$) the transition $L_0 \rightarrow L$ is accompanied by a change magnitude and direction v_0. This complicates the situation, but the quality the picture of the phenomenon is preserved. The aim of this work is to consider the main features of the Cherenkov radiation of tachyons symmetry breaking effect and its possible observed manifestations.

We are representing two cases [63].

Case 1. Let there be a subgroup of "privileged" inertial systems L_0, in which the radiation from a given tachyon (and, consequently, its charge distribution) is symmetrical with respect to v_0. All L_0 systems are obtained from one another by a continuous Lorentz transformation with $V \uparrow\uparrow v_0$.

In all systems L outside L_0, the radiation will not be axisymmetric, and

this symmetry breaking occurs in the absence of a medium whose motion could cause it. This situation is only possible if the tachyon of some "built-in"

vector **e**, which selects a certain direction in space. In the absence of external forces, this direction (which can be different for different tachyons due to the isotropy of space) is a "conserved quantity".

This can be formulated as the following statement: if there is at least one frame of reference in which the Cherenkov radiation of tachyons is axisymmetric, then, due to the requirements of Lorentz invariance, the tachyon must be "vector" particle in the above sense.

The physical nature of the vector **e**, apparently, cannot be established from general principles alone. However, from the above, it is clear that the transformation properties of e are the same as those of a segment of length (in particular, e does not change when $L_0 \to L$ passes from $V \perp \mathbf{e}$). Therefore, **e** is not; can be spin s (especially since tachyon has s = 0 [9]). Therefore, it is natural to assume that the vector e is related to the electric dipole moment of the tachyon, i.e. e=d=ql, where q is the charge, l is the length of the dipole.

For $d \neq 0$, electromagnetic radiation would also be observed for a neutral tachyon in accordance with the fact that for it kinematically allowed photoproduction and pair annihilation processes

$$\hbar\omega_1 + \hbar\omega_2 \leftrightarrow \tau + \tilde{\tau} \tag{2.82}$$

and crossing-symmetric with (2.1) photodecay reaction

$$\tau_1 \to \tau_2 + \hbar\omega_1 + \hbar\omega_2 \tag{2.83}$$

equivalent to Cherenkov radiation (the two-photon nature of these processes is due to the zero spin of the tachyon).

It should be emphasized, however, that the assumption of a dipole nature of **e**, although it seems natural, is by no means necessary.

The vector **e** may or may not be a dipole [63].

In accordance with what has been said, we will consider the features of CHIT in two different cases:

1) A tachyon with an electric charge q at d = 0 (this case, the vector e has a non-dipole nature);
2) Electrically neutral tachyon with dipole moment d = e.

Let us first consider a tachyon in the subgroup L_0 (all those belonging to L_0 values will be marked with the index "0"). Due to the nonpoint nature of the tachyon [63] it has effective dimensions – a constant radius a_0 perpendicular to v_0 and a longitudinal length //experiencing Lorentz contraction at $v_0 \to c$:

$$l = \tilde{\gamma}^{-1}(v_0)l_0, \tilde{\gamma}(v) = \left(\frac{v^2}{c^2} - 1\right)^{-1/2} = \text{ctg}\theta. \quad (2.84)$$

Here l_0 is the "intrinsic" length of the tachyon, θ is the angle between v_0 and $\mathbf{k}_0$. At $v_0 = v_c = \sqrt{2}c$ we have $l = l_0$. For a "spherically symmetrical" tachyon l_0=2a_0, and the tachyon is an ellipsoid of revolution, disk-shaped at $c < v_0 < v_c$, cigar-shaped for $v_0 > v_c$ and a ball for $v_0 = v_c$.

To determine the Cherenkov radiation of tachyons, you need to know the charge form factor of the tachyon $\rho(k)$ in k-space. In case 1, we will proceed from the considered in [63] the model of a uniformly charged "ball" of radius a_0. Its form factor $\rho(k)$, taking into account (2.84), has the form [63]

$$\rho_0(k_0) = \frac{3}{2\sqrt{2}} \frac{\sin\sqrt{2}a_0\tilde{k}_0 - \sqrt{2}a_0\tilde{k}_0\cos\sqrt{2}a_0\tilde{k}_0}{(a_0\tilde{k}_0)^3}, \tilde{k}_0 = k_0\sin\theta_0. \quad (2.85)$$

In case 2, consider the distribution $\rho = \rho^+ + \rho^-$, where

$$\rho^+ = \begin{cases} \rho, 0 \le r \le a_0, z_1 \le z \le z_2, 0 \le z_1 \le z_2, \\ 0, r > a_0, z_1 < z_1, z > z_2, \end{cases} \quad (2.86a)$$

$$\rho^- = \begin{cases} -\rho, 0 \le r \le a_0, -z_2 \le z \le -z_1 z_1 \le z \le z_2, \\ 0, r > a_0, -z_1 < z, z < -z_2 \end{cases} \quad (2.86b)$$

(r,z are cylindrical coordinates in L_0 with the oz-axis parallel to the vector v_0.

Expression (2.86) describes two uniformly and oppositely charged "cylinders" with radius a_0, height b=$b_0\tilde{\gamma}^{-1}(v_0)$ = z_2 – z_1, distance between centers (dipole length) l = $l_0\tilde{\gamma}^{-1}(v_0)$ = z_2 + z_1 and density charge $\rho = q\tilde{\gamma}(v_0)/\pi a_0^2 b_0$. For $z_1 > 0$ cylinders are spatially separated ($l_0 > b_0$), For z_1 = 0 they have a common base they $l_0 = b_0$.

After applying the Fourier-Bessel transformations to (2.86), we have

$$\rho_0(k_r, k_z) = 8\pi i\rho \frac{a_0}{k_r k_z} J_1(a_0 k_r)\sin\frac{b_0 k_z}{2\tilde{\gamma}(v_0)}\sin\frac{l_0 k_z}{2\tilde{\gamma}(v_0)}. \quad (2.87)$$

Here J_1 are the Bessel functions of the first orders. The total power of the Cherenkov radiation of tachyons in L_0 is expressed in terms of the form factor $\rho(k)$ [63]

$$\frac{d\tilde{E}_0}{dt_0} = v_0 f_0, f_0 = \theta_0 \int_0^\infty |\rho_0(k_0\sin\theta_0, k_0\cos\theta_0)|^2 k_0 dk_0, \quad (2.88)$$

where the reaction force f_0 is an invariant in L_0. From (2.88) follows the expression for the radiation power in the range ω_0, $\omega_0 + d\omega_0$ in the direction

$\mathrm{n}_0 = \frac{\mathrm{k}_0}{k_0}$ with azimuth angle φ_0:

$$\frac{d\tilde{E}_0(\omega_0,\varphi_0)}{dt_0} = \frac{1}{2\pi} v_0 |\rho_0(k_0,n_0)|^2 \tilde{k}_0 d\tilde{k}_0 d\varphi_0. \quad (2.89)$$

Substituting here (2.85) and (2.86) we obtain the spectrum of Cherenkov radiation of tachyons in L_0 for the cases 1 and 2, respectively:

$$\frac{d\tilde{E}_0(\omega_0,\varphi_0)}{dz_0} = \frac{9}{16}\frac{q^2}{\pi}\left\{\frac{\sin\sqrt{2}a_0\tilde{k}_0 - \sqrt{2}a_0\tilde{k}_0\cos\sqrt{2}a_0\tilde{k}_0}{(a_0\tilde{k}_0)^3}\right\}^2 \tilde{k}_0 d\tilde{k}_0 d\varphi_0; \quad (2.90)$$

$$\frac{d\tilde{E}_0(\omega_0,\varphi_0)}{dz_0} = \frac{32}{\pi}\left\{\frac{q}{a_0 b_0} J_1(a_0\tilde{k}_0)\sin\frac{b_0\tilde{k}_0}{2}\sin\frac{l_0\tilde{k}_0}{2}\right\}^2 \frac{d\tilde{k}_0}{\tilde{k}_0^3}\, d\varphi_0. \quad (2.91)$$

For $l_0 \to \infty$ formula (2.91) describes the total radiation of two independent charges $+q$ and $-q$. Indeed, in this case $\sin^2\frac{l_0\tilde{k}_0}{2}$ oscillates infinitely fast and is replaced by its average value of ½, so

$$\lim_{l_0\to\infty}\frac{1}{2}\frac{d\tilde{E}_0(\omega_0,\varphi_0)}{dz_0} = \frac{8}{\pi}\left\{\frac{q}{a_0 b_0} J_1(a_0\tilde{k}_0)\sin\frac{b_0\tilde{k}_0}{2}\right\}^2 \frac{d\tilde{k}_0}{\tilde{k}_0^3}\, d\varphi_0.$$

The use in (2.87) of only one integral corresponding to one of the "cylinders" will lead to the same value. Therefore, the factor $4\sin^2\frac{l_0\tilde{k}_0}{2}$ describes the change in the radiation power of the frequency ω_0 when the charge q is replaced by a dipole ($+q$, $-q$). This multiplier "modulates" spectrum of an individual charge, canceling the frequencies for which $n\lambda = l\cos\theta_0, \lambda = 2\pi c/\omega, n = 1,2,\ldots$ (interference condition, known for Cherenkov dipole in an isotropic medium).

On Fig. 2.6 [63] shows the spectra of Cherenkov radiation of tachyons with energy measured in units $\varepsilon = q^2/a_0$, for cases (2.90) and (2.91) under the condition $a_0/l_0 = l_0/b_0 = 2$.

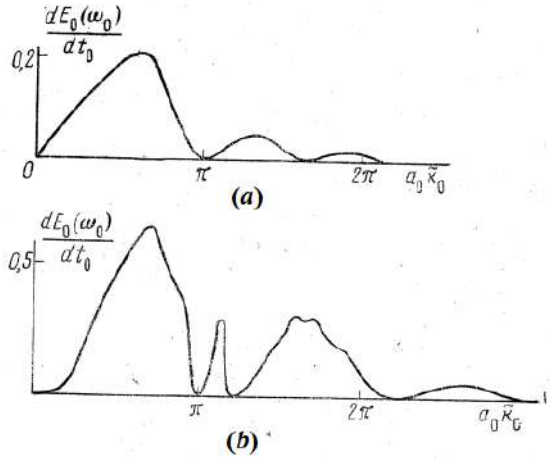

Fig 2.6: The spectra of Cherenkov radiation of tachyons [63]

It's clear that in the case of a charged tachyon, the main part of the Cherenkov radiation of tachyons energy is concentrated in the wavelength range

$$\lambda_m \sim a_0 \sin\theta_0. \tag{2.92}$$

In the spectrum of a dipole, the envelope can generally form three humps in the regions

$$\lambda_{m_1} \sim a_0 \sin\theta_0, \lambda_{m_2} \sim b_0 \sin\theta_0, \lambda_{m_3} \sim l_0 \sin\theta_0, \tag{2.93}$$

determined by virtue of (2.84) by the projections of the transverse and longitudinal dimensions of the tachyon a_0, b_0, l_0 on the direction of radiation. The area under the humps and thus, the shares of the Cherenkov radiation of tachyons energy distributed between them are related as: $a_0 : b_0 : l_0$.

From (2.92), (2.93) it can be seen that both for the charge and for the dipole $\lambda_m \to 0$ at $v_0 \to c$. When $v_0 \to \infty$ we have for the charge $\lambda_m \to a_0$, and for the dipole

$$\lambda_m \sim \begin{cases} a_0, a_0 > l_{0,} \\ l_0, l_{0,} > a_0. \end{cases} \tag{2.94}$$

The second difference between the spectrum (2.91) and (2.90) is in the faster decay: long-wavelength asymptotic ($\frac{d\tilde{E}_0}{d\lambda_0} \sim \lambda_0^{-3}$ for charge and $\frac{d\tilde{E}_0}{d\lambda_0} \sim \lambda_0^{-5}$ for dipole, $\lambda_0 \gg a_0, b_0, l_0$). For real sources in a medium with a refractive index $n(\omega)$ his difference is significant, since it is the long-wavelength (optical) asymptotic behavior that is "filtered out" by the condition $v >$

$^{c}/_{n(\omega)}$ in the form of the observed Cherenkov radiation. For tachyon there is no filtering condition, and radiation with $\lambda_0 \leq a_0, b_0, l_0$ plays the main role,

Therefore, the reaction f_0 and the total radiation power are approximately the same for both charged and neutral tachyons with the same a_0, l_0 and q.

Let us pass to the system L, moving with the speed $V \perp \mathbf{e}$ in the positive direction of axis direction x_0; directing the $\tilde{x},\ \tilde{y}, \tilde{z}$ axes of the system L parallel to the axes x_0, y_0, z_0 in L_0, we obtain for the components and the magnitude of the tachyon speed v in L:

$$v_x = -V, v_z = \gamma^{-1}(V)v_0, \gamma(V) = \left(1 - \frac{V^2}{c^2}\right)^{-1/2}, \quad (2.95)$$

$$v^2 = v_0^2 - V^2\left(1 - \frac{v_0^2}{c^2}\right), v_0 = \gamma(V)\sqrt{v^2 - V^2}. \quad (2.96)$$

According to (2.95) in L the vectors v and $\mathbf{e}$ form an angle χ with each other, for which

$$\sin\chi = {}^{V}/_{v}. \quad (2.97)$$

This angle is thus an additional degree of freedom of the tachyon, which determines the orientation of the vector $\mathbf{e}$ with respect to the direction his speed. The value of χ can in principle be measured from the observed features of the Cherenkov radiation of tachyon [63].

From the invariance of spherical waves, the envelope of which forms radiation front, it follows that in L there is also a radiation cone under angle θ to the vector v, and cos θ =c/ v. Hence, with the help of (2.95)-(2.96) we find

$$\sin\theta_0 = {}^{\sin\theta}/_{\cos\chi}, \beta = {}^{V}/_{c} = {}^{\sin\chi}/_{\cos\theta}, 0 < \sin\chi \leq \cos\theta. \quad (2.98)$$

To find the spectrum in L, we write the Lorentz transformations of the corresponding quantities for $V \perp$ **e**:

$$\omega_0 = \gamma(V)(1 + \beta\cos\psi)\omega, \quad (2.99)$$

$$d\tilde{E}(\omega_0, \varphi_0) = \gamma(V)(1 + \beta\cos\psi)d\tilde{E}(\omega, \varphi), \quad (2.100)$$

$$dt_0 = \gamma^{-1}(V)dt. \quad (2.101)$$

here ψ is the angle between V and the considered direction of radiation $\mathbf{n}$, φ is the azimuth angle with the polar axis oz along v. Using the relation $\cos\psi = \sin\theta\cos\chi\cos\varphi - \sin\theta\sin\chi$ and taking into account (2.98) – (2.101), we obtain

$$\frac{d\tilde{E}(\omega,\varphi)}{dt} = \frac{1 - \mathrm{tg}^2\chi\,\mathrm{tg}^2\theta}{1 + \mathrm{tg}\chi\,\mathrm{tg}\theta\cos\varphi}\frac{d\tilde{E}(\omega_0,\varphi_0)}{dt_0}. \quad (2.102)$$

Since the component k_y does not change under the transformation $L_0 \rightarrow L$, we have $k\sin\theta\sin\varphi = k_0\sin\theta_0\sin\varphi_0$. This implies

$$\frac{\sin\varphi_0}{\sin\varphi} = \frac{\omega}{\omega_0}\cos\chi, \frac{\omega}{\omega_0} = \frac{1+\mathrm{tg}\chi\mathrm{tg}\theta\cos\varphi}{\sqrt{1-\mathrm{tg}^2\chi\mathrm{tg}^2\theta}}\cos\chi. \quad (2.103)$$

With the help of these relations and (2.89) we obtain the spectrum in L in the form [63]

$$\frac{d\tilde{E}(\omega,\varphi)}{dz} = \frac{\sin^2\theta}{2\pi}\left|\rho_0\left(\frac{1+\mathrm{tg}\chi\mathrm{tg}\theta\cos\varphi}{\sqrt{1-\mathrm{tg}^2\chi\mathrm{tg}^2\theta}}k\cos\chi\mathrm{n}_0(\mathrm{n})\right)\right|^2 kdkd\varphi. \quad (2.104)$$

According to (2.104), in the general case, Cherenkov radiation of tachyon depends on the angles φ, χ, i.e., the intensity is different for different mutual orientations e and v and different n, forming a radiation cone. The asymmetry disappears at $\chi \rightarrow 0$, except for the case $v = \infty$, i.e. $\theta = \frac{\pi}{2}$. As can be seen from (2.98), as $\theta \rightarrow \frac{\pi}{2}$ we have $\chi \rightarrow 0$, $\theta_0 \rightarrow \frac{\pi}{2}$, and (2.104) takes the form

$$\frac{d\tilde{E}(\omega,\varphi)}{dz} = \frac{1}{2\pi}\left|\rho\left(\frac{1+\beta\cos\varphi}{\sqrt{1-\beta^2}}k\cos\chi\mathrm{n}_0(\mathrm{n})\right)\right|^2 kdkd\varphi. \quad (2.105)$$

This expression becomes axisymmetric under the condition $V \rightarrow 0$, imposed directly on the velocity V. Thus, the condition x = 0 you divides the subgroup L_0 in all cases except for $v = \infty$.

Outside L, only the mirror symmetry of the Cherenkov radiation of tachyon with respect to plane A given by the vectors **e** and v. In A, there is a minimum ($\varphi = 0$) and maximum ($\varphi = \pi$) spectral brightness of Cherenkov radiation of tachyon. Their ratio, due to (2.104) equal to [63]

$$\frac{d\tilde{E}(\omega,0)}{d\tilde{E}(\omega,\pi)} = \left|\frac{\rho_0(\eta k n_0(0)\cos\chi)}{\rho_0(\eta^{-1}kn_0(\pi)\cos\chi)}\right|^2, \eta = \left(\frac{1+\mathrm{tg}\chi\mathrm{tg}\theta}{1-\mathrm{tg}\chi\mathrm{tg}\theta}\right)^{1/2}, \quad (2.106)$$

depends on the form factor $\rho(k)$ and, therefore, is different for the charge and for a dipole.

Integrating (2.104) over *k* and φ, we find the total power and reaction force *f* in L. Integration over *k* gives, taking into account (2.88),

$$\frac{d\tilde{E}(\varphi)}{dt} = -\frac{1}{2\pi}\frac{1-\mathrm{tg}^2\chi\mathrm{tg}^2\theta}{(1+\mathrm{tg}\chi\mathrm{tg}\theta\cos\varphi)^2}f_0 v d\varphi. \quad (2.107)$$

From here we obtain the ratio of the minimum and maximum integral brightness Cherenkov radiation of tachyon

$$d\tilde{E}(0)\Big/d\tilde{E}(\pi) = \eta^{-4}, \quad (2.108)$$

which no longer depends on the form factor and therefore can serve (for known v) to determine χ.

Next, integrating (2.107) over φ, we find [63]

$$\frac{d\tilde{E}}{dt} = -\frac{f_0 v}{\sqrt{1-\mathrm{tg}^2\chi\,\mathrm{tg}^2\theta}} = fv. \tag{2.109}$$

Using the relations between the mass m and energy E the speed of the tachyon, we can write (2.109) in the form [63]

$$\frac{dE}{dt} = -\frac{d\tilde{E}}{dt} = \frac{f_0}{mc}\left(\frac{E^2+m^2c^4}{E^2-m^2c^4\mathrm{tg}^2\chi}\right)^{1/2}, 0 < \mathrm{tg}\chi < E/mc^2. \tag{2.110}$$

Formula (2.110) generalizes the result of [16] that does not there is a universal expression for the Cherenkov radiation of tachyon loss of the form $\frac{dE}{dt} = W(E)$. This negative conclusion [263] is valid if we consider the function W to depend on only one variable E. If we introduce the second independent variable χ required, as shown above, for a complete description of the tachyon, we obtain a simple expression for the losses (2.110), valid in any reference systems.

Relations (2.107) - (2.110) are valid for any $\rho(k)$, i.e. do not depend on specific tachyon models. Therefore, they can be considered common proof of the "vector nature" of the tachyon, and the identification of the vector e with d is, as already noted, only more or less plausible specification.

Thus, the following conclusions follow from the above consideration [63]:

1. Experiments [6 3] to detect Cherenkov radiation of tachyons were doomed in advance to failure due to the extremely low output of radiation in the optical range.
2. The Cherenkov radiation of tachyons energy maximum lies in the region of wavelengths $\lambda \sim a_0$ and for $m \approx m_e$ (m_e is the electron mass) corresponds to the γ-range. In the absence of indications in favor of $m \ll m_e$, it is precisely this range that to navigate in the preparation of experiments on the detection of Cherenkov radiation of tachyons. However, exact calculations in this area require quantum theory Cherenkov radiation of tachyons.
3. An essential feature of the Cherenkov radiation of tachyons is the azimuthal asymmetry associated with the "vector" of the tachyon.
4. The vector nature of the tachyon leads to the presence of two new degrees of freedom φ and χ, which have the meaning of the azimuthal and polar angles of the vector e with respect to the velocity v, and for

a given quantity v, the possible values of v are limited by the region $0 \leq sin\chi < {}^{c}/_{v}$.

5. If e has a dipole nature, then even for a neutral tachyon, electromagnetic radiation is just as unremovable a feature as gravitational radiation. In this case, in contrast to the point dipole in medium, the radiation power of a neutral tachyon with a dipole moment ql_0 is of the same order of magnitude as for a tachyon with charge q and dimensions $a_0 \sim l_0$.
6. For both charged and neutral tachyons, there is universal loss formula ${}^{dE}/_{dt} = W(\chi, E)$, valid in all reference systems and depending on χ. Movement of a free tachyon in general curvilinear case with 3 acceleration a is parallel to e, and the value of $v\sin\chi$ is motion integral.
7. From the identity of these properties for charged and neutral tachyons, the conclusion follows that the main results are insensitive theory to the choice of a specific model for the tachyon form factor.

2.8 Conclusions

1. Short analysis of main theories and models of Cherenkov and supercontinuum radiation is represented.
2. Frank-Tamm theory of Cherenkov radiation is observed.
3. E. Fermi theory is analysed.
4. A. Bohr theory of the influence of atoms interactions on the penetration of particles through matter.
5. Short analysis of possible mechanisms of supercontinuation radiation is made.
6. Macroscopic I. Golub model of Cherenkov radiation and its applications for the explanation main peculiarities of supercontinuum radiation is analyzed.
7. Main applications Cherenkov and supercontinuum radiation are shown.
8. Short analysis of Cherenkov radiation of tachyons are represented.

Chapter - 3

The Main Problems of Thermodymical Modelling the Nucleation and Crystallization

Even eternity cannot resist the movement of time.

Ramayana

3.1 Introduction

In modern Physical Chemistry the nucleation, the initial process that occurs in the formation of a crystal from a solution, a liquid, or a vapor, in which a small number of ions, atoms, or molecules become arranged in a pattern characteristic of a crystalline solid, forming a site upon which additional particles are deposited as the crystal grows [57, 70, 73, 74, 82, 87, 99-101, 103, 115, 116, 119, 132, 134-137, 152, 163, 167, 171, 173, 189, 192, 195, 250, 252, 273].

In general, there are no strict theories that would describe all possible processes of nucleation and crystallization [1, 18-22, 25]. Therefore, we will focus on the most general concepts that allow us to highlight the most essential characteristics of these processes. In the case of real crystal growth, as a rule, less general models are used, which allow controlling the bull-like process.

This is the main reason that we consider thermodynamic macroscopic models in this section [22, 70, 73, 101, 119, 132, 136, 163, 195, 206, 207, 252, 273].

Nucleation processes are classed as heterogeneous or homogeneous. In the former, the surface of some different substance, such as a dust particle or the wall of the container, acts as the center upon which the first atoms, ions, or molecules of the crystal become properly oriented; in the latter, a few particles come into correct juxtapositionin the course of their random movement through the bulk of the medium. Heterogeneous nucleation is more common, but the homogeneous mechanism becomes more likely as the degree of supersaturation or supercooling increases. Substances differ widely in the likelihood that they will crystallize under conditions in which the crystalline state is the inherently stable one; glycerol is a well-known example of a compound prone to super cooling.

Classical nucleation theory (CNT) is the most common theoretical model used to quantitatively study the kinetics of nucleation [19, 132, 136, 195, 243].

Nucleation is the first step in the spontaneous formation of a new thermodynamic phase or a new structure, starting from a state of metastability. The kinetics of formation of the new phase is frequently dominated by nucleation, such that the time to nucleate determines how long it will take for the new phase to appear. The time to nucleate can vary by orders of magnitude, from negligible to exceedingly large, far beyond reach of experimental timescales. One of the key achievements of classical nucleation theory is to explain and quantify this immense variation.

Continuous crystallization is a collection of sub-processes such as solution feeding, supersaturation generation, heat transfer, evaporation, primary nucleation, secondary nucleation, crystal growth, agglomeration and particle suspension. While it sets the rate of formation of new crystalline particles over which the crystallizing mass is distributed in a continuous crystallization process, the sub-process of crystal nucleation is poorly understood and controlled. Once a supersaturation is created crystallization can commence. Crystallization is a collection of the subprocesses of crystal primary nucleation, crystal growth, secondary nucleation and agglomeration, which are all governed by the prevailing supersaturation as well as other parameters. The rates of these subprocesses determine the crystalline product quality [19, 132, 136, 195, 243].

3.2 Crystal Nucleation

The crystallization involves the formation of a particulate crystalline phase from a thermodynamically metastable solution [1, 25]. A continuous crystallization process will have a clear (particle free) undersaturated solution as an input and a slightly supersaturated suspension as an output. The product crystals will need to be generated in the crystallizer by creating the supersaturation driving force for crystallization using an external action.

One of the ways to define the driving force for crystallization is by the supersaturation ratio [19, 132, 136, 195, 243].

$$S/S=c/c^*. \tag{3.1}$$

The supersaturation ratio S is defined by the concentration c and solubility c^* at the current value of the parameters being adjusted to generate supersaturation (temperature, solvent mixture composition, pH *etc*). Note: concentration can have various units (*e.g.*, mole fraction or mg per mL solvent), which will result in different values for S and therefore it is important that it is clearly specified which units are used [19, 132, 136, 195, 243]. The supersaturation can be increased by, for instance, a concentration increase through solvent evaporation or a solubility decrease by decreasing the

temperature. Crystal growth would reduce the solution concentration and thus the supersaturating.

If the concentration exceeds the solubility, the supersaturation ratio $S > 1$, the solution is supersaturated and any crystals present can grow. If the concentration is lower than the solubility ($S < 1$) the solution is undersaturated and any crystals present will tend to dissolve. At thermodynamic equilibrium the solution is saturated, concentration and solubility are equal ($S = 1$), any crystals present will be maintained in equilibrium with the flux of molecules arriving and leaving the collective crystal surface being in balance. Since the supersaturation ratio drives the crystallization process, the solubility of a compound is a crucial parameter in the crystallization process design. For instance, a strongly increasing solubility with temperature and a sufficiently small solubility at a low temperature direct the preferred supersaturation generation method towards cooling. In addition, the difference between the inlet concentration and the end point solubility is strongly associated with the yield and productivity of a crystallization process [19, 132, 136, 195, 243].

Within an industrial crystallization process, crystals can be formed from an initially clear solution (primary nucleation) or due to the presence of parent crystals (secondary nucleation). In turn, primary nucleation generally is divided into homogeneous and heterogeneous nucleation. In a supersaturated solution new crystals can be formed in the absence of crystalline solids of the same substance, which is termed primary nucleation, or in the presence of crystalline solids of the same substance, which is termed secondary nucleation. These processes may be represented as primary and secondary nucleation [132, 195]. Both primary and secondary nucleation as well as crystal growth kinetics vary widely under thermodynamically metastable conditions. However, the nucleation rate varies over many orders of magnitude while growth rate has more gentle increase with increasing supersaturation. During heterogeneous primary nucleation, the crystals form at surfaces such as dust particles, crystallizer wall, air–solution interface or deliberately added template particles. Homogeneous primary nucleation takes place in the absence of heterogeneous particles in a clear solution. It is important to note that in the laboratory and more so in large-scale processes on an industrial scale, the presence of many different heterogeneous particles or surfaces is impossible to avoid. Despite their importance, usually no information is available on the amount and kind of heterogeneous particles that are finally responsible for the occurrence of heterogeneous nucleation [19, 132, 136, 195, 243].

Thus, while an unseeded batch cooling crystallization process usually relies on primary nucleation to provide the crystals, during a continuous

crystallization process the omnipresent crystals continuously generate more crystals through secondary nucleation. Only in extreme cases are there indications that homogeneous nucleation is the dominant nucleation mechanism. Introduction of crystals into a crystallization process is based on either nucleation or seeding. Seeding relies on addition of previously formed crystals while nucleation implies birth of new crystals. The nucleation rate expresses the number of new crystals that are generated per unit of time per unit solution volume at a given composition and temperature. Nucleation events could be evenly distributed across the bulk fluid volume. However, it may more often be the case that locally extreme conditions (supersaturation, fluid dynamics, mixing points) lead to local nucleation events. While the resulting suspension is distributed over the entire crystallizer, the generation of crystals through nucleation can be highly localized [19, 132, 136, 195, 243].

Now we represent primary nucleation more detail. In supersaturated solutions, the nucleation rate varies highly non-linearly with supersaturation.

Theory describes the supersaturation dependent nucleation rate J as a function of a supersaturation dependent nucleation barrier $B/\ln^2 S$ [19, 132, 136, 195, 243]:

$$J = AS\exp(-B/\ln^2 S) \tag{3.2}$$

Where A and B are constants. The nucleation barrier is very large for supersaturated solutions close to the solubility line resulting in a negligible nucleation rate and prolonged lifetimes of the metastable solutions. At very high supersaturations, far away from the solubility line, the energy barrier for nucleation vanishes and spinodal decomposition takes over from nucleation [19, 132, 136, 195, 243].

The values of the nucleation rate constants A and B depend on the primary nucleation rate mechanism taking place. Primary nucleation can take place in the bulk volume of a particle free solution (homogeneous primary nucleation) or at interfaces (heterogeneous primary nucleation) due to the presence of crystallizer wall, solution–air interface and suspended foreign particles such as dust particles. Heterogeneous particles or surfaces promoting heterogeneous nucleation are characterized by B-values that are much lower than those in the case of homogeneous nucleation from a clear solution: the enhanced heterogeneous nucleation is due to the reduction of the nucleation barrier. This, even though the A-value for heterogeneous nucleation is orders of magnitude lower than that for homogeneous nucleation. Since there will always be interfaces or particles present in industrial solutions to nucleate

onto, often heterogeneous nucleation is assumed to be the dominant primary nucleation mechanism [19, 132, 136, 195, 243].

However, if nucleation events are heterogeneous and are related to external fluid interfaces, such as vessel walls or fluid–air interface with a defined surface area, it may be appropriate to express nucleation rate as number of crystals generated per unit surface area per unit time. Furthermore, if nucleation events are related to some other localized environment, such as a region of high shear (*e.g.*, due to pump or agitator), inlet stream mixing point or external field impact (*e.g.*, by ultrasonic transducer), it may be appropriate to express nucleation rate simply as number of crystals generated per unit time within the given local volume [19, 132, 136, 195, 243].

Dependencies of the nucleation rate on solution composition and temperature within the metastable zone vary widely from system to system. There are currently no reliable tools able to quantitatively (and often even qualitatively) predict how nucleation rates depend on solution composition and temperature, and even the fundamental mechanisms (homogeneous or heterogeneous; single step or multistep) are strongly debated in scientific literature. Until there is major progress in predictive computational tools in this area, information about nucleation and growth rates needs to be obtained experimentally.

Experimental measurements of crystal nucleation rates are challenging because nuclei are small so that they have to grow into a detectable range, and nucleation and growth are inextricably linked. In order to measure the nucleation rate, it is possible to count the increase in the number of detectable particles assuming that the change of number of particles is only due to nucleation [19, 132, 136, 195, 243], or it is possible to determine induction times from which primary nucleation kinetics can be estimated using various assumptions (isothermal/polythermal, constant/variable nucleation rate, single/multiple nuclei, growth time to detection, *etc.*) [132, 195].

Fouling and encrustation can be related to (heterogeneous) nucleation and agglomeration of crystals in regions with high local supersaturations such as cooling surfaces, mixing points and contact lines of boiling liquid, air and crystallizer wall. Fouling needs to be monitored [132, 195] and mitigated when operating continuous crystallization processes as it can compromise the steady state operation as well as product quality attributes.

Primary nucleation in stagnant fluid in absence of external fields is typically addressed in textbooks: but what about effects such as mixing, shear, pressure and electromagnetic fields? Effects of pressure waves (ultrasound),

high power lasers and fluid shear on nucleation have been observed: can we understand and use them to develop better crystallization processes [19, 132, 136, 195, 243]?

Now we represent mixing-induced supersaturation [19, 132, 136, 195, 243]. The effect of local concentration gradient can be important when supersaturation is mixing-induced, *e.g.*, in antisolvent or reactive crystallization, where two fluid streams need to be mixed to obtain required solution composition. If the mixing process is much slower than the nucleation process at the final solution composition, it can be expected that nucleation would proceed within the mixing region before mixing is completed and local composition heterogeneity in the mixing region would significantly influence resulting nucleation outcome [19, 132, 136, 195, 243]. On the other hand, if the mixing process is much faster than nucleation, it can be expected that nucleation would only proceed once mixing is complete and local concentration gradients would not be significant. The significance of mixing can thus be assessed by comparison of characteristic times of mixing τ_m and of nucleation τ_n and by analogy with chemical reactions, we can define a dimensional ratio of the two timescales τ_m/τ_n, similar to the Damköhler number [19, 132, 136, 195, 243]. While mixing time scales have been investigated and quantified across a range of mixing conditions, [19, 132, 136, 195, 243] it is less straightforward to quantify nucleation time scales (*e.g.*, inverse of induction time couples both nucleation and growth time scales and is dependent on relevant volume where nucleation occurs as well as observation method).

Influence of shear on the processes of nucleation may be represent in next way [19, 132, 136, 195, 243]. Heterogeneity of flow environment is inherent in vessels, pipes and pumps. Uniform flow field can be achieved in some idealized heometry environments such as Couette (in the gap between two cylinders with inner cylinder rotating [19, 132, 136, 195, 243] or cone-and-plate cells). In pressure driven laminar flow in pipes the shear rate varies from zero in the center to the maximum value at the pipe wall. Ranges of shear rates experienced by fluids can vary widely depending on the nature of agitation, agitator shape, size and movement, vessel geometry and resulting flow regimes (*e.g.*, stirred tanks, Taylor–Couette flows, oscillatory flows) [19, 132, 136, 195, 243].

The effect of local flow environment on nucleation has been repeatedly noted in previous literature but in early reports it was unclear whether effects were due to primary or secondary nucleation (Fig. 3.1 and Fig. 3.2 [146, 243]).

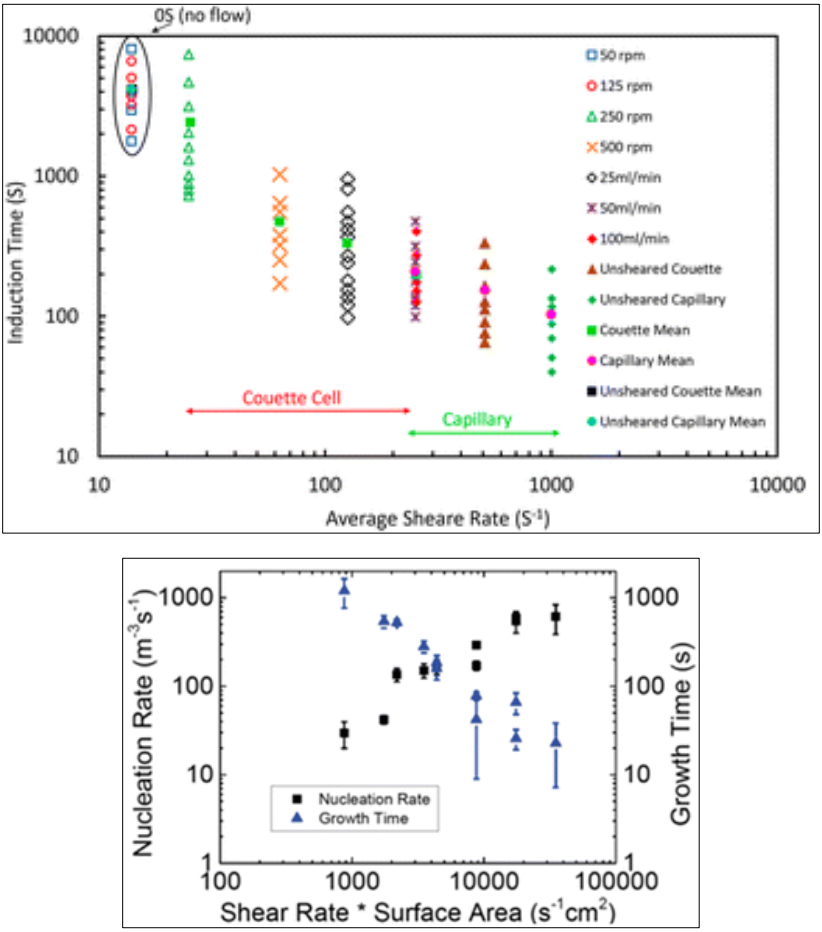

Fig 3.1: Induction times, nucleation rates *J*, and growth times t_g estimated from a model fit as a function of the product of the average shear rate and surface area [146, 243]

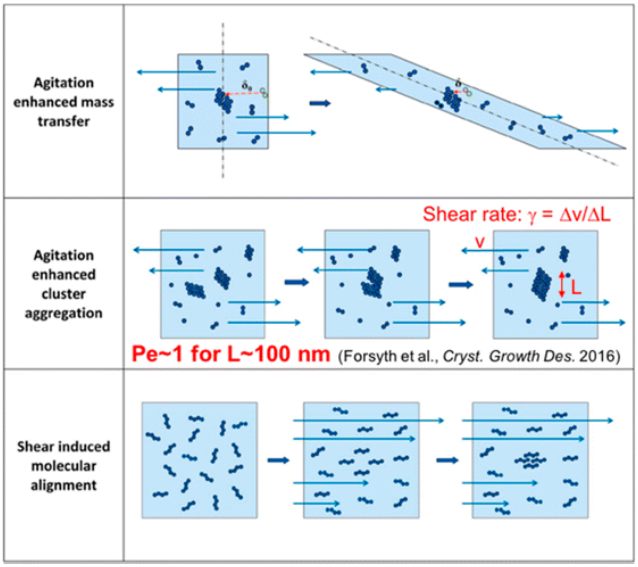

Fig 3.2: Effect of shear and fluid micro-mixing on nucleation [146, 243]

Influences of external fields (ultrasound [243], laser [208, 232, 233], electromagnetic [195, 243]) on the nucleation processes were researched too.

The principal benefit of using external fields, such as ultrasound or laser, to control nucleation lies in avoiding the problems typically encountered with conventional seeding; inconsistent seed attributes and seed history, incomplete seed wetting and dispersion resulting in polycrystalline particle formation, seed dissolution due to delayed seed addition, *etc.* [19, 132, 136, 195, 243]. Well-controlled nucleation offers the possibility of exquisite control of product particle size. These aspects are particularly important in continuous crystallization where seeding is an essential element in the start-up process required to minimize the peak supersaturation attained and so to delay the onset of encrustation. The benefit of externally induced nucleation in starting up a continuous crystallization is that it can be initiated at supersaturation levels lower than the metastable zone limit for spontaneous nucleation and potentially at levels lower than would be considered robust for conventional seed addition.

In a classical continuous crystallization, following successful initiation *via* seed addition, the next major operational challenge is to manage the secondary nucleation rate such that the available surface area for crystal growth is commensurate with achieving almost complete desupersaturation within the target residence time whilst also producing crystals with the

required size distribution. Typical strategies for commodity materials manufacture revolve around making large particles which are easy to isolate by filtration and washing. This is usually achieved by actively suppressing nucleation and operating at modest supersaturations with extended residence times [19, 132, 136, 195, 243].

Nucleation is classified as either homogeneous, if it arises entirely through random thermal fluctuations in the liquid, or heterogeneous, if the presence of another phase in contact with the liquid facilitates the process.

Peculiarities of homogeneous nucleation may be represent in next way [19, 132, 136, 195, 243]. Of the many factors affecting the rate of nucleation, the most important (that is, those which are most variable with supercooling or supersaturation) are the work, or Gibbs free energy, of forming a nucleus, and the rate of transport of atoms from the liquid onto incipient nuclei. These are both exponentially dependent on supercooling and/or temperature. Other influences are lumped into the pre-exponential factor, which is not constant with temperature or supercooling, but is much less sensitive to them than are the exponential factors.

According to classical chemical kinetic theory [19, 132, 136, 195, 243], the rates of many processes are proportional to the exponential of a free energy of activation ΔG_a

$$R_0 = K\exp\left[-\frac{\Delta G_a}{RT}\right], \tag{3.3}$$

where the constant K includes various geometric and population factors, as well as a vibrational frequency factor that is dependent on temperature. The free energy of activation is in effect an energy barrier that must be surmounted as the system goes from its initial to final state, even though the free energy of the final state may be considerably lower than that of the initial state. Such an energy barrier opposes the beginning of the precipitation of one phase within another, because the energy of the interface between the two phases contributes a term to the total free energy of the system. The free energy change on crystallization is thus [19, 132, 136, 195, 243].

$$\Delta G = \left({}^{V\Delta G_c}/_{V_m}\right) + \sum a\sigma, \tag{3.4}$$

where V is the volume of the crystallized material, ΔG_c is the bulk free energy change per mole, V_m is the molar volume, a represents the area of each of the various surfaces of the crystals, and σ is the specific surface energy, or surface tension, of each. Energies of edges and corners will also be significant if the new crystals or nuclei are small. For a given negative (favorable) ΔG_c,

the total free-energy change ΔG_a is a function of the size of the nuclei (Fig. 3. 3) [56, 132]. The peak of the curve in Fig. 3.3 defines the contribution from the surface energy of a spherical nucleus to the activation energy, and a nucleus of the radius at which this peak occurs is called the critical nucleus: any nuclei larger than this will grow spontaneously, because the total free energy is reduced by their growth, but any smaller nuclei are unstable and prone to dissolution. The fact that a few nuclei may reach the critical size and grow to macroscopic crystals is due to random thermal fluctuations in the liquid.

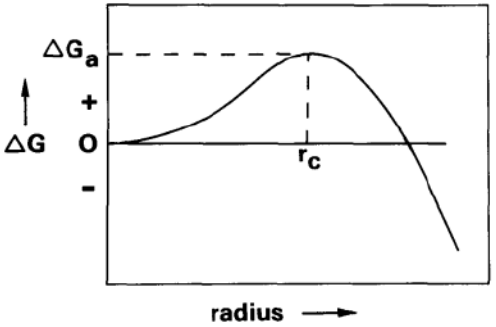

Fig 3.3: Gibbs free energy of spherical nuclei versus size. Nuclei above the critical size, r_C, should grow spontaneously, as the free energy of the system is hereby reduced. The free energy of the critical size nucleus, G_a, is the free energy of activation for nucleation (neglecting transport processes) [56, 132]

The surface energy of a crystal is of course dependent on shape, since different faces or other surfaces have different values of a. Critical-size nuclei are expected to have the equilibrium shape [56, 132, 195, 243], which is simply the shape that minimizes the Gibbs free energy (Equation (3.4)) at constant volume. This shape can be predicted from the crystal structure by the methods of Hartman and Perdok [56, 132, 195, 243]. However, there is little to be gained by this, because the absolute values of surface, edge, and corner energies cannot easily be predicted or measured. Therefore, for simplicity, nuclei will be assumed to be spherical, with the value of σ representing an average for all parts of the surface. Equation (3.4) then becomes

$$\Delta G = \frac{4}{3}\pi r^3 \left(V\Delta G_c / V_m\right) + 4\pi r^2 \sigma, \tag{3.5}$$

where r is the radius. Differentiating this with respect to r yields the critical radius, r_c:

$$\Delta G_a = -\frac{2\sigma V_m}{\Delta G_c}, \tag{3.6}$$

which, substituted back into Equation (3.5), gives

$$\Delta G_a = -\frac{16\pi\sigma^3 V_m^2}{\Delta G_c^2}. \quad (3.7)$$

This is the maximum free energy of a nucleus, and therefore it is the activation energy appearing in Equation (3.3) and Fig. 3.3. For crystallization from melts, the bulk free energy of crystallization ΔG_c is conventionally related to supercooling, $\Delta T = T_l - T$, where T_l is the equilibrium liquidus or fusion temperature and T is the actual temperature. A derivation of this relation for one-component systems will be found in many texts, but here the general relation for multicomponent systems will be given. For the free energy change of the system ΔG_c^l with crystallization of any component at the equilibrium liquidus temperature T_l we have

$$\Delta G_c^l = \Delta H_f + \Delta\tilde{H}_m - T_l\left(\Delta S_f + \Delta\tilde{S}_m\right) = 0, \quad (3.8)$$

where ΔH_f and ΔS_f are the molar enthalpy and entropy of crystallization of the pure component, and $\Delta\tilde{H}_m$ and $\Delta\tilde{S}_m$ are the partial molar enthalpy and entropy of mixing at the liquidus composition. This equation is essentially equivalent to Weill Equation [56, 132, 195, 243] but includes the assumption that the enthalpy of crystallization of the pure component is independent of temperature. This assumption is not strictly true, and if the heat capacities of the crystal and its own liquid are known for the temperature interval of interest, the variation of ΔH_fs with temperature can be taken into account in evaluating the integral in Weill Equation) [56, 132, 195, 243]. However, the values of the heats of fusion and the heat capacities are seldom known with sufficient precision to warrant this correction. Defining ΔS_t as the total entropy change on crystallization, we have

$$\Delta S_t = \Delta S_f + \Delta\tilde{S}_m = \frac{\Delta H_f + \Delta\tilde{H}_m}{T_l}. \quad (3.9)$$

Assuming now that not only ΔH_f but also $\Delta\tilde{H}_m$ is insensitive to changes in temperature, the free energy change at the actual temperature T of nucleation is

$$\Delta G_c^T = \Delta H_f + \Delta\tilde{H}_m - T\frac{\Delta H_f + \Delta\tilde{H}_m}{T_l}. \quad (3.10)$$

If we also substitute Equation (3.9) into Equation (8), we obtain

$$\Delta G_c^l = \Delta H_f + \Delta\tilde{H}_m - T_l\frac{\Delta H_f + \Delta\tilde{H}_m}{T_l} = 0, \quad (3.11)$$

which, subtracted from Equation (8), yields

$$\Delta G_c^T = \Delta T\frac{\Delta H_f + \Delta\tilde{H}_m}{T_l} = \Delta T\Delta S_t. \quad (3.12)$$

For a one-component system, the relation simplifies to

$$\Delta G_c^T = \Delta T \frac{\Delta H_f}{T_f} = \Delta T \Delta S_f, \tag{3.13}$$

where T_f is the fusion temperature of the pure component. Enthalpies of mixing in multi-component systems can be obtained from calorimetric measurements [56, 132, 195, 243]. Depending on the magnitude of ΔH_f of the crystallizing component, the enthalpy of mixing may or may not be important: for example, the low ΔH_f of silica means that small heats of mixing will have a large relative effect on ΔG_c, whereas the same $\Delta \widetilde{H}_m$ would be much less significant for pyroxene or olivine, which have much higher ΔS_f.

Transport factor may be estimate by next method [56, 132, 195, 243]. The overall rate is also proportional to the rate of arrival of atoms on the crystal surface, and there is another energy barrier associated with atomic movement across the interface and/or through the liquid. The activation energy of this process, ΔG_{tr}, can be added to that of critical nucleus formation, or separated into a factor which has the form of diffusivity *D*.

$$D = K \exp\left[-\frac{\Delta G_{tr}}{RT}\right], \tag{3.14}$$

and since $\Delta G_{tr} = \Delta H_{tr} - T\Delta S_{tr}$,

$$D = K \exp\left[-\frac{\Delta S_{tr}}{R}\right] \exp\left[-\frac{\Delta H_{tr}}{RT}\right] = K' \exp\left[-\frac{\Delta H_{tr}}{RT}\right]. \tag{3.15}$$

For crystallization of simple compounds from their own liquids, *D* can be predicted to a first approximation (within one or two orders of magnitude) by the Stokes-Einstein relation [56, 132, 195, 243]:

$$D = \frac{kT}{3\pi r_0 \eta}, \tag{3.16}$$

where *k* is Boltzmann constant, η is viscosity and r_0 is the radius of the diffusing particle. In silicates, the nature of the growth unit or "diffusing particle" is usually unknown, so that r_0 cannot be specified, but this relation is normally used only to obtain relative values of the transport. A more serious problem in silicate liquids is that the viscosity is generally determined by aluminum-oxygen and silicon-oxygen linkages, whereas other cations seem to be free to move about in the interstices. The measured diffusivities of univalent and divalent ions are many orders of magnitude greater in high-silica liquids than is predicted from the Stokes-Einstein relation [56, 132, 195, 243]. The application of this relation in general to crystallization in multicomponent silicate systems is therefore evidently invalid.

Pre-exponential Factor and Overall Expression may be received in next way [56, 132, 195, 243]. The above derivation of the critical nucleus factor is

simplified in that it neglects the rate of the reverse reaction, and the fact that a state of equilibrium does not exist with respect to incipient nuclei while macroscopic crystals are being formed. The average number of atomic clusters n_i per unit volume containing any specific number of atoms is given by the Boltzmann distribution [56, 132, 195, 243]:

$$n_i = N\exp\left[-\frac{\Delta G_i}{RT}\right]. \tag{3.17}$$

where N is the number of atoms per unit volume and ΔG_i is the free energy required to form each cluster. A statistical-mechanical derivation of the rate would be based on the probability of individual clusters within such populations either increasing or decreasing their size. However, Equation (17) itself describes a state of equilibrium, and is no longer valid when clusters larger than the critical size are continually growing into macroscopic crystals. Such considerations do not affect the exponential part of the rate equation, but do find expression in the pre-exponential part, along with the other factors mentioned above as included in K in Equation (3.3). A complete expression for nucleation rate includes Equation (3.3), with the value of ΔG_a from Equation (3.7), multiplied by the transport factor (Equation (3.15)) and the pre-exponential factor. The value of ΔG_c in terms of AT from Equation (3.12) can also be inserted. A widely-quoted equation is that of Turnbull and Fischer [56, 132, 195, 243], which is based on the theory of absolute reaction rates:

$$R_n = n^* N \frac{kT}{h}\left(\frac{\sigma}{kT}\right)^{1/2}\left(\frac{2V_a}{9\pi}\right)^{1/2}\exp\left[-\frac{16\pi\sigma^3}{3\Delta G_c^2 RT}\right]\exp\left[-\frac{\Delta H_a}{RT}\right], \tag{3.18}$$

where n^* is the number of atoms on the surface of a critical-size nucleus, N is the number of atoms of the precipitating substance per unit volume of liquid, k and h are Boltzmann's and Planck's constants, and Va is the volume per atom of the precipitating substance. Nuclei are assumed to be spherical in this version of the equation. The proportionality of n^* to σ and ΔG_c is obtained from Equation (3.6); thus the pre-exponential factor is dependent on $\sigma^{5/2}$, $T^{1/2}$, and ΔG_c^{-2} or $(\Delta S_t\, \Delta T)^{-2}$.

The application of Equation (18) to high degrees of supercooling is doubtful, because it was derived on the explicit assumption that $l/n \ll 1$, where n is the number of atoms in a critical nucleus; in reality, the size of the critical nucleus decreases with increasing supercooling. However, no other applicable expressions seem to be much better in this respect, and Equation (3.18) does show the qualitative features that are found in the laboratory, beginning with the experiments of Tamman, and Tamman and Mehl [56, 132, 195, 243]. These features include the following: an initial interval of ΔT over which the nucleation rate is small or negligible, called hereafter the critical ΔT of

nucleation; a rapid rise of nucleation rate to a peak with increasing ΔT; and a usually slower decrease thereafter, as the exponential factor due to the critical nucleus approaches unity and the transport factor begins to control the rate. Increasing the value of surface energy increases the critical Δ of nucleation and shifts the peak of the curve to higher ΔT; increasing ΔS, has the opposite effect.

It is generally conceded that the essentially thermodynamic approach outlined above is not likely to lead to accurate expressions for nucleation rate, because macroscopic thermodynamic quantities like surface energy are not practicable when applied to the very small atomic or molecular units involved in nucleation [56, 132, 195, 243]. Future advances in quantitative nucleation theory will probably depend on approaches through statistical mechanics. Although much has already been done in this line [56, 132, 195, 243], progress is slow, even for structurally simple substances. Application of statistical mechanics to silicate crystallization will require elucidation of the actual atomic structures of the melt and of crystal surfaces, and the dependence of these structures on temperature and pressure.

Simple model of heterogeneous nucleation may be represent as. The formation of nuclei on preexisting solid phases can greatly reduce the critical ΔT of nucleation because the surface energy associated with the nucleus is reduced: solid-solid surface energy is generally less than the solid-liquid surface energy, especially if there is epitaxy [56, 132, 195, 243]. Much has been written on heterogeneous nucleation [56, 132, 195, 243], but most of this literature pertains to growth from the vapor, in part because direct observation of the substrate is easier than in melt growth. No general theory of heterogeneous nucleation can be offered, since the reduction in surface energy is dependent not only on the identity of the substrate material, but also on its physical state (surface roughness, grain size, presence of dislocations, and the like).

The factors affecting the rate are the same as for homogeneous nucleation, however, and a gross picture of the difference between homogeneous and heterogeneous nucleation may be obtained simply by reducing the value of σ in Equation (3.18). A complete absence of material that could serve as a substrate for heterogeneous nucleation in a melt is in practice unattainable, and it is generally considered that there is no such thing as completely homogeneous nucleation. It is especially difficult to minimize heterogeneous nucleation in the laboratory, primarily because of the large ratio of container surface area to sample volume. A liquid-vapor interface seems to be much less likely to promote heterogeneous nucleation than a liquid-solid interface, presumably because of much larger surface energies. For example, Murase

and McBirney [56, 132, 195, 243] measured surface energies of 250- 350 *ergs·cm*$^{-2}$ for typical silicate melts in air, whereas crystal-liquid surface energies for silicates tend to be in the neighborhood of 50 *ergs·cm*$^{-2}$ or less (see below). For nucleation on the liquid-gas interface, it is the crystal-gas surface energy which is pertinent, but there is no reason to believe that this would be appreciably less than the liquid-gas surface energy. The technique of suspending liquid-silicate beads in platinum wire loops (Lofgren, this volume) is usually more successful in minimizing heterogeneous nucleation than are experiments in which the silicate is crystallized in capsules or crucibles [56, 132, 195, 243]. Presumably this is because the liquid-solid interface is largely eliminated in favor of a liquid-gas interface [56, 132, 195, 243]. The frequent failure of vapor bubbles to act as nucleation sites [56, 132, 195, 243] also testifies to the high energy of the gas interface.

In natural magmas [56], external surfaces are always much less important because of the greater volume of the liquid, and heterogeneous nucleation is not necessarily expected to be as completely dominant as it is in most laboratory experiments. Nevertheless, various "foreign" particles may be present, and later-forming crystals can always nucleate on early ones. Textural and other evidence suggest a considerable range in the degree of heterogeneity of nucleation in igneous rocks (see below and Lofgren, this volume).

Incubation time may be estimate as [56, 132, 195, 243]. The statistical Boltzmann distribution of sizes of atomic clusters in the liquid (Equation (3.17)) depends on temperature, with larger clusters being favored by a lower temperature. If a melt is equilibrated at a temperature above the liquidus and then quenched to an appreciable ΔT, it takes time for the new distribution of cluster sizes to become established. The new distribution will be steady-state rather than equilibrium if nuclei are being formed, but in any case the nucleation rate is depressed while this state is being attained. A number of different theoretical expressions for the incubation or induction period τ necessary for the nucleation rate to reach its steady-state value have been offered [56, 132, 195, 243], but most have the form

$$\tau = \frac{n^2}{D}, \tag{3.19}$$

where n is the number of atoms in the critical nucleus and D is the transport factor (Equation (3.15)). The most important aspect of incubation time is its significance with respect to correlation of laboratory results with natural igneous rocks, since sudden temperature changes are much more common in the former. Lofgren (this volume) discusses the abundant evidence of the effects of incubation time in laboratory experiments.

In rapidly crystallizing systems it is sometimes observed that introduction of a single seed into the supercooled liquid causes abundant nucleation on many centers not connected with the location of the original seed [56, 132, 195, 243]. This has been attributed to the phenomenon of cavitation, the most reasonable explanation for which is that the collapse of cavities produced by volume change on rapid crystallization generates a shock wave [56, 132, 195, 243]. The shock wave locally raises the pressure and the liquidus temperature, thereby increasing ΔT and causing nucleation. In some systems it is also possible to initiate nucleation by stirring, tapping the container or other mechanical agitation, which may have a similar effect.

3.3 Crystal growth theories

There are three principal processes in crystal growth, any of which may be the controlling factor in the overall growth rate:

1) Interface kinetics – the movement of material across the interface and its attachment on the crystal surface;
2) Material transport – the movement of material through the liquid; and
3) Heat transfer – the removal of latent heat of crystallization from the interface [56, 132, 195, 243].

Which of these processes is the dominant factor depends on the relative diffusion and heat-transfer rates, the particular growth mechanism, and the supercooling. Generally, interface kinetics is dominant at low supercooling, while either material transport or heat transfer becomes more important at high supercooling. According to Tiller [56, 132, 195, 243], the total supercooling or supersaturation can in principle be subdivided into contributions from each process, one of which is normally the controlling factor. The fundamental rate equation of Jackson [56, 132, 195, 243] is based on tracing the free-energy state of the system through all these processes. Only by considering all processes can the growth rate be predicted quantitatively and a priori; however, by identifying the dominant process or processes and making suitable approximations, one can obtain semi-empirical relationships that may be useful in describing the dependence of growth rate on ΔT. All the growth-rate equations developed below are in fact based on such simplifications.

The mechanisms of attachment of atoms onto the crystal surface are divided into two main types, continuous growth and layer growth. In continuous growth, atoms are able to attach themselves wherever they land; this type of growth is normally associated with a "rough" or nonplanar interface, which has a high concentration of unsatisfied bonds and therefore high surface energy. In layer or lateral growth, normally associated with a

"smooth", planar, or singular interface, with a low concentration of unsatisfied bonds and low surface energy, atoms are not strongly localized on the surface, although once they land there, there may be small probability of their leaving again. Atoms may move rather freely over the surface (surface diffusion), and are usually able to attach themselves permanently only at the edge of layers or steps, where they are in effect bonded to two surfaces. In layer growth, there is usually some difficulty in starting a new layer, but once initiated, the layers can spread rapidly across the surface [56, 132, 195, 243]. Crystals with macroscopically flat, crystallographically rational faces have presumably grown by the layer mechanism, whereas smoothly rounded crystals more probably have grown by the continuous mechanism, but it should be realized that there is not necessarily a sharp distinction between the two mechanisms; insofar as it is possible to observe or model the actual microscopic surface structures of crystals, they appear to be neither perfectly smooth nor ideally rough.

The nature of the interface in simple compounds can be predicted by Jackson theoretical model [56, 132, 195, 243], who proposed that the surface roughness is determined by the value of the parameter

$$\alpha = \frac{\Delta S_f}{R}\xi, \tag{3.20}$$

where ξ, the anisotropy factor, is the fraction of bond energy in a monolayer that attaches the atoms of the layer to each other, rather than to the preexisting crystal surface. Values of α less than about 2 should correspond to a rough interface, while values greater than 4 should correspond to a smooth interface. It would appear intuitively that this should also predict the growth mechanism, that is, continuous versus layer growth, and this seems to be borne out in practice [56, 132, 195, 243], but Jackson *et al*. [56, 132, 195, 243] warn that the connection is not justified theoretically.

Although Jackson's theory has been very successful for simple substances, its application to structurally complex silicates is not straightforward. In metals or simple molecular crystals, the entropy of melting per mole presumably corresponds to the entropy per actual growth particle, but the true growth units in igneous melts are unknown. There is certainly no justification for using the value of ΔS_f for the usual gramformula units, which are only mathematical conventions. Entropies of melting per atom for oxides and silicates are mostly in the range 4(SiO_2) to 3.6(MgO) $cal{\cdot}mol^{-1}{\cdot}degree^{-1}$. The anisotropy factor is not defined for growth layers more than one atom thick, since the model itself only considers one atomic layer, but when growth layers are greater than one atom thick, ξ is presumably at least qualitatively

correlated with the attachment energy of Hartman [56, 132, 195, 243]) or the template fraction of Dowty [56]. Both of these quantities are measures of the bond energy per layer, holding that layer to the crystal surface.

In multicomponent systems, ΔS_f should presumably be replaced by ΔS_t (Equation (3.9)), and therefore the probability of having a smooth interface is usually increased over that in the pure system. Small weight percentages of water can have a large effect on liquidus temperature and should be rather important in this respect. For example, cristobalite is not faceted and grows by a continuous mechanism from a pure anhydrous SiO_2 melt [25], but quartz in rhyolites and especially water rich "porphyries" is often euhedral. Quartz grown in the laboratory from water-rich granite and granodiorite melts is also faceted [56]. The interface model of Temkin [56] is somewhat more comprehensive than that of Jackson, in that it considers more than one layer, but it generally seems to lead to similar predictions about surface structure and/or mechanism. This and other aspects of interface structure are reviewed by Woodruff [56].

The only energy barrier, or activation energy, encountered when atoms are able to attach directly to the surface is that of transport across the interface, similar to ΔG_{tr} for nucleation (Equation (3.14)), although Turnbull [56] points out that transport is not precisely the same for growth and nucleation. The rate of attachment, R_{att}, is then

$$R_{att} = K \exp\left[-\frac{\Delta G_{tr}}{RT}\right]. \tag{3.21}$$

Atoms detaching themselves from the surface must also overcome the bulk free energy difference between crystal and liquid, so the rate of detachment R_{det} is

$$R_{det} = K' \exp\left[-\frac{\Delta G_{tr}}{RT}\right] \exp\left[-\frac{\Delta G_c}{RT}\right]. \tag{3.22}$$

The net growth rate R_{cont} is the difference between (3.21) and (3.22):

$$R_{cont} = R_{att} - R_{det} = F d_0 \upsilon \exp\left[-\frac{\Delta G_{tr}}{RT}\right]\left(1 - \exp\left[-\frac{\Delta G_c}{RT}\right]\right), \tag{3.23}$$

here showing explicitly the factors in the pre-exponent, which include F, the volume fraction of the precipitating substance in the liquid; f, the fraction of sites available on the surface; d_0, the thickness of a single atomic layer; and υ, the atomic vibrational frequency in the liquid, which is proportional to temperature. When the crystal consists of more than one type of atom, the values of f and d_0, would need to be averaged over the crystal structure. The value of f should approach unity for very rough interfaces.

3.4 Macroscopic theory of homogeneous nucleation

Initially, the theory of phase formation was developed for homogeneous systems, for example, for the process of formation of a liquid drop from supersaturated vapor. The foundations of the thermodynamic theory of the formation of nuclei of a new phase were laid by J. Gibbs [73, 195]. The macroscopic theory of homogeneous condensation of supersaturated vapor was developed in the works of Volmer [252], Becker [22], Dering [195], Frenkel [70], Zel'dovich [273]. Until recently, the theory of crystallization from supercooled melts or supersaturated solutions was based on the macroscopic theory of nucleation. Until a certain time, it satisfactorily described nucleation. However, a number of experiments on the initial stages of electrocrystallization make it necessary to reconsider the fundamental provisions of the macroscopic theory of nucleation [195, 243].

The process of nucleation in thermodynamics is described as follows [195, 243]. In any system, the transition from one stable state to another is considered as a change in the conditions corresponding to the minimum of one of its thermodynamic potentials. A homogeneous system can also exist in a metastable state near the point of a first-order phase transition. Sooner or later, a substance that is in a metastable state must pass into another - stable one. This transition is hampered by the fact that the formation in a given phase of objects of small sizes of another phase, due to the additional contribution of the surface energy of these objects, leads to an increase in the free energy of the system as a whole, and therefore such a transition is thermodynamically unfavorable.

For any metastable phase, there is a minimum size that the resulting critical nucleus must have. The critical nucleus is in unstable equilibrium with the metastable phase. The onset of the phase transition is determined by the probability of the appearance of nuclei of precisely these sizes.

The formation of a new phase is associated with the formation of a phase interface. Gibbs took the surface layer as a new "surface phase", different from the bulk phase in that its thickness is extremely small compared to the extent in the other two dimensions, and therefore considered the surface layer as a geometric separating surface, applying to it the general thermodynamic equations.

The surface area (Σ) is, along with the volume (V), a new parameter characterizing the state of the system. An increase in the surface of the system at constant temperature and volume is accompanied by the expenditure of work. Let σ denote the generalized force corresponding to the parameter Σ.

Then the elementary work for increasing the surface by $d\Sigma$ (for T and V = const) is equal to [195]:

$$\delta A = -dF = -\sigma d\Sigma, \tag{3.24}$$

where F is the Helmholtz free energy. The Helmholtz energy differential can be written as

$$dF = -SdT - pdV + \sigma d\Sigma. \tag{3.25}$$

The value σ characterizing the equilibrium between two contiguous phases is called the surface tension.

$$\sigma = dF_{\Sigma}/d\Sigma. \tag{3.26}$$

The equilibrium condition in a system consisting of two phases with an interface is:

$$T_1 = T_2 \text{ and } \mu_1 = \mu_2. \tag{3.27}$$

Condition of equilibrium of the first and second phases:

$$dF = -p_1 dV_1 - p_2 dV_2 + \sigma d\Sigma. \tag{3.28}$$

At the moment of equilibrium $dF = 0$, then, if we assume that $V_1+V_2=V$=const, the pressure can be determined by the formula:

$$p_2 = p_1 + \sigma d\Sigma/dV_2. \tag{3.29}$$

Taking into account that in the chosen assumption a new phase of a spherical shape is considered, then the curvature of its surface is:

$$d\Sigma/dV_2 = d(4\pi r^2)/d(4/3pr^3) = 2/r. \tag{3.30}$$

Substituting (1.7) into (1.6), we obtain the Laplace equation:

$$p_2 = p_1 + 2\sigma/r \text{ or } \Delta p = 2\sigma/r. \tag{3.31}$$

From the Laplace equation, the expression for the radius of the critical nucleus has the form:

$$r_{cr} = \frac{2\sigma}{\Delta p}. \tag{3.32}$$

The minimum work of formation of a critical nucleus is determined by the change in the large thermodynamic potential Ω. Before the formation of the nucleus, its potential is equal to:

$$\Omega = -p_1(V_1 + V_2). \tag{3.33}$$

After the formation of the nucleus

$$\Omega = -p_1V_1 - p_2V_2 + \sigma\Sigma. \tag{3.34}$$

Expression to work:

$$A = d\Omega = -(p_2 - p_1)V_2 + \sigma N. \quad (3.35)$$

Substituting the value of r_{cr} from formula (1.9), we obtain:

$$A = \frac{16\pi\sigma^3}{3(p_1-p_2)^2}(p_1 - p_2)^2. \quad (3.36)$$

If p_0 denotes the pressure of both phases with a flat interface between them, then with a slight overcooling or overheating $\delta p_1 = p_1 - p_0$, $\delta p_2 = p_2 - p_0$ are relatively small and are related by the relation $v_1\delta p_1 = v_2\delta p_2$, where v_1 and v_2 are the molecular volumes of the nucleus and the metastable phase. Considering this,

$$A = \frac{16\pi\sigma^3 v_2^2}{3(v_1-v_2)^2(\delta p)^2}. \quad (3.37)$$

The choice of a specific thermodynamic potential depends on what parameters in the system remain constant. At constant temperature and pressure of the external environment (T = const and p = const), the work of formation of the nucleus is equal to the change in the Gibbs potential: $A = \Delta G$. The Gibbs energy of the medium can be expressed in terms of the chemical potential:

$$G = \mu N, \quad (3.38)$$

where N is the number of molecules, μ is the chemical potential per molecule. Before the formation of the nucleus

$$G = \mu_1 N, \quad (3.39)$$

after the formation of the nucleus, the Gibbs energy of the system is

$$G^* = \mu_1 N_1 + \mu_2 N_2 + \sigma\Sigma, \quad (3.40)$$

Where N_1 is the number of vapor molecules, N_2 is the number of molecules in the nucleus, $(N_1 + N_2) = N$; μ_2 is the chemical potential of the substance in the new phase without taking into account surface effects (i.e. for a flat surface). Then the expression for working through the change in the Gibbs potential:

$$A = \Delta G' = G^* - G = (\mu_2 - \mu_1)\, N_2 + \sigma\Sigma. \quad (4.41)$$

For a spherical nucleus, taking into account that $N_2 = \frac{4\pi r^3}{3v_2}$,

$$A = \frac{4\pi r^3(\mu_2-\mu_1)}{3v_2} = 4\pi r^2\sigma. \quad (3.42)$$

The critical size of the nucleus is found from the condition for the maximum change in the Gibbs energy (condition of unstable equilibrium) [195]

$$\left(\frac{\partial \Delta G}{\partial r}\right)_{r=r_{cr}} = 0. \quad (3.43)$$

As a result, the expression for the critical nucleus is:

$$r_{cr} = \frac{2\sigma v_2}{\Delta\mu}. \quad (3.44)$$

Taking into account the weak change in the chemical potential and the equilibrium condition, we find:

$$\mu_2(T, p_2) = \mu_1(T, p_1) + \frac{\partial \mu_2}{\partial p_1}(p_2 - p_1) \quad (3.45)$$

From here

$$p_2 - p_1 = \frac{[\mu_1(T,p_1) - \mu_2(T,p_2)]}{v_2}.. \quad (3.46)$$

In the macroscopic theory of nucleation, "supersaturation" is defined as an increase in vapor pressure or a decrease in temperature below the phase transition point. In this case, $\Delta\mu$ is expressed either as a function of p/p_∞ ($p\infty$ is the saturation vapor pressure above the flat interface) or in terms of ΔT.

The vapor pressure that is in equilibrium with the droplet increases as the droplet size decreases. The increase in the chemical potential in this case is associated with the vapor pressure and is determined by the condition of equilibrium of the system with the nucleus of a new phase. This equation is called the Thomson equation [195]:

$$\Delta\mu = kT \ln(p/p_\infty). \quad (3.47)$$

Recall that here the chemical potential is taken per molecule. If we go over to the chemical potential per mole, then in equation (3.47) the Boltzmann constant is replaced by the gas constant R, in which case the remaining equations use molar rather than molecular volume.

If consider $v = v_2 N_A$ and the Thomson equation, then the formula for definition of the critical size has the form:

$$r_{cr} = \frac{2\sigma v}{RT\ln(p/p_\infty)}. \quad (3.48)$$

Given the latter, the expression to work with would be:

$$A = \frac{16\pi\sigma^3 v^2}{3[RT\ln(p/p_\infty)]^2}. \quad (3.49)$$

At the interface between liquid and vapor, the surface tension varies from 0.01 J/m^2 for volatile liquids to 2 J/m^2 for metals [195]. At a supersaturation of 1.5, which is considered common in real experiments, we obtain the value of the critical radius from 100 to 1 *nm*.

Note that at such dimensions, continuous thermodynamic quantities, one of which is surface tension, lose their meaning. In a critical nucleus, even according to the macroscopic theory, there should be several tens of hundreds of molecules. It is difficult to determine the phase-separating surface in such nuclei and to separate the properties into bulk and surface properties. This is one of the fundamental shortcomings of the macroscopic theory, which cannot be overcome within the framework of the theory itself. But since the theory provides a qualitatively good explanation of the phenomena that occur in reality, interest in it does not weaken, attempts to modify it continue, in particular, to more accurately determine the surface tension [195].

The rate of formation of a drop is proportional to the probability of its formation. The probability of the formation of a nucleus depends on the minimum work of formation A and temperature T:

$$\omega = \omega_0 e^{-\frac{A}{kT}}, \quad (3.50)$$

where ω_0 is the coefficient of proportionality.

Using (3.50), we can express the rate of nucleation as a function of supersaturation:

$$J = Ce^{-\frac{\Delta G}{kT}} \quad (3.51)$$

where C is a pre-exponential factor, the definition of which depends on the choice of the kinetic scheme of cluster formation. Taking into account expressions (3.41) and (3.49), the expression for the nucleation rate will take the form:

$$J = C\exp\left[-\frac{16\pi\sigma^3 v^2}{3kT[RT\ln(p/p_\infty)]^2}\right]. \quad (3.52)$$

The variety of final expressions obtained for the nucleation rate is related to the variety of kinetic schemes and interpretations chosen when finding the pre-exponential factor. Options for finding the pre-exponential factor are presented in [195]. Until now, there is no rigorous statistical solution of the problem. When the forming cluster has a crystalline structure, it must be taken into account that its energy is determined not only by the number of particles, but also by their mutual arrangement, i.e. cluster geometry. The need to take into account the structure and shape of a cluster in the processes of mass crystallization is discussed in [195].

In the macroscopic theory of vapor condensation, it is assumed that saturated vapor is essentially monomeric. The scheme of removal of the nucleus from the system, splitting into individual atoms and introduction into

the system again in the form of monomers belongs to Becker and Dering [6]. The total number of atoms remains constant, and the number of individual monomers does not decrease. It is possible to satisfy two requirements at once: the inexhaustibility of the initial phase, which is necessary for the implementation of the stationary stage of the process, and the low degree of transformation in it at any time, since large centers are removed from the system. This scheme of the process is widespread and is considered classical.

The number of clusters of the *n*-th size, arising in a fluctuation way, according to the Boltzmann principle, is expressed by the equation:

$$N_n = N_0. \tag{3.53}$$

According to this equation, very large clusters should be present in any gas. Frenkel [70] called them heterophase fluctuations, in contrast to ordinary density fluctuations. The role of heterophase fluctuations increases as the vapor approaches saturation. However, in an unsaturated vapor, clusters cannot grow into fog droplets. And only in a supersaturated vapor do the sizes of critical nuclei decrease to such an extent that clusters manage to overcome the energy barrier through fluctuations. Frenkel's theory differs from the Volmer-Weber-Becker-Dering theory in that the latter ignores the possibility of cluster formation in saturated and, moreover, in unsaturated steam. The latter is a drawback of the theory, since already Boltzmann, Clausius, van der Waals and their other contemporaries associated the deviation of the behavior of real gases from the laws for an ideal gas with the formation of associated complexes in the gas. Mass spectrometric studies confirm the presence of dimers, trimers, and larger clusters even in unsaturated vapor [195].

An attempt to take into account the equilibrium concentrations of clusters of different sizes was made by Mayer [195]. However, the proposed scheme turned out to be mathematically too difficult and has not yet been accurately realized. In addition, it did not introduce the concept of a cluster as a long-term aggregation, which was done by Frenkel [70] and a number of other scientists.

During crystallization from melts, as supersaturation, i.e. deviation from the phase transition point, overcooling is considered [195]. If we denote by T_m the melting point, and by T_n the same value for particles of size n, the supercooling will be:

$$\Delta T = T_m - T_n. \tag{3.54}$$

From the condition $T_m = T_n$ it follows:

$$\Delta\mu = \Delta S \cdot \Delta T, \tag{3.55}$$

where $\Delta S = S_{sol} - S_{liq}$, S_{sol} and S_{liq} – entropy respectively for liquid and solid states.

It is known that the change in entropy during crystallization can be expressed in terms of the heat of crystallization (L_{cr})

$$\Delta S = L_{cr}\Delta T. \tag{3.56}$$

Then the expression for the change in the chemical potential during crystallization from melts has the form:

$$\Delta\mu = \frac{L_{cr}\Delta T}{T_{cr}}. \tag{3.57}$$

Expressions for the critical nucleus and nucleation rate for crystallization from melts, taking into account (3.57), have the form:

$$r_{cr} = \frac{2\sigma v T_{cr}}{L_{cr}\Delta T} \tag{3.58}$$

$$A = \frac{16\pi\sigma^3 v^2 T_{cr}}{3[L_{cr}\Delta T)]^2}. \tag{3.59}$$

Nucleation rate at a given supercooling:

$$J = C\exp\left[-\frac{16\pi\sigma^3 v^2 T_{cr}}{3[L_{cr}\Delta T)]^2}\right]. \tag{3.60}$$

When crystallizing from solutions, instead of the relative supersaturation expressed in terms of pressure, the ratio of the concentrations of the supersaturated solution and the equilibrium value is used: c/c_{eq}. Then the change in the chemical potential is expressed as:

$$\Delta\mu = kT\ln\frac{c}{c_{eq}}. \tag{3.61}$$

3.5 Thermodynamics and kinetics of electrochemical nucleation

Of great interest is the process of nucleation in heterogeneous systems on foreign particles or substrates present in them [101, 132, 195]. It is at these heterogeneous centers that a new phase begins to emerge. Heterogeneous centers have different properties. They can be charged or neutral, the surface of an insoluble heterogeneous center can be fully or partially wettable. The critical size of a nucleus during nucleation on wettable centers can be determined by the film thickness. Characteristics of the nucleation process, such as the number of formed centers and their average size, largely depend on these parameters.

The main thing in the thermodynamics of heterogeneous nucleation is finding the work of nucleation or chemical potential.

Knowing the work of formation or the chemical potential of the condensate as a function of the number of molecules in the condensate makes it possible to calculate all the thermodynamic characteristics that are important for the kinetics of nucleation. There are a large number of works on the kinetics and thermodynamics of heterogeneous nucleation [36–45], which present reviews of the main results of studies on the problem of heterogeneous nucleation. The development of research methods, in particular, scanning probe microscopy, made it possible to test the previously developed theory and find the limits of its application [101, 132, 195]. It was shown in [195] that, at high supercoolings of the bcc phase, a homogeneous nucleation mechanism is realized in carefully annealed crystals, while at low supercoolings, a heterogeneous mechanism is realized, characterized by activation coefficients that are several orders of magnitude smaller than homogeneous ones. Osipov [195] considered the coalescence of clusters in thin films. A theory is proposed that describes subcritical, subcritical, and supercritical nuclei independently of each other, and the resulting solutions are "stitched" together at the boundaries.

One of the cases where heterogeneous nucleation manifests itself is electrocrystallization.

The process of electrochemical production of metal coatings begins with the appearance of nuclei of a growing film. The nature of their formation and growth largely determines the properties of functional coatings and films; therefore, a large number of reviews and monographs are devoted to the problem of studying the initial stages of electrocrystallization [101, 132, 195]. These works analyze in detail the theoretical models and the most important experimental studies in the field of studying the electrolytic nucleation of metals.

During heterogeneous nucleation, in the framework of the macroscopic theory, the liquid embryo on the substrate surface has the shape of a spherical segment, and the change in the Gibbs energy ΔG^* during its formation is proportional to the work of homogeneous nucleation ΔG:

$$\Delta G^* = \Phi(\Theta) \cdot \Delta G, \tag{3.62}$$

where $\Phi(\Theta)$ is the shape factor, equal to the ratio of the volumes of a spherical segment and a ball of the same radius and depending on the contact angle Θ. A similar relationship is also valid for the formation of crystalline nuclei, but the expression for the shape factor depends on the configuration of the crystal.

It was shown in [195] that a force acting on the three-phase contact line

(vapor-liquid-substrate) tends to reduce the curvature of the drop. With allowance for this effect, the calculation of the work of formation of a critical nucleus and its size gives values that are 1–2 orders of magnitude greater than when considering changes in only the volume and surface energies of the nucleus.

Phase formation in electrocrystallization has specific features. The presence of an electric double layer and an electric charge on particles (ions) arriving at the electrode surface requires that the kinetics of charge transfer be taken into account (these issues are considered in detail in reviews [101, 132, 195]). Layers of ad atoms of the deposited metal and oxides on the substrate surface have a significant effect on the kinetics of phase formation.

To describe electrochemical nucleation, let us consider an ideal system, which is an inert electrode immersed in an electrolyte (the term "inert" implies the absence of chemical interaction between the deposited metal and the substrate). In the absence of an external potential difference, an equilibrium potential φ_{eq} is established on the cathode, and when an electric current is passed through the cathode, the potential φ is established. The cathode overvoltage (η) is defined as the potential difference:

$$\eta = \varphi - \varphi_{eq}. \tag{3.63}$$

In this case, the chemical potential also changes:

$$\Delta\mu = \mu - \mu_{eq} = ze\eta, \tag{3.64}$$

where z is the valence of the deposited ions, e is the electron charge. The electrode overvoltage characterizes the deviation of the system from the equilibrium position, i.e. supersaturation [101, 132, 195]. This expression is valid if the current flow does not change the chemical potential of the solution. Such conditions are realized with a slight change in the volume concentration of the electrolyte and are characteristic of the initial stages of electrocrystallization of metals.

For the formation of a metal nucleus, it is necessary to expend work proportional to the difference in chemical potentials. This expression is obtained from the expression for homogeneous nucleation (3.49) and (3.62):

$$A = \Phi(\Theta)\ \frac{16\pi\sigma^3 v^2}{3[\Delta\mu)]^2}. \tag{3.65}$$

Critical nucleus radius during electrocrystallization:

$$r_{cr} = \frac{2\sigma v}{zF\eta}, \tag{3.66}$$

where F is Faraday's constant.

However, there is another point of view on the nature of supersaturation during the electrocrystallization of metals. The authors of [68–75] believe that the energy of nucleation is determined not by the difference in electrochemical potentials, but by the excess amount of ad atoms of the deposited metal on the surface electrode and consider it necessary to subtract the junction overvoltage from the total cathode overvoltage.

This approach corresponds to the concept of the independence of the stages of ion discharge with the formation of ad atoms and, in fact, nucleation from the discharged atoms present on the substrate surface, which actually denies the possibility of the formation of a nucleus by the direct incorporation mechanism, which, according to some authors [101, 132, 195], is most probable for electrochemical nucleation processes.

An analysis of the relationship between the work of formation of a nucleus, its critical size, and the rate of nucleation was carried out in [195]. Regardless of the phase formation model, the following expressions for the work A and the nucleation rate J can be written:

$$A = \Delta G = -n\,\Delta\mu + F(n,\Delta\mu) \tag{3.67}$$

$$J = K(\Delta\mu)\cdot\exp(-\Delta G/RT) \tag{3.68}$$

where n is the number of atoms in the nucleus, $K(\Delta\mu)$ is the kinetic factor in the equation for the nucleation rate, $F(n,\Delta\mu)$ is the change in the surface energy of the system during the formation of a complex of n atoms. After taking the logarithm and differentiating, you can get the formula:

$$n_{cr} = RT\left[\frac{d(\ln J)}{d(\Delta\mu)}\right] - RT\left[\frac{d(\ln K)}{d(\Delta\mu)}\right] + \frac{dF(n,\Delta\mu)}{d(\Delta\mu)}. \tag{3.69}$$

When considering nucleation processes in narrow supersaturation intervals, the change in the surface energy and kinetic factor can be neglected, then

$$n_{cr} = RT\left[\frac{d(\ln J)}{d(\Delta\mu)}\right]. \tag{3.70}$$

This equation makes it possible to determine the size of the critical nucleus from the experimental dependence of the nucleation rate on supersaturation, regardless of the nucleation model used. According to the analysis of the effect of the pre-exponential factor in Eq. (3.68) and the surface energy $F(n,\Delta\mu)$ on the critical size of the nucleus, carried out in [195], the error in determining ncr from Eq. (3.70) does not exceed 1–2 atoms.

Equation (3.70) is used to describe the kinetics of nucleation in supersaturated systems. There are various approaches to establishing a

particular form of the $K(\Delta\mu)$ function [101, 132, 195] that take into account the state of the substrate and the kinetics of addition of ad atoms to the growing cluster. Processing of experimental data within the framework of various models of electrochemical nucleation gives close values of the work of nucleation and the critical size of the nucleus, which is, as a rule, 1–10 atoms. Since it is impossible to guarantee that all possible effects are taken into account when constructing one or another nucleation model, one should not attach great importance to the absolute values of n_{cr}. It is important to establish the regularities of the relative change in the work of nucleation as a result of the influence of various factors (overvoltage, adsorption of solution components, energy state, nature and structure of the substrate).

3.6 Stranski-Krastanov theory

Stranski–Krastanov growth (SK growth, also Stransky–Krastanov or Stranski–Krastanow) [19, 206, 207, 243] is one of the three primary modes by which thin films grow epitaxially at a crystal surface or interface. Also known as 'layer-plus-island growth', the SK mode follows a two step process: initially, complete films of adsorbates, up to several monolayers thick, grow in a layer-by-layer fashion on a crystal substrate. Beyond a critical layer thickness, which depends on strain and the chemical potential of the deposited film, growth continues through the nucleation and coalescence of adsorbate 'islands'. This growth mechanism was first noted by Ivan Stranski and Lyubomir Krastanov in 1938 [207]. It was not until 1958 however, in a seminal work by Ernst Bauer published in Zeitschrift für Kristallographie, that the Stranski–Krastanov, Volmer–Weber, and Frank–van der Merwe mechanisms were systematically classified as the primary thin-film growth processes [19, 206, 207, 243]. Since then, SK growth has been the subject of intense investigation, not only to better understand the complex thermodynamics and kinetics at the core of thin-film formation, but also as a route to fabricating novel nanostructures for application in the microelectronics industry.

The growth of epitaxial (homogeneous or heterogeneous) thin films on a single crystal surface depends critically on the interaction strength between adatoms and the surface. While it is possible to grow epilayers from a liquid solution, most epitaxial growth occurs via a vapor phase technique such as molecular beam epitaxy (MBE). In Volmer–Weber (VW) growth, adatom–adatom interactions are stronger than those of the adatom with the surface, leading to the formation of three-dimensional adatom clusters or islands. Growth of these clusters, along with coarsening, will cause rough multi-layer films to grow on the substrate surface. Antithetically, during Frank–van der Merwe (FM) growth, adatoms attach preferentially to surface

sites resulting in atomically smooth, fully formed layers. This layer-by-layer growth is two-dimensional, indicating that complete films form prior to growth of subsequent layers [19, 206, 207, 243]. Stranski–Krastanov growth is an intermediary process characterized by both 2D layer and 3D island growth. Transition from the layer-by-layer to island-based growth occurs at a critical layer thickness which is highly dependent on the chemical and physical properties, such as surface energies and lattice parameters, of the substrate and film [19, 206, 207, 243]. Fig. 3.4 is a schematic representation of the three main growth modes for various surface coverages.

Determining the mechanism by which a thin film grows requires consideration of the chemical potentials of the first few deposited layers [19, 206, 207, 243]. A model for the layer chemical potential per atom has been proposed by Markov [132] as:

$$\mu(n) = \mu_\infty + [\varphi_a - \varphi_a'(n) + \varepsilon_d(n) + \varepsilon_e(n)], \tag{3.71}$$

where μ_∞ is the bulk chemical potential of the adsorbate material, φ_a is the desorption energy of an adsorbate atom from a wetting layer of the same material, $\varphi_a'(n)$the desorption energy of an adsorbate atom from the substrate, $\varepsilon_d(n)$ is the per atom misfit dislocation energy, and $\varepsilon_e(n)$ the per atom homogeneous strain energy. In general, the values of φ_a, $\varphi_a'(n)$, $\varepsilon_d(n)$, and $\varepsilon_e(n)$ depend in a complex way on the thickness of the growing layers and lattice misfit between the substrate and adsorbate film.

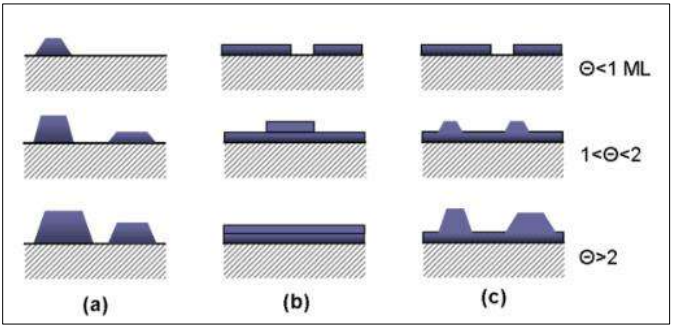

Fig 3.4: Cross-section views of the three primary modes of thin-film growth including (a) Volmer–Weber (VW: island formation), (b) Frank–van der Merwe (FM: layer-by-layer), and (c) Stranski–Krastanov (SK: layer-plus-island). Each mode is shown for several different amounts of surface coverage, Θ [132]

In the limit of small strains, $\varepsilon_d(n) \ll \mu_\infty$, the criterion for a film growth mode is dependent on $\frac{d\mu}{dn}$.

- VW growth: $\frac{d\mu}{dn} < 0$ (adatom cohesive force is stronger than surface adhesive force), (3.72)
- FM growth: $\frac{d\mu}{dn} > 0$ (surface adhesive force is stronger than adatom cohesive force). (3.73)

SK growth can be described by both of these inequalities. While initial film growth follows an FM mechanism, i.e. positive differential μ, nontrivial amounts of strain energy accumulate in the deposited layers. At a critical thickness, this strain induces a sign reversal in the chemical potential, i.e. negative differential μ, leading to a switch in the growth mode. At this point it is energetically favorable to nucleate islands and further growth occurs by a VW type mechanism [132]. A thermodynamic criterion for layer growth similar to the one presented above can be obtained using a force balance of surface tensions and contact angle.

Since the formation of wetting layers occurs in a commensurate fashion at a crystal surface, there is often an associated misfit between the film and the substrate due to the different lattice parameters of each material. Attachment of the thinner film to the thicker substrate induces a misfit strain at the interface given by $\frac{a_f - a_s}{a_s}$. Here a_s are the film and substrate lattice constants, respectively. As the wetting layer thickens, the associated strain energy increases rapidly. In order to relieve the strain, island formation can occur in either a dislocated or coherent fashion. In dislocated islands, strain relief arises by forming interfacial misfit dislocations. The reduction in strain energy accommodated by introducing a dislocation is generally greater than the concomitant cost of increased surface energy associated with creating the clusters. The thickness of the wetting layer at which island nucleation initiates, called the critical thickness h_c, is strongly dependent on the lattice mismatch between the film and substrate, with a greater mismatch leading to smaller critical thicknesses. Values of h_c can range from submonlayer coverage to up to several monolayers thick [132]. Fig. 3.5 illustrates a dislocated island during SK growth after reaching a critical layer height. A pure edge dislocation is shown at the island interface to illustrate the relieved structure of the cluster.

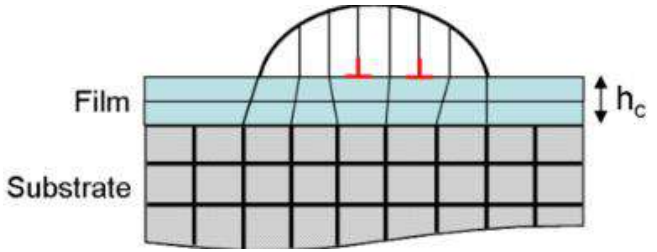

Fig 3.5: SK growth showing island formation after obtaining a critical thickness, h_c. Lines represent lattice planes with thicker lines for the substrate lattice and thinner lines for the growing film. Edge dislocations are highlighted in red at the film/island interface [132]

In some cases, most notably the Si/Ge system, nanoscale dislocation-free islands can be formed during SK growth by introducing undulations into the near surface layers of the substrate [19, 132, 206, 207, 243]. These regions of local curvature serve to elastically deform both the substrate and island, relieving accumulated strain and bringing the wetting layer and island lattice constant closer to its bulk value. This elastic instability at h_c is known as the Grinfeld instability (formerly Asaro–Tiller–Grinfeld; ATG) [132]. The resulting islands are coherent and defect-free, garnering them significant interest for use in nanoscale electronic and optoelectronic devices. Such applications are discussed briefly later. A schematic of the resulting epitaxial structure is shown in Fig. 3.6 which highlights the induced radius of curvature at the substrate surface and in the island. Finally, strain stabilization indicative of coherent SK growth decreases with decreasing inter-island separation. At large areal island densities (smaller spacing), curvature effects from neighboring clusters will cause dislocation loops to form leading to defected island creation [132].

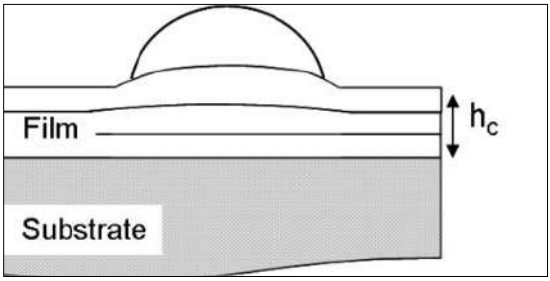

Fig. 3.6. Coherent island formation under SK growth. Local curvature of the near surface region surrounding the island leads to elastic deformation of the island and wetting layer thereby reducing the accumulated strain. These islands are defect free [132]

3.7 Walton's microscopic theory of nucleation

The microscopic theory of homogeneous nucleation developed by Walton [195, 257] arose due to the limited application of the macroscopic theory of nucleation. First of all, this concerned the use of the spherical drop model and the surface energy for the nucleus. These two assumptions are valid for large clusters and have been have been verified for a cluster of about 100 atoms in size [195, 257], where a good agreement between theory and experiment was observed, in which crystallization took place at low values of supersaturation. However, it was experimentally shown in [195, 257] that the critical nucleus upon condensation from the vapor phase contains only nine atoms. For such small clusters, the use of surface energy to calculate the free energy of crystallization is not applicable [195, 257]. In addition, the question arises about the shape of the embryo. For example, if a cluster contains about six atoms, then its shape is very far from a spherical drop, and the cluster energy will strongly depend on the relative position of the atom in the nucleus. Consequently, the macroscopic theory of nucleation does not work in these cases.

At high supersaturations for vapor phase crystallization, Walton proposed the following approach. He proposed a new criterion for the stability of a critical nucleus.

Consider a nucleus that contains n atoms. In the case when the size of the critical nucleus is small, the sum of its potential energies (En) has a discontinuous character and strongly depends on the geometric shape of the nucleus. Because of this, it is impossible to obtain an analytical expression for the potential energy of the nucleus as a function of n. However, due to the fact that the number of atoms in the nucleus is small, it is possible to study all possible configurations of atoms in the nucleus and establish empirical criteria for the stability of the critical nucleus.

The solution of this problem is very complicated, but it has a singular advantage in which the structure of the critical nucleus is considered. When using the existing approach, it is possible to specify the structure of the nucleus at a given saturation, thereby greatly facilitating this task. The main criterion for sustainability Walten considered the binding energy (ΔE) of atoms in a crystalline nucleus, which, with an equal number of atoms in the nucleus, depends even more strongly on the configuration of the crystalline nucleus. Crystalline nuclei that have a higher binding energy than others that contain equal numbers of atoms are more likely to grow.

This must be taken into account in order to obtain an expression for the rate of nucleation, which is valid for small clusters. A certain problem is to

obtain an expression relating the rate of nucleation and substrate temperature, as well as the rate of delivery of atoms from vapor. For this, it is first necessary to calculate the equilibrium concentration of clusters. The distribution function will have a minimum corresponding to clusters that are critical nuclei. The rate of nucleation can be obtained by multiplying the number of critical nuclei by the rate of addition of individual atoms.

The distribution function can be represented as [195, 257]:

$$Z = A \sum \exp(-E/kT) \tag{3.74}$$

where A is a constant for this calculation, and E is the sum of the potential energies of ad-atoms. The summation occurs over all possible configurations of N ad-atoms on the surface.

Consider the term under the sum sign, corresponding to the division of the total number N of atoms into N_1 single atoms, N_2 pairs, N_3 3-dimensional, and so on. His contribution to the amount:

$$T = \prod_n \frac{1}{N_n!}\left[\beta_n N_0 exp\left({}^{E_n}/_{kT}\right)\right]^{N_n}, \tag{3.75}$$

where $\left({}^{\beta_n N_0}/_{N_n}\right)^{N_n}$ is the number of configurations of N_n clusters of size n on N_0 adsorption sites, ε_n is the potential energy of a cluster of size n.

The distribution function will be the sum of all these terms:

$$Z = T = A \sum_{N_n} \prod_n \frac{1}{N_n!}\left[\beta_n N_0 exp\left({}^{E_n}/_{kT}\right)\right]^{N_n}, \tag{3.76}$$

The most likely distribution will be the largest term in the sum. We restrict ourselves to the case when only one cluster configuration is possible. This occurs when the growing new phase repeats the structure of the substrate, i.e. epitaxial growth observed at the initial stages of electrocrystallization [195, 257]. It has been experimentally found that the resulting phase has a high degree of preferential orientation [195, 257], so that this limitation is valid.

If the number of clusters is much less than the number of individual ad-atoms, we can make the following approximation:

$$N_n = N_0 \left({}^{N_1}/_{N_0}\right)^n \exp\left[{}^{(\varepsilon_n - n\varepsilon_1)}/_{kT}\right]. \tag{3.77}$$

In the usual theory of nucleation, a critical nucleation is a cluster that has an equal probability of growing or dissolving. In microscopic theory, a critical nucleus is a cluster whose growth probability is less than or equal to 0.5, but which, after the addition of one atom in the cluster, acquires a growth

probability greater than 0.5. The cluster that is obtained by adding a single atom to the critical nucleus will be called the smallest stable cluster. Thus, the rate of nucleation becomes the rate at which clusters of critical size become "supercritical". Then the rate of formation of nuclei will be:

$$I = N_n \Gamma_{n^*}^{+*}, \tag{3.78}$$

where $\Gamma_{n^*}^{+*}$ is the rate at which individual atoms attach to an n^* size nucleus. $\Gamma_{n^*}^{+*}$ can be estimated in kinetic theory. If the atoms diffuse over the surface with an average velocity v, then

$$\Gamma_{n^*}^{+} = \sigma_{n^*} N_1 v, \tag{3.79}$$

where σ_{n^*} is the capture width of the critical nucleus for an individual atom. To some extent

$$v = av\exp\left(-{E_S}/{kT}\right), \tag{3.80}$$

a is the distance between adsorption sites, ν is the attachment frequency, and E_S is the activation energy for surface diffusion. Thus,

$$\Gamma_{n^*}^{+} = \sigma_{n^*} N_1 av\exp\left(-{E_S}/{kT}\right). \tag{3.81}$$

Consider the size of the critical nucleus. As mentioned above, a nucleus can consist of several atoms, so it makes sense to separate two-dimensional and three-dimensional nuclei. Let us assume that a crystalline nucleus is formed and supersaturation is constant. Depending on the oversaturation (substrate temperature or overvoltage during electrocrystallization), the critical nucleus has a different number of atoms [195, 257].

Consider the case when a pair of atoms is formed. The rate of formation of nuclei is the rate of formation of a pair:

$$I = N_1 \Gamma_1^{+}, \tag{3.82}$$

where Γ_1^{+} is the rate at which individual atoms are captured by other individual atoms, can be determined by the formula:

$$\Gamma_1^{+} = \sigma_1 N_1 \nu. \tag{3.83}$$

The resulting equation is valid only if the pair of atoms does not decay. Then the interaction energy or the binding energy of a pair of atoms (ΔE_2) becomes an important parameter. Therefore, taking into account the binding energy, the expression for the velocity will take the form:

$$\Gamma_2^{+} = 2\nu\,\nu\exp\left(-\frac{\Delta E_2 + E_S}{kT}\right). \tag{3.84}$$

For a pair of atoms, the geometry of the cluster is not important, since defined unambiguously. At other supersaturations, the smallest stable cluster will be a cluster of three atoms. It should be noted that an individual atom must combine with a pair so that the resulting configuration has the highest binding energy. For example, three atoms in a line are less stable than those connected in a triangle. For convenience in calculating the activation energy of surface diffusion of two-dimensional clusters, its value is taken constant. It should be noted that for three-dimensional clusters (and this may be a cluster of 4 atoms), an ad-atom joining the cluster must make an additional diffusion jump to the top of the cluster.

From the foregoing, we can conclude that in order to apply the microscopic theory, it is necessary to know the values of the binding energy in a cluster and the surface diffusion energy, which will be the subject of our research.

The application of the microscopic theory of nucleation in electrocrystallization has a small number of examples, most of which are related to the unification of the macroscopic heterogeneous theory of nucleation and microscopic [195, 257]. For example, in the analysis of experimental data on three-dimensional nucleation, the expression for the stationary rate obtained in the framework of the microscopic theory [195, 257] was used:

$$J = KN_0 \exp\left[\frac{(n_{cr}+\alpha)zF\eta}{RT}\right], \tag{3.85}$$

where K is a parameter that weakly depends on the overvoltage, N_0 is the number of active centers on the substrate on which nucleation can occur, and α is the electrochemical transfer coefficient.

According to this model, the number of atoms in a critical nucleus can be arbitrarily small and even zero. In this case, the critical nucleus is the active center of the substrate, the attachment of one atom to which makes such a complex a stable aggregate capable of spontaneous growth at a given supersaturation.

In the microscopic theory [195, 257], supersaturation is assumed to be equal to the cathode overvoltage η, and the work of formation of a critical nucleus is calculated by the formula:

$$A = \Delta G = -n_{cr}\Delta\mu + F(n_{cr}), \tag{3.86}$$

where the function $F(n_{cr})$ characterizes the difference in energy of the n_{cr} -atomic complex and n_{cr} atoms that are part of an infinite crystal:

$$F(n) = n\varphi_{1/2} - \sum \varphi_i, \quad (3.87)$$

where $\varphi_{1/2}$ is the work of separating an atom from the semicrystal position, φ_i is the work of separating an atom from an i-atomic cluster. In its physical meaning, $F(n)$ is the equivalent of the surface energy of a complex consisting of n atoms. In contrast to the macroscopic approach, in this case the work of nucleation is not a continuous function of n.

In [195, 257], within the framework of the microscopic theory, a model of stationary nucleation during the electrochemical formation of alloys was proposed. It is shown that for a two-component system containing A and B cations with charges z_A and z_B,

$$J = K_i a_i \exp\left\{\frac{[-\alpha_i z_i F E_\infty + F(n_{AB}) + n_a z_a + n_b z_a + \alpha_i z_b F\eta]}{RT}\right\}, \quad (3.88)$$

where i = A or i=B, depending on how the critical nucleus of the AB alloy is formed, by attaching the last atom A or B, K is the rate constant, weakly dependent on overvoltage, and is the activity of the ion in the electrolyte, $n_{AB}=n_A + n_B$ is the number of atoms in the critical nucleus, $F(n_{AB})$ is its surface energy, E_∞ is the equilibrium potential of the alloy. This equation can be reduced to a form more convenient for analyzing the concentration dependence of the nucleation rate [195, 257].

3.8 Advantages and minuses of thermodynamically methods of nucleation and crystallization

The advantages of thermodynamic modeling methods include its simplicity and the ability to qualitatively explain the main regularities of the corresponding process with the help of a small number of heuristic parameters [132, 243].

These models make it possible to describe the processes of crystallization from steam (from the gas phase), from solutions, and from melts [19, 20, 22].

The growth of single crystals from the gas phase is mainly used to obtain epitaxial films and thread-like crystals (epitaxy is the oriented growth of a single crystal layer of one substance on the surface of a crystal of another substance); such films (layers) are important elements of electronic circuits, magnetic memory devices, integrated optics, etc [132, 243].

Sublimation methods, i.e. crystallization of a substance from its own vapor, are convenient for those substances that sublimate easily, without passing into the liquid phase (naphthalene, phosphorus, silicon carbide) [132, 243].

Crystal growth from solutions is based on the diffusion of solute atoms (molecules) from a supersaturated solution to a growing crystal [132, 243].

Supersaturation is formed in different ways: due to an increase in the concentration of a dissolved substance during evaporation (evaporation) of the solvent, a decrease in the temperature of the solution (at the same time, the concentration of the solution increases due to a decrease in the solubility of the substance when the temperature decreases), the formation of a temperature difference, etc [132, 243].

Single crystals are grown using seeds of small crystals, preferably with a minimum number of structural defects and a certain faceting: such that the growing crystal acquires the desired shape (habit) and orientation [132, 243]. From solutions, it is possible to grow single crystals with a fairly perfect structure, without internal stresses, of almost any size (weighing tens of kilograms).

The general disadvantage of all methods of this group is low growth rates, that is, a longer duration of the growing process (months).

Methods of growing from melts are as follows [132, 243]:

In the Kiropoulos method, when growing single crystals, [132, 243] a change in the temperature of the melt is used.

There are several variants of this method. Local cooling of the melt in the volume where the crystal originates and grows is common. Methods are used when there is spontaneous germination or growing on a seed.

In the Chochralsky method, unlike the Kiropoulos method, the temperature of the melt is kept constant. melt, is wetted by the melt and rises above its surface with the melt adhering to it at a speed of 1-40 mm/h, which does not exceed the linear speed of crystallization.

In the Chochralsky method, a flat front of crystallization is maintained, which allows to reduce mechanical stresses during cooling and ensures uniform distribution of the alloying impurity in the volume of the crystal. The lifting mechanism that extracts the seed is cooled by running water. The crystal actually grows not in the melt, but above the melt, and its growth is not limited by the size of the crucible.

The advantage of Chochralsky method [132, 243] is the lack of direct contact between the crystal and the walls of the crucible, so it is convenient for growing single crystals of substances that have a large jump in volume upon solidification. In addition, contamination of the crystal due to its interaction with the crucible material is excluded. The ability to change the temperature

of the melt and the growth rate allows obtaining low-dislocation crystals. All this ensured the widespread use of the Czochralsky method, especially for growing single crystals of silicon, germanium, corundum, garnets, niobates, as well as single crystals of metals. Using this method, almost dislocation-free single crystals of Si and Ge were obtained for the first time.

The Bridgman-Stockbarger method (or directional crystallization method) [132, 243] involves moving the crucible with the melt in a tubular electric furnace (sometimes the furnace is raised and the tube remains stationary). The movement of the crucible or furnace is carried out with the help of an electric motor or a clock mechanism.

Methods of zonal crystallization [132, 243] of a substance came into practice after Bridgman showed that during directional crystallization, impurities are pushed out by the growing crystal and concentrated in the liquid phase. The essence of the zone melting method is as follows. A monocrystalline seed (crystal seed) is placed at one end of the shuttle crucible loaded with the initial polycrystalline material. With a special heater, the ingot is melted in a small area - in a narrow zone in the seed. The crucible is moved relative to the heater, in the zone of local heating the substance melts, and after it crystallizes, and the seed begins to grow. At the same time, impurities that have greater solubility in the liquid phase are displaced in the direction of movement of the crystallization front, that is, at the end of the ingot. By repeating this movement several times, you can obtain a high degree of purification and structural perfection of the grown single crystal.

The problem of creation the nano- and microstructures by stationary methods may be chemical and epitaxial. In this case, we can receive structures with sizes more as 10 nm. But polycrystalline structures may be received with help other methods of crystal growing too.

Thus, when growing a water-soluble mixture from which we have to grow the desired crystal, with even a slight increase in the rate of lowering the temperature, instead of one center of crystallization, we get quite a lot. Due to this, multiple crystals with the same crystal structure and different directions of growth can form. Such crystals are called twins.

At the same time, a set of crystals with different crystallographic modifications with different directions can be formed. Such structures are called drusen [132, 243].

There are no theories of such phenomena, since such processes were undesirable during the growth of single crystals. The exception is titanium, which consists of two phases, cubic and hexagonal.

However, such research should be initiated and continued in order to find new effective methods for obtaining nanostructures.

The development of methods for obtaining different allotropic phases of materials that are difficult to obtain by traditional methods can be a promising direction for the development of modern materials science.

In general, thermodynamic models allow describing only the macroscopic processes of nucleation and crystallization. In connection with the expansion of the role of methods of obtaining nano and microstructures, the problem of their modeling has arisen. For this, in some cases, kinetic models are better suited, which allow to take into account microscopic processes more adequately.

3.9 Conclusions

1. The main problems of using the thermodynamical methods for modeling processes of nucleation and crystallization are represented.
2. The influence of problem of saturation of proper crystalized media is analyzed.
3. Values of thermodynamical regimes of nucleation and crystal growth are discussed.
4. Peculiarities of modeling homogeneous systems are shown.
5. Main properties of modeling heterogeneous systems are represented.
6. Stranski-Krastanov theory of crystal growth is discussed.
7. Walton microscopic model of nucleatization is analyzed.
8. Pluses and minuses of thermodynamically methods of nucleation and crystallization and necessary of search and creation more précising models are discussed too.

Chapter - 4

The Main Problems of Electrodymical Modelling the Nucleation and Crystallization

I will recognize yours among a thousand traces

Oles Berdnyk

4.1 Introduction

The nucleation concept must be generalizing on other type processes, including electromagnetic and pulses [1 – 41].

To expand the methods of obtaining nuclei of various crystallographic modifications, it is advisable to use the methods of elionic technologies [1-18, 21-24, 26-29, 31-39]. The use of different types of irradiation: ion, electron, and especially laser allows forming nuclei of both structures with a smaller order of symmetry and structures with a higher order of symmetry [2-6]. At the same time, a cascade of structures can be formed as their order of symmetry decreases.

These nucleation theories and models must base on other physical and chemical aspects as thermodynamical. The main role is played by the excitation saturation mode of the corresponding radiation absorption centers and the mechanisms of their non-radiative relaxation, which lead to the required phase transformations [2-6].

V. Stafeev phason model [2, 20] is represented electrostatic theory which takes into account the existing and changing electrostatic state of the compound to form the nuclei of new phases or aggregate states of matter (phases). Therefore, we analyzed this theory and its some applications.

Cascade model of step-on-step excitation of corresponding chemical bonds in the regime of saturation the excitation allow to explain the processes of creation surface and volume laser-induced structures in various solid: from amorphous to crystals, in both directions. At the same time, it is possible to use both schemes of two-dimensional and three-dimensional crystal lattices and their phase diagrams. Energy calculations can be carried out both for chemical bonds and for the coordination numbers of an atom in a crystal

lattice. Since we are talking about structural phase changes of a substance, it is advisable to use physicochemical methods of calculation, not quantum mechanical ones. There is no sense in Brillouin zones say, since when new phases are formed, it is different for each phase.

In this case, cascade processes of conversion of radiation energy into matter and, conversely, matter into radiation are of great importance [2-6]. This makes it possible to control the modes of nucleation of new phases both on the surface and in the volume of the irradiated material. In contrast to continuous nucleation and crystallization, in this case we must have irradiation modes with non-radiative relaxation. For ions and electrons, these can be both continuous and pulse irradiation modes, which allow you to dial in the appropriate integral dose, and for laser irradiation, only pulse. Therefore, we must build models and theories of these processes taking these features into account.

4.2 Vitaliy Stafeev phason model

The problem of the creation new phase centers (phasons) is represented in Stafeef model [2, 20]. It is electrostatic theory. Short review of this theory will be analyzed in this chapter.

Experimental data [20] shown that phasons are mono dispersive particles. Its sizes are depended from properties of its matter and environment of its formation. New condenced phase centers may be generated under vaporation, on substrate, in gas or liquid environment and directly in solid state. Under change of chemical compound phasons change its sizes in jumping way. For various matters minimal sizes of phasons are changed from 1 to 20 nm [20]. Nanoparticles with these sizes are observed in soli state. It is structural defects – clusters [20]. In some environment crystallization centers are covered by shell, its form stands more lock-in. Its nanoparticles are analogous to special “atoms” – small bricks of new matter [20]. It may be included in solution, including solid, and created own condensed matter. For objects of little sizes, classical thermodynamical approaches and characteristics (surface energy a.o.) cannot be used. However, must be existed some physical characteristics of matter and environment, which are determined minimal sizes of phasons.

As rule take into account, that nanoparticles are neutral [20]. But investigations in region of phase transitions were shown that new phase centers (phasons) must be have electrical charge. For example [162], between growth ice layer from water may be generated sufficiently great (decathlons and hundreds Volts) difference of electrical potentials. Under phase transitions in liquid crystals great difference of electrical potentials is observed [20].

Atoms is determined the properties of chemical elements, molecules – chemical properties of substance. Must be existed structural unit that determine physical and other properties of condensed phases of substance. Last is depended not only from state of substrate but from its phase. Phasons may be completed from comparatively small numbers of molecules. Some quantitative threshold must be existed. Beginning from this threshold molecular cluster is transformed to thermodynamically stable phasons [20].

One of the important parameter of any phase is electrochemical potential. Therefore, on its border with another phase junction difference of electrical potentials, which is stipulated of difference of electrochemical potentials, must be generated. It may be realized only in presence in each with contact phase's electrical charges with opposite signs. Cluster of bound molecules may be thermodynamically stable center of new phase after formation of proper junction difference of potentials only.

Minimal size of phason is determined from condition, that unit electrical charge *q* in environment with electrical constant ε on its capacity *c* is provided the generation of necessary junction difference of potentials $\varphi = q/\varepsilon c$. Center of new phase with minimal sizes was called phason [20]. These centers may be having various forms. For simplification of further analysis we allow that center of new phase is spherical capacitor with diameter d_o. For this suggestion [20]:

size of phason – $d_o = 3{,}6/\varepsilon\varphi$, нм;

number molecules in phason – $n_f = 10^2\ \pi\rho d_o^3/M$;

mobility – $\mu = \varepsilon\varphi/6\pi\eta = 5{,}3\cdot10^{-7}\ \varepsilon\varphi/\eta$, $cm^2/V\cdot s$;

diffusive coefficient – $D = 4{,}6\cdot10^{-11}\ \varepsilon\varphi T/\eta$, cm^2/s,

where φ in Volts; q in Coulomb; η viscosity in Poissons; N – Avogadro number; T – temperature; M – molecular weight; ρ is density of phason substrate in g/cm^3.

Diameter, mobility and diffusive coefficient of phasons are determined of electric constant of surrounding environment and difference of electrochemical potentials.

Sign of difference of electrochemical potentials is determined the sign of charge of center of new phase. For vacuum and gas, the role of difference of electrochemical potentials has energy of chemical affinity to electron (or proton) atoms and molecules of phason substrate w. For positive sign of affinity to electron phason charge will be negative, for positive to proton –

positive. Knowledge of phason size allow estimating the affinity to electron (proton) its substance or difference of electrochemical potentials phason and substance of basic phase.

Phasons may be creating more large clusters – polyphasons. It must be quantized on sizes $d = nd_o$, where n = 1, 2, 3.

Scientists from Berkeley laboratory under researches of properties of lead drop in solid crystal of aluminum for T = 423 °C are measured that lead drops have discrete sizes really [20].

Relationship to electron in Al w = 0,46 eV, in Pb w = 1,14 eV and difference of energy of relationship is 0,68 eV. Proper size aluminum phason is d = 5,3 nm, that is near to observing size of lead drops – 5 nm. According to experimental data [20] nanoparticles of lead are repulsed mutually, that with hear point of view couldn't be. In this theory all phasons have alike electrical charge and therefore Coulomb force of repulse are basic in this case. After increasing of phasons sizes energy of deformation of aluminum lattice is increased and lead drops begin be going to in thick group for decreasing of deformation of aluminum crystal, which is corresponded to experimental data [20].

Some data show that phase transitions are sharp, that is to say that transitional region is absented practically. However, other experimental data show that phase transition is fluent under temperature [20]. Phasons of low temperature phase are presented in stable region of high temperature phase and, on the contrary, phasons of high temperature phase are presented in stable region of low temperature phase. Concentration and sizes of phasons are increased under approach to point of phase transition, in which one phase is changed on another phase. For example, in fullerite (C_{60}) for temperature 260 K phase transition: simple cubic lattice – verge central lattice, is realized. Transition is endothermic and realized in thermal region 20-40 K – in this case two phases are coexisted [20].

Estimations of physical characteristics of basic phasons are next.

Phasons of carbons

Atom of carbon C has value of energy of relationship to electron w = 1,263 eV [20]. Minimal size of phason (d = 2,85 nm) practically is considered with minimal size phasons (2,5 nm), which are received with help laser sprayer of ultradispersion diamond layers [20]. Average size nanoparticles of diamond, which are received with help of detonating synthesis, is 4,2 nm [20]. Minimal size of diamond phasons, which are grown from hydrogen-methane

mixture on silicon substrate, is near to 5 nm [162]. Last increasing size is bound with influence of substrate and high temperature of condensation (850°C).

Smut. After incineration of toluene and acetone the appearance of spherical clusters with sizes 15,5 and 24,5 nm with charges 2 i 3 q are observed. Difference in size is near to 9 nm. Elementary phason – cluster with unit charge – must has size ~ 8 – 9 nm end energy of relationship ~0,4–0,5 eV. These results are confirmed predicted quantized of phason sizes.

Molecule of carbon C_2 has relationship to electron w = 3,39 eV and create phasons with twin number of atoms. All molecules of fullerenes have twin number of atoms too [20]. Size of phason of molecules C_2 in gas environment d_o = 1,06 nm practically is equaled with size stable spherical molecule fullerene-60 ("near to 1 nm" [20]). Internal cavity of fullerene has size ~ 0,7 nm [20].

Fullerenes with more large number of molecules are less stable and have ellipsoidal form. Therefore, for receiving more large capacity we must have more large number of molecules and sizes. For example, in fullerene C_{84} d_o = 1,12 nm [20]. An inclusion in fullerene of atoms of another materials is changed it electrochemical potential and size. Last fact is observed in experiment [20].

Fullerite. In crystal of fullerenes C_{60} (fullerites) distance between centers of molecules is 1,06 nm. In crystal of fullerite with cubic structure for dense packing distance between molecules of C_{60} is equaled 1,006 nm [20]. Accounting density of phason material of molecule C_2 is equaled 1,76 g/cm^3 in our model. But density of solid state must be less on account of cavities, which are generated under condensation of spherical phasons. Density of fullerite is 1,65 g/cm^3 [20]; 1,69 g/cm^3 [20]. In this case we have good coordination with accounting data.

Molecule of carbon C_3 has affinity to electron 2,5 eV, therefore accounting size of it phason is d_o = 1,44 nm and volume bigger in 2,5 times then volume of phason molecule C_2.

Affinity to electron of molecule of fullerene C_{60} w = 2,57 eV, fuleren C_{70} w = 2,69 eV. Size of phasons of molecules of fullerenes C_{60} in environment with $\varepsilon = 1$ d_o = 1,4 nm. Experimental data – "near to 1,5 nm".

Fullerenes in solutions are existed as clusters – polyphasons with number of molecules 6–20 [20], which are created for time ~10^{-6} s. Further in time many days it grows to few hundred nanometers, but it are unstable and disintegrate after shaking. Clusters have fractal structure (as pizza) with fractal parameter k = 2,1. Number particles in cluster is $n_f = (d/d_o)^k$ [20]. Absorptive spectrum of fullerenes is depended from composition of solvent.

Size of clusters is depended from chemical composition of solvent. This result is confirmed the diffusive researches [20]. In benzol (ε = 2,28, w = 0,56 eV) accounting size of phasons C_{60} 0,78 nm, phasons C_{70} d_o = 0,74 nm. Experimental data: height 0,78 nm, diameter 0,694 nm [20]. In CS_2 (ε = 2,28, w = 0,85 eV) accounting size of phason C_{60} d_o = 0,79 nm; size of phason C_{70} d_o = 0,74 nm. Experimental data $d_o = 0{,}357 \times 2 = 0{,}71$ nm [20]. Viscosity of benzol $\eta = 6{,}5 \times 10^{-3}$ Poissons, therefore diffusive coefficient of fullerenes' must be $\sim 10^{-5}$ cm^2/s, that near to values of diffusive coefficients in analogous materials [162].

Phasons may be basis for creation structures with quantum dots.

Therefore, for evaporation InAs with help method molecular-beam epitaxy on GaAs substrate grown pyramidal phasons have alike sizes [20]. For temperature of substrate 460°C pyramid with quadratic basis is grown (side a = 12 nm and height h = 6 nm). These pyramids are equivalent to sphere with diameter ~ 8 nm. If process of evaporation was interrupted to achievement of optimal sizes by phason, then transition molecules to new phase centers is realized to achievement of optimal sizes by phason. If assume, that growth pyramids are InAs phasons, then value of energy of relationship to electron in InAs for temperature 460°C is w = 0,45 eV. This value is placed between values of energy of relationship for room temperature for In (w = 0,3 eV) and As (w = 0,8 eV), that explain observed results. Increasing of pressure of As vapor is caused the decreasing of value of basis of pyramid and it volume. Increasing of As concentration displacing w in side of it value for As, that is caused the decreasing of phason sizes.

On the basis of this conception, sizes of phasons of any materials may be estimated, if it relationship to electron is famous. Values of phasons sizes for basic technological elements, which estimated with help values of energy relationship to electron, have next meanings.

Elements – d, nm: Al – 7; Co – 4; Ni – 5,5; Mo – 3; Ag – 2,8; In – 12; Sn – 3,2; Au – 1,6; Si – 2,6; Cu – 2,9; Ge – 2,9; Sb – 3,3; Ga – 12; Te – 1,8; As – 4,5.

It is real values for phasons. For example, minimal size of tin drops, which fly from edge after action of strong electrical field [20] ~ 2 nm. In metal alloys [20] structural defects have analogous sizes: in Cu+Au – 1,5 nm, in Au+Pd – (2–3) nm, in Cu+Al – 2 nm, in Fe+Al – (4–5) nm. For evaporating in vacuum films Ti–Si–B–N [20] size of centers is 2–4 nm.

According to this model we can explain size and chemical composition of nanostructures, which are created after laser irradiation GaAs by pulse of second harmonic Neodymium-laser (Fig. 4.11) [16]. Pulse duration 15 ns.

The results from Fig. 4.1 may be explained in next way. Sizes of nanohills near basis are ~200 nm. This result is coordinated with estimations of sizes of crystallization centers according to cascade model [2]. However, according to Kapayev-Kopayev-Molotkov theory [4] and Prinsloo-Lee experimental data [4] arsenic atoms must be placed on the tops of nanohills. According to Stafeev model pure precipitate of arsenic has diameter 4,5 nm, therefore polyphazons, which is enriched of arsenic atoms, are created on tops of nanohills. Gallium phasons have sizes 12 nm, therefore it generation more possible near surface of crystal [2].

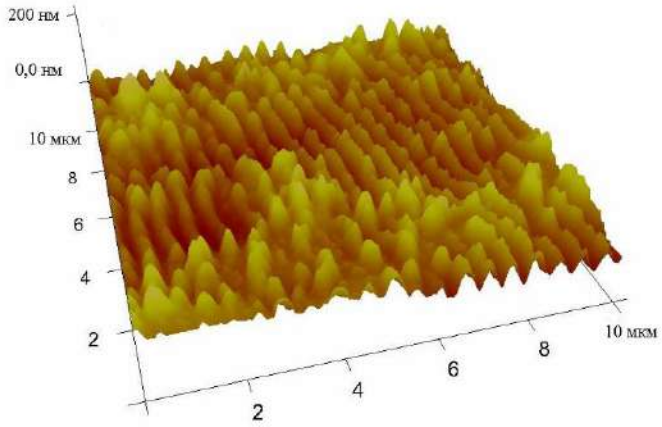

Fig 4.1: AFM 3D image of GaAs surface after irradiation by YAG:Nd laser at I=5.5 MW/cm^2 [16]

Ice phasons in water

Electrochemical potential of ice is less as in water [20], therefore ice phasons in water will have positive electrical charge.

For temperature 20^{o}C junction difference of potentials ice and water is equaled 15 meV, therefore size of phason d_o = 3 nm, number of molecules 400 – 500. According to experimental data [162], water have fluctuation of density with minimal size 3 nm, that practically is corresponded to our estimation. According to [20] for temperature 0^{o}C one electrical charge belong to claster with $3 \cdot 10^7$ water molecules, it correspond of phason size d_o = 100 nm. According to value $\varepsilon\varphi$ from [20] quantity d_o = 6,1 nm [162] much less from experimental, therefore estimated in [20] value of difference of electrochemical potentials in this thermal region is value-added. Naturally phasons may be united in multicharged polyphasons.

Water density ρ has maximal value for temperature ~ 4°C. It decrease for decreasing and increasing of temperature (Fig. 4.2).

Ice density ρ_l is less as water density, therefore increasing of quantity of water molecules in ice phasons will be compensate the increasing of density more thick phase. Thermal dependence of his thick phase may estimate with help extrapolation of the thermal dependence of water density from region of high temperatures, another words "normal" thermal dependency, in region of low temperature. In Fig. 4.2 it is represented the line ρ_o. Thermal dependency of density of ice centers ρ_l may be received with help extrapolation of ice density from region of low temperatures (less as 0°C). Part of ice-similar phase $\delta = (\rho_0 - \rho)/(\rho_0 - \rho_l)$.

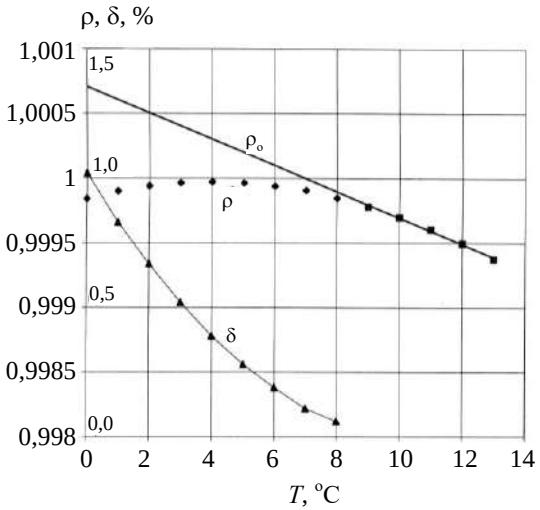

Fig 4.2: Dependence from temperature the water density ρ and part of ice-similar phase δ [20]

Estimated with help of this method thermal dependency of part of ice-similar phase is represented in Fig. 4.2 (curve δ). It is lesser as estimating value in [20] and decreases with increasing of temperature.

For drawing to frozen temperature quantity and sizes of ice phasons are increased and its proportion for temperature 0°C is near one percent. Therefore, concentration of phasons with size $d_o \sim 100\ nm$ is equaled $N_f \approx 10^{13}\ cm^{-3}$. A concentration of hydrogen ions for this temperature $-N_H = 1{,}8 \cdot 10^{13}\ cm^{-3}$. So, near half hydrogen ions in water are included in phasons of ice centers.

In water after melting polyphasons of ice are existed in quantity, which is much large as in thermodynamical equilibrium state. It may be stipulated the special properties of melting water, which are disappeared after 15-20 hours [20].

Difference of electrical potentials that appear under phase transition water-ice firstly was investigated be Vorkman and Reynolds [20]. In pure distillated water between ice and electrode, which is placed on distance ~0,5 cm, difference of electrical potentials near to 60 V in water is observed, moreover ice charging positively. This difference is depended from type of dissolved ions and may be change sign from positive to negative. For example, in water solution with ~10^{-7} M NH_4SO_4 is appeared the difference of potentials more as 200 V. For dissolution HCl in water ice grasp only ions H^+. With increasing of concentrations of dissolved materials appearing difference of potentials is decreased. Next admission was made [20]: large electrical charging complexes are condensed on surface of layer growing ice. One ion is place in $3 \cdot 10^7$ water molecules.

According to model in [20], in process of freezing of water on cooling surface may be condensate charging ice phasons. Therefore, our surface is charged comparatively to water. Electrochemical potential of ice is less as pure water; therefore, ice phasons and surface of ice have positive charge. When velocity of growing the ice layer is 1 μm/s and phason size – 100 nm 10^{11} single charged ice phasons are condenced on square 1 cm^2, that cause the appearance of electrical current $I = 10^{11}$ q/c = $1{,}6 \cdot 10^{-8}$ A. This current is caused the generation of electrical field $E = I\sigma^{-1}$. In pure water $\sigma = 1{,}6 \cdot 10^{-8}$ $(Ohm \cdot cm)^{-1}$, therefore generating electrical field has value E ~ 1 V/cm; for ice $\sigma = 1{,}9 \cdot 10^{-10}$ $(Ohm \cdot cm)^{-1}$, therefore E ~ 80 V/cm.

Dissolved in water materials practically aren't grasped of ice clasters, therefore the difference of electrochemical potentials ice-water will be depend from type of dissolved impurity and its concentration. Accordingly, appearing on border of growing ice the difference of potentials will be depend from value pH of solution up to change of it sign.

Heat capacity**.** An appearance of ice phasons is accompanied of separation of energy of phase transition water-ice and of absorption of energy, which is necessary for the formation of charged polyphasons in water. It may be estimated from the comparison of value of heat capacity C_p near temperature 0°C and it extrapolated value with region of temperatures 15–20°C, in which role of ice phasons is neglicted (Fig. 4.3) [20].

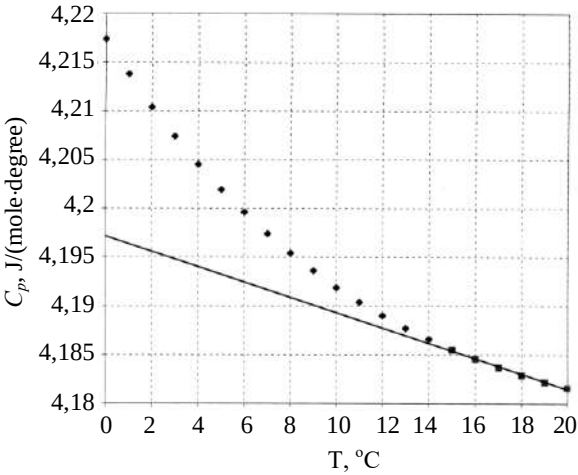

Fig 4.3: Dependence of heat capacity from temperature [20]

Estimated additional heat capacity under temperature 0°C is equaled ~$2 \cdot 10^{-3}$ *J/g·grad*. Proper value of hiding heat of creation ice polyphasons in water is next

$$Q = \Delta C_p (\Delta\delta / \Delta T)^{-1}. \quad (4.1)$$

Under 0°C it is ~$2 \cdot 10^{-3}$ *J/g·grad*. Under 0°C Q~11 J/g, in region of temperatures (3–7) °C Q~8,5 J/g.

Thermoelectrical and electrogravitational effects [20]. Positive charged ice polyphasons in electrical field E are displaced from anodic region (region of it birth with separation of energy Q) to catodic region (region of it melting with absorption of energy Q). In this fielg energy $Q_f = \mu E \delta \rho_l Q S$ is transmitted. In stationary conditions heat flow is balanced of heat capacity $\lambda S dT/dx$, where λ – coefficient of heat capacity of water, S – square. Appeared thermal gradient $dT/dx \sim \mu E \delta \rho_l Q / \lambda$. Under T = 0°C thermal gradient is appeared in water $dT/dx \sim 4 \cdot 10^{-4} E$ K/*cm*, under temperature 8°C it decrease approximately on order.

Flow of polyphasons is formatted in water under presence in water thermal gradient, it create electrical current $qD\{\partial(mN_f)/\partial T\} \times dT/dx$, which is balanced of current of conductivity σE. Appeared electrical field $E = \{qD\partial(mN_f)/\partial T\}\sigma^{-1} dT/dx$.

In pure water under temperature ~0 °C σ ~$1{,}5 \cdot 10^{-8}$ $(Ohm \cdot cm)^{-1}$, therefore $E \sim 4 \cdot 10^{-7} dT/dx$ *V/cm*, if conductivity is determined of phasons only then $E = (kT/q) \times \{\partial(mN_f)/\partial T\}(mN_f)^{-1} dT/dx$.

For location of cooling zone adown in gravitational field ice polyphasons in water are moved upwards, that is caused of appearance of difference of electrical potentials. It is electrogravitational effect.

Water phasons in air [20]. Energy of affinity to electron of molecules H_2O in air is equaled 0,9 *eV*, therefore water and ice phasons will be have negative charge. Under room temperature d_o~4 *nm*, μ~0,26 $cm^2/V{\cdot}s$. Near negative charged surface of Earth electrical field is equaled ~130 *V*/*m*. Negative charged polyphasons in this field must rise up against to gravitational force with velocity ~0,3 *cm*/*s*. It are hanged in air under sizes ~1 *μm* and charge ~250 *q*, that is corresponded to sizes of mist drops. Energy of affinity of molecule H_2O to proton H^+ w = 7,23 *eV*, therefore phasons of oxonium (H_3O) in air will be have positive charge, diameter ~0,5 *nm* and mobility ~2 $cm^2/V{\cdot}s$. In electrical field of earth it be move down with velocity ~2,6 *cm*/*s*.

Electrical conductivity of dielectrical liquids is determined of own phasons [20]. Phasonic mechanism of electrical conductivity, unlike to ionic, isn't corresponded to irreversible chemical modifications. Phasons, which is carried charge, generating and without observing changes of material. Under ionic mechanism of conductivity to one charge is corresponded one "portable" molecule. Phasonic mechanism of run of current is accompanied the displacement of macroquantities of matter. Phason with one electrical charge is included hundreds, thousands and millions molecules. A creation of polyphasons is caused the increasing of quantity of materials, which is carried of unit electrical charge proportionally to square of number its charges. This fact is interpreted as change of step of dissociation of molecules.

In pure water near temperature of freezing a contribution of ice phasons in electroconductivity is 1% and hasn't observable value.

Luminary carrying of materials is realized under small electrical currents. A division of liquid on channels with liquids flows in opposite directions is realized after increasing current density. Charging phasons is moved in ones channels, basic part of liquid with opposite charge is moved in another channels in opposite directions.

After increasing of electrical field the velocity of polyphason motion is increased and flow is transformed to turbulence with creation of "curls". This phenomenon is corresponded to liquid crystals.

Liquid crystals. Basic peculiarities of phenomena in the region of phase transitions are clearly represented for liquid crystals [20].

Thermal dependence of current under stable electrical voltage 95 *V* is

represented in Fig. 4.4a [20]. Centers of low temperature phase of cholesterylcaprylate in decan have more large density in comparative to liquid phase, therefore under cooling it lower after action of gravitational forces. Phasons are charged and its motion is caused the electrical current and appearance of difference of potentials with opposite polarity to applied voltage. In region of phase transition current flows against to external voltage.

In Fig. 4.4b) thermal dependence of "discharged" current that appear in layer under cooling (curve *a*, Fig. 4b*)* and after heating (curve b, Fig. 4b*)* without external voltage. In region of phase transitions strong surges of current are observed: under cooling in one side and under heating in opposite side.

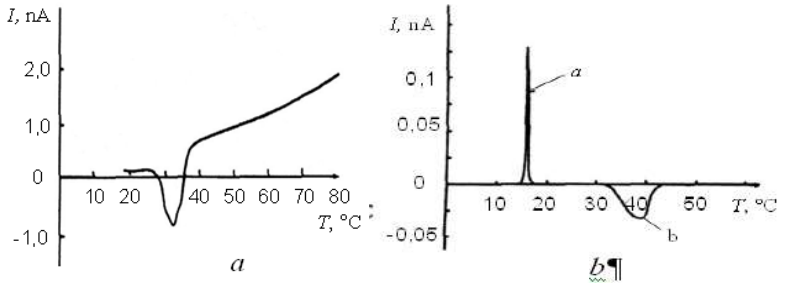

Fig 4.4: Thermal dependence of current: *a* – for stable external voltage 95 *V*; *b* – discharged under cooling and heating of layer EBBA [20]

Phasons of low thermal phase are created and lowered in volume and it cause electrical current. Under increasing of temperature phasons of liquid phase are surfaced and caused electrical current of back direction. Full quantities of charges that created under cooling and heating are equaled approximately. Last result proofs the equivalence of phasons sizes. Under heating rate of creation is less because phasons are created on surface, but under cooling – in all volume of liquid phase. This fact is determined various forms of discharged curves.

Phasons of cholesterylcaprylate in 0,8*N* solution in decan hang under voltage 5 *V* in layer with depth ~1 *mm* [20]. According to these data relation of carrying charge to phason mass is equaled $2{,}5 \cdot 10^{-7}$ *C/g*. Thus, size of phasons of this material in decan is $d \sim 1$ *μm*. In region of phase transitions centers of low temperature phase are observed. It causes the scattering of light in visible spectral range – "blue" liquid crystals, another words phasons have sizes ~1 *μm*. Electric constant of decan $\varepsilon \sim 2$, therefore estimated value $\varphi \sim 2$ *mV*, if growing centers are one-charged phasons.

In pure dialectical liquids own electroconductivity is determined of own

phasons. In the region of phase transition quantity of phasons is increased sharply that explain the jumps of electroconductivity, viscosity and breach of Valden-Pisarzhevski law [20].

Photon crystals. Spherical particles of amorphous SiO_2 are created on the basis the reaction hydrolysis of tetraether of orthosilicon acid (tetraetaxilan $Si(OC_2H_5)_4$) in ethanol (C_2H_5OH) in presence of hydroxide of ammonia (NH_4OH) [20]. At first stage spherical particles with sizes ~5 nm are created, it format amorphous spherical particles with sizes in borders 200 – 600 nm. Standard size of particles is 260 nm. Average scatter is ~ 3 % [20].

Spherical particles SiO_2 with sizes ~5 nm is phasons of molecules SiO_2. On the sizes of spherical particles we can estimate the quantity $\varepsilon\varphi = 3{,}6/d_0$ ~0,7 mV under $\varepsilon = 1$ for phason of molecule SiO_2. Spherical particles, which are generated by phasons of molecules SiO_2, will be have the quantity $\varepsilon\varphi$ in corresponding times less, another words for $\varepsilon = 1$ $\varphi \approx 14$ mV. Since $\varepsilon\varphi$ has small value therefore these large particles are formatted relatively slowly as phasons of fullerenes.

Phasons of biological objects. Any biological object is organic phase in proper environment. Under investigations of microobjects, including biological, we often postulate that these objects are electrical neutral [20]. But really in biological objects microcomponents have negative charge with number of carriers q to few tens [20]. These properties are used for its separation with help of method of electrophoreses.

Minimal biological objects are viruses. Minimal sizes are existed for various viruses: 24 nm (virus of tobacco mosaics), 28 nm (viruses of poliomyelitis, yellow mosaics of turnip a.o.). It have, as rule, spherical form. Therefore, these viruses may be represented as elementary biological phasons with unitary electrical charge in environment with electric constant $\varepsilon = 1$. Under it sizes we can estimate energy of affinity of viruses– w ~ 130–150 meV. A Relationship to proton of organic molecules is equaled few electron-volts, which is corresponded of size of separate little molecules, another words much less as size of virus. Therefore, energy of affinity of viruses is relationship to electron and viruses in air must have negative charge.

Biological objects with size to 1 μm must be charged negatively and carried charge of few decathlons q, these results are observed experimentally [20].

For room temperature virus mobility in air μ~0,04 $cm^2/V{\cdot}s$, diffusive coefficient $D \sim 10^{-3}$ cm^2/s. Near to surface of Earth electrical field is equaled

~130 V/m, therefore viruses will be move to up from it surface with velocity 1,5 m/hour. It is favored of some clearance of lower layers of atmosphere from biological and other microobjects with sizes less as few hundreds nanometers. It go to cosmos and decrease it negative charge.

Electrical currents. Since all objects are charged therefore it motion must be accompanied of electrical current and appearance of proper magnetic field.

Biologic object with size ~10 cm will be carried electrical charge 10^{-12} C in air. Under motion with velocity (30-40) km/hour a flock with thousands of these objects is created electrical current ~1 μA. Existing electromagnetic field is performed regulative role under motion of flock.

A blood has charge relatively to walls of blood vessels, therefore it flow must be performed of electrical current and proper electromagnetic field. Respectively external magnetic field must be acted on blood flow and motion of its microparticles (erythrocytes a.o.). May be it cause to magnetic- and meteosensitivity of peoples and other living organisms.

Electrochemical potentials of water and surrounding of it coasts are various, therefore on its borders junction difference of potentials are existed that depend from PH water. Water must be charged. Therefore current of river, including underground, must accompany of electromagnetic field. May be exactly electromagnetic field of underground water flows allow to search it by help of dowsers.

Water surface must be charged relatively to air. Surface density of electrical charges is 10^{-9} C/m^2. Therefore, waves and flows of water must generated electromagnetic fields. Exactly warm currents as Holfstrem, Kurosivo a.o. [20] are charged relatively to surrounding cooler environment. Therefore, these colossal flows are surrounded of electromagnetic field. Flows of sea water, which are caused with rotation of Earth and attraction of Sun and Moon, must surround of electromagnetic field too.

Great quantity of dusting particles is fallen on Earth from cosmos. Since it must be charged therefore these flows are surrounded of electrical current and proper electromagnetic field. It must influence on atmosphere phenomena.

Plasma crystals [20]. In free environment materials may have forms of atoms, molecules, clusters and as particles of condensed matter phase. In generally this set of particles must be neutral. If it is consisted with various materials or various phases, then its components must be electrical charged because these components have various quantity of relationship to electron (proton) or various electrochemical potentials. This set of particles and

molecules is created quasineutral plasma. Phasons in free “cool” dusting plasma are charged and in some conditions can format similar to crystal structures with lattice number, which is caused of electrical charges of phasons of this material. Now we have “plasmic crystals”. For example, in [20] "dusting plasma" was formatted from spheres of borosilicon glass with sizes 50-63 μm and estimated electrical charge ~$7 \cdot 10^5$ q. Elementary one-charged phason of this material must be have size ~1 nm and quantity φ ~ 4-5 V. These phasons were created ranked structures with lattice number ~300 μm.

Dusting clouds in cosmic space are consisted from particles with little sizes. It must be electrical charged; therefore, external electrical and magnetic fields must be influenced on proper phenomena. It is related to dusting tails of comets too.

Thus, Vitaliy Stafeev theory of phasons is “electrostatic” addition to other theories of nucleation.

4.3 Cascade models of step-on-step excitation of proper chemical bonds in the regime of saturation the excitation

We can use direct crystal chemical methods of calculation for problems of nucleatization and crystallization too.

The profiles of the distribution the photostimulated donor centers in subsurface layers InSb and *InAs* are represented in Fig. 4.5 [4].

The samples of p-type conductivity are irradiated. For intensity of irradiation $I_0 > 0{,}01$ $J \cdot cm^{-2}$ for *InSb* and $I_0 > 0{,}012$ $J \cdot cm^{-2}$ for *InAs* the n-layers on p-type materials are created. For intensity of irradiation $I_0 < 0{,}1$ $J \cdot cm^{-2}$ for *InSb* and $I_0 < 0{,}16$ $J \cdot cm^{-2}$ for *InAs* the profiles of the distribution of donor centers are represented the Buger-Lambert law (law of absorption the light in homogeneous media). For further increasing the irradiated intensity the profiles of the concentration donor centers have diffusion nature. The visible destruction of the irradiated semiconductor melting, the change of the surface color) had place for $I_0 > 0{,}3$ $J \cdot cm^{-2}$ for *InSb* and $I_0 > 0{,}5$ $J \cdot cm^{-2}$ for *InAs*. This effect has oriental character (Fig. 4.6) [4]. For crystallographic direction {111} the process of the creation damages is more effective as for direction {110}.

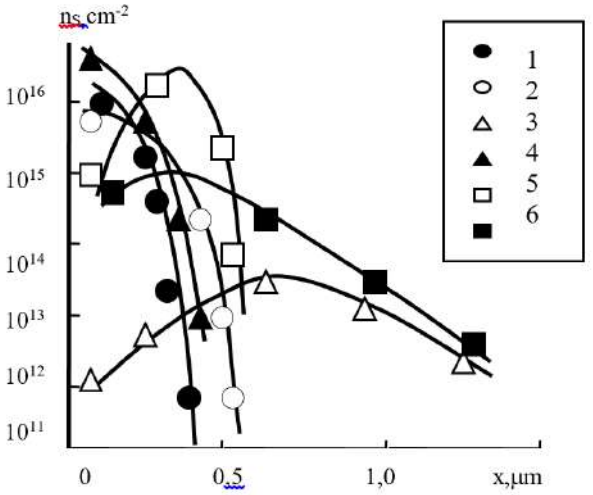

Fig 4.5: The profiles the distribution the layer concentration of the donor centers in inverse layers *InSb* and *InAs* after ruby laser irradiation with various density of energy (monoimpulse regime): 0,07 (1); 0,1 (2); 0,16 (3); 0,16 (4); 0,25 (5); 0,5 J·cm^{-2} (6). 1-3 – *InSb*, 4-6 – *InAs* [4]

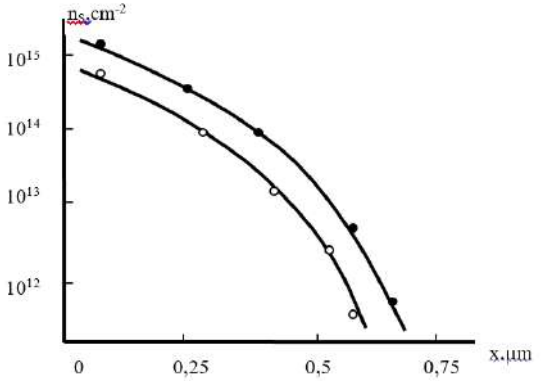

Fig 4.6: The oriental effect of the creation ruby laser stimulated damages in *InSb*: – {111}; - {110}; I_0 =0,1 *J·cm*$^{-2}$ [4]

Analogous results were received for the indium arsenide too. Time and energy characteristics of processes on Fig. 4.5 may be estimated with the help of next way. In further we'll use two-dimensional representation of crystal lattice *InSb* (Fig.4.7). Bond 1 is corresponded to band gap and has value 0,18 *eV*, bond 2 – 1,95 *eV* and bond 3 – 2,15 *eV* [4]. For *InAs* bond 1 has value 0,36 *eV*, bond 2 – 3,8 *eV* and bond 3 – 4,2 *eV* [4].

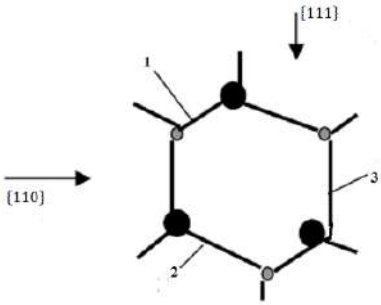

Fig 4.7: Two-dimensional picture the crystal lattice A_3B_5 (including *InSb* and *InAs*) the cubic symmetry. Bond 1 is pure covalent [4]

Method of the estimation of level of saturated excitation of proper chemical bonds may be used for the selection of optimal regime for optical pumping of semiconductor laser [4] and for creation stable *n–p*-junctions on semiconductors [4] and for the creation layers with new phases, including nanostructures [4].

For these crystals the energy of these bonds are equaled the energy of band gap E_g (0,18 *eV* for *InSb* and 0,36 *eV* for *InAs* at room temperature). On Fig. 7 this bond is signed as 1. For this bond ions *In* and *Sb* (or *In* and *As*) are placed on minimal distance (the sum of proper covalent radiuses). Other chemical bonds in this crystal symmetry have more long sizes. With geometrical point of view in crystal direction {111} the cross section of effective interaction the light quantum with bond 1 is more effective than for direction {110}. The angle among bond 1 and direction {110} is 37,5°. Quanta of ruby laser in linear regime of the irradiation are not interacted with another bonds practically because it energies are less than energy of this bond. The correlation of effective square of bond 1 for directions {110} and {111} is explained the proper experimental data (oriental effect of creation donor centers see Fig. 4.6).

Energy density, which was required for the excitation of “band gap” bonds, is equalled

$$E_1 = 2h\nu \frac{3}{4\pi r_k^3}, \qquad (4.2)$$

factor 2 is included the large reflection of irradiation from surface of indium antimonite. For *InSb* $E_1 = 8.6\ {}^{J}/_{cm^3}$. Next phase of excitation is the ionization second valence bonds with energy 1,95 *eV* (for two-dimensional representation of crystal lattice *InSb*, Fig. 7). With including first processes $r_{k_2} \approx 0.45\ nm$ for our second process. Therefore,

$$E_2 = 2h\nu \frac{3}{4\pi r_{k_2}^3} \quad (4.3)$$

For *InSb* $E_2 = 1510 {}^{J}/_{cm^3}$. After including the depth of irradiated layer (from 0,2 μm to 0,6 μm) the diapason of change energy intensity is next: from $E_{1s} = 8.6 \cdot 10^{-5} {}^{J}/_{cm^2}$ to $E_{2s} = 0.03 {}^{J}/_{cm^2}$. Further increasing of intensity the radiation lead to the ionization third valent bond with energy 2,15 *eV*. The regime of saturation of its excitation lead to the melting of irradiated semiconductor. For the *InSb* this value is $E_{3s} = 0.16 {}^{J}/_{cm^2}$.

Straight method of the estimation the energetic characteristics this processes may be realized in the next way. Energy of "disruption" of chemical bonds of one type is equalled

$$E_{di} = N_i E_i, \quad (4.4)$$

where N_i – a density of proper bonds; E_i – energy of a disruption (ionization) one bond.

For the $InSb$ $N_1 = N_2 = N_3 = {N_0}/{2}$ and are equaled $1.4 \cdot 10^{22} cm^{-3}$, $E_1 = E_g = 0.18\, eV$ and therefore $E_{d1} = N_1 E_g = 403.2 {}^{J}/_{cm^3}$ and $E_{d2} = N_2 E_2 = 4368 {}^{J}/_{cm^3}$. Surface density of irradiation may be determined with the help of next formula [3, 4]

$$E_{sis} = \frac{E_{di}}{\alpha_i}, \quad (4.5)$$

where α_i – proper absorption factor, for the first bonds of *InSb* $\alpha_1 = 2 \cdot 10^5 cm^{-1}$, for second – $\alpha_2 \sim 10^5 cm^{-1}$. Second absorption factor is nonlinear and take into account the effect of blooming. For *InSb* these values are next E_{s1s} =0.002 ${}^{J}/_{cm^2}$ and E_{s2s} =0.04368 ${}^{J}/_{cm^2}$. These values must be multiplied on 2 (with including reflection) and therefore real values are next E_{s1sr} =0.004 ${}^{J}/_{cm^2}$, E_{s2sr} =0.08797 ${}^{J}/_{cm^2}$ and $E_{\Sigma r(2)} \approx 0.092 {}^{J}/_{cm^2}$. Energy of "disruption" of third chemical bonds (Fig.4.4) is equaled $E_{d3} = N_3 E_3 = 4816 {}^{J}/_{cm^3}$. If $\alpha_3 \sim 10^5 cm^{-1}$ we have E_{s2s} =0.04816 ${}^{J}/_{cm^2}$ and E_{s3sr} =0.096 ${}^{J}/_{cm^2}$. Summary surface density of energy of three bonds is equaled $E_{\Sigma r(3)} \approx 0.188 {}^{J}/_{cm^2}$. Value $E_{\Sigma r(2)} \approx 0.092 {}^{J}/_{cm^2}$ is represented of curve 2 on Fig.4.5 and $E_{\Sigma r(3)} \approx 0.188 {}^{J}/_{cm^2}$ – curve 3 on Fig. 4.5.

Large difference between estimations of cascade and straight methods is caused of neglect or real geometry of "photon" zone and the disruption of "selected" bonds only. But cascade approximation may be used for the estimation of process of the formation wave zone. An eclipse of "photon" zones is the beginning of the formation wave zone. Practically minimal value $E_{1sr} = 8.6 \cdot 10^{-5}\ {}^{J}/_{cm^3}$ for $InSb$ is the threshold for the formation of various electromagnetic wave oscillations, including plasmic. This value may be represented as maximal value of optical pumping for the receiving laser generation with $h\nu = E_g = 0.18\ eV$ in *InSb* and $E_g = 0.36\ eV$ in *InAs*. For *InAs* $E_{1srInAs} \sim 1.8 E_{1srInSb}$ [4].

It should be noted that light absorption mechanisms play an important role in the formation of crystalline phases. Thus, the irradiation of unalloyed antimonite and indium arsenide with the radiation of a pulsed neodymium and ruby laser leads to the formation of donor layers and a decrease in the symmetry of the starting material. Therefore, this radiation is not suitable for annealing ion-implanted layers of these materials [4, 31, 32, 39].

The fact is that this radiation leads to phase modifications of the pure material. The use of CO_2 laser radiation leads to annealing of defects and crystallization of ion-implanted layers. Moreover, the irradiation modes (impulse or stationary) do not matter, the main role is played by the integral dose. That is, in this case, we have photochemical processes [4, 32].

Now we show the using of cascade model for the explanation experimental data of laser-induced phase transformations in silicon, germanium, carbon and titanium. It was called as case the structural phases [2].

Now we represent some experimental data.

The AFM picture of Ge surface after Nd laser irradiation is represented in Fig. 4.8 [114].

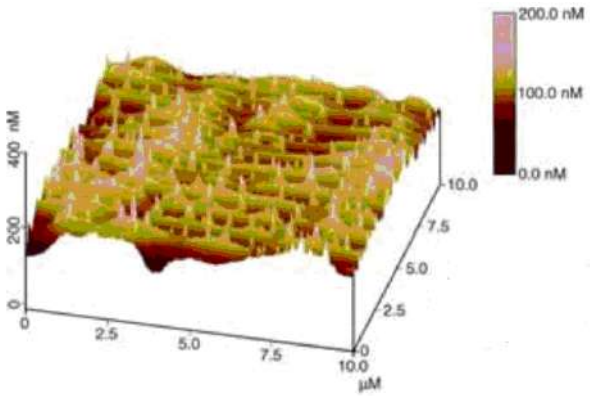

Fig 4.8: Three-dimensional AFM image of nanostructures after Nd:YAG laser irradiation with density of power 28 MW/cm^2 on *Ge* surface [114]

More large columns (height 20 μm, diameter 2 – 3 μm) were received after irradiation of pulse series the nanosecond eximer KrF-laser (wavelength 248 *nm*, pulse duration 25 *ns*) (Fig. 4.9). This figure illustrates the high aspect ratio silicon micro-columns that were formed in air after 1000 laser shots at an energy density, E_d, between 2.7 and 3.3 J/cm^2. The columns are ~20 μm long and ~2~3 μm in diameter. Moreover, surface-height profilometry performed using a Dektak II profiler revealed that most of the length of the microcolumns, 10 – 15 μm, protrudes above the original Si surface [129].

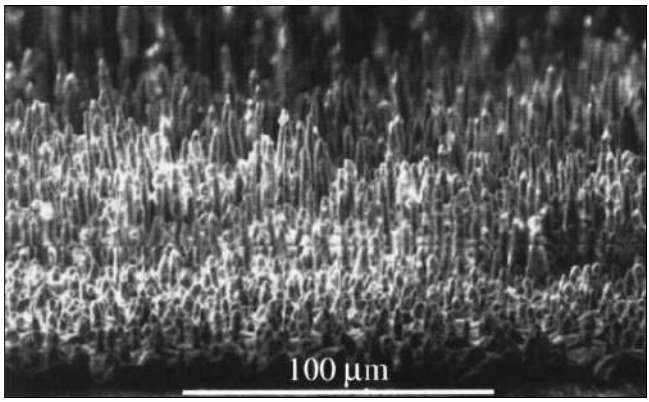

Fig 4.9: SEM images of silicon microcolumns after 1000 laser shots in air at $E_d = 3 J/cm^2$ [129]

The microcolumn morphology changes if the atmosphere is changed during laser irradiation. Fig. 4.10 shows several columns in a specimen that was first irradiated with 600 pulses in air and 1200 pulses in $N_2/5\%O_2$ [129].

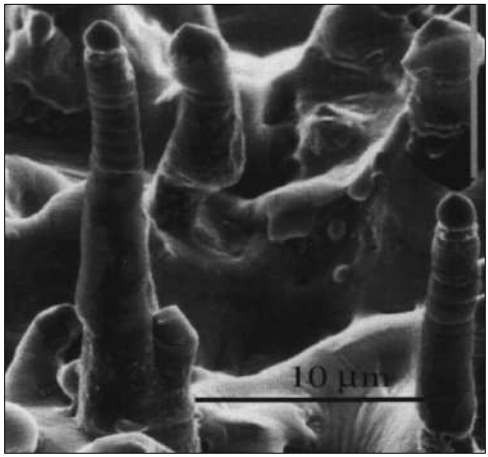

Fig 4.10: SEM image showing a change in *Si* microcolumn morphology con-trolled by the ambient gas composition at E_d 2.7 J/cm^2. The arrows indicate the height achieved after 600 laser pulses in air (N_2 – 18% O_2); the remainder of the columns was grown by 1200 laser pulses in N_2 – 5% O_2 [129]

The importance of the gas environment was emphasized, when a plasma etchant, SF_6, was used as the ambient gas during laser irradiation of silicon [129]. In SF_6 extremely long structures are produced that look at first like walls surrounding very deep central holes (see Fig. 4.11) [129].

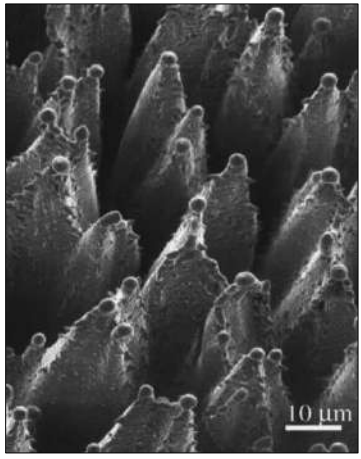

Fig 4.11: Walled Si structure produced by 2040 laser pulses at E_d =1.5 J/cm^2 in 1 atm of SF_6 [129, 130]

Laser-induced silicon nanostructures (λ = 0,8 μm, τ_i = 100 fs, number of pulses 200) with d_3=90 nm, which was generated after irradiation structures

of changing polarization with d_2=120 nm, when orientation of vector $\vec{E}$ was changed on 90° relatively to initial action. Power of laser irradiation was less in two time as for initial structure. Generated periodical structures (Fig. 4.12 and Fig. 4.13) are nanocolumns with height to 400 nm with spatial period 90 nm and orientation wave vector $\vec{g} \parallel \vec{E}$ [109, 157]. Where ğ is beam propagation direction.

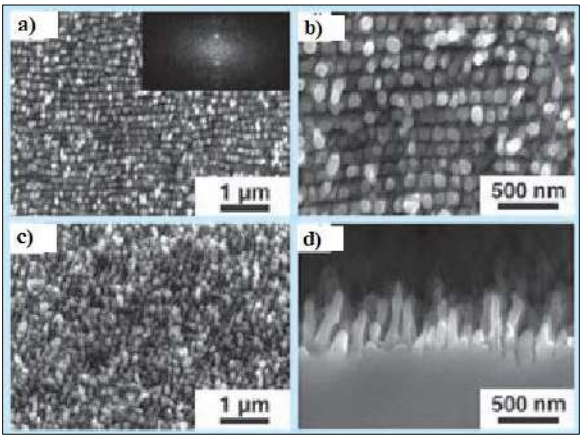

Fig 4.12: Nanocolumns, which are generated after irradiation structures of silicon with d_2=120 nm, (wavelength of irradiation 800 nm, number of pulses – 200, density of energy of irradiation 0,5 kJ/m^2): a) and b) turn of polarization on 90°, c) turn of polarization on 45°, d) cross chip of nanocolumns. On insertion to Fig. 2.8a – Fourier-picture of structures [157]

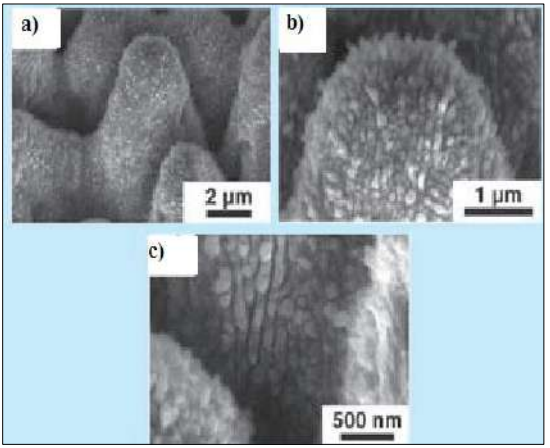

Fig 4.13: Surface silicon nanocolumns of little scale, which have orthogonal orientation to a crests of nanorelief of large scale [157]

An influence of pulses number on the processes of formation of laser-induced periodic nanostructures on titanium plate is observed in [207]. Sapphire laser system was used for the irradiation. It had next parameters: wavelength 800 nm, repetition rate 1 *kHz*, pulse length 100 *fs*, beam diameter 4 mm and density of energy of irradiation 0,25; 0,75 and 1,5 J/cm^2. Interference structures are generated for the irradiation with energy density 0,25 *J*/*cm*^{2} [207]. Evolution of creation laser-induced surface structures are represented in Fig. 4.14.

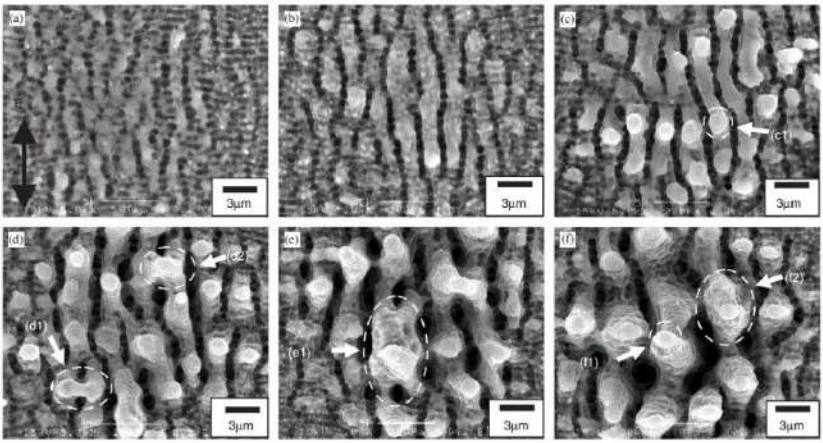

Fig 4.14: Microstructures produced on the titanium plate at the laser fluence of 0.75 J/cm^2 for (a) 10, (b) 25, (c) 50, (d) 70, (e) 90 and (f) 110 pulses [207]

The period of the parallel periodic microstructures as a function of the number of laser pulses is shown in Fig. 4.15 [207].

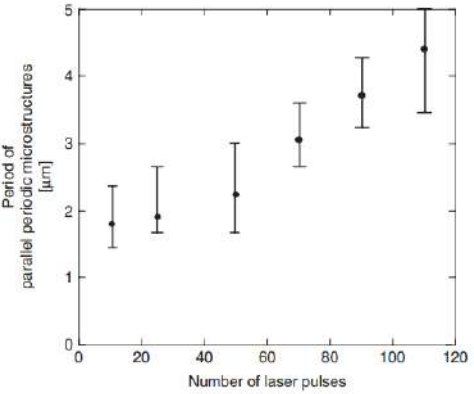

Fig 4.15: Period of parallel periodic microstructures as a function of number of laser pulses [207]

The question about the influence of saturation of excitation on effects of Relaxed Optics may be represented as process of transitions between stable and metastable phases too. Now we'll estimate the influence of parameters of irradiation (including spectral) on irreversible changes and transformations in *Si* and *Ge*. Spectral dependences of absorbance of various structural modification of *Si* are represented in [2-6]. Now we'll be estimated intensities of eximer, Ruby and Neodymium laser irradiation (wavelengths of irradiation are 0,248 μm, 0,69 μm and 1,06 μm properly of silicon and germanium, which are necessary for the creation of proper irreversible changes in irradiated semiconductor. As shown in [4], absorbance of the Neodimium laser radiation in silicon is equaled 100 cm^{-1}, second harmonic of Neodimium laser – 10^4 cm^{-1}, eximer laser – 10^6 cm^{-1}.

Crystal semiconductors *Si* and *Ge* have, basically, the structure of diamond. Volume atomic density of elementary lattices may estimate according to formula [19]

$$N_a = \frac{\rho N_A}{A}, \quad (4.6)$$

where ρ – density of semiconductor, N_A – Avogadro number, A – a weight of one gram-atom. For *Si* $N_{aSi} = 5 \cdot 10^{22} cm^{-3}$, and for *Ge* $N_{aGe} = 4.4 \cdot 10^{22} cm^{-3}$.

But *Si* and *Ge* may be crystallized in lattices with hexagonal, cubic, trigonal and monoclinic symmetry. Phase diagram of Si as function of coordination number is represented on Fig. 4.16 [18].

Coordination number (CN) 8 is corresponded of diamond lattice, CN 6 – hexagonal lattice, (CN) 4 and (CN) 3 – other two lattices. It should be noted that melting temperatures of these phases are various. Volume density of CN is equaled $CN \cdot N_a$. For diamond symmetry of lattice this value is $8N_a$. In other words, a change in the coordination number is not necessarily related to a change in type of crystal syngonia. Thus, the coordination numbers 8 and 6 can correspond to two different cubic symmetries, and at the same time, CN 6 corresponds to hexagonal syngonia [40], which corresponds to the corresponding experimental data [2, 4].

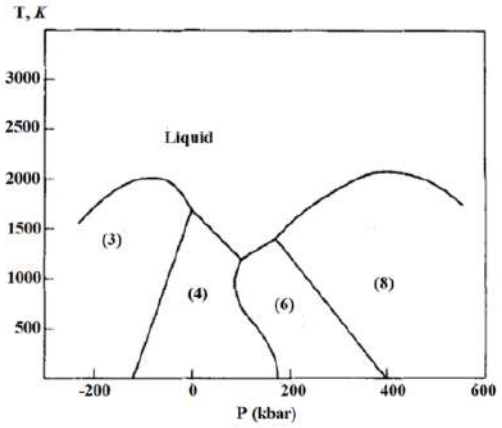

Fig 4.16: A schematic phase diagram for *Si*(CN). The coordination numbers (CN) of the various phases are indicated. The diagram is based on common features of the phase diagrams of column IV elements as described by the references cited in Pistorius's review (Ref. 8 in [18]). Starting from a high temperature $>3\times10^3$K and subject to a constraint of average density $\langle\rho\rangle = \rho(4)$, a hot micronucleus will tend to bifurcate into the most stable phases (highest T_m) which straddle *Si*(4) in density. These are *Si*(3) and *Si*(8), as indicated by the diagram [18]

Roughly speaking, transition from one phase to another for regime of saturation of excitation may be modeled as one-time breakage of proper numbers of chemical bonds, which are corresponded to the difference of CN of proper phases. For example, two bonds breakage is caused the phase transition from diamond to hexagonal structure. One bond breakage in the regime of saturation is caused to generation of laser radiation.

Results of calculation of volume densities of energy, which are necessary for breakage of proper number of bonds in regime of saturation of excitation, are represented in Table 4.1. [4]

Table 4.1: Volume density of energy I_{vi} (10^3 J/cm^3), which is necessary for the breakage of proper number of chemical bonds in the regime of saturation of excitation in *Si* and *Ge*

	I_{v1}	I_{v2}	I_{v4}	I_{v5}
Si	12,8 – 14,4	25,6 – 28,8	51,2 – 57,6	63 – 72
Ge	6,3 – 8,4	12,6 – 16,8	25,2 – 33,6	31,5 – 42

It conceded that energies of all chemical bonds for elementary lattice are equivalent (*Si* and *Ge* are pure homeopolar semiconductors) [19]. For silicon energy of covalent bonds *Si-Si* are equaled 1,2–1,8 *eV*; for germanium energy

of covalent bonds *Ge–Ge* are equaled 0,9–1,6 *eV* [2, 4]. Minimal values of these energies are corresponded of Pauling estimations. These values are corresponded the energy on one CN: according to radiation physics of status solid Zeits energy of creation one radiation defect in silicon is equal 12,7 *eV* for diamond lattice [39].

Surface density of energy on proper numbers of CN for proper lasers irradiation may receive after division of results of Table 2.3 on proper absorbance. This procedure allows to transit from bulk to surface density of energy, which is necessary for the receiving of proper phenomena. Results of these calculations are represented in Table 2.4.

It should be noted that real regimes of irradiation must be more (process of light reflection wasn't included in our estimations). In addition we aren't include the relaxation (time) processes for the scattering of light on stable centers (self-absorption in crystals) as for *InSb* and *InAs* [174, 194].

Table 4.2: Surface density of energy I_{si} (J/cm^2), which are necessary for the breakage of proper numbers of chemical bonds in *Si* and *Ge* crystals after proper lasers irradiation in regime of saturation the excitation [174, 194]

	I_{s1}	I_{s2}	I_{s4}	I_{s5}
Si, 1,06 μm	128 – 144	256 – 288	512 – 576	630 – 720
Si, 0,53 μm	1,28 – 1,44	2,56 – 2,88	5,12 – 5,76	6,3 – 7,2
Si, 0,248 μm	0,0128 – 0,0144	0,0256 – 0,0288	0,0512 – 0,0576	0,063 – 0,072
Ge, 1,06 μm	0,63 – 0,84	1,26 – 1,68	2,52 – 3,36	3,15 – 4,2
Ge, 0,53 μm	0,32 – 0,42	0,63 – 0,84	1, 26 – 1,68	1,58 – 2,1

Remark to Table 2: absorbencies of *Si* (Neodimium laser) – 100 cm^{-1}; *Si* (second harmonic of Neodimium laser) –10^4 cm^{-1}; *Si* (eximer laser) – 10^6 cm^{-1}. *Ge* (Neodimium laser) –10^4 cm^{-1}; *Ge* (second harmonic of Neodimium laser) – 210^4 cm^{-1}.

Height of surface nanostructures for the nanosecond regime of irradiation is maximal (200 *nm*, Fig.4.8) for the germanium [2] for small number of pulses and for silicon (20 – 50 μm, Fig. 4.9 – Fig. 4.11) for large number of pulses [7, 8]. For the silicon (Fig. 2.2) height of laser-generated surface nanostructures is change from 10 nm to 20 nm. This difference can be explained in next way. Index of light absorption with wavelength 532 nm of Ge crystal with diamond symmetry is more as silicon with this symmetry for the nanosecond irradiation. However, surface part of irradiated germanium is transited to hexagonal phase. It is experimental data. Other result given's phase

transitions. The hexagonal lattice of germanium has greater size as diamond modification. Therefore, hexagonal nanostructures are greater and more stable as polycrystalline or metallic nanohills.

The qualitative explanation of possible mechanisms of creation microcolumns or nanohills may be determined with help next model. We can determine the change of the height and volume of corresponding structural unit on pulse. This procedure may be used for the comparative regimes of irradiation. Now we are demonstrated this method for silicon. Results of these estimations are represented in Table 4.3 and Table 4.4.

Table 4.3: Geometrical characteristics of laser-induced surface structures (microcolumns and nanohills)

Material	**λ_{ir}, *nm***	**Height**	**V_{con}**	**V_{cyl}**	**ΔV_{con}**	**ΔV_{cyl}**	**Ref.**
Ge	1064	200 *nm*	32054 nm^3	31400 nm^3	157 nm^3	160 nm^3	Fig. 4.8
Si	248	30 μm	282,6 μm^3	288,5 μm^3	0,236 μm^3	0,240 μm^3	Fig. 4.9
Si	248	50 μm	11775 μm^3	11343 μm^3	5,77 μm^3	5,56 μm^3	Fig. 4.11
Si	800	400 *nm*	20933 nm^3	22608 nm^3	52,33 nm^3	56,52 nm^3	Fig. 4.12

Table 4.4: Geometrical characteristics of laser-induced surface structures (microcolumns and nanohills). Conic and cylindrical parameters

Material	**λ_{ir}, nm**	**r_{con}**	**r_{cyl}**	**E_{s1}**	**Ref.**
Ge	1064	20 *nm*	10 *nm*	1,32 *pJ*	Fig. 4.8
Si	248	3 μm	1,75 μm	0,76 μJ	Fig. 4.9
Si	248	15 μm	8,5 μm	10,59 μJ	Fig. 4.11
Si	800	7 *nm*	4,25 *nm*	0,076 *pJ*	Fig. 4.12

Energy characteristics of laser-induced surface structures (microcolumns and nanohills) are represented in Table 4.5.

Table 4.5: Energy characteristics of laser-induced surface structures (microcolumns and nanohills)

Material	**λ_{ir}**	**Height**	**E_{con}**	**E_{cyl}**	**ΔE_{con}**	**ΔE_{cyl}**	**Ref.**
Ge	1064	200 *nm*	0,40-0,54 *fJ*	0,40-0,53 *fJ*	0,0020-0,0027 *fJ*	0,0020-0,0026 *fJ*	Fig. 4.8
Si	248	30 μm	7,2-8,1 *nJ*	7,4-8,3 *nJ*	6,0-6,8 *pJ*	6,2-6,9 *pJ*	Fig. 4.9
Si	248	50 μm	0,30-0,34μJ	0,29-0,33μJ	0,15-0,17 *nJ*	0,14-0,16 *nJ*	Fig. 4.11
Si	800	400 *nm*	0,54-0,60 *fJ*	0,58-0,65 *fJ*	0,0013-0,0015 *fJ*	0,0014-0,0016 *fJ*	Fig. 4.12

Mechanisms of creation other laser-induced nanostructures may be explained on the basis cascade model of step-by-step excitation of

corresponding type and number of chemical bonds in the regime of saturation of excitation (Tables 4.1 and 4.2). According to this model decrease of symmetry of irradiated matter is occurred with increase of intensity of irradiation (Nd laser irradiation of silicon, germanium and carbon) [274, 294].

It should be noted that real regimes of irradiation must be more (process of light reflection wasn't included in our estimations). In addition, we aren't include the relaxation (time) processes for the scattering of light on stable centers (self-absorption in crystals) as for *InSb* and *InAs* [4]. For physical-chemical modeling of phase transformations in irradiated materials, it is possible to use such quantities as the energies of formation of the

The lack of study of other crystallographic modifications of silicon compared to the diamond structure is due to the fact that the electronic and optoelectronic industry uses cubic modification and more complex methods of obtaining by more trivial methods of crystallization.

It is also important to estimate the corresponding energies of crystal lattices. Calculation according to the phase diagram Fig. 8 was taken from the value of the energy of defect formation for silicon and germanium. Then it was divided by the coordination number and we got the energy corresponding to one configuration number. This model made it possible to explain the nature of the appearance of hedgehog-like structures on silicon by series of nanosecond pulses with a wavelength of 248 nm [21, 22] and femtosecond pulses with a wavelength of 800 nm [23]. According to the estimates in Table 1, there is a cascade of structures (from bottom to top): cubic, hexagonal, and triclinic symmetry [2]. In this way, we can find out the energy difference per atom in different lattices of crystallographic lattices. The disadvantage of this method is that we assume that all bond energies are the same, which is only true for a diamond-type lattice.

It should be noted that the methods of calculating the energies of defect formation, as well as the energies of the crystal lattice, give certain scatters in the results. So, for example, the value of the energy of defect formation for silicon for a diamond lattice is equal to the sum of eight energies of covalent chemical bonds according to L. Pauling [2-6].

Modeling the change in the number of coordination numbers is a rather complex problem. Since, if in the diamond modification all bond energies are the same, then in other crystallographic modifications this is not the case. Therefore, for more precise calculations, we must use energies of corresponding real crystal lattices [33].

We can introduce criterion of efficiency the using of laser radiation for generation proper structures.

$$\Delta = \frac{E_{con(cyl)}}{E_{s1}} \quad . \tag{4.7}$$

Estimations of data Table 4.3 – Table 4.5 are represented in Table 4.6.

Table 4.6: Efficiency of using the various regimes of laser irradiation for creation proper surface structures

Material	**λ_{ir}**	**Δ_{con}**	**Δ_{cyl}**	**Ref.**
Ge	1064	$3,0\cdot10^{-4}-4,1\cdot10^{-4}$	$3,0\cdot10^{-4}-4,0\cdot10^{-4}$	Fig. 2.3
Si	248	$9,5\cdot10^{-3}-10,6\cdot10^{-3}$	$9,7\cdot10^{-3}-10,9\cdot10^{-3}$	Fig. 2.5
Si	248	$0,028-0,032$	$0,029-0,031$	Fig. 2.6
Si	800	$7,1\cdot10^{-3}-7,9\cdot10^{-3}$	$7,6\cdot10^{-3}-8,6\cdot10^{-3}$	Fig. 2.8

Relative efficiency of using laser irradiation for silicon for various regimes of irradiation may be determined with help next formula

$$\eta = \frac{\Delta V_i}{\Delta V_{\max}}. \tag{4.8}$$

Relative efficiencies for silicon from data of Table 4.6 are represented in Table 4.7.

Table 4.7: Relative efficiencies for silicon from data of Table 2.5

Material	**λ_{ir}**	η_{con}	η_{cyl}	**Ref.**
Si	248	0,0432	0,0409	Fig. 2.5
Si	248	1	1	Fig. 2.6
Si	800	$10,2\cdot10^{-9}$	$9,1\cdot10^{-9}$	Fig. 2.8

On the basis of data of Tables 4.6 and 4.7 we can made next conclusions:

1) Influence of wavelength irradiation on formation the nanohills and microcolumns: radiation of eximer laser is more effective as irradiation with wavelength 800 nm;
2) Oxidation process of irradiated silicon is decreased the speed of generation the surface structures;

3) Speed of generation the surface laser-induced structures is increased with increasing of number the pulses.

4.4 Temperature rise induced by a laser beam [223, 224]

The damage produced by ion-implantation techniques requires annealing of the surface region to restore device-quality crystal perfection. Laser annealing procedures have been found promising. Kachurin *et al.* and Gat *et al.* [103] have developed a continuous-scanning argon ion beam technique. There is considerable interest, therefore, in a solution for the temperature rise induced by a Gaussian laser beam when the scan time is long compared to the time (microseconds) for a steady state to become established. A knowledge of the temperature rise (and its spatial distribution) permits an analysis of solid-state epitaxial regrowth as the mechanism responsible for laser annealing.

Because the thermal conductivity *K(T)* in silicon is reduced by a factor of about 5 at the final elevated temperatures, the ability of heat to flow away from the illuminated region is reduced and the temperature rise is enhanced relative to a linear solution. Thus, it is absolutely essential to solve the *nonlinear* diffusion equation for the temperature rise. In spite of the large nonlinearity, we shall show in this letter that it is possible to obtain a *closed-form* solution of the nonlinear problem that is relatable in a simple manner to our previous solution[5] of the corresponding linear problem.

The temperature *T* obeys the conventional heat equation

$$C\frac{\partial T}{\partial t} = -divJ + G, J = -K(T)\nabla T, \tag{4.9}$$

where *G* is the heat source, *C* is the specific heat, and *J* is the heat flow. We relate this problem to an associated linear problem by introducing a new temperature scale,

$$\Theta(T) = \int_{T_0}^{T} \frac{K(T)}{K_0} dT. \tag{4.10}$$

where T_0 is room temperature (300 °K in our numerical calculations) and $K_0 = K(T_0)$ is the corresponding thermal conductivity. The choice, Eq. (4.10), has been made so that

$$K_0\nabla\Theta(T) = K(T)\nabla T, \Delta\Theta = -\frac{G(r,z))}{K_0} + \frac{C}{K_0}\frac{\partial T}{\partial t}. \tag{4.11}$$

[We have written *G(r,z)* because we are concerned with the case of cylindrical symmetry, but the symmetry is not needed for the arguments made in this letter.] For the stationary case, the last term can be omitted, and 6 obeys the *linear* equation we have previously solved. If we let $\Theta = \Theta(r, z)$ represent this linear solution, then the corresponding solution to the nonlinear problem

may be obtained by inverting Eq. (4.10) to obtain T in terms of Θ. For example, it is approximately true (with $\varepsilon < 1$) that

$$K(T) = K(T_0)\left({}^{T_0}/_{T}\right)^{\varepsilon}, \tag{4.12}$$

so that

$$\Theta(T) = \left({}^{T_0}/_{\varepsilon}\right)\left[1 - \left({}^{T_0}/_{T}\right)^{\varepsilon}\right]. \tag{4.13}$$

The inverse relation is then simply

$$T = T_0\left(1 - {}^{\varepsilon\Theta}/_{T_0}\right)^{-{}^{1}/_{\varepsilon}} \rightarrow T_0 exp\left({}^{\Theta}/_{T_0}\right), \tag{4.14}$$

where the limiting result applies when $\varepsilon \rightarrow 0$. The contours of constant Θ (i.e., constant temperature in the linear case) thus remain the contours of constant temperature T in the nonlinear case. This conclusion does not depend on the particular relations, Eq. (4.12), but is true for any $K(T)$, any geometry, and any heat source distribution.

In [223] we have obtained the solution to the linear problem with a source

$$G(r,z) = \alpha I_0 exp(-\alpha x) f({}^{r}/_{W}). \tag{4.15}$$

[Here $I_0 f({}^{r}/_{W})$ represents the intensity entering the surface corrected for reflectivity.] The solution can be written

$$\Theta(r,z) = \Theta_{max} N(R,Z,W), \tag{4.16}$$

where

$$\Theta_{max} = \frac{P}{2\pi K_0}\left\langle\frac{1}{r}\right\rangle \tag{4.17}$$

would be the maximum temperature rise, in the linear case, at $r = z = 0$ for absorbed power

$$P = I_0 \int_0^{\infty} f({}^{r}/_{W}) 2\pi r dr = 2\pi I_0 w^2 \int_0^{\infty} f(R) R dR, \tag{4.18}$$

provided that the power is absorbed in an infinitesimal layer at the surface, i.e., that $W = \alpha w$ is infinite, where $1/\alpha$ is the penetration depth of the laser beam, w is its radius, and $f(R)$ describes the shape of the beam in the dimensionless variable $R = r/w$. The average

$$\left\langle\frac{1}{r}\right\rangle = w^{-1}\frac{\int_0^{\infty} f(R) dR}{\int_0^{\infty} f(R) R dR}, \tag{4.19}$$

describes an average inverse beam width dependent on the beam shape. With $Z = \alpha z$, the factor $N(R,Z,W)$ de scribes the spatial distribution in R and Z of the temperature rise as well as the reduction in (linear) temperature rise at

$R = Z = 0$ when W is not infinite. For the case of Gaussian beam $f(R) = \exp(-R^2)$ and

$$\langle \frac{1}{r} \rangle = \pi^{1/2} w^{-1} \text{ (Gaussian)}, \tag{4.20}$$

whereas for a square shape, $f(R) = 1$ for $R < 1$, and zero elsewhere, so that

$$\langle \frac{1}{r} \rangle = 2w^{-1} \text{ (square well case)}. \tag{4.21}$$

The temperature rise when the thermal conductivity can be written as

$$T(r,z) = T_0(1 - \varepsilon N(R,Z,W)(2\pi K_0 T_0)^{-1})^{-1/\varepsilon}. \tag{4.22}$$

This result simplifies to an exponential when $\varepsilon \to 1$. These results are illustrative only. The experimental $K(T)$ of Fulberson *et al.* [224] and Glassbrenner and Slack [224] has been used to construct $\Theta(T)$ for silicon []. Thus, the inverse function $T(\Theta)$ is available to determine $T(r,z)$ from the linear solution $\Theta(r,z)$.

The maximum temperature rise at $r = z = 0$, using Eq. (4.22) as an illustration, is given by

$$T_{max} = T_0 \left(1 - \varepsilon N(0,0,W) \left(2\pi^{1/2} K_0 T_0 w_0\right)^{-1}\right)^{-1/\varepsilon}. \tag{4.23}$$

for the case of a Gaussian beam. The reduction factor $N(0,0,W)$ calculated from

$$N(0,0,W) = \frac{1}{\pi^{1/2}} \int_0^\infty \exp\left(-\frac{1}{4}\lambda^2\right) \frac{W}{W+\lambda} d\lambda, \tag{4.24}$$

according to []. In [] we supply approximate expressions for N as well as the closed-form evaluation

$$N(0,0,W) = WD\left(\frac{1}{2}W\right) - \frac{W}{\pi^{1/2}} exp\left(-\frac{1}{4}W^2\right) Ei\left(\frac{1}{4}W^2\right), \tag{4.25}$$

where $D(x)$, Dawson's integral

$$D(x) = exp(-x^2) \int_0^x exp(t^2) dt, \tag{4.26}$$

and $Ei(x)$ the exponential integral, are tabulated functions.

Although complete expressions for the spatial distribution $N(R,Z,W)$ are given in [], we record here the important case $W = \infty$ when the energy is all absorbed in an infinitesimal layer at the surface.

$$M(R,Z,\infty) = \int_0^\infty J_0(\lambda R)\, exp\left(-\frac{1}{4}\lambda^2\right) d\lambda. \tag{4.27}$$

where $M(R,Z,\infty) = \pi^{1/2} N(R,Z,\infty)$. On the surface $Z = 0$ itself, we obtain the new closed-form result

$$N(R,Z,\infty) = exp\left(-\frac{1}{2}R^2\right) I_0\left(\frac{1}{2}R^2\right). \quad (4.28)$$

where $I_0(x)$ is the modified Bessel function of order zero. If either R or Z is >>1,

$$M(R,Z,\infty) \rightarrow \frac{1}{(R^2+Z^2)^{1/2}} \quad (4.29)$$

and the contours of constant temperature approach hemispheres (see Fig. 4.17).

The origin, $R = Z = 0$, and the contours shown in Fig. 4.17 have values of M equal to $\left[\pi^{1/2}, 1, 1/2, 1/3, 1/4, 1/5, 1/6\right]$ respectively. The linear temperature rise (Θ) on these contours may be obtained by multiplying these numbers by $\left(P/w\right)/(2\pi K_0)$. For the value P/w = 1,7×l0^3 *W/cm*, quoted as representative in [224], the linear temperature rise Θ on these contours and the corresponding nonlinear rise T-T_0 (from Fig. 4.18) on the same contours are given in []. The steady-state results quoted here are valid since the millisecond scan times are long compared to the time Cw^2/K «microseconds required to come to equilibrium.

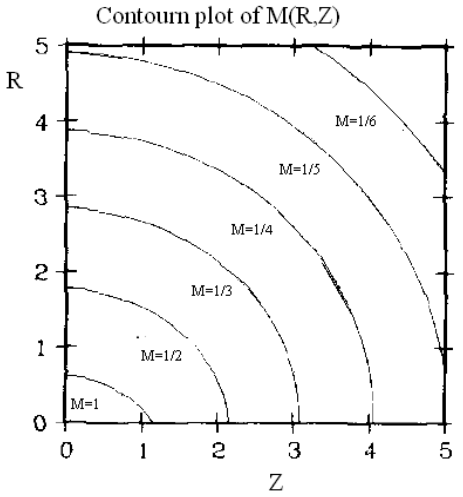

Fig 4.17: A contour plot is given for $M(R,Z) = \pi^{1/2}N(R,Z)$. For large R and Z, $M \rightarrow (R^2 + Z^2)^{1/2}$ so that the contours approach circles. Contours are shown for $M = 1/6, 1/5, 1/4, 1/3, 1/2$ and 1. The maximum value of M is $\pi^{1/2}$ at $R = z = 0$. The contours of temperature T for the nonlinear case are the same as these for M in the linear case.

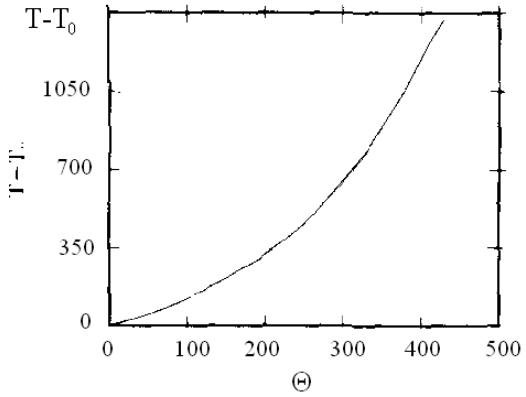

Fig 4.18: The linear temperature rise Θ and nonlinear rise $T–T_0$ are compared in Si. Θ (T) was calculated by numerical integration of Eq. (4.10) using experimental data

The maximum linear temperature rise of 343°C results in a much larger nonlinear rise of 858 °C and a maximum temperature of 858 + 300 – 273 = 885°C. This is close to the 900°C previously estimated. The 2.7 eV activation energy of the regrowth velocity results in strong temperature sensitivity of the laser annealing process and a need for the accurate temperature calculations provided here.

Thermoplastic action of pulse-periodic laser radiation on surface of solid is analyzed in [20].

4.5 Some remarks

Lattice energy – the energy (U) spent on breaking the crystal lattice into its components with the transfer to the distance of the absence of interaction, taken with the opposite sign. If the lattice is ionic, then this is the energy of rupture into the corresponding ions; if atomic or molecular, then this is the energy of rupture into atoms, molecules, etc. for molecular lattices, this is only a small part of the bond energy in the lattice, since the bonds of atoms inside molecules do not enter into it. Energy of crystal lattice for molecular lattices is equal to the van der Waals forces (see Chemical van der Waals bond). It has now been established that abs. most natural compounds, in particular oxygen ones, are not ionic, but at best semi-ionic and semi-covalent. In this regard, many conclusions based on the use of energy the crystal lattice, usually calculated as ionic ones, are of little value [33]. There are a number of methods for calculating energy the crystal lattice for binary compounds: according to the Born-Haber circular process, according to the Born-Lande formula and its simplified variants – the Kapustinsky formulas, etc.

According to the circular process [33]

$$U_i=Q+S+D+I-E, \quad (7)$$

where Ui is the energy of the ionic lattice; Q is the heat of formation, S is the heat of sublimation, D is the dissociation energy, I is the ionization energy, and E is the electron affinity energy. According to the Born-Lande formula [33]

$$U_i=(aW_1 W_2 Ne^2)/R (1-1/m), \quad (8)$$

where a is the Madelung constant, W1 and W2 are the ion valences, R is the interatomic distance, Ne2 is the product of the Avogadro number and the elementary electron charge squared, m is the coefficient. repulsion of electron shells. In geological sciences usually use the Kapustinsky formula [33]

$$U_i=256.1 (E_n W_k W_a)/(r_k+r_a), \quad (9)$$

where En is the number of structural units. Wk and Wa are the valencies of the cation and anion, rk and ra are their radii, or an even more simplified Fersman formula [33]

$$U_i=256.1(E_c A+E_c B+\cdots+E_c X), \quad (10)$$

which has a universal character in terms of the values of Ek, which make up the compounds of ions, i.e., in terms of energy coefficient of components the calculation of energy the crystal lattice.

For atomic compounds, the circular process is simplified [33]:

$$Uat = Q + S + D,$$

for molecular compounds: Um = S(AB), where S(AB) is the energy of sublimation of molecules. For the theoretical calculation, the formula is used where k is a coefficient, similar to the coefficient. Madelung, μ is the dipole moment. Idea about energy the crystal lattice plays an important role in the geoenergetic analysis of geochemical processes, so the correct use of this concept is very important.

Methods of Vitaliy Stafeev phason and cascade models complement thermodynamic methods and allow more adequately to include the microscopic aspects of the nucleation and crystallization.

Laser-induced crystallization and crystal growth are observed in [41]. Femtosecond multiphoton excitation of solutions leads to their ablation at the focal point, inducing local bubble formation, shockwave propagation, and convection flow. This phenomenon, called “laser microtsunami” makes it possible to trigger crystallization of molecules and proteins from their supersaturated solutions. Femtosecond laser ablation of a urea crystal in

solution triggers the additional growth of a single daughter crystal. Intense continuous wave (CW) near infrared laser irradiation at the air/solution interface of heavy-water amino acid solutions results in trapping of the clusters and evolves to crystallization. A single crystal is always prepared in a spatially and temporally controlled manner, and the crystal polymorph of glycine depends on laser power, polarization, and solution concentration. Upon irradiation at the glass/solution interface, a millimeter-sized droplet is formed, and a single crystal is formed by shifting the irradiation position to the surface. Directional and selective crystal growth is also possible with laser trapping.

It should be noted that when laser radiation is focused in a transparent medium, the following cascade of processes may occur: focusing, diffraction stratification of the beam, Cherenkov radiation, and interference of this Cherenkov radiation [3].

These processes can occur in all media from gases to solids. It is on the basis of the cascade of these processes that the laser-induced optical breakdown in silicon carbide and potassium chloride was explained. The same model can be used to explain the laser-induced growth of crystals from solution. It is the generation of Cherenkov (continuous cone) radiation that complements the tsunami effect from a physicochemical point of view, which allows breaking the corresponding chemical bonds, which in turn leads to both the creation of new molecules and a change in their phase state, that is, to crystallization.

Moreover, this can happen without interference, the main thing is the formation of short-wave radiation, which is absorbed more intensively than the incident radiation [3].

4.6 Conclusions

1. The problem of electromagnetic modelling the nucleation and crystallizations processes are is analyzed.
2. Short review of elionic methods of generation the nano- and microstructures is represented.
3. Vitaliy Stafeev electrostatic model of phasons as example of kinetic model of nucleation and its applications is observed.
4. It was shown, that cascade model of excitation of proper chemical bonds for two-dimensional sphalerite lattice may be used for the explanation the electrical properties of the laser-induced structures.
5. For structural modeling of transitions between allotropic phases of silicon and germanium and creation of proper nucleations was used its phase diagram.

6. Cascade model of step-by-step excitation the chemical bonds in the regime of saturation the excitation allows explaining main structural phase transformations in laser-irradiated matter.
7. For physical-chemical modeling of phase transformations in irradiated materials, it is possible to use such quantities as the energies of formation of the corresponding crystal lattices and their volumes.
8. Prospects for the development of kinetic modeling methods and the expansion of their field of application are also discussed.

Chapter - 5

Shock Processes in Nonlinear and Relaxed Optics

Give me matter, and I will show you how

the world should be formed from it.

I. Kant

5.1 Introduction

The problem of observation the shock directed (ordered quantum) and disordered electromagnetic processes [6, 12, 29, 30, 44, 47, 64, 106, 140, 141, 155, 160-161, 168, 172, 174-179, 191, 251, 265-269] is one of main problems in Nonlinear and Relaxed Optics. First processes have local short range action coherent nature. They are caused by direct short-term chain processes of scattering (absorption) of light directly in the coherent zone of interaction. Therefore, these processes have a clearly defined orientation character and kinetic nature. Second processes have dynamical nature and do not have such a clearly expressed orientation dependence. First processes are the classical nonlinear optical phenomena, including Cherenkov radiation and shock laser-induced optical breakdown of matter. Second processes are represented noneequilibrium and irreversible plasma and simple to it processes.

An example of the connection between these two processes can be the work of A. Bohr "The influence of atoms interactions on the penetration of particles through matter" [33], in which Cherenkov and bremsstrahlung radiation are considered from the point of view of energy loss of incident particles in matter. In the optical case, these particles are photons [232, 233]. From point of view of Nonlinear Optics laser-induced generation of supercontinuum radiation is set of various Nonlinear Optical phenomena [58]. But supercontinuum radiation is optical-induced Cherenkov radiation. Therefore, Cherenkov radiation is Nonlinear Optical phenomenon. Classic Nonlinear Optical phenomena are caused by resonance homogeneous polarization, Cherenkov radiation – result of heterogeneous polarization [233]. Short review of corresponding experimental data are represented. Laser-induced optical breakdown is complex shock process. It can be plasmic, relatively disordered; and coherent, relatively ordered. Coherent shock processes have

electromagnetic nature, incoherent shock processes have thermal nature. These characteristics are determined the geometrical sizes of interaction zone. One of the stage of this process is conic super continuum radiation. Comparative analysis of main models of this radiation (Cherenkov radiation, self-phase, four-wave mixing, X-waves) is represented in chapters I and II of this book. We show that last three models cannot explain all peculiarities of super continuum radiation. It is caused of insufficiently complete experimental results that do not allow creating models that are more adequate. All peculiarities of super continuum conic radiation explain direct cascade model of laser-induced optical breakdown [232, 233]. This model include chain of next processes: diffraction stratification, surface generation of Cherenkov radiation on each cone of diffractive stratification, interference of short-wave part of Cherenkov radiation and optical breakdown in the maximum of this interferogram [232, 233]. Questions related to the nature and difference of electromagnetic and acoustic impact processes are also discussed.

5.2 Experimental data

Many of the measurement techniques used to characterize filaments rely on the assumption that the physical phenomena involved in filamentation keep a clear separation between spatial and temporal effects. Filament are therefore often characterized in terms of pulse duration, beam diameter, peak intensity, and averaged quantities such as the fluence (time integrated intensity) or the power. When strong coupling between space and time occurs as in the generation of filaments, many of these concepts, however, lose their meaning.

Recently, evidence of strong space–time coupling was revealed by use of an imaging spectrometer allowing a map of the far-field angular spectra of 200-*fs* optical pulses that have undergone beam collapse and filamentation in a Kerr solid or liquid [35]. The far-fields exhibit an X-shape and a strong modulated on-axis emission (Fig. 5.1). This fringe pattern was observed by studying the evolution of the spectra with increasing input powers, revealing the complexity of the space time coupled phenomena from angular-spectral characterization. He *et al*. [58] characterized the conical emission in Kerr and non-Kerr liquids pumped with ultrashort laser pulses and observed X-shaped angular spectra. These X-shaped angular spectra were reinterpreted only recently as a manifestation of the spontaneous dynamics of ultrashort laser pulses undergoing filamentation, which tends to generate a stationary conical wave [58]. An analysis of the role of nonlinear losses in the filament dynamics was made in the framework of a monochromatic approach, where the role of chromatic dispersion was neglected [58]. In this case, a theoretical analysis confirmed the existence of weakly localized conical stationary solutions to the

nonlinear Schrödinger equation in the presence of multiphoton absorption [237]).

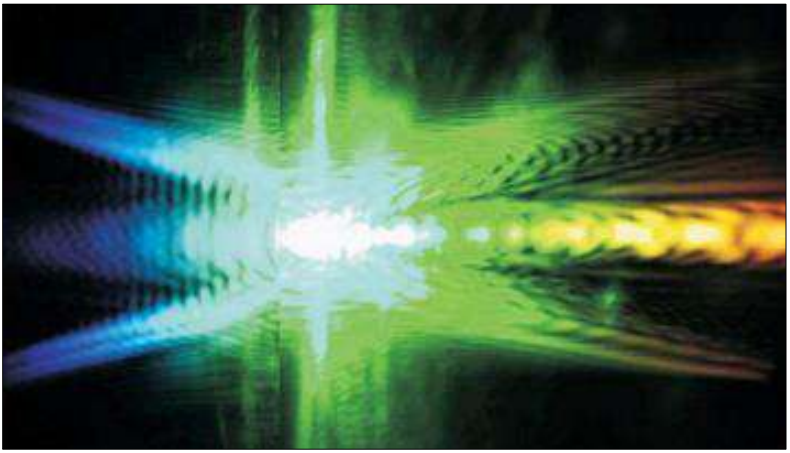

Fig 5.1: Nonlinear X-waves retain their characteristic profiles when measured in Fourier space. To make this image, an X-wave was sent through a lens and onto a spectrograph. The horizontal axis is angular frequency and the vertical axis is wave number (Courtesy of Paolo Di Trapani.) [237]

In contrast, nonlinear X waves represent conical stationary solutions to the nonlinear Schrödinger equation in the presence of chromatic dispersion but when nonlinear losses are neglected; nonlinear X-waves are expected to be robust against nonlinear losses and the corresponding solutions to an extended nonlinear Schrödinger model fully accounting for nonlinear losses and chromatic dispersion should play the role of attractors for the dynamics of filamentation. Paolo Di Trapani and his collaborators discovered they could send short, intense laser pulses through a transparent crystal of lithium triborate without the pulses' typical spreading [237]. In the Como experiment, the pulses emerged from the laser aperture with the usual Gaussian profile. However, when they encountered the dispersive medium of the crystal, nonlinear interactions spontaneously transformed them into a new shape that in longitudinal cross section looks like an X. Fig. 5.1 shows an example.

Nonspreading "X- waves" had been created before, but in the lower-power linear regime using special equipment. In the nonlinear regime, by contrast, the X-wave appears to embody a naturally occurring mode of the light–matter interaction (Fig. 5.2) [35].

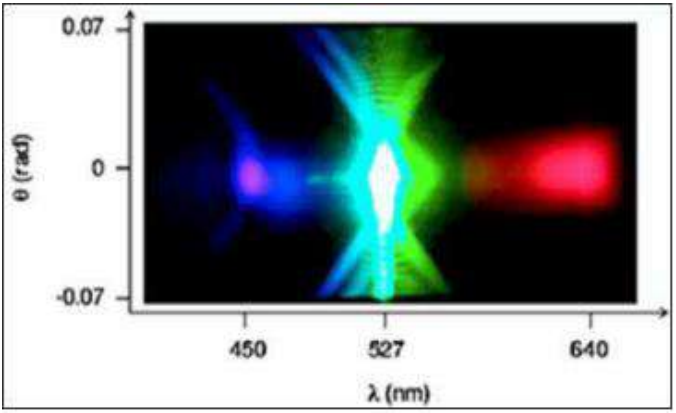

Fig 5.2: Double X *θ.ß* spectrum of a 527 *nm*, 3 *μJ* laser pulse undergoing filamentation in water. Each X-pattern exhibits a gap in frequency characterizing the velocity of each split pulse. The reduced visibility of the red tail was attributed to the increased absorption at the wavelengths [237]

By studying the conical emission of a blue femtosecond laser filament in air, it is shown that self-improvement of the beams' spatial mode quality occurs for a self-guided laser pulse (Fig. 5.3) [237].

Fig. 5.4 show conical emission accompanying a self-guided pulse for various regimes of irradiation.

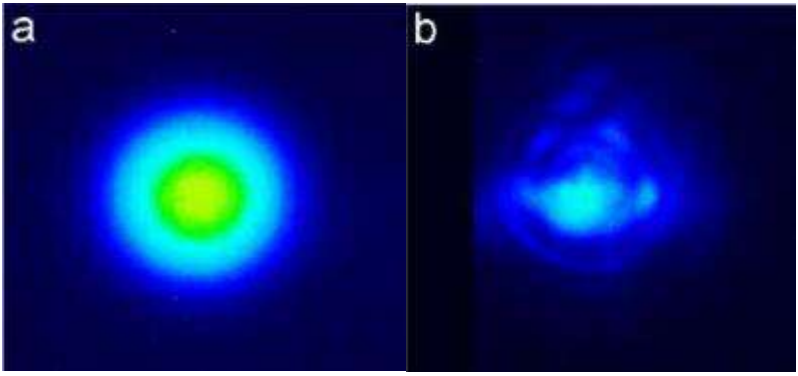

Fig 5.3: Conical emission and laser pattern measured after 20 *m* of propagation in air from a 400 *nm* laser pulse. (a) Surrounding conical emissiononly, with the power spectrum close to that of the incident laser pulse removed by a colour filter. The external diameter of the blue ring is about1 cm. (b) strongly attenuated total laser beam at the same distance [237]

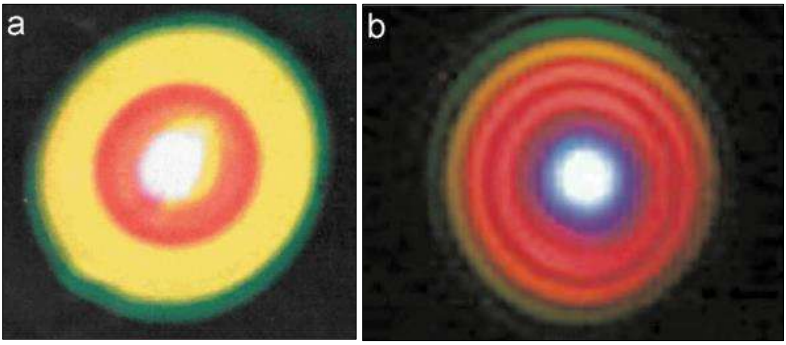

Fig 5.4: Conical emission accompanying a self-guided pulse. (a) A central white core (the filament) is surrounded by Newton's rings having a divergence of the order of the mrad [157]. (b) Conical emission measured at 25 *m* from a 5 *mJ*, 45 *fs*, 800 *nm* pulse [157]

Laser-induced optical breakdown was researched in [267]. Two damages region in a crystal with moderately high density of inclusions were received in [267] for potassium chloride after irradiation by CO_2-laser pulses (wavelength 10.6 μm, duration of pulse 30 *ns*). The laser was known to be operating in the lowest-order transverse Gaussian mode. There were several longitudinal modes, however, which contributed a time structure to the pulse, periodic at the cavity round-trip time. The phase relationships between the longitudinal modes varied from shot to shot, changing the details of the time structure and causing the peak of the envelope to fluctuate by ±15% [267]. These results are presented in Fig. 5.5 [267].

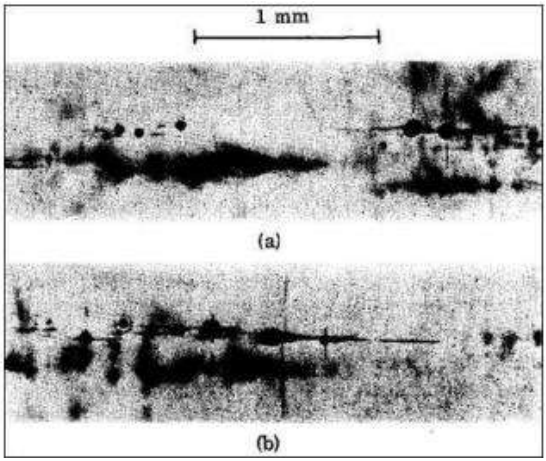

Fig 5.5: Two damages region in a crystal *KCl* with moderately high density of inclusions. The round black objects are bubbles. The radiation, incident from left to

right, was yust at the intrinsic breakdown threshold. In one case (a) there was damage only at the inclusions. In (b), intrinsic breakdown occurred as evidenced by the pointed bubble. The straight lines represent cleavage [267]

Successive laser shot (1/sec) were focused into bulk single crystals using a 1-inch focal length "Irtran 2" lens. The breakdown was monitored by observing the visible light from the focal region and by examining the damaged region under the microscope. It was found that most of the crystals suffered some damage even at relatively low power levels. The threshold of this type of damage varied by an order magnitude from one position in the crystal to another. At any particular energy level, damage would occur on the first laser shot or not at all. Fig. 5.5 (a) shows that spatial inhomogeneities are in fact inclusions [267]. The damage bubbles occur randomly near, not necessarily in, the tiny focal volume. At a well-defined power threshold, an elongated pointed bubble forms, its vertex falling at the focus (Fig. 5.5 (b)). This power level is regarded as the bulk intrinsic breakdown threshold. Its value is reproducible in crystals from different manufacturers, with inclusions or without. When no inclusion free samples of a compound were available, the considerations mentioned above were using to determine the dielectric strength [267].

Experimental data, which are included microscopic structure of optical breakdown in 4H-SiC (silicon carbide), are represented in Fig. 5.6. Sectional area of receiving structures was ~ 22 μm, the depth of ~ 50 μm. As seen from Fig. 5.6 (c) we have five stages disordered regions, which are located at a distance from 2 to 4 μm apart vertically [160, 161]. Branches themselves in this case have a thickness from 150 to 300 nm. In this case there are lines in the irradiated nanocavity with spherical diameter of from 10 *nm* to 20 *nm*. In this case irradiated structures have crystallographic symmetry of the initial structure. In this case diffraction processes may be generated in two stages: 1-formation of diffraction rings of focused beams [232, 233] and second-formation of diffracting gratings in the time of redistribution of second-order Cherenkov radiation [232, 233]. Second case is analogous to the creation of self-diffraction gratings in NLO, but for Fig. 5.6 (c) and Fig. 5.7 (b) our gratings are limited by Mach cone of Cherenkov radiation. Roughly speaking only Fig 5.6 (e) and Fig. 5.7 are represented "clean" breakdown.

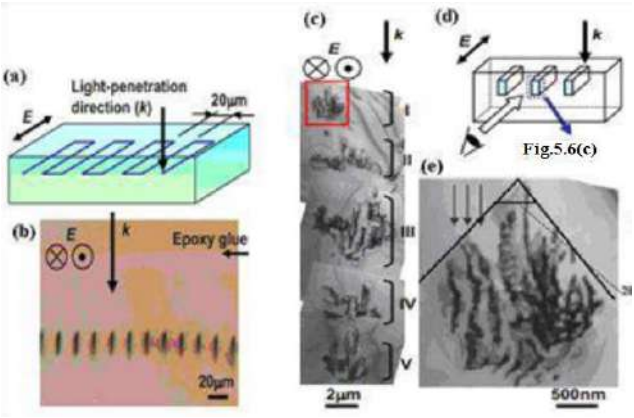

Fig 5.6: (a) Schematic illustration of the laser irradiated pattern. The light propagation direction (k) and electric field (E) are shown. (b) Optical micrograph of the mechanically thinned sample to show cross sections of laser-irradiated lines (200 *nJ*/pulse). (c) Bright-field TEM image of the cross section of a line written with pulse energy of 300 *nJ*/pulse. (d) Schematic illustration of a geometric relationship between the irradiated line and the cross-sectional micrograph. (e) Magnified image of a rectangular area in (c) [160, 161]

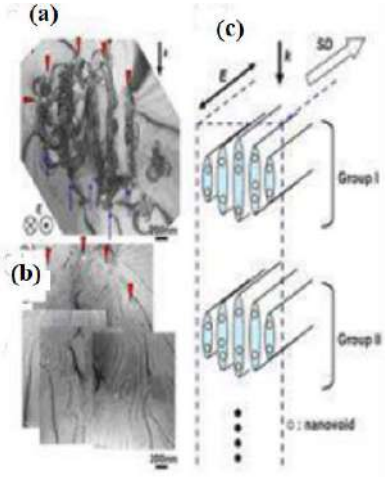

Fig 5.7: Laser-modified layers with a spacing of 150 nm are indicated by arrows. (a) Bright-field TEM image of a portion of the cross section of a line written with a pulse energy of 200 nJ/pulse. (b) Zero-loss image of a same area as in (a) with nanovoids appearing as bright areas. Correspondence with (a) is found by noting the arrowheads in both micrographs. (c) Schematic illustrations of the microstructure of a laser modified line. Light-propagation direction (k), electric field (E), and scan direction (SD) are shown. Only two groups (groups I and II) of the laser-modified microstructure are drawn [160, 161]

Photographic series of a laser-produced bubble in water are showing in Fig. 5.8. The series starts 10μs after optical breakdown, i.e. bubble generation, and proceeds with 10μs interframe time. Maximum bubble radius is about 750 μm [120].

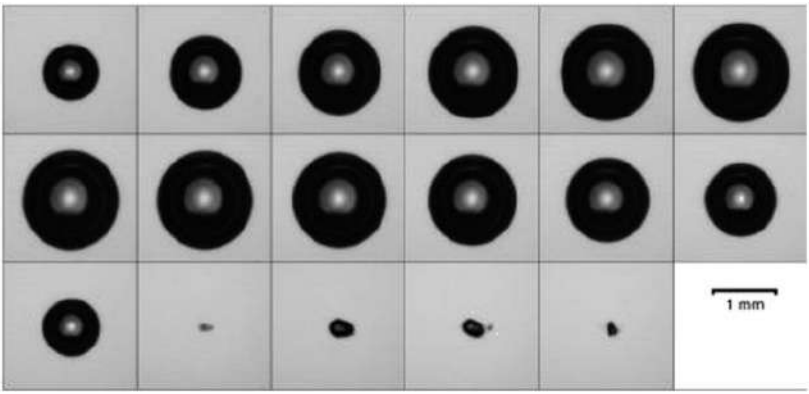

Fig 5.8: Photographic series of a laser produced bubble in water. The series starts 10µs after optical breakdown, i.e. bubble generation, and proceeds with 10µs interframe time. Maximum bubble radius is about 750μm [120]

Bubble asymmetry, induced by the nonspherical shape of the laser plasma, is minimized, when the bubble is generated at the beginning of the positive pressure cycle of the sound wave. The bubble is then compressed first and stays small for some time, so that the higher surface tension pressure for smaller bubble radii can act longer in conjunction with dissipation to form a spherical bubble. Fig. 5.9 shows this result. A small spherical bubble as obtained without sound (Fig. 5.9, left frame [120]) is expanded to larger and larger radii with increasing sound pressure amplitude thereby staying highly spherical.

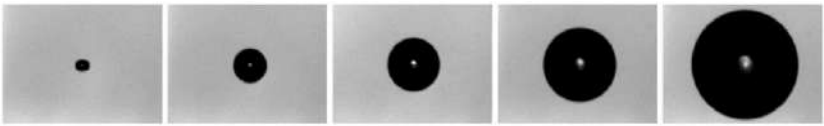

Fig 5.9: Laser induced bubble in a sound field of 43.68 *kHz* photographed at maximum expansion with increased sound pressure amplitudes (from left to right): no sound (0 *bar*), 1.76, 2.28, 3.12, 4.65 *bar*. The static pressure is p_{stat} = 1 *bar*. The image width is 454 μm. Bubble generation with a femtosecond laser pulse is effected at the beginning of the positive pressure cycle of the sound wave [120]

5.3 Main peculiarities of classic theories of shock processes

Consider a stationary homogeneous gas flow that moves at a speed *V*

relative to a stationary frame of reference S [18, 45, 107, 162, 216]. If the speed V of the flow exceeds the speed c of sound in the gas (relative to the gas itself), then the flow is called supersonic; if V is less than c, then the flow is called subsonic. The properties of a supersonic flow are significantly different from the properties of a subsonic flow. In this regard, an important flow characteristic is the ratio M of the flow speed to the speed of sound in it [18, 45, 107, 162, 216]:

$$M = \frac{\vec{V}}{c}. \tag{5.1}$$

This number is called the Mach number.

One of the features of a supersonic flow is that small perturbations of gas density (and other quantities) cannot propagate in any direction in such a flow. Indeed, the speed of propagation of disturbances relative to S is equal to the sum $\vec{V} + c\vec{n}$, where $\vec{n}$ is the direction of propagation of disturbances relative to the gas. Therefore, all possible velocities of propagation of disturbances relative to S can be obtained if the vector is set aside from the fixed point O (at which the disturbances occur) and $\vec{V} + c\vec{n}$, if fixed V, all possible directions are given to the vector $\vec{n}$. As a result of such a vector change, the end of the vector $\vec{V} + c\vec{n}$ will be tangent to a sphere with radius c centered at the end of the vector V [18, 45, 107, 162, 216].

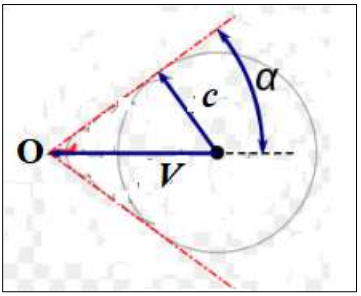

Fig 5.10: Mach cone

From what has been said, it is clear that in a subsonic flow $(V < c)$ the vector $\vec{V} + c\vec{n}$ can have any direction $\vec{n}$, while in a supersonic flow the vector (with any direction) will lie inside the cone (or on its surface) with its apex at the source of disturbance O and with the resulting tangent sphere of radius c centered at the end of the vector $\vec{V}$. The half-tilt angle α of this cone is determined by equality

$$\sin\alpha = \frac{c}{V} = \frac{1}{M}. \quad (5.2)$$

Therefore, small disturbances in the supersonic flow can propagate only in the specified cone.

The second feature of a supersonic flow is, as is known from experience, the possibility of a shock wave. This is the name given to a wave of significant compression of the medium associated with a sharp increase in pressure and temperature; at the same time, almost sudden changes in parameters occur in a very thin layer of the medium and are accompanied by the flow of matter through this layer. Shock waves arise when a supersonic flow of gas flows around bodies, during explosions and other strong environmental disturbances.

Let's consider the shock wave theory, deviating from the processes that take place in a fairly thin layer of the medium, where its parameters change greatly. This allows us to replace such a layer with a discontinuity surface, i.e., a surface on which the parameters of the medium tolerate a discontinuity.

Limiting to the case of stationary gas flow, when the rupture surface will be stationary relative to the frame of reference in which the gas movement is considered. The quantities characterizing the state of the gas before passing through the surface of the rupture and after it are connected by the laws of conservation of mass, momentum, and energy. Accordingly, there must be continuous flows of matter, momentum, and energy on the surface of the rupture.

To formulate these conditions, let's take some element of the discontinuity surface and associate a coordinate system with it, directing the *x*-axis along the normal $\overline{n}$ to the element. Then we construct a cylinder with an axis directed along *x*, an equal cross-section $d\vec{\sigma}$, and with bases that lie on different sides of the considered element of the discontinuity surface, infinitely close to this element. Then, applying the integral relation (continuity equation and energy change equation) [18, 45, 107, 162, 216] to the medium located in this cylinder and taking into account the stationarity of the flow, we obtain the conditions

$$\rho_1 v_{x1} = \rho_2 v_{x2}, \quad (5.3)$$

$$p_1 + \rho_1 v_{x1}^2 = p_2 + \rho_2 v_{x2}^2, \quad (5.4)$$

$$\rho_1 v_{x1} v_{y1} = \rho_2 v_{x2}\, v_{y2}, \quad (5.5)$$

$$\rho_1 v_{x1} v_{z1} = \rho_2 v_{x2}\, v_{z2}, \quad (5.6)$$

$$\rho_1 v_{x1}\left(\frac{v_1^2}{2}+h_1\right)=\rho_2 v_{x2}\left(\frac{v_2^2}{2}+h_2\right), \tag{5.7}$$

where the index 1 refers to the gas before passing through the rupture surface, and the index 2 refers to the gas after such passage.

It can be seen from these conditions that there can be a tangential gap, i.e., a gap in which there is no flow of matter through the surface of the gap, then $v_{x1}=v_{x2}=0$. In this case $p_1=p_2$, the jumps in density and tangential velocity components v_y and v_z are arbitrary. If the flow of matter through the rupture surface is different from zero (i.e. $v_{x1}\neq 0, v_{x1}\neq 0$), then a shock wave occurs. In that case, the tangential velocity components of the form (5.3) are continuous

$$v_{y1}=v_{y2},\ v_{z1}=v_{z2},, \tag{5.8}$$

and the density, pressure and normal component of the velocity change in a jump. These changes depend on the conditions (5.3), (5.4), as well as the condition

$$\frac{v_{x1}^2}{2}+h_1=\frac{v_{x2}^2}{2}+h_2, \tag{5.9}$$

which follows from (5.7) taking into account 5.4) and (5.8).

Now consider a stationary shock wave perpendicular to the flow direction, i.e. consider a direct seal jump. In this case, the tangential velocity components are equal to zero and, accordingly, $v_x=v$. Therefore, conditions (5.3), (5.4) and (5.9) can be written in the form

$$\rho_1 v_1=\rho_2 v_2,, \tag{5.10}$$

$$p_1+\rho_1 v_1^2=p_2+\rho_2 v_2^2, \tag{5.11}$$

$$\frac{v_1^2}{2}+h_1=\frac{v_2^2}{2}+h_2. \tag{5.12}$$

The obtained conditions determine the final changes of all thermodynamic quantities during the passage of the medium through the shock wave, including the change in entropy. This is connected with dissipative processes, which are caused by the viscosity and thermal conductivity of the gas, which occur in those very thin layers of gas, the thickness of which is neglected even in this theory. Therefore, the movement of an ideal fluid through a shock wave is an irreversible flow, that is, a flow for which, according to the second law of thermodynamics [18, 45, 107, 162, 216].

$$s_2>s_1. \tag{5.13}$$

Formulas (5.10) – (5.12) result in a number of relations. For example,

denoting the medium flow density through $j = \rho v$ and taking into account its continuity on the rupture surface, from (5.10) we obtain

$$v_1 = \frac{j}{\rho_1}, v_2 = \frac{j}{\rho_2}, \tag{5.14}$$

and excluding from (2.97) using (2.100) the speed v_1 and v_1, we find

$$j = \frac{p_2 - p_1}{\frac{1}{\rho_1} - \frac{1}{\rho_2}}. \tag{5.15}$$

It follows that either $p_2 > p_1$ and $\rho_2 > \rho_1$ or $p_2 < p_1$ and $\rho_2 < \rho_1$. But, in fact, a density jump is realized, since only the condition $p_2 > p_1$ and $\rho_2 > \rho_1$ corresponds to the condition (5.13). Note also that the jump in the compaction of the form of continuity of the flow of matter is accompanied by a drop in the gas velocity after the passage of the shock wave ($v_2 < v_1$). This decrease in the gas velocity also means that the velocity *u* of the stationary shock wave in relation to the gas in front ($u_1 = -v_1$)and behind ($u_2 = -v_2$) is different ($u_2 > u_1$).

Finally, excluding velocity from (5.13) and using (5.14) and then using (5.15), we find the enthalpy jump:

$$h_2 - h_1 = \frac{1}{2}(p_2 - p_1)\left(\frac{1}{\rho_2} + \frac{1}{\rho_1}\right). \tag{5.16}$$

This relation, called the Hugoniot adiabat (or shock adiabat), determines the dependence between ρ_2 and p_2 and for given ρ_1 and p_1.

As example, we represent a shock wave in an ideal gas [162, 216].

Find the ratio of the temperature T_2 of the ideal gas behind the front of the shock wave to the temperature T_1 of the gas in front of the front of this wave, assuming that the pressure p_1, p_2, and the ratio $\gamma = {c_p}/{c_\tau}$ for this gas are known. Find similar relations for densities and velocities.

Using the thermal equation of state of an ideal gas, the expression for enthalpy, as well as $c_p - c_\tau = {k}/{m}$ (*k* is Boltzman constant), we find from the adiabatic equation (5.16)

$$\frac{T_2}{T_1} = \frac{(\gamma+1)p_1 + (\gamma-1)p_2}{(\gamma-1)p_1 + (\gamma+1)p_2}. \tag{5.17}$$

Hence, using the equation of state and (2.102), we obtain that

$$\frac{\rho_2}{\rho_1} = \frac{(\gamma-1)p_1 + (\gamma+1)p_2}{(\gamma+1)p_1 + (\gamma-1)p_2} = \frac{v_1}{v_2}. \tag{5.18}$$

We also give an expression for the entropy difference (see (2.16))

$$s_2 - s_1 \approx c_\tau ln\left[\left(\frac{p_2}{p_1}\right)\left(\frac{\rho_1}{\rho_2}\right)^\gamma\right]. \quad (5.19)$$

In the case of shock waves of greater intensity, that is, in the case when

$$p_2 >> \frac{\gamma+1}{\gamma-1}p_1, \quad (5.20)$$

from (5.17) – (5.19) we find

$$\frac{T_2}{T_1} = \frac{\gamma+1}{\gamma-1}\frac{p_2}{p_1}, \quad (5.21)$$

$$\frac{\rho_2}{\rho_1} = \frac{\gamma+1}{\gamma-1} = \frac{v_1}{v_2}, \quad (5.22)$$

$$s_2 - s_1 \approx c_\tau ln\left(\frac{p_2}{p_1}\right). \quad (5.23)$$

It follows from (5.21) and (5.22) that the jump in temperature and pressure can grow indefinitely, while jumps in density and speed are limited to certain values. For example, for a monatomic gas $\gamma = 5/3$ and, accordingly, in the approximation (5.20), the equation holds

$$\rho_2 = 4\rho_1, v_2 = {}^{v_1}/_4; \quad (5.24)$$

for diatomic gases $\gamma = 7/5$ and thus

$$\rho_2 = 6\rho_1, v_2 = {}^{v_1}/_6. \quad (5.25)$$

5.4 On the pressure developed in a liquid during the collapse of a Spherical Cavity. Rayleygh concept

Reynolds's description of the sounds emitted by water in a kettle as it comes to the boil, and their explanation as due to the partial or complete collapse of bubbles as they rise through cooler water, I proposed to myself a further consideration of the problem thus presented; but I had not gone far when I learned from C. Parsons that he also was interested in the same question in connexion with cavitation behind screw-propellers, and that at his instigation S. Cook, on the basis of an investigation by Besant, had calculated the pressure developed when the collapse is suddenly arrested by impact against a rigid concentric obstacle. During the collapse the fluid is regarded as incompressible. In the present note I have given a simpler derivation of Besant's results, and have extended the calculation to find the pressure in the interior of the fluid during the collapse. It appears that before the cavity is closed these pressures may rise very high in the fluid near the inner boundary [176-178].

Besant problem [176] was formulating in next form: "An infinite mass of homogeneous incompressible fluid acted upon by no forces is at rest, and a spherical portion of the fluid is suddenly annihilated; it is required to find the instantaneous alteration of pressure at any point of the mass, and the time in which the cavity will be filled up, the pressure at an infinite distance being supposed to remain constant."

Since the fluid is incompressible, the whole motion is deter- mined by that of the inner boundary. If U be the velocity and R the radius of the boundary at time t, and u the simultaneous velocity at any distance r (greater than R) from the centre, then

$$u/_U = R^2/_{r^2}, \tag{5.26}$$

and if ρ be the density, the whole kinetic energy of the motion is

$$\frac{1}{2}\rho \int_R^\infty u^2 4\pi r^2 dr = 2\,\pi\rho U^2 R^3. \tag{5.27}$$

Again, if P be the pressure at infinity and R_0 the initial value of R, the work done is

$$\frac{4\pi P}{3}(R_0^3 - R^3). \tag{5.28}$$

When we equate (5.27) and (5.28) we get

$$U^2 = \frac{2P}{3\rho}\left(\frac{R_0^3}{R^3} - 1\right), \tag{5.29}$$

expressing the velocity of the boundary in terms of the radius. Also, since $U = dR/_{dt}$,

$$t = \sqrt{\frac{3\rho}{2P}}\int_R^{R_0} \frac{R^{3/2}dR}{(R_0^3 - R^3)^{1/2}} = R_0\sqrt{\frac{3\rho}{2P}}\int_\beta^1 \frac{\beta^{3/2}d\beta}{(1-\beta^3)^{1/2}} \tag{5.30}$$

if $\beta = R/_{R_0}$. The time of collapse to a given fraction of the original radius is thus proportional to $R_0\rho^{1/2}P^{-1/2}$ a result which might have been anticipated by a consideration of "dimensions." The time τ of complete collapse is obtained by making $\beta = 0$. An equivalent expression is given by Besant, who refers to Cambridge Senate House Problems of 1847 [176].

Writing $\beta^3 = z$, we have

$$\int_0^1 \frac{\beta^{3/2}d\beta}{(1-\beta^3)^{1/2}} = \frac{1}{3}\int_0^1 z^{-1/6}(1-z)^{-1/2}dz,$$

which may be expressed by means of gamma functions. Thus

$$\tau = \sqrt{\frac{\rho}{6P}}\frac{\Gamma(5/6)\Gamma(1/2)}{\Gamma(4/3)} = 0.91468R_0\sqrt{\frac{\rho}{P}}. \tag{5.31}$$

According to (5.29) U increases without limit as R diminishes. This indefinite increase may be obviated if we introduce, instead of an internal pressure zero or constant, one which increases with sufficient rapidity. We may suppose such a pressure due to a permanent gas obedient to Boyle's law. Then, if the initial pressure be Q, the work of compression is $4\pi Q R_0^3 \log\left(R_0/R\right)$, which is to be subtracted from (5.28). Hence

$$U^2 = \frac{2P}{3\rho}\left(\frac{R_0^3}{R^3} - 1\right) - \frac{2Q}{\rho}\frac{R_0^3}{R^3}\log\left(R_0/R\right), \tag{5.32}$$

and $U = 0$ when

$$P(1 - z) + Q\log z = 0, \tag{5.33}$$

z denoting (as before) the ratio of volumes R^3/R_0^3. Whatever be the (positive) value of Q, U comes again to zero before complete collapse, and if $Q > P$ the first movement of the boundary is outwards. The boundary oscillates between two positions, of which one is the initial.

The following values of P/Q are calculated from (5.33) (Table 5.1)

Table 5.1 [176]

z	P/Q	z	P/Q
0.001	6.9147	1	arbitrary
0.01	4.6517	2	0.6931
0.1	2.5584	4	0.4621
0.25	1.8484	10	0.2538
0.5	1.3863	100	0.0465
1	arbitrary	1000	0.0069

Reverting to the case where the pressure inside the cavity is zero, or at any rate constant, we may proceed to calculate the pressure at any internal point. The general equation of pressure is

$$\frac{1}{\rho}\frac{dp}{dr} = -\frac{du}{dt} - u\frac{du}{dr}, \tag{5.34}$$

u being a function of r and t, reckoned positive in the direction of increasing r. As in (1), $u = UR^2/r^2$, and

$$\frac{dU}{dt} = \frac{1}{r^2}\frac{d}{dt}(UR^2).$$

Also

$$\frac{d}{dt}(U^2R) = 2RU^2 + R^2\frac{dU}{dt},$$

and by (5.29)

$$\frac{dU}{dt} = -\frac{P}{\rho}\frac{R_0^3}{R^4},$$

so that

$$\frac{d}{dt}(U^2R) = 2RU^2 - \frac{P}{\rho}\frac{R_0^3}{R^2}.$$

Thus, suitably determining the constant of integration, we get

$$\frac{p}{P} - 1 = \frac{R}{3r}\left(\frac{R_0^3}{R^3} - 4\right) - \frac{R^4}{3r^4}\left(\frac{R_0^3}{R^3} - 1\right). \quad (5.35)$$

At the first moment after release, when $R = R_0$, we have

$$p = P\left(1 - {}^{R}/_{r}\right). \quad (5.36)$$

When $r = R$, that is on the boundary, $p = 0$, whatever R may be, in accordance with assumptions already made.

Initially the maximum p is at infinity, but as the contraction proceeds, this ceases to be true. If we introduce z as before to represent ${}^{R_0^3}/_{R^3}$, (10) may be written [176]

$$\frac{p}{P} - 1 = \frac{R}{3r}(z - 4) - \frac{R^4}{3r^4}(z - 1), \quad (5.37)$$

and

$$\frac{dp/P}{dr} = \frac{R}{3r^2}\left[\frac{(4z-4)R^3}{r^3} - (z - 4)\right]. \quad (5.38)$$

The maximum value of p occurs when

$$\frac{r^3}{R^3} = \frac{4z-4}{z-4}, \quad (5.39)$$

and then

$$\frac{p}{P} = 1 + \frac{(z-4)R}{4r} = 1 + \frac{(z-4)^{4/3}}{4^{4/3}(z-1)^{1/3}} \quad (5.40)$$

So long as z, which always exceeds 1, is less than 4, the greatest value of p, *viz*. P, occurs at infinity; but when z exceeds 4, the maximum p occurs at a

finite distance given by (5.39) and is greater than *P*. As the cavity fills up, z becomes great, and (5.40) approximates to

$$\frac{p}{P} = \frac{z}{4^{4/3}} = \frac{1}{4^{4/3}}\frac{R_0^3}{R^3}, \tag{5.41}$$

corresponding to

$$r = 4^{4/3}R = 1.587R. \tag{5.42}$$

It appears from (5.41) that before complete collapse the pressure near the boundary becomes very great. For example, if $R = \frac{1}{20}R_0$, $p = 1260P$.

This pressure occurs at a relatively moderate distance outside the boundary. At the boundary itself the pressure is zero, so long as the motion is free. S. Cook considers the pressure here developed when the fluid strikes an absolutely rigid sphere of radius *R*. If the supposition of incompressibility is still maintained, an infinite pressure momentarily results; but if at this stage we admit compressibility, the instantaneous pressure P' is finite, and is given by the equation

$$\frac{P'^2}{2\beta'} = \frac{1}{2}\rho U^2 = \frac{P}{3}\left(\frac{R_0^3}{R^3} - 1\right), \tag{5.43}$$

β' being the coefficient of compressibility. *P*, *P*', β' may all be expressed in atmospheres. Taking (as for water) β' =20,000, *P* = l, and $R = \frac{1}{20}R_0$, Cook finds

P' = 10300 atmospheres = 68 tons per sq. inch, and it would seem that this conclusion is not greatly affected by the neglect of compressibility before impact [176].

5.5 Modelling and discussions

Other theories and models

The main extensions of Rayleigh's theory are Rayleigh–Plesset, Gilmore; and Keller–Miksis models.

The basic model is the Rayleigh model [120]:

$$\rho R\ddot{R} + \frac{3}{2}\rho\dot{R}^2 = p_i - p_e, \tag{5.44}$$

where an overdot means differentiation with respect to time. The difference in pressure, $p_i - p_e$, drives the bubble motion. The form of the inertial terms on the left-hand side is due to the spherical three-dimensional geometry that is transformed to one radial dimension in the differential equation. Both, pi and pe, become functions of radius *R* and time *t*, when gas and vapour fill the bubble, and when surface tension σ, liquid viscosity μ and

a sound field, $p(t)$, are taken into account. With these inclusions, the Rayleigh model takes the form [120]

$$\rho R\ddot{R} + \frac{3}{2}\rho\dot{R}^2 = p_{gn}\left(\frac{R_n}{R}\right)^{\kappa} + p_i - p_e - p(t) - \frac{2\sigma}{R} - \frac{4\mu}{R}\dot{R}, \tag{5.45}$$

with

$$p_{gn} = \frac{2\sigma}{R_n} + p_{stat} - p_v, \tag{5.46}$$

p_{gn} being the gas pressure inside the bubble at rest, pstat the static pressure and p_v the (here constant) vapour pressure. The pressure $p(t)$is an external pressure applied at the bubble wall. In the case of a single frequency ultrasonic excitation of the bubble, it can be written in the form

$$p(t) = -\,p_a \sin(2\pi\nu_a t), \tag{5.47}$$

varying sinusoidally with frequency ν_a and having a pressure amplitude p_a. The '–' sign is convenient for starting the oscillation at $t = 0$ with an expansion of the bubble at rest. This model and some variants are called Rayleigh–Plesset models [120].

A more advanced model is the Gilmore model [120] that incorporates sound radiation into the liquid from the oscillating bubble, whose surface acts like the membrane of a spherical loudspeaker. For strong oscillations, i.e. strong compression of the contents inside the bubble, the model is further augmenting by a van der Waals hard-core law to account for a noncompressible volume of the inert gas inside the bubble [120]. This bubble model reads as:

$$\left(1 - \frac{\dot{R}}{C}\right)R\ddot{R} + \frac{3}{2}\left(1 - \frac{\dot{R}}{3C}\right)\dot{R}^2 = \left(1 - \frac{\dot{R}}{C}\right)H + \frac{R}{C}\left(1 - \frac{\dot{R}}{C}\right)R\frac{dH}{dR}, \tag{5.48}$$

where

$$H = \int_{p_{r\to\infty}}^{p_{r=R}} \frac{dp(\rho)}{\rho}. \tag{5.49}$$

$$p(\rho) = A\left(\frac{\rho}{\rho_0}\right)^{n_T} - B. \tag{5.50}$$

$$p_{r=R} = \left(p_{stat} + \frac{2\sigma}{R_n}\right)\left(\frac{R_n^3 - bR_n^3}{R^3 - bR_n^3}\right)^{\kappa} - \frac{2\sigma}{R} - \frac{4\mu}{R}\dot{R}\,. \tag{5.51}$$

$$p_{r\to\infty} = p_{stat} + p(t). \tag{5.52}$$

$$C = \sqrt{c_0^2 + (n_T + 1)H}. \tag{5.53}$$

The additional parameters and variables in this model are the sound velocity in the liquid at normal conditions, c_0, the sound velocity at the wall of the bubble, C, the enthalpy, H, the parameters of the equation of state, where

the Tait equation (5.50) is chosen with its parameters A, B, n_T and the van der Waals constant, b. A vapour pressure may be introduced in (5.51) as in (5.45) and (5.46).

A further model is the Keller–Miksis model [120] that also incorporates sound radiation from the oscillating bubble, but features a retarded time t − R/c in the equations. A model equivalent to this model to first order in 1/c, c being the sound velocity in the liquid, and dispensing with the retarded time reads

$$\left(1-\frac{\dot{R}}{c}\right)R\ddot{R}+\frac{3}{2}\left(1-\frac{\dot{R}}{3c}\right)\dot{R}^2=\left(1+\frac{\dot{R}}{c}\right)\frac{p_1}{\rho}+\frac{R}{\rho c}\frac{dp_1}{dt}, \tag{5.54}$$

with

$$p_1=\left(p_{stat}+\frac{2\sigma}{R_n}\right)\left(\frac{R_n}{R}\right)^{3\kappa}-\frac{2\sigma}{R}-p_{stat}-p(t)-\frac{4\mu}{R}\dot{R}, \tag{5.55a}$$

$$p(t)=-p_a\sin(2\pi\nu_a t). \tag{5.55b}$$

Here, too, a van der Waals law may be introduced as in (5.51) for the gas inside the bubble or a vapour pressure as in (5.45) and (5.46). The connection between the different bubble models has been explored by Prosperetti and Lezzi [62, 63]. Typical values of the parameters for gas bubbles in water, as used in the calculations with the Keller–Miksis model, are p_{stat} = 100 *kPa*, p_v = 2.33 *kPa*, σ = 0.0725 *N* m^{-1}, κ = 1.67 (noble gas), μ = 0.001 *Pa s*, c = 1500 *m* s^{-1} and ρ = 998 *kg* m^{-3}. The radius of the bubble at rest, R_n, covers the range from below a micrometre (nanobubbles, microbubbles) to several millimetre, but may reach large values in underwater explosions, either by underwater sparks or with explosives. The driving frequency, νa, typically takes values from a few hertz to a few megahertz, but may extend into the gigahertz range. The driving pressure amplitude, p_a, may vary between zero pascal (no sound field) and several megapascal. Theory will not be stretched beyond the three basic bubble models (Rayleigh–Plesset; Gilmore; Keller–Miksis), as they give an astonishing precise description of most experiments on spherical bubble oscillation.

These theories are used for all sources of excitation of shock waves in liquids without exception. It can be both acoustic and light stimuli.

Light induced bubbles come with a shock wave upon generation as the material of the fluid is strongly heated [120] and develops a high pressure that is radiated into the liquid. The bubble expansion follows on a slower time scale. These bubbles have various lifetime. Their lifetime is determined by the formula.

$$T_c = 0.915 R_{max} \sqrt{\frac{\rho}{p_{stat} - p_v}}. \quad (5.56)$$

These models do not include the background history of bubbles and possible channels of conversion of incident radiation. Despite this, it satisfactorily explains the experimental results on the emergence and evolution of bubbles in liquids.

After all, there is no need to take into account the nature of the pressure. Whatever pulses are in the liquid, we consider only the thermal and plasma aspects of the laser breakdown. In order to have a more adequate picture, which would allow us to clarify the microscopic nature of the corresponding processes, we must conduct a more precise experiment.

To do this, we must remember that according to I. Newton, optics studies the processes of transformation of light into matter and, conversely, the transformation of matter into light. We only have to find the chain of these transformations. It is this approach that can more adequately explain the phenomena of laser-induced optical breakdown and the formation of bubbles and nanovoids.

The first thing that comes to mind is that the focused radiation should form diffraction circles, which leads to diffraction delamination of the incident laser beam (Fig. 5.2, Fig. 5.5). In other words, thin layers of intense interaction of initial radiation with matter are formed.

Since the initial radiation is focused, it causes the occurrence of heterogeneous polarization of the medium, which in turn is the source of generation of a whole range of non-linear optical effects, which leads to a continuous spectrum. But since the cone of initial radiation is transformed into a set of diffractionally stratified cones of heterogeneous polarization of the medium. Then the radiation occurs inside the cones, the generators of which are perpendicular to the generator cones of polarization. And this, according to A. Bohr [33], is Cherenkov radiation.

The first laser-induced filaments were received in the liquid. Later researches shown that analogous phenomena are generated in solid and gas matter too. Therefore, first models were created for the nonlinear Kerr media and were used for all types of irradiated matter [232]. Strongly speaking, these filaments are sparks of optical breakdown. More universal concept is physical-chemical.

However, Kerr media are represented liquids basically. For solid state basic phenomena are laser-induced electrostriction [191]. In the gas case we can

have other nonlinear optical phenomena. Therefore, we must select more universal concept for the determination P_{cr}. It may be physical-chemical method. In this case we must have concentration of proper centers of scattering (absorption) of laser radiation, which are generated proper nonlinear optical phenomenon, and its activation energy. The self-focusing is nonlinear optical process. Therefore, P_{cr} or the critical value of energy may be determined in next way. Volume density of energy of the creation self-focusing process may be determined with help next formula W_{crvol} [232, 233]

$$W_{crvol} = E_a N_{nc}, \tag{5.57}$$

where E_a – energy of activation proper "nonlinear" centers; N_{nc} – their concentration.

Surface density for optical thin may be determined as [232, 233]

$$W_{crsur} = {}^{W_{crvol}}/_{\alpha}, \tag{5.58}$$

where α – absorbance index. Integral value of energy may be determined as [232, 233]

$$W_{crin} = W_{crsur} \cdot S, \tag{5.59}$$

where S – the square of irradiation.

In this case [232, 233]

$$P_{cr} = {}^{W_{crin}}/_{\tau_{ir}}, \tag{5.60}$$

where τ_{ir} is duration of laser irradiation.

The determination the concentration of scattering centers must be determined with conditions of proper experiment. It is determined by the conditions of observation the proper phenomena.

Next step of determination the density of energy in our cascade is condition of diffraction stratification. This condition may be determined with help of sizes the diffraction rings. We can estimate density of energy in plane of creation the diffraction stratification for n=5.

The explanation of creation the laser-induced filaments have various interpretation. Firstly [232, 233], it is the creation wave-guide zones after point of collapse. In this case filaments have little lifetime.

Conic part of filament radiation has continuum spectrum: from ultraviolet to infrared. At first this effect was called superbroadening. Therefore, it may be interpreted as laser-induced Cherenkov radiation [232, 233]. The angle 2θ in the vertex of an angle of Fig. 5.6 (e) is double Cherenkov angle. In this case

we have frozen picture of laser-induced destruction of 4H-SiC with help Cherenkov radiation [232, 233].

The Cherenkov radiation is characterized by two peculiarities [59, 96, 232, 233, 279, 280]

1) Creation of heterogeneous shock polarization of matter and,
2) Radiation of this polarization.

The methods of receiving shock polarization may be various: irradiation by electrons, γ-radiation, ions and excitation with help pulse fields. The stratification of this radiation on other type's radiation (volume, pseudo-Cherenkov a.o.) has relative character and may be represented as laser-induced Cherenkov radiation. Therefore, in future we'll be represent conical part of filament radiation as Cherenkov.

This fact may be certified with macroscopic and microscopic ways [232, 233].

First, macroscopic may be represented according to [77]. The similarity between charge particle and light-induced Cherenkov radiation one can invoke the analogy between Snell's law and Cherenkov radiation [107]. This natural since both effects can be derived in the same way from the Huygens interference principle. In [77] the point of intersection of a light pulse impinging at an angle φ on a boundary between two media moves with velocity $V = {}^{c}/_{n_1 \cos\varphi}$. This relation with Snell's law, gives the Cherenkov relation (Golub formula) [77].

$$\cos\theta = {}^{c}/_{n_2(\omega)V}. \tag{5.61}$$

This formula allows explain the angle differences for various type of Cherenkov radiation. In this case, V may be represented as velocity of generation the optical-induced polarization too [232, 233].

Thus, the refraction law a light at the boundary between two media is the same as the condition for Cherenkov emission by a source moving along the boundary. In nonlinear medium the emitted frequencies may be differ from the excitation frequency. The Cherenkov relation is still valid since the constructive interference occurs at a given Cherenkov angle for each Fourier frequency component of the light-induced nonlinear polarization. In a sense, one can speak about a nonlinear Snell-Cherenkov effect [77].

The microscopic mechanism of laser-induced Cherenkov radiation is expansion and application of Niels and Aage Bohrs microscopic theory of Cherenkov radiation as part of deceleration radiation on optical case [232, 233].

For optical case, the Bohrs hyperboloid must be changed on Gaussian distribution of light for mode TEM_{00} or distribution for focused light of laser beam [232, 233]. In this case, Cherenkov angle may be determined from next formula

$$\theta_{ch} + \alpha_{ir} = {}^{\pi}/_{2} \text{ or } \theta_{ch} = {}^{\pi}/_{2} - \alpha_{ir}, \tag{5.62}$$

where α_{ir}– angle between tangent line and direction of laser beam.

Angle α_{ir} was determined from next formula [232, 233]

$$tan\alpha_{ir} = {}^{d_b}/_{l_f}, \tag{5.63}$$

where d_b – diameter of laser beam, (7 *mm*), l_f – length of focusing or self-focusing. In our case α_{ir} is angle of focusing or self-focusing.

This formula is approximate for average angle α_{ir}.

The Golub formula (5.61) was used for the determination product $n_2(\omega)V_{nlpol}$ [232, 233]. Self–focusing and Cherenkov angles and product $n_2(\omega)V$ were estimated for *LiF*, CaF_2, fused silica, water and glass BK-7 in [232].

Thereby microscopic modified A. Bohr theory and macroscopic Golub model are mutually complementary methods [232, 233].

The decreasing of Cherenkov angle and product $n_2(\omega)V$ for increasing of laser radiation intensity are corresponded to increasing of nonlinear refractive index and decreasing of velocity of polarization (multiphotonic and multiwave processes) [232, 233].

In whole microscopic mechanism of laser-induced Cherenkov radiation may be represented as nonequilibrium spectrum of all possible Nonlinear Optical phenomena in the local points of propagation the laser beam [3, 4, 193, 213]. It may be Raman and Brillouin scattering, up- and down-conversion, generation of harmonics and various interference of these processes and phenomena, which are generated the continuous spectrum from ultraviolet to infrared regions [232, 233].

The estimation of sizes the cascade of volume destructions of Fig. 5.6 c) may be explains in next way [232, 233]. The sizes (diameters) of proper stages d_{nir} of cascade are proportionally to corresponding diffraction diameters d_{ndif}

$$d_{nir} = k\, d_{ndif}, \tag{5.64}$$

where *k* is the proportionality constant.

The diffraction diameters d_{ndif} may be determined with help condition of diffraction-pattern rings (modified Rayleygh ratio)

$$d_{ndif} = n\lambda. \tag{5.65}$$

The estimations of first five diffraction diameters d_{ndif} for λ = 800 *nm* were represented in [232, 233].

The distance between diffraction spots and proper moving foci may be determined with help next formula [232, 233].

$$l_{nf} = \frac{d_{ndif}}{2tan^{\varphi}/_{2}}. \tag{5.66}$$

These distances for φ_1 = 20º and φ_2 = 30º were represented in [231]. In general case the angle φ is depended from homogeneity of irradiated matter or intensity of irradiation.

Qualitative explanation of development of cascade the destructions may be next. The focus of each diffraction zone (spot) is the founder proper shock optical breakdown. However, foci with more high number may placed in the "zone" of influence of previous foci. Therefore, only first stage of Fig. 5.6 (c) is represented pure shock mechanism (Mach cone). Mach cones are characterized the second and third stages of Fig. 5.6 (c). But its maximums are displaced from center. It may be result if interaction second and third shock waves with previous shock waves: first – for second wave and first and second for third wave. The chock mechanism of destruction certifies a linear direction of optical breakdown. This direction is parallel to direction of shock wave and radiated spectrum is continuum as for Cherenkov radiation and as for observed laser-induced filaments in water and air [4, 8]. Thus, basic creator of optical breakdown traces is secondary Cherenkov radiation and shock waves. This radiation is absorbed more effectively as laser radiation and therefore the creation of optical breakdown traces is more effectively as for beginning laser radiation. Cherenkov radiation is laid in self-absorption range of 4H-*SiC*, but 800 *nm* radiation – in intrinsic range. For the testing of this hypothesis we must measure the spectrum of secondary radiation. In this case we can use physical-chemical cascade model of excitation the proper chemical bonds of irradiated matter in the regime of saturation the excitation [248, 273].

The conclusion about diffractive stratification of focused radiation may be certified by experimental data of Fig. 5.6 (c).

These results are corresponded to Lugovoy-Prokhorov theory [59] too:

distance between contiguous elements is smaller as distance between microscopy ocular and first stage of cascade (correlation of this distance is proportional to λ/d) but distance between contiguous elements of cascade is equal and proportional to half wavelength [232].

Cherenkov radiation has next peculiarity. We know fact that induced radiators give possibility to receive two coherent light sources. This fact is used for the standard interference [232]. Analogous phenomenon must be observed for Cherenkov radiation too [232, 233]. If we transmit light beam through two little volumes of similar matter, then we receive two coherent sources. This property is characterized for any wavelength of continuous Cherenkov spectrum [232]. Therefore, interference for Cherenkov radiation have broad spectral region [59, 96, 232, 233, 279, 280].

Qualitative explanation of development of cascade the destructions (Fig. 5.6(c)) may be next [232, 233]. The focus of each diffraction zone (spot) is the founder proper shock optical breakdown. But foci with more high number may placed in the "zone" of influence of previous foci. Therefore, only first stage of Fig. 5.6 (c) is represented pure shock mechanism (Mach cone). Mach cones are characterized the second and third stages of Fig. 5.6 (c). But its maximums are displaced from center. It may be result if interaction second and third shock waves with previous shock waves: first – for second wave and first and second for third wave. The chock mechanism of destruction certifies a linear direction of optical breakdown. This direction is parallel to direction of shock wave and radiated spectrum is continuum as for Cherenkov radiation and as for observed laser-induced filaments in water and air [232, 233]. Thus, basic creator of optical breakdown traces is secondary Cherenkov radiation and shock waves. This radiation is absorbed more effectively as laser radiation and therefore the creation of optical breakdown traces is more effectively as for beginning laser radiation. Cherenkov radiation is laid in self-absorption range of 4H-*SiC*, but 800 *nm* radiation – in intrinsic range [232, 233]. For the testing of this hypothesis we must measure the spectrum of secondary radiation. In this case, we can use physical-chemical cascade model of excitation the proper chemical bonds of irradiated matter in the regime of saturation the excitation.

We can rough estimate basic peculiarities of energy distribution in Mach cone may be used next formula [232, 233]

$$E_{1ob} = \frac{\pi^2}{4}\left(\sum_{i=1}^{5} n_{iav}^2\, l_{iav}\right) r^2 N_{aSiC} E_{Zth}, \qquad (5.67)$$

where n_{iav}– average visible number of filaments in proper group of cascade, l_{iav}=1000 *nm* – average length of filaments in proper group of cascade, r = 10 *nm* – average radius of filament, N_a – atom density of 4H-*SiC*.

The atom density of 4H-*SiC* may be determined with help next formula [17]

$$N_a = \frac{n\rho N_A}{A}, \tag{5.68}$$

where ρ – density of semiconductor, N_A – Avogadro number, A – a weight of one gram-molecule, n – number of atoms in molecule. For 4H-*SiC* $N_{aSiC} = 9.4 \cdot 10^{21} cm^{-3}$.

For further estimation we use next approximation $n_{1av} = n_{2av} = n_{3av} = n_{4av} = n_{5av} = 100$, (see Fig. 5.6 (c).

Energy, which is necessary for the optical breakdown our nanotubes may be determined in next way. Zeitz threshold energy for 4H-*SiC* is equaled $E_{Zth} \sim 25\ eV$ [270]. Let this value is corresponded to energy of optical breakdown. Therefore, summary energy E_{1ob} is equaled

$$E_{1ob} = N_{asnt} \cdot E_{Zth} = 23.2\ nJ. \tag{5.69}$$

This value is equaled of ~ 8% from pulse energy or ~ 30% from the effective absorbed energy of pulse. In this case we have more high efficiency of transformation initial radiation to "irreversible" part of Cherenkov radiation. It is result of more intensive excitation comparatively with classical methods of receiving the Cherenkov radiation. In this case we have pure photochemical processes. The experimental data for intrinsic absorption (Fig. 4.5) show that for short pulse regime of irradiation (femtosecond regime) basic processes of destruction the fused silica and calcium fluoride are photochemical (multiphoton absorption in the regime of saturation the excitation). However, basic peculiarity of experimental data Fig. 5.6 and Fig. 5.7 is transformation the initial laser radiation (wavelength 800 *nm*) to continuum Cherenkov radiation. From length of optical breakdown in 4H-SiC we can determine average absorption index of Cherenkov radiation. It is ~ 10^4 cm^{-1}. This value is corresponded to violet-blue range of absorption spectrum of 4H-*SiC* [232, 233].

The difference between generations of surface continuum radiation [233] and optical-induced Cherenkov radiation is next. At first time we have collective electromagnetic processes, which are may be represented as processes with velocity less as phase speed of light in media. Mainly, it is wave processes. In the case of Cherenkov radiation, we have directed quantum optical processes, which can have represented as processes with velocity more as phase speed of light in matter. Roughly speaking last processes may be having velocity less as phase speed of light in media but it must be local (quantum) [232, 233]. In this case, we must determine the new phase speed of

light as speed of collectivization of electromagnetic oscillations for corresponding frequency in irradiated media because we have continuum spectrum of irradiation. In this case, the summary speed of interaction light and matter is determined the summary time of corresponding chain of direct optical processes.

Cherenkov radiation may be represented as back process of Nonlinear Optics too. Roughly speaking Nonlinear Optics is optics of nonlinear polarization. However, intense laser irradiation is generated nonlinear polarization and Cherenkov radiation [232, 233]. Therefore, these processes have identical nature [233].

We can estimate chain of critical value of energy for the 4H-*SiC* from physical-chemical point of view too.

Critical value of energy, which is necessary for the beginning of self-focusing, may be determined in next way. Volume density of energy of the creation self-focusing process may be determined with help formula (5.57). In further we made next approximation [273]: $E_a = h\nu = 1.5\ eV$. Then we have for *SiC* $W_{crvol} = 2.4 \cdot (10^{-5} - 10^{-3})\ {}^{J}/_{cm^3}$.`For *SiC* α = 0,1 cm^{-1}. And $W_{crsur} = 2.4 \cdot (10^{-4} - 10^{-2})\ {}^{J}/_{cm^2}$.

Integral value of energy may be determined according by formula (9). For Fig. 5.6(c) for r = 2 μm, S = 1,256·10^{-7} cm^2. Therefore $W_{crin} = 3.0 \cdot (10^{-11} - 10^{-9})\ J$. For r = 1 mm we have $W_{crin} = 1.9 \cdot (10^{-6} - 10^{-4})\ J$.

These estimations are corresponded to estimations, which are received with help formulas for Kerr media. Roughly speaking they are equaled [248, 273]. For the gases this method allows to estimate the energy of its optical breakdown.

Next step of determination the density of energy in our cascade is condition of diffractive stratification. This condition may be determined with help of sizes the diffractive rings. We can estimate density of energy in plane of creation the diffractive stratification for n = 5.

Maximum diameter of diffractive pattern is determined for fifth diffractive ring. For this case, average density of energy in plane of diffractive rings is equivalence.

We can estimate corresponding correlation between energies for the next processes: laser irradiation, diffractive stratification, Cherenkov radiation and optical breakdown [248, 273].

A density of laser irradiation is equaled

$$W_{avdr} = {E_p}/{S}. \quad (5.70)$$

Where E_p – energy of laser pulse. For E_p = 200 *nJ* and E_p = 300 *nJ* and S =1.256·10^{-7} *cm*^{2} we have next value of W_{avdr} 1.6 *J*/*cm*^{2} and 2.4 *J*/*cm*^{2}. If we multiple these value of the absorbance index of *SiC* α = 0,1 *cm*$^{-1}$ then we are receiving the volume density of energy $W_{avdrvol}$ 0.16 *J*/*cm*^{3} and 0.24 *J*/*cm*^{3}. Really value is 0,4 from represented data (reflectance is 0.6) and are 0,064 and 0.096 *J*/*cm*^{3} [231].

Correlation ${W_{avdrvol}}/{W_{crvol}}$ for real values for *SiC* is equaled from 27 to 2700 [231].

Density of energy of optical breakdown W_{ob} for *SiC* is equaled 18800 *J*/*cm*^{3}. Therefore, correlation ${W_{ob}}/{W_{avdrvol}}$ is equaled 78333 and 117600 [231].

The analogous chain processes may be mage for other media (*LiF*, water, hard water, CaF_2, *NaCl*, CS_2, CCl_4, C_2HCl_3 and fused silica) [231].

Concept of diffractive stratification allows explaining the surface character of Cherenkov radiation. This radiation is generated in the region of corresponding focused diffractive ring [232, 233].

In Rayleygh case cavitations' bubbles have sizes from a few millimeters to a few centimeters [232, 233].

In our case (Fig. 5.7 (c)) sizes of our nanovoids are equaled 15 – 20 *nm*. Therefore, we must change "sound" mechanism of creation cavitations bubbles on electromagnetic. Roughly speaking, this problem was resolved with help change speed of sound or speed of light.

The sizes of nanovoids (Fig. 5.7 (c)) may be determined with help modified Rayleygh model [120, 174, 176] and its form – the help methods of continuum mechanics [232, 233] in next way.

Nanovoids may be represented as results of the laser-induced laser-induce breakdown and creation of cavitations bubbles [232, 233] too. The light pressure may be determined with help of next formula [191]

$$p_0 = \frac{E_{ir}}{\tau_i c S}, \quad (5.71)$$

where E – energy of irradiation, τ_i – pulse duration, S – area of irradiation zone, c – speed of light. For circle symmetry

$$S = \pi r^2, \quad (5.72)$$

where r – radius of laser spot.

For the estimations of maximal radius of nanovoids we must use modified Rayleygh formula [170, 232, 233]

$$R_{max} = \frac{2R}{0.915r}\sqrt{\frac{E_{ir}}{\pi\tau_{ir}cE}}, \tag{5.73}$$

where T_c – the time of creation the nanovoid (bubble), R is radius of nanovoid, r – radius of irradiated zone, E – Young module, E_{ir} – energy of one pulse. τ_{ir} – duration of pulse [232, 233].

If we substitute r = 250 *nm*, R = 10 *nm*, E=600 *GPa* [148, 182, 232, 233], E_{ir}=300 *nJ*, τ_{ir} = 130 *ps*, c=3·10^8 *m/s*, than have R_{max}=11 *nm*.

The speed of shock waves for femtosecond regime of irradiation is less as speed of sound. However, we have two speeds of sound in elastic body: longitudinal v_{ls} and transversal v_{ts} [232, 233]. Its values are determined with next formulas

$$v_{ls} = \sqrt{\frac{E(1-\nu)}{\rho_0(1+\nu)(1-2\nu)}}, \text{ and } v_{ts} = \sqrt{\frac{E}{\rho_0(1+\nu)}} \tag{5.74}$$

where ν – Poisson's ratio [232, 233]. The ratio between of these two speeds is equaled

$$\alpha = \frac{v_{ts}}{v_{ls}} = \sqrt{\frac{(1-2\nu)}{2(1-\nu)}}. \tag{5.75}$$

However, this ratio must be true for shock waves too. Therefore, for silicon carbide for ν = 0,45 [148, 182, 232, 233] α = 0,33. Roughly speaking last ratio is determined the step of ellipsoidal forms of our nanovoids (Fig. 4.5 (h)).

In [232, 233] allow estimating maximal longitudinal and transversal $R_{\max i}, i \in (l,t)$. These values are 6 *nm* and 19 *nm* properly.

In this case we represented 4H-SiC as isotropic plastic body. For real picture we must represent hexagonal structure. But for the qualitative explanation of experimental data of Fig. 5.7 this modified Rayleygh model allow explaining and estimating the sizes and forms of receiving nanovoids [232, 233].

As we see, for laser-induced breakdown we must include self-focusing processes too. The problem of creation initial inoculating concentration of electrons is one of main problems Nonlinear Optics too. Therefore, we must include in the problem of optical breakdown the heterogeneity materials and heterogeneity of interaction light and matter, including diffraction

stratification, generation of continuum radiation (including Cherenkov radiation), interference Cherenkov radiation and direct optical breakdown. These addition factors allow explaining basic peculiarities of interaction laser irradiation and matter, including gases [232, 233]. But for more long time of irradiation we have second-order processes of disorder radiation, including reradiation and reabsorption [232, 233]. In this case we may be having processes of heating and creation of plasma clouds [267-269]. For shorter regime irradiation a probability of cascade step-by-step laser-induced direct multiphotonic excitation is increased and therefore we have third scenario of these processes [232, 233]. Thus, methods of Relaxed Optics allow integrating processes of radiated and non-radiated relaxation (Nonlinear and Relaxed Optics) of first-order optical excitation in one system and allow explaining processes of laserinduced optical breakdown and shock processes with one point of view. For qualitative explanation of corresponding experimental data we must add using methods by physical-chemical models and methods of diffraction stratification and laser-induced Cherenkov radiation [232, 233]. Laser-induced shock processes have specific peculiarities. In general case we have electromagnetic and acoustic shock processes [232, 233]. Formally, these processes have similar nature. Speed of electromagnetic shock processes (speed of polarization the media in the result of corresponding interaction) must be more as phase speed of light in media. In this case, phase speed of light in media has next physical nature: it is speeding of collectivization the electromagnetic oscillations for proper frequency. Roughly speaking it is electromagnetic characteristic of media, which is corresponded to its electron and ion subsystems. Example of this type process is Cherenkov radiation. In this case, we have radiated reaction of media on heterogeneity excitation of media in shock regimes of interactions. Speed of acoustic shock processes (speed of motion proper object in media) must more as speed of sound in media [232, 233]. But speed of sound is media is average heat speed of media, which is connected with atomic structure of media. Examples of these processes are next: flight of airplane or rocket in with supersonic speed; various explosions. Roughly speaking, explosions may be characterized as chemical process with speed more as sound speed in media. Mach number is characterized in this case the macroscopic “detonation” of corresponding process. Both processes (electromagnetic and acoustic) are characterized by Much cone, which is created by proper vectors of speed processes or object and speed characteristic of media (polarization or sound) [232, 233]. Laser-induced shock processes may be represented as analogous to acoustic explosions. But this process is realized with electromagnetic speed. In this case we must have “electromagnetic” explosion as Cherenkov radiation [232,

[233]. Due to the similarity of electromagnetic and acoustic processes of kinetic processes, we can use both to estimate the parameters of impact processes, to determine the size of nanovoids, using the electromagnetic modified Rayleigh model (formula (5.73)) and to determine the shape of nanovoids, acoustic formula (5.75). The formation the laser-induced shock processes may be explained with help concept of coherent structures of Relaxed Optics [6]. In this case generation of proper shock process may be represented as chain of coherent processes of interaction light and matter with electromagnetic speed. In this case, summary speed of chain process must be less as phase speed of light in media but speed of each term of this chain must be more as phase speed of light in media. It is basic peculiarity of formation laser-induced shock processes comparatively with other electromagnetic processes. From point of view the kinetic concept of Relaxed Optics [234] we must have multiphotonic process in the regime of saturation the excitation [232, 233]. In whole the nonequilibrium and irreversible shock processes may be having electromagnetic and acoustic nature [232, 233]. Nature of laser-induced breakdown is determined by speed of energy transfer from laser irradiation to matter. For impurity mechanisms of absorption, the laser radiation may be realized next scenario [232, 233]:

1) Multiphotonic absorption is comparatively low intensity but time of irradiation is long run. In this case, we have heating of matter in the region of the absorption of laser radiation and thermal mechanism of optical breakdown. Other words absorptive energy may be represented as heat, which is cause the heating of media and its thermal breakdown. These process is characterized the speed of sound in matter and time of creation the heating of irradiated material is equaled ~ $(10^2 - 10^3)\tau_i$ for millisecond and nanosecond regimes of irradiation [232, 233].

2) Multiphoton absorption is higher, but it may be source of other collective physical phenomena-generation of plasma, which may be used for the breakdown of irradiated matter. It is plasma mechanism of optical breakdown. Time of formation the plasma in irradiate matter is lesser and roughly speaking it determine the speed of light. In whole the speed of this process is lesser as phase speed of light in irradiated matter. But this time is depending from intensity of irradiation too.

3) Multiphotonic absorption is higher as in case 2 and may be source of direct optical breakdown. However, this process must have speed more as phase speed of light in media. The dimensions of the cavities

that are formed during electromagnetic and acoustic breakdown are proportional to the square root of the corresponding velocity (formula (5.73). Taking this into account, the sizes of acoustic voids in silicon microbead will be on the order of a centimeter. The cone of Cherenkov radiation in the optical case is determined by a cascade of successive light scattering and the corresponding nonlinear polarization of the medium. Therefore, the angle of the Cherenkov radiation is perpendicular to the propagation front of the nonlinear polarization. If the system tends to thermodynamic equilibrium, this trend disappears. This is confirmed by the fact that there is no big difference between nanosecond (Fig. 5) and femtosecond (Fig. 6 and Fig. 7) irradiation modes. The efficiency of radiation conversion into breakdown energy is on the order of 10-15 percent. In general, this is determined by the integral photon efficiency of the corresponding cascade process. A. Bohr's model can be applying to relaxation-optical processes, since in this case the displacement of atoms is directly proportional to the intensity of excitation. But in the case of laser irradiation, we have one irradiation cone and a certain number of diffraction cones. Each diffraction cone is a source of Cherenkov radiation defined by a Mach cone, the characteristics of which are determined by the laser-generated nonlinear characteristics of the irradiated medium. The spectrum of Cherenkov radiation in the case of A. Bohr is determined by a set of hyperboloids, i.e. electromagnetic traces of tracks of incoming particles, and with uniform irradiation; it will be more or less uniform. In the case of optically-induced Cherenkov radiation, the short-wavelength region, as can be seen from Fig. 5.6 and Fig. 5.7, will be concentrated near the optical axis. There is formally no difference between acoustic and electromagnetic shock wave processes. However, when forming nanovoids, we are not dealing with wave but quantum multiphoton processes, which ultimately determine the formation of nanovoids.

Laser-induced shock processes have specific peculiarities. In general case we have electromagnetic and acoustic shock processes [232, 233]. Formally these processes have similar nature.

Speed of electromagnetic shock processes (speed of polarization the media in the result of corresponding interaction) must be more as phase speed of light in media. In this case phase speed of light in media has next physical nature: it is speeding of collectivization the electromagnetic oscillations for proper frequency. Roughly speaking it is electromagnetic characteristic of

media, which is corresponded to its electron and ion subsystems. Example of this type process is Cherenkov radiation. In this case we have radiated reaction of media on heterogeneity excitation of media in shock regimes of interactions.

Speed of acoustic shock processes (speed of motion proper object in media) must more as speed of sound in media [120, 232, 233]. But speed of sound is media is average heat speed of media, which is connected with atomic structure of media. Examples of these processes are: flight of airplane or rocket in with supersonic speed; various explosions. Roughly speaking, explosions may be characterized as chemical process with speed more as sound speed in media. Mach number is characterized in this case the macroscopic "detonation" of corresponding process.

Both processes (electromagnetic and acoustic) are characterized by Much cone, which is created by proper vectors of speed processes or object and speed characteristic of media (polarization or sound) [232, 233].

Laser-induced shock processes may be represented as analogous to acoustic explosions. However, this process is realized with electromagnetic speed. In this case, we must have "electromagnetic" explosion as Cherenkov radiation [232, 233].

The formation the laser-induced shock processes may be explained with help concept of coherent structures of Relaxed Optics [233, 235]. In this case generation of proper shock process may be represented as chain of coherent processes of interaction light and matter with electromagnetic speed. In this case summary speed of chain process must be less as phase speed of light in media but speed of each term of this chain must be more as phase speed of light in media. It is basic peculiarity of formation laser-induced shock processes comparatively with other electromagnetic processes. From point of view the kinetic concept of Relaxed Optics [235] we must have multiphotonic process in the regime of saturation the excitation.

In whole the nonequilibrium and irreversible shock processes may be having electromagnetic and acoustic nature [232, 233].

But laser-induced optical breakdown is possible only in volume of irradiated matter. On surface we will be have ablation for thermal and plasma mechanisms of laser-induced optical breakdown and sublimation for plasma and direct mechanisms of optical breakdown.

Now we used physical-chemical method of estimation for the modeling experimental data for *KCl* (Fig. 5.5). Density of atoms of *KCl* was determined

with help formula (5.68) and it equal $3.1 \cdot 10^{22} cm^{-*3}$ Zeits energy for KCl has value ~ 30 eV [229].

Results of modeling are represented in Table 5.2.

Table 5.2: Main characteristics for laser-induced optical breakdown for *KCl* (Fig. 5.5)

Figure	$d_{average}$, μm	*l, mm*	V_{ob}, 10^{-7} cm^{-7}	N_{ob}, 10^{15}	E_{KClob}, 10^{-2} J
Fig. 5.5(a)	0,5	2	1,57	4,87	2,32
Fig. 5.5(b)	0,5	3	2,36	7,31	3,48

We used next approximations. Photography of Fig. 5.5 gives a blurry image compared to the bright-field TEM image of Fig. 5.6. Therefore, we can't see the microstructure of optical breakdown. And we use rough average approximations for diameter $d_{average}$ and length l of cascade laser-induced optical breakdown of Fig. 5.5 [233]. Volume of cascade was determined as cylinder volume.

Fig. 5.5 is similar to Fig. 5.6 c). However, regimes of irradiation of Fig. 5.5 are similar to mode TEM_{01}. Therefore, we have two channels of generation the cascade of laser-induced optical breakdown.

The distances between bubbles of Fig. 5.5 (b) are more as between regions of destruction of Fig. 5.6(c). Nevertheless, conditions of focusing the radiation in these both cases are equivalence. Therefore, the distances between neighboring bubbles l_2 of Fig. 5.5(b) and neighboring regions of destruction l_1 of Fig. 5. 6(c) are connected by next formula [233]

$$l_2 = \frac{d_{ndif2}\tan\left(\varphi_1/_2\right)}{d_{ndif1}\tan\left(\varphi_2/_2\right)} l_1 = \frac{\lambda_2 \tan\left(\varphi_1/_2\right)}{\lambda_1 \tan\left(\varphi_2/_2\right)} l_1. \qquad (5.76)$$

In whole, the correlation of this distasnces is depended from wavelength of irradiation and focusing angles, including intensity of irradiation? Which is determined the step o f homogeneity of irradiated matter. If we substitute in formula (5.76) $\lambda_2 = 10.6 \mu m$ and $\lambda_1 = 0.8 \mu m$ and $\varphi_1 = \varphi_2$ then we'll receive

$$l_2 = 13.25 l_1. \qquad (5.76a)$$

Energy characteristics of irradiation weren't represented in [267] but were reference on [21]. Therefore, we select value 2 *J*/*pulse* from [232, 233]. In this case we have effective using energy. Methods of estimations of energy characteristics of Table 4.1 are rougher as for 4H-*SiC*. But we must suppose that focused laser irradiation has diffraction stratification, generation of Cherenkov radiation and interference of this Cherenkov radiation. On Fig. 5.5

(b) 5-7 steps of cascade optical breakdown we see. Sources of Cherenkov radiation id diffraction stratified cones.

If this scenario is true, we have as for 4H-SiC effective transformation the energy of laser radiation to cascade of laser-induced breakdown for *KCl* too. This value is 11,6 – 17,4 percents.

We can estimate sizes and forms of possible nanovoids for potassium chloride too. Let's take the ratio of the radius of the irradiation zone to the radius of the nanowire as 50. The energy of irradiation is 2 *J*. The duration of irradiation is 50 *ns*. Young's modulus 29.67 *GPa*, Poisson's ratio 0.216.

After substitution these data to formula (5.73) we have $R_{maxKCl} = 62.5nm$. Ellipticity of *KCl* nanovoids may be determined from (5.75). $\alpha_{KCl} = 0.6$.

Let us now estimate the maximum bubble radii for the acoustic case. For this, in formula (5.73), you need to change the speed of light to the speed of sound (5.73 a).

$$R_{max}^{ac} = \frac{2R}{0.915r}\sqrt{\frac{E_{ir}}{\pi\tau_{ir}c_s E}}, \qquad (5.73\text{ a})$$

where c_s is speed of sound.

As a result, we get $R_{maxSiC}^{ac} = 1.7\mu m$ and $R_{maxKCl}^{ac} = 28\mu m$. The shape of the voids does not change, they just increase in size by 2-3 orders of magnitude.

If we take the ratio of the acoustic formula (5.73 a) and the optical formula (5.73), then for the same irradiation modes we have the ratio

$$\frac{R_{max}^{ac}}{R_{max}} = \sqrt{\frac{c}{c_s}}. \qquad (5.77)$$

However, a comparison with the experimental results (Fig. 5.6) shows that the main role in the formation of nanovoids is played by electromagnetic rather than acoustic processes. This is explained by the fact that in this case a chain of close-range coherent processes of transformation of both optical radiation into the excitation of the medium and the corresponding relaxation of the medium is implemented, in other words, there is a chain of interconnected coherent transformations.

In the acoustic case, the entire environment reacts, while the results of the interaction of light with matter managed to "collectivize" and that is why the result of the interaction can be considered as the result of the action of a quasi-classical body (in this case, a laser pulse) on the environment.

Experimental data, which are represented in Fig. 5.5 and Fig. 5.6, are similar to bead lightning [232, 233] and resembles a frozen picture in a travelling wave lamp [232, 233]. But for the formation these processes we must have two electrodes and modulated external field. For the case of laser-induced breakdown we have only laser field, its nonlinear transformation, including diffractive stratification of laser beam, a generation of Cherenkov radiation and its interference, and multiphoton absorption. In this case we have inner nonlinear and relaxed optical processes.

As we see basic mechanism the inhomogeneities cascade damages of laser-induced optical breakdown is nonlinear optical transformation of initial radiation. Inclusions in 4H-SiC and KCl are distributed homogenously and therefore one can't be the source of laser-induced heterogeneities.

Possible applications of phenomena and processes of laser-induced breakdown of matter may be distributed on two groups: positive and negative [233].

Negative processes are connected with laser-induced destruction of corresponding elements of optoelectronic systems and decreasing of its lifetime. Therefore, in this case we must use only low intensity irradiation and unfocused irradiation. These procedures must be included in work regimes of fiber optic communication lines and other devices of modern photonics.

Positive application may be next. Well known the using laser irradiation for the laser-annealing of ion-implanted layers of semiconductors [233] and for the increasing the lifetime of magnetic sensors and other elements of nuclear reactors [233]. In this case we have low intensity of irradiation of light scattering on unstable or metastable centers, basically photochemical processes.

Next stage of possible applications laser-induced, including optical breakdown, processes is next. Focused laser irradiation may be used as source of diffraction stratification of initial laser irradiation, a generation of Cherenkov radiation, interference of this Cherenkov radiation and the creation cascade of destruction, which can use as volume diffractive lattices or other elements of controlling the laser irradiation and as elements of multifunctional heterostructures (Fig. 4.5 and Fig. 4.6). These multifunctional structures may be used as passive and active elements with various system values. Roughly speaking it may be semireproducing devices.

The laser-induced optical breakdown of matter may be used for the change functional properties of optoelectronic devices and elements and for the creation new systems.

In more general case the methods of Relaxed and Nonlinear Optics may be used for the creation new elements of optoelectronic systems with nonequilibrium and irreversible properties [233].

It may be used for the creation new circle elements and devices and expansions of functional activity of existing devices.

The laser-induced optical breakdown of air may be used for energy transmission over long distances [233].

An interchange of Relaxed and Nonlinear optical processes may be used for the creation new devices for the work in aggressive and hard-to-reach media, including chemical and nuclear industries, cosmos, ocean and for the creation new chapters of laser technologies [233].

Possible applications of phenomena and processes of laser-induced breakdown of matter may be distributed on two groups: positive and negative [233].

Negative processes are connected with laser-induced destruction of corresponding elements of optoelectronic systems and decreasing of its lifetime. Therefore, in this case we must use only low intensity irradiation and unfocused irradiation. These procedures must be included in work regimes of fiber optic communication lines and other devices of modern photonics.

Positive application may be next. Well known the using laser irradiation for the laser-annealing of ion-implanted layers of semiconductors [104, 218] and for the increasing the lifetime of magnetic sensors and other elements of nuclear reactors [232]. In this case we have low intensity of irradiation of light scattering on unstable or metastable centers, basically photochemical processes.

Next stage of possible applications laser-induced, including optical breakdown, processes is next. Focused laser irradiation may be used as source of diffraction stratification of initial laser irradiation, a generation of Cherenkov radiation, interference of this Cherenkov radiation and the creation cascade of destruction, which can use as volume diffractive lattices or other elements of controlling the laser irradiation and as elements of multifunctional heterostructures (Fig. 5.5, Fig. 5.6 and Fig. 5.7). These multifunctional structures may be used as passive and active elements with various system values. Roughly speaking it may be semireproducing devices.

The laser-induced optical breakdown of matter may be used for the change functional properties of optoelectronic devices and elements and for the creation new systems.

In more general case the methods of Relaxed and Nonlinear Optics may be used for the creation new elements of optoelectronic systems with nonequilibrium and irreversible properties [232, 233].

It may be used for the creation new circle elements and devices and expansions of functional activity of existing devices.

The laser-induced optical breakdown of air may be used for energy transmission over long distances [232, 233].

An interchange of Relaxed and Nonlinear optical processes may be used for the creation new devices for the work in aggressive and hard-to-reach media, including chemical and nuclear industries, cosmos, ocean and for the creation new chapters of laser technologies [232, 233].

Thus, laser-induced shock processes can cause both electromagnetic and acoustic processes. This is due to the light absorption conditions, the properties of the irradiated material, and the secondary relaxation processes of the shock excitation.

5.6 Conclusions

1. Main concepts of modeling the laser-induced shock processes in Nonlinear and Relaxes Optics are observed.
2. Short review of corresponding experimental data is represented.
3. Elements of classical (acoustic) theory of shock processes are discussed.
4. Short analysis of Rayleygh theory of cavitation is represented.
5. Main extensions of Rayleigh's theory Rayleigh–Plesset, Gilmore; and Keller–Miksis models are discussed.
6. Necessary of transition to chain methods of modeling the shock processes of Nonlinear and Relaxed Optical processes is formulating.
7. Peculiarities of optical-induced Cherenkov radiation and laser-induced breakdown are discussing.
8. The difference between acoustic and electromagnetic shock processes shown on the example the generation laser-induced nanovoids in silicon carbide and potassium chloride.
9. Comparative analysis of other properties of acoustic and electromagnetic chock processes is representing too.

References

1. Abraham F.F. Homogeneous nucleation theory: Suppl. to Adv. Theor. Chem. Ch. 14. – N.Y.: Acad, press, 1974. – 263 p.
2. Adamson A. W., Gast A. P. Physical chemistry of surfaces – N.-Y.: John Wiley @ Sons, Inc.,1997. – 782 p.
3. Agraval G. Nonlinear fibering optics. – Moscow: Mir, 1996. –324 p. (In Russian)
4. Ahuja R., Ferreira da Silva A., Persson C., Osorio-Gullién G., Pepe I., Järendahl K., Lindquist O. P. A., Edwards N. V., Wahab Q., Johansson B. Optical Properties of 4H-SiC.// J. Appl. Phys., vol. 91, is. 4, 2002. – P. 2099 – 2103.
5. Aközbek N., Scalora M., Bowden C. M., Chin S. L. White-light continuum generation and filamentation during the propagation of ultra-short laser pulses in air.// Opt. Commun. Vol.191, 2001. – P. 353–362.
6. Akulichev V. A. Acoustic cavitation in low-temperature liquids.// Ultrasonics, vol. 24, 1984. – P. 8–18.
7. Alexander A. J., Camp P. J. Non-photochemical laser-induced nucleation.// *J. Chem. Phys.* Vol. 150, is. 4, 2019. – P. 040901-040904.
8. Aleksenko A. G. Graphen. – Moscow: Binom, 2014. – 168 p. (In Russian)
9. Alfano, R. R. Ed. The Supercontinuum Laser Source. – NY.> Springer, 2006. – 537 p.
10. Alfano R. R., Shapiro S. L. Emission in the region 4000 to 7000 Å via four-photon coupling in glass.// Phys. Rev. Lett. Vol. 24, is. 11, 1970. – P. 584–587.
11. Andrews H. L., Boulware C. H., Brau C. A., Jarvis J. D. Dispersion and attenuation in a Smith-Purcell free electron laser.// Physical review special topics – accelerators and beams, vol. 8, is.5, 2005. – P. 050703-1 – 050703-9.
12. Apeksimov D. V., Bukin O. A., Bykova E. E., Geints Yu. E., Golik S. S., Zemlyanov A. A., Ilyin A. A, Kabanov A. M., Matvienko G. G., Oshlyakov V. K., Petrov A.V., Sokolova E. B. Impact of femtosecond

laser pulses for millimetre water drops.// News of higher educational institutions. Physics, vol. 55, № 9/2, 2012. – P. 187-190 (In Russian)

13. Arutyunyan V.M., Oganesyan S.G. Stimulared Cherenkov effect. // Progress of Physical sciences, vol. 164, No.10, 1998. – P.1089-1125. (In Russian)

14. Avsarkisov S.A., Jibuti Z.V., Dolidze N.D., Tsekvava B.E. Low-themperature crystallization of amorphous silicon under laser irradiation.// J. Techn. Phys., vol.32, No.6, 2006. – P. 55-60 (In Russian)

15. Aumiler D., Ban T., Pichler G. Femtosecond laser-induced cone emission in dense cesium vapor. Phys. Rev. A. Vol. 71, is. 6, 2005. – P. 063803-1 – 063803-4.

16. Baldeck P. L., Alfano R. R. Intensity effects on the stimulated four photon spectra generated by picosecond pulses in optical fibers.// J. Lightwave Technol. LT-5, 1987. – P.1712– 1715.

17. Baranskyy P. I., Klochkov V. P., Potykevich I. V. Semiconductor electronics. Reference book. – Kiev: Naukova Dumka, 1975. – 704p. (In Russian)

18. Batra R. C. Elements of Continuum Mechanics. – Reston: American Institute of Aeronautics and Astronautics, 2005. – 325 p.

19. *Bauer E. Phänomenologische Theorie der Kristallabscheidung an Oberflächen. I. //Zeitschrift für Kristallographie. Vol.110, 1958. – S. 372–394.*

20. Bazylev V. A.; Glebov, V. I.; Denisov Eh. I.; Zhevago N. K.; Kumakhov M. A.; Khlebnikov A.S.; Tsinoev, V. G. X-ray Cherenkov radiation. Theory and experiment.// JETP, vol. 81, is. 11, 1981. – P. 1664-1680.

21. Beaulieu A. J. Transversally excited atmospheric pressure CO_2 lasers,. Phys. Lett., vol.16, is.12, 1970. – P.504-505.

22. Becker R. Kinetische Behandlung der Keimbildung in übersättigten Dampfen // Ann. Physik. – 1935. – Bd.24, H.8. – S.719 – 752.

23. Beaud, P., Hodel W., Zysset B., Weber H. P. Ultrashort pulse propagation, pulse breakup, and fundamental soliton formation in a single-mode optical fiber.// IEEE J. Quantum Electron. QE-23, 1987. – P.1938–1946.

24. Bilaniuk O. M. P., Deshpande V. K., Sudarshan F. C. G. «Meta» relativity.// Amer. J. Phys., vol. 30, 1962. – P. 718-723.

25. Birnbaum M. Semiconductor surface damage produced by Ruby Laser.// Journal of Applied Physics, vol. 36, Issue 11, 1965. – P. 3688–3689.

26. Bleko V., Karataev P., Konkov A., Kruchinin K., Naumenko G., Potylitsyn A., Vaughan T. Coherent Cherenkov radiation as an intense THz source.// Journal of Physics: Conference Series, vol. 732, 2016. – P. 012006-1 – 012006-7.

27. Bloembergen N. 1973, The influence of electron plasma formation on superbroadening in light filaments. Opt. Commun. Vol. 8, 1973. – P.285–288.

28. Blumenthal, Deborah T.; Corn, Benjamin W.; Shtraus, Natan (August 2015). Flashes of light-radiation therapy to the brain.//Radiotherapy and Oncology, vol. 116, is.2, 2015. – P. 331–333.

29. Bobytski Ya. V., Matviyishyn G. L. Laser technologies. Part 1. – Lviv: Lvivska Politekhnika Publishing, 2015. – 319 p. (in Ukrainian)

30. Bobytski Ya. V., Matviyishyn G. L. Laser technologies. Part 2. – Lviv: Lvivska Politekhnika Publishing, 2020. – 320 p. (in Ukrainian)

31. Bockris John O'M. Reddy Amulya K. N. Modern electrochemistry. V.1, 2. – New York: Cluwer Publishing, 2002. – 769p.

32. Bogatyryov V.A., Kachurin G.A. The creation low resistively n-layers on *InSb* with help the impulse laser irradiation.// Physics and technical of semiconductors, v.11, No.1, 1977. – P.100-102. (In Russian).

33. Bohr A. The influence of atoms interactions on the penetration of particles through matter. In: Bohr N. The penetration of atomic particles through matter. Moscow: Inostrannaya literatura, 1950. – P. 105-143.

34. Boky G. B. Crystal chemistry. – Moscow: Nauka, 1971. – 400 p. (In Russian)

35. Bolotovskiy B. M., Ginzburg V. L. Vavilov-Cherenkov and Doppler effects in the time the motion of sources with speed greater as light speed in vacuum.// Advanced in physical science. Vol. 106, Is. 4, 1972. – P. 577-592 (In Russian)

36. Bondarenko N. G., Eremina I. V., Talanov V. I. Broadening of spectrum in self-focusing of light in crystals. JETP Letters. Vol.12, is. 3, 1970. – P.125–128. (In Russian)

37. Botsaris G. D. Secondary Nucleation – A Review. In Mullin J. (ed.). Industrial Crystallization. – Berlin: Springer, 1976. – P. 3–22.

38. Boyraz, Ö., J. Kim, M. N. Islam, F. Coppinger, and B. Jalali, 2000, “10 Gb/ s multiple wavelength, coherent short pulse source based on spectral carving of supercontinuum generated in fibers,” J. Lightwave Technol. 18, 2167–2175.

39. Brewer, R. G. Frequency shifts in self-focused light.// Phys. Rev. Lett. Vol.19, is. 1, 1967. – P.8–10.

40. Brodeur A., Chin S. L. Band-gap dependence of the ultrafast white-light continuum.// Phys. Rev. Lett., vol. 80, no. 20, 1998. – P. 4406–4409.

41. Burton W. K., Cabrera N. Crystal growth and surface structure. Part I. //Discussions of the Faraday Society. Vol. 5, 1949. – P. 33-39.

42. Burton W. K., Cabrera N. Crystal growth and surface structure. Part II. // Discuss. Faraday Soc. Vol. 5, 1949. – P. 40-48.

43. Buts V. A. Parametric Cherenkov radiation (development of the idea) // Questions of atomic science and technology. No. 4, 2004. – P. 70-75. (In Russian)

44. Byun Ki-Taek, Kwak Ho-Young. A Model of Laser-Induced Cavitation.// Japanese Journal of Applied Physics. Vol. 43, No. 2, 2004. – P. 621–630

45. Chandramouli P. N. Continuum mechanics. – New Delhy: Yes Dee Publishing Pvt. Ltd., 2014. – 854 p.

46. Chekalin S. V., Kandidov V. P. From self-focusing light beams to femtosecond laser pulse filamentation. Advanced in physical science. Vol. 56, Is. 2, 2013. – P.123-140 (In Russian)

47. Chernetska A. A simulation of laser-induced optical breakdown the environment. Magister thesis. – Lutsk: Lesya Ukrainka Volyn National University, 2021. – 67 p. (In Ukrainian)

48. Chiao, R. Y., Garmire E., Townes C. H. Selftrapping of optical beams.// Phys. Rev. Lett. 13, 1964. – P.479–482.

49. Conti C, Trillo S, Di Trapani P, Valiulis G, Piskarskas A, Jedrkiewicz O, Trull J. Nonlinear electromagnetic X-waves. //Phys. Rev. Lett. Vol. 90, Is. 17, 2003. – 170406-l –170406-4.

50. Corcum P. B., Rolland C., Shrivasan-Rao T. Supercontinuum generation in gases. Phys. Rev. Lett. Vol. 57, Is. 18, 1986. – P. 2268-2271

51. Costache E., Kouteva-Anguiriva S., Reif J. Sub-damage-threshold femtosecond laser ablation from crystallic Si:surface nanostructures and phase transformations.// Appl. Phys. A, vol. 79, 2004. – P. 1429 – 1432.

52. Danos M., Geshwind S., Lashinsky H., Van Trier A. Cherenkov Effect at Microwave Frequencies.// Phys. Rev., vol.92. – P. 828-829.

53. Dianov, E. M., A. Ya. Karasik, P. V. Mamyshev, A. M. Prokhorov, V. N. Serkin, M. F. Stel'makh, and A. A. Fomichev, 1985, Stimulated-Raman conversion of multisoliton pulses in quartz optical fibers.// Pis'ma Zh. Eksp. Teor. Fiz., Vol. 41, 1985. – P. 242–244 (In Russian).

54. Di Trapani P, Valiulis G, Piskarskas A, Jedrkiewicz O, Trull J, Conti C, *et al*. Spontaneously generated X-shaped light bullets. Phys. Rev. Lett., vol.91, is. 9, 2003. – 093904-1 – 093904-4.

55. Donachie M. J. Titanium: A Technical Guide. – Ohio: Materials Park, 2000. – 380 p.

56. Dowty E. Crystal Growth and nucleation theory and the numerical simulation of igneous crystallization. Chapter 10. Physics of Magmatic Processes, edited by R.B. Hargraves. Princeton: Princeton University Press, N.J., 1980. – P. 419-485.

57. Druzhinin A. O., Ostrovskij I. P., Kogut Yu. R. Filamentous crystals of silicon, germanium and their solutions in sensor electronics. – Lviv: National University "Lvivska Polytekhnika" Press, 2010. – 200 p. (In Ukrainian)

58. Dudley J. M., Genty G., Coen S. Supercontinuum generation in photonic crystal fiber. Reviews of modern physics. Vol. 78, 2006. – P. 1135-1185.

59. Dyshko A. L., Lugovoi V. N., Prokhorov A. M. Self-focusing of Intense Light Beams. // JETP Letters, vol. 6, Is. 5, 1967. – P. 146–148 (In Russian).

60. https://en.wikipedia.org/wiki/Cherenkov_radiation

61. Faccio D, Porras M, Dubietis A, Bragheri F, Couairon A, Di Trapani P. Conical emission, pulse splitting and X-wave parametric amplification in nonlinear dynamics of ultrashort light pulses. Phys. Rev. Lett., vol.96, is. 19, 2006. –193901-1 – 193901-4.

62. Fainberg Ya. B., Khizhnyak N.A.. Loss of energy by a charged particle when passing through a layered dielectric // JETP. vol. 32, issue 4, 1957. – P. 883-895 (In Russian)

63. Faingold M. I. To the problem Cherenkov radiation of tachyon.// Theoretical and mathematical physics, vol. 47, is 3, 1981. – P. 395-406. (In Russian)

64. Fedosyuk V.M. Nanostructural films and nanowires. – Minsk: Belorussian University Press, 2006. – 311 p. (In Russian)

65. Feinberg G. Possibility of faster-than-light particles.// Phys. Rev. Vol. 159, No. 5, 1967. – P.1089-1105.

66. Felsen L. B., Marcuvitz N. Radiation and Scattering of Waves. – New York: John Wiley @ Sons, 1994. – 924 p.

67. Fermi E. The Ionization Loss of Energy in Gases and in Condensed Materials. Phys. Rev. Vol. 57, 1940. – P. 485-493.

68. Fork R. L., Shank C. V., Hirlimann C., Yen R., Tomlinson W. J. Femtosecond white-light continuum pulses. Opt. Lett., vol. 8, is. 1, 1983. – P. 1–3.

69. Frank I. M. Vavilov-Cherenkov radiation. Theoretical aspects. – Moscow: Nauka, 1988. – 286 p. (In Russian)

70. Frenkel Ya.I. Kinetic theory of liquids / Yakov Ilyich Frenkel. – M.: Publishing House of the Academy of Sciences of the USSR, 1945. – 342 p. (In Russian)

71. Friberg S. R., DeLong K. W. Breakup of bound higher-order solitons. Opt. Lett. Vol. 17, 1992. – P.979–981.

72. Gaeta, A. L. Catastrophic collapse of ultrashort pulses.// Phys. Rev. Lett. Vol. 84, 2000. – P.3582–3585.

73. Gibbs J. V. Thermodynamics. Statistical mechanics. – Moscow: Nauka, 1982. –584 p. (In Russian)

74. Gillam J.E., MacPhee C.E. Modelling amyloid fibril formation kinetics: mechanisms of nucleation and growth.// Journal of Physics: Condensed Matter. Vol. 25, Is. 37, 2013. – 373101(20 p.).

75. Golovchenko, E. A., Mamyshev P. V., Pilipetskii A. N., Dianov E. M. Mutual influence of the parametric effects and stimulated Raman scattering in optical fibers.// IEEE J. Quantum Electron. Vol. 26, 1990. – P.1815–1820.

76. Golovchenko, E. A., Mamyshev P. V., Pilipetskii A. N., Dianov E. M. Numerical analysis of the Raman spectrum evolution and soliton pulse generation in single-mode fibers.// J. Opt. Soc. Am. B. Vol. 8, 1991. – P. 1626–1632.

77. Golub I. Optical characteristics of supercontinuum generation.// Optics Letters. Vol. 15, Is.6, 1990. – P. 305-307.

78. Golub I., Shuker R., Eres G. On the optical characteristics of the conical emission.// Optics Communications. Vol. 57, Is. 2, 1986. – P. 143-145.

79. Gordon, J. P. Theory of the soliton self-frequency shift.// Opt. Lett. Vol. 11, 1986. – P. 662–664.

80. Gouveia-Neto A. S., Faldon M. E., Taylor J. R. Solitons in the region of the minimum group-velocity dispersion of single-mode optical fibers.// Opt. Lett. Vol. 13, 1988. – P.770–772.

81. Grigonis A., Medvid A., Onufrijevs P., Babonas J., A Reza A. Graphitization of amorphous diamond-like carbon films by laser irradiation. Optical Materials. Vol. 30, 2008: – P. 749-752.

82. Haken H. Synergetics. – Moscow: Mir, 1980. – 406 p. (In Russian)

83. Hasegawa A., Tappert F. Transmission of stationary nonlinear optical pulses in dispersive dielectric fibers. I. Anomalous dispersion.// Appl. Phys. Lett. Vol. 23, 1973. – P.142–144.

84. Hegazy M.S., Elsajed-Ali H.E. Nonthermal laser-indused formation of crystalline Ge quantum dots on Si (100). // J. Appl. Phys., vol. 112, No.2, 023118, 2012. – P.1–5.

85. Hersher M. Laser-induced damage in transparent media.// J. Opt. Soc. Am., vol.54, is.4, 1964. – P. 563-567.

86. Hirata K., Haraguchi K. Crystallization of fused silica surfaces by ultra-violet laser irradiation. // J. Appl. Phys., vol. 104, No.12, 2008. – P.1–4.

87. Holovchak R. Ya. Structural-topological Self-organization of Networks Systems of Chalcohenide Glasses. D. Sc. Thesis. – Lviv: Orest Vlokh Insitute of Physical Optics? 2016. – 329 p. (In Ukrainian)

88. Holzwarth R., Reichert J., Udem Th., Hänsch T. W. 2001, Optical frequency metrology and its contribution to the determination of fundamental constants. In Atomic Physics 17, edited by E. Arimondo, P. DeNatale, a M. Inguscio./ AIP Conf. Proc. No. 551. AIP, New York, 2001. – P. 58–72.

89. Hong Lei, Wang Xincai, Rusli, Wang Hao, Zheng Hongyu, Yu Hongyu. Crystallization and surface texturing of amorphous-Si induced by UV laser for photovoltaic application.// J. Appl. Phys., vol. 111, is. 4, 2012. – P. 043106-1 – 04306-6.

90. ‘Ilev, I., Kumagai H., Toyoda K., Koprinkov I. Highly efficient wideband continuum generation in a singlemode optical fiber by

powerful broadband laser pumping.// Appl. Opt. Vol.35, 1996. – P. 2548-2553.

91. Il'ichev N. N., Korobkin V. V., Korshunov V. A.,. Malyutin A. A, Okroashvili T. G., Pashinin P. P. Superbroadening of the spectrum of ultrashort pulses in liquids and glasses.// Pis'ma Zh. Eksp. Theor. Phiz. Vol. 15, 1972. – P.191–194 (In Russian)

92. Islam M. N., Sucha G., Bar-Joseph I., Wegener M., Gordon J. P., Chemla D.S. Broad bandwidths from frequency-shifting solitons in fibers. // Opt. Lett. Vol.14, 1989. – P. 370–372.

93. Islam M. N., Sucha G., Bar-Joseph I., Wegener M., Gordon J. P., Chemla D.S. 1989b, Femtosecond distributed soliton spectrum in fibers.// J. Opt. Soc. Am. B. Vol..6, 1989. – P. 1149–1158.

94. Isselin J.-C., Alloncle A.-P., Autric M. Laser-induced breakdown in water: process for shock waves generation./ High-Power Laser Ablation, 1998. – P. 363-369.

95. Ivanisik A. I., Isayenko A. Yu., Korotkov P. A., Ponezha G. V. Phase-modulated parametric antiStokes stimulated Brillouin scattering of Cherenkov type in the region of self-focusing excited radiation.// Ukr. Phys. Journal, vol. 57, is.10, 2012. – P.1000-1010 (In Ukrainian)

96. Jelley J. V. Čerenkov radiation and its applications. – Moscow: Inostrannaya literatura, 1960. – 334 p. (In Russian)

97. Jones, W. J., Stoicheff B. P. Inverse Raman spectra: Induced absorption at optical frequencies. Phys. Rev. Lett., vol. 13, 1964. – P.657–659.

98. Jones, D. J., Diddams S. A., Ranka J. K., Stentz A. J., Windeler R. S., Hall J. L., Cundiff S. T. Carrierenvelope phase control of femtosecond mode-locked lasers and direct optical frequency synthesis.// Science. Vol. 288, 2000. – P. 635-639.

99. Kashchiev D. On the relation between nucleation work, nucleus size and nucleation rate // J.Chem.Phys. Vol. 76, 1982. – P. 5098-5102.

100. Kaischew R., Stoyanov S., Kashchiev D. Recent investigations on nucleation and crystal growth processes. // Journal of Crystal Growth. Vol. 52, № 1, 1981. – P. 3 – 13.

101. Kashchiev D. Nucleation. Basic theory with applications/ D. Kashchiev. – Oxford: Butterworth – Heinemann, 2000. – 544 p.

102. Keller Joseph B., Miksis Michael. Bubble oscillations of large amplitude. // J. Acoust. Soc. Am., vol. 68, is. 2, 1980. – P. 628-633.

103. Kelton K., Greer A. L. Nucleation in Condensed Matter: Applications in Materials and Biology. – Amsterdam: Elsevier Science & Technology, 2010. – 460 p..

104. Khaybullin I.B., Smirnov L.S. Impulse annealing of semiconductors. The state of the problem and unresolved questions (Review).// Physics and technical of semiconductors, v.19, No.4, 1985. – P.569-589 (In Russian).

105. Khizhnyak M. A. Theory of wave processes. – Kharkiv: Shtrych, 2003. – 304 p. (In Ukrainian)

106. Kielich S. Molecular nonlinear optics. – Moscow: Nauka, 1981. – 671 p. (in Russian)

107. Ki-Taek Byun and Ho-Young Kwak. A model of laser-induced cavitation. // Jap. J. Appl. Phys., vol. 43, is. 2, 2004. – P. 621-630.

108. Knight J. C. Photonic crystal fibres.// Nature (London). Vol. 424, 2003. – P.847-851.

109. Kobzev A. P. Cherenkov radiation mechanism. // EPAN, vol.41, is.3, 2010. – P. 830-867. (In Russian)

110. Kock W. E. Lasers and holography.An introduction to coherent optics. – Moscow: Mir, 1971. – 137 p. (in Russian)

111. Kodama Y., Hasegawa A. Nonlinear pulse propagation in a monomode dielectric guide.// IEEE Photonics Technol. Lett. Vol. QE-23, 1987. – P. 510–524.

112. Kosma K., Trushin S. A., Fuß W., Schmid W. E. Characterization of the supercontinuum radiation generated by self-focusing of few-cycle 800 nm pulses in argon.// Journal of Modern Optics, vol. 55, no. 13, 2008. – P. 2141–2177.

113. Krylov, D., Leng L., Bergman K., Bronski J. C., Kutz J. N. Observation of the breakup of a prechirped N-soliton in an optical fiber.// Opt. Lett. Vol. 24, 1999. – P. 1191–1193.

114. Kubota H., Tamura K. R., Nakazawa M. Analyses of coherence-maintained ultrashort optical pulse trains and supercontinuum generation in the presence of solitonamplified spontaneous-emission interaction.// J. Opt. Soc. Am. Vol. B 16, 1999. – P.2223-2232.

115. Kukta R.V., Freund L.B. Minimum energy configuration of epitaxial material clusters on a lattice-mismatched substrate.// Journal of the

Mechanics and Physics of Solids. Vol. 45, Is. 11–12, 1997. – P. 1835-1860.

116. Kukushkin S. A., Osipov A. V. Thin-film condensation processes. Physics-Uspekhi. Vol. 41, Is. 10, 1998. – P. 983-1014.

117. Kulcsar F., Teherani D., Altmann H. Study of the spectrum of Cherenkov light.// Journal of Radioanalytical Chemistry, vol. 68, no. 1-2,1982. – P.161-168.

118. Kurbatov L.N., Stoyanova I.G., Trokhimchuck P.P., Trokhin A.S. Laser annealing of semiconductors $A_{III}B_{V}$. //Reports of Soviet Academy of Science, vol. 268, No.3, 1983. – P. 594–597, (In Russian)

119. *Laudise R. A. The growth of single crystals. – Englewood cliffs: Prentice-Hall Inc., 1970. – 352 p.*

120. Lauteborn W., Kurz T. Physics of bubble oscillations. // Rep. Progr. Phys. Vol. 77,2010. – 106501 (88 p.)

121. Ley Hong, Xincai Wang, Rusli, Hao Wang, Hongyu Zheng, Hongyu Yu. Crystallization and surface texturing of amorphous Si by UV laser for photovoltaic application.// J. Appl. Phys, vol 11, Issue 4, 043106, 2012. – P. 1–6.

122. Lezzi A., Prosperetti A. Bubble dynamics in a compressible liquid: II. Second-order theory.// J. Fluid Mech., vol. 185, 1987. – P. 289–321.

123. Lin C., Stolen R. H. New nanosecond continuum for excited-state spectroscopy.// Appl. Phys. Lett. Vol. 28, 1976. – P. 216–218.

124. Lugli Francesca, Zerbetto Francesco. An introduction to bubble dynamics.// Physical Chemistry Chemical Physics, Vol. 9, 2007. – P.2447-2456.

125. Luo C., Ibanescu M., Johnson, S. G., Joannopoulos J. D. // Science. Vol. 299, 2003. – P. 368-371.

126. Luther G. G., Newell A. C., Moloney J.V., Wright E. M. Short pulse conical emission and spectral broadening in normally dispersive media.// Opt. Lett. Vol. 19, Is. 11, 1994. – P. 789-791.

127. Macleod A. J., Noble A., Jaroszynski D. A. Cherenkov Radiation from the Quantum Vacuum. Phys. Rev. Lett. Vol. 22, is. 16, 2019. – P. 161601-1 – 161601-6.

128. Makin V.S. Peculiarities of the formation the ordered micro and nanostructures in condensed matter after laser excitation of surface

polaritons modes. D. Sc. Thesis. – Saint-Petersburg: State university of information technologies, mechanics and optics, 2013. – 384 p. (In Russian)

129. Manassah, J. T., Alfano R. R., Mustafa M. Spectral distribution of an ultrafast supercontinuum laser source.// Phys. Lett., vol. 107A, 1985. – P. 305–309.

130. Manassah, J. T., Ho P. P., Katz A., Alfano R. R. Ultrafast supercontinuum laser source.// Photonics Spectra 18, 1-1984. – P. 53–59

131. Marguet S. The Physics of Nuclear Reactors. – Berlin: Springer, 2017. – 1300p.

132. *Markov I. V. Crystal Growth for Beginners: Fundamentals of Nucleation, Crystal Growth, and Epitaxy. – Singapore: World Scientific, 2017. – 632 p..*

133. Matsko A. B., Liang Wey, Savchenkov A. A., Elihanu D., Maleki L. Optical Cherenkov radiation in overmoded microresonators.// Optics Letters, vol. 41, is. 13, 2016. – P. 2907-2910.

134. Matthews J. W. Epitaxial Growth. – New York: Academic Press, 1975. – 560p.

135. Mayer J. E. The Statistical Mechanics of Condensing Systems. II // J. Chem. Phys. – Vol.5, №1, 1937. – P.74 – 83.

136. McGinty J., Yazdanpanah N., Price C., ter Horst J. H., Sefcik J. Chapter 1: Nucleation and Crystal Growth in Continuous Crystallization, in *The Handbook of Continuous Crystallization. – London: Royal Society of Chemistry,* 2020. – P. 1-50

137. Medvid' A. Nano-cones Formed on a Surface of Semiconductors by Laser Radiation: Technology, Model and Properties/ Nanowires Science and Technology ed. Nicoletta Lupu. – Vukovar: Inech, 2010. – P.61-82.

138. Mendez-Villuendas E., Saika-Voivod I., Bowles R. K. A limit of stability in supercooled liquid clusters. The Journal of Chemical Physics. Vol. 127, Is. 15, 2007. 154703

139. Milchev A. Electrocristallyzation. Fundamentals of nucleation and growth. – N.Y.: Kluwer Acad. Publ., 2002. – 265 p.

140. Miloslavskiy V. K. Nonlinear Optics. – Kharkov: Karazin University Prees, 2008. – 312 p. (In Russian)

141. Minardi S., Gopal A., Tatarakis M., Couairon A., Tamosăuskas G., Piskarskas R., Dubietis A., Di Trapani P. Time-resolved refractive index and absorption mapping of light-plasma filaments in water.// Opt. Lett. Vol.33, Is. 1, 2008. – P.86-88.

142. Mishra S. Laser Beam MicroMachining.// Optics and Lasers in Engineering. Vol. 73, 2015. – P. 89-122.

143. Mitschke, F. M., Mollenauer L. F. Discovery of the soliton self-frequency shift.// Opt. Lett. Vol. 11, 1986. – p. 659-661

144. Mollenauer, L. F., Stolen R. H., Gordon J. P. Experimental observation of picosecond pulse narrowing and solitons in optical fibers.// Phys. Rev. Lett. Vol. 45, 1980. – P. 1095–1098.

145. Mollenauer, L. F., Stolen R. H., Gordon J. P., Tomlinson W. J. Extreme picosecond pulse narrowing by means of soliton effect in single-mode optical fibers.// Opt. Lett. Vol. 8, 1983. – P.289-291.

146. Morioka, T., Kawanishi S., Mori K., Saruwatari M. Nearly penalty-free, 4 ps supercontinuum Gbit/s pulse generation over 1535–1560 nm.// Electron. Lett. Vol.30, 1994. – P. 790-791.

147. Morioka, T., Mori K., Saruwatari M. More than 100-wavelength-xx channel picosecond optical pulse generation from single laser source using supercontinuum in optical fibres.// Electron. Lett. Vol. 29, 1993. – P. 862-864.

148. Moskovskikh D. O. Production of Submicrometer Powder of Silicon Carbide and Nanostructural Ceramics on its Basis. Ph. D. Thesis. – Moscow: National Research Technological University Steel and Alloys, 2015. – 166 p. (In Russian)

149. Muggli P., Yoshii J., Katsouleas T.C. Cherenkov radiation from a magnetized plasma: a diagnostic for PBWA experiments./ Proceedings of the 1999 Particle Accelerator Conference, New York, 1999. – P. 3654 – 3656.

150. Nagura C., Suda A., Kawano H., Obara M., Midorikawa K. Generation and characterization of ultrafast white-light continuum in condensed media. Appl. Opt. Vol. 41, Is. 18, 2002. – P. 3735-3742

151. Nahin, P. J. Oliver Heaviside: The Life, Work, and Times of an Electrical Genius of the Victorian Age. – Baltimore: Johns Hopkins University Press, 1988. – 362 p.

152. Nakamuro T., Sakakibara M., Nada H., Harano K., Nakamura E.

Capturing the Moment of Emergence of Crystal Nucleus from Disorder. //Journal of the American Chemical Society. Vol. 143. Is. 4, 2021. – P. 1763-1767.

153. Nakazawa M., Suzuki K., Kubota H., Haus H. A. High-order solitons and the modulational instability.// Phys. Rev. A Vol. 39, 1989. – P.5768-5776.

154. Nakazawa, M., Tamura K. R., Kubota H., Yoshida E. Coherence degradation in the process of supercontinuum generation in an optical fiber.// Opt. Fiber Technol. Vol.4, 1998. – P. 215-223.

155. Niemz M. H. Thresold dependence of laser-induced optical breakdown on pulse duration. // Appl. Phys. Lett., vol. 66, is. 10, 1995. – P. 1181-1183.

156. Newton I. Optics: or a Treatise of the Reflections, Refractions, Inflections and Colors of Light. 4-th edition. – London: Printer for William Innys at the Welt-End of St. Paul's, 1730. – 386 p.

157. Nibbering E. T. J., Curley P.F., Grillon G., Prade B.S., Franco M.A., Salin F., Mysyrowicz, A. Conical emission from self-guided femtosecond pulses in air. Opt. Lett., vol. 21, is. 1, 1996. – P. 62–64.

158. Nishioka H., Odajima W., Ueda K., Takuma H. Ultrabroadband flat continuum generation in multichannel propagation of terawatt Ti:sapphire laser pulses. Opt. Lett. Vol. 20, Is. 24, 1995. – P.2505-2507.

159. Nowak, G. A., Kim J., Islam M. N. Stable supercontinuum generation in short lengths of conventional dispersion-shifted fiber. //Appl. Opt. Vol. 38, 1999. – P.7364-7369.

160. Okada T., Tomita T., Matsuo S., Hashimoto S., Kashino R., Ito T. Formation of nanovoids in femtosecond laser irradiated single crystal silicon carbide.// Material Science Forum, vol. 725, 2012. – P.19 – 22.

161. Okada T., Tomita T., Matsuo S., Hashimoto S., Ishida Y., Kiyama S., Takahashi T. Formation of periodic strain layers associated with nanovoids inside a silicon carbide single crystal induced by femtosecond laser irradiation. J. Appl. Phys., v. 106, p.054307, 2009. – 5 p.

162. Olkhovsky I. I. Theoretical mechanics course for physicists. 2-nd ed. – Moscow: Moscow University publishing house, 1978. – P. 575 p.

163. *Parker R. L. Crystal growth mechanisms: energetics, kinetics and transport. Solid state physics* (eds.) Seitz F., Turnbull D., Ehrenreich H. *Vol. 25. – New York @ London: Academic Press, 1970. – P. 1-151.*

164. Pedraza A. J., Fowlkes J. D., Lowndes D. H. Silicon microcolumn arrays growth by nanosecond pulse laser irradiation.// Appl. Phys. Lett. 74(10), 1999. – P. 2222-2224.

165. Pedraza A. J., Guan Y. F., Fowlkes J. D., Smith D. A. and Lowndes D. H. Nanostructures produced by ultraviolet laser irradiation of silicon. I. Rippled structures. // J. Vac. Sc. @ Techn. B., vol. 22, no.10, 2004. – P. 2823-2835.

166. Philips J.C. Metastable honeycomb model of laser annealing.//Journal of Applied Physics, No.12, Vol. 52, 1981. – P.7397-7402.

167. Pimpinelli A., Villain J. Physics of Crystal Growth. – Cambridge: Cambridge University Press, 1998. – 400 p.

168. Plesset M. S. The dynamics of cavitation bubbles.// J. Appl. Mech. Vol. 16, 1949. – P. 277-282

169. Popescu I. M., Preda A. M., Cristescu C. P., Sterian P. E., Lupaşcu A.I. Probleme resolvate de fizica lazerilor. – Bucureşti: Editura technică, 1975. – 443 p. (In Romanian)

170. Potemkin F. V., Mareev E. I. Shock waves and cavitation bubbles dynamics as a function of the tightly focused femtosecond laser energy in distilled water and acetone.// Scientific Notes of Physical Faculty. Mikhail Lomonosov Moscow State University, 133401, 2013. – 9 p. (In Russian)

171. Pound G. M., La Mer V. K. Kinetics of Crystalline Nucleus Formation in Supercooled Liquid Tin.// Journal of the American Chemical Society. Vol. 74, is. 9, 1952. – P. 2323-2332.

172. Prosperetti A., Lezzi A. Bubble dynamics in a compressible liquid: I. First-order theory.// J. Fluid Mech., vol. 168, 1986. – P. 457-478.

173. Pruppacher H.R., Klett J.D. Microphysics of Clouds and Precipitation. 2nd Edition. – Dordrecht: Kluwer Academic, 1997. – 954 p.

174. Ranka J. K., Windeler R. S., Stentz A. J. Visible continuum generation in air-silica microstructure optical fibers with anomalous dispersion at 800 nm.// Opt. Lett. Vol. 25, 2000. – P.25–27.

175. Rayleygh (J. W. Strutt). On the instability of Jets. Londom Math. Soc. Proc., Vol. X, 1879. – P.4-13.

176. Rayleygh (J. W. Strutt). On the pressure developed in a Liquid during the Collapse of a Spherical Cavity.// The London, Edinburgh and Dublin

Philosophical Magazine and Journal of Science. Vol. 34, 1917. – P.94-98.

177. Rayleygh (J. W. Strutt). The theory of sound. Vol. 1. – London: Macmillan and co., 1894. – 342 p.

178. Rayleygh (J. W. Strutt). The theory of sound. Vol. 2. – London: Macmillan and co., 1896. – 504 p.

179. Rayleygh (J. W. Strutt). Wave theory of light. – Moscow: URSO, 2009. – 136 p. (In Russian)

180. Reeves W. H., Skryabin D. V., Biancalana F., Knight J. C., Russell P. St. J., Omenetto F. G., Efimov A., Taylor A. J. Transformation and control of ultra-short pulses dispersion-engineered photonic crystal fibres.// Nature (London). Vol. 424, 2003. – P. 511–515.

181. Russell, P. St. J. Photonic crystal fibers.// Science. Vol. 299, 2003. – P.358–362.

182. Ryndya S. M. Peculiarities of Thin Films SiC structure, which is formatted on Si and Al_2O_3 substrates by method of pulse laser precipitation. Ph. D. Thesis. – Moscow: L. Ya Karpov Scintific Research Physical-Chemical Institute, 2014. – 158 p. (In Russian)

183. Salem AB, Cherif R, Zghal M. Nonlinear Fiber Optics: Application to Supercontinuum Generation. Ch. 6. In: Lakshminarayanan V and Bhattacharya I. Advances in Optical Science and Engineering, Springer Proceedings in Physics 166. Berlin, etc.: Springer Verlag, 2015. – P. 37-47.

184. Salihoglu O., Kűrűm U., Gul Yaglioglu H., Elmali A., Aydinli A. Femtosecond laser crystallization of amorphous Ge. // Appl. Phys., vol. 109, Is.12, 123102, 2011. – P. 1- 6.

185. Sarkisyan D., Paul B. D., Cundiff S. T., Gibson E. A., Gallagher A. Conical emission by 2-ps excitation of potassium vapor.// J. Opt. Soc. Am. B. Vol. 18, No. 2, 2001. – P. 218-224.

186. Satsuma, J., Yajima N. Initial value problems of one-dimensional self-modulation of nonlinear waves in dispersive media.// Prog. Theor. Phys. Japan Suppl. Vol. 55, 1974. – P.284-306.

187. Self-Focusing: Past and Present. Eds. R.W.Boyd, S.G. Lukishova, Y.-R. Shen, Springer Series: Topics in Applied Physics, Vol. 114. – NY: Springer, 2009. – 605 p.

188. Sengupta P. Classical electrodynamics. – New Delhi: New Age International, 2000. – 225 p.

189. Scharifker B. Theoretical and experimental studies of multiple nucleation // Electrochim. Acta. Vol. 28, 1983. – P. 879 - 889.

190. Schütz J., Hodel W., Weber H. P. Nonlinear pulse distortion at the zero dispersion wavelength of an optical fibre.// Opt. Commun. Vol. 95, 1993. – P. 357-365.

191. Sharma B. S. Laser-induced dielectric breakdown and mechanical damage in silicate glasses. Ph. D. Thesis. –Burnaby: Simon Fraser University Press, 1968. – 123 p.

192. Shen M., Carey J. E., Crouch C. H., Kandyla M., Stone H. A., Mazur E. High-density regular arrays of nano-scale rods formed on silicon surfaces via femtosecond laser irradiation in water.// Nanoletters, vol. 8, is. 7, 2008. – P. 2087-2091.

193. Shen Y. R. The principles of Nonlinear Optics. – New York a. o.: Wiley-Interscience, 2003. – 563 p.

194. Shimizu Fujio. Frequency broadening in liquids by a short light pulse.// Phys. Rev. Lett., vol. 19, is.19, 1967. – P. 1097-1100.

195. Shtapenko E. F. Kinetics of Structure Formation and Properties of Electrodeposited Metal Films. D. Sc. Thesis. – Dnipro: V. Lazaryan Dnipro National University of Railway transport, 2016. – 354 p. (In Russian)

196. Silberberg Y. Solitons and two-photon absorption.// Opt. Lett. Vol. 15, 1990. – P.1005–1007.

197. Skryabin D.V., Kartashov Y.V., Egorov O.A., Sich M., Chana J. K., Tapia Rodriguez L. E., Walker P. M., Clarke E., Royall B., Skolnick M. S., Krizhanovskii D. N. Backward Cherenkov radiation emitted by polariton solitons in a microcavity wire.// Nature communications, vol. 8, is.1, 2017. – P. 1554-1562.

198. Smiths S. J., Purcell E. M. Visible Light from Localized Surface Charges Moving across a Grating.// *Phys. Rev., vol. 92, 1953. – P. 1069-1070.*

199. Smith W. L., Liu P., Bloembergen N. Superbroadening in H_2O and D_2O by a self-focused picosecond pulse YAlG:Nd laser.// Phys. Rev. A. Vol. 15, Is. 6, 1977. – P. 2396-2403.

200. Stafeev V.I. Elementary structural units of condenced phases and its

proper electrical phenomena // Applied physics, No.4, 2005. – P.31-38. (In Russian)

201. Staikov G. Electrocrystallization in Nanotechnology. – Weinheim: Wiley – VCH, 2007. – 265 p.

202. Stetsiuk O. B. Modeling of shock processes of Nonlinear and Relaxed Optics. Mag. Degree Thesis. – Lutsk: EENU, 2020. – 76 p. (In Ukrainian)

203. Stoicheff B. P. Characteristics of stimulated Raman radiation generated by coherent light.//Phys. Lett. Vol. 7, 1963. – P. 186-188.

204. Stolen, R. H., Lee C., Jain R. K. Development of the stimulated Raman spectrum in single-mode silica fibers.// J. Opt. Soc. Am. B. Vol. 1, 1984. – P. 652–657.

205. Stolen, R. H., Mollenauer L. F., Tomlinson W. J. Observation of pulse restoration at the soliton period in optical fibers.// Opt. Lett. Vol. 8, 1983. – P. 186-188.

206. Stransky I. N., Kaishev R. On the theory of crystal growth and the formation of crystalline nuclei // UFN. Vol.21, Issue 4, 1939. – P.408 - 465. (In Russian)

207. Stranski I. N., Krastanow L. Zur Theorie der orientierten Ausscheidung von Ionenkristallen aufeinander./ Abhandlungen der Mathematisch-Naturwissenschaftlichen Klasse IIb. Akademie der Wissenschaften, Wien. Vol. 146, 1938. – S. 797–810.

208. Sugiyama T., Masuhara H. Laser-Induced Crystallization and Crystal Growth.// Chemistry - An Asian Journal. Vol. 6, Is. 11, 2011. – P. 2878-2889.

209. Supercontinuum white light lasers. https://www.nktphotonics.com/products/

210. Tai, K., Hasegawa A., Bekki N. 1988 Fission of optical solitons induced by stimulated Raman effect.// Opt. Lett. Vol.13, 1988. – P. 392–394.

211. Tamm, I.E.; Frank, I.M. Coherent radiation of fast electrons in a medium.// Dokl. Akad. Nauk SSSR, vol.14, is. 1, 1937. – P. 107-111.

212. Tamura K. R., Kubota H., Nakazawa M. 2000, Fundamentals of stable continuum generation at high repetition rates.// IEEE J. Quantum Electron. Vol. 36, 2000. – P.773–779.

213. Tauc Ya. Optical properties of semiconductors in visible and ultraviolet

ranges.// Uspekhi fizicheskikh nauk. Vol. 94, Is.3, 1968. – P. 501-533. (In Russian)

214. Tendler Irwin I., Hartford Alan; Jermyn, Michael; Pogue Brian W. (25 October 2019). Experimentally Observed Cherenkov Light Generation in the Eye During Radiation Therapy.//International Journal of Radiation Oncology, Biology, Physics, Vol. 106, Is. 2, 2019. – P. 422–429.

215. Tidman D. A. A quantum theory of refractive index, Cherenkov radiation and the energy loss of a fast charged particle.// Nuclear Physics. Vol. 2, 1956/57. – P. 289-346.

216. Trokhimchuck P. P. Continuum mechanics. – Lutsk: Vezha-Print, 2018. – 168 p. (In Ukrainian)

217. Trokhimchuck P.P. Diffraction: Concepts and Applications./ Recent Review and Research in Physics. Ed. Jayminkumar Rajanikant Ray, S.S. Sharma, vol. 1, ch. 3. New Dehly: AkiNik Publications, 2022. – P. 37-67.

218. Trokhimchuck P. P. Foundation of Relaxed Optics. Lutsk: Vezha, 2006. – 294 p.; Foundations of Relaxed Optics. Lutsk: Vezha, 2011. – 627 p.

219. Trokhimchuck P. P. Laser-induced optical breakdown of matter: retrospective and perspective./ Advances in Engineering Technology. Ed. Jaivir Sindh, vol. 4, part 7. New Dehly: AkiNik Publications, 2020. – P. 101-132

220. Trokhimchuck P. P. Modelling of the elionic-induced sputtering (sublimation) of matter.// Applied Questions of Mathematics modeling. Vol. 4. No. 2.1. 2021. – P. 234-244.

221. Trokhimchuck P.P. Nonlinear and Relaxed Optical Processes. Problems of interactions. – Lutsk: Vezha-Print, 2013. – 280 p.

222. Trokhimchuck P.P. Nonlinear Dynamical Systems. – Lutsk: Vezha-Print, 2015. – 276 p. (In Ukrainian)

223. Trokhimchuck PP. Photon Efficiency: Retrospective and Perspective.// IJARPS, vol.9, is. 5, 2022. – P. 1 - 14.

224. Trokhimchuck P. P. Problem of saturation of excitation in Relaxed Optics.// Journal of Optoelectronics and Advanced Materials. Vol. 14, Is.2-3, 2012. – P. 363–370.

225. Trokhimchuck, P. P. Problems of modeling diffraction and interference processes in Nonlinear and Relaxed Optics. //IJARPS. Vol. 6, Is. 7, 2019. – P. 5-17.

226. Trokhimchuck P.P. Problems of modeling the creation the surface laser-induced structures in Relaxed Optics.// Bulletin of Karazin Kharkiv National University. Physics. Is. 27, 2017. – P. 35 – 43.

227. Trokhimchuck P. P. Problems of modeling the phase transformations in Nonlinear and Relaxed Optics (review) // Int J. Eng. Res. @ Developm. (IJERD). Vol.14, Is.2, 2018. – P. 48-61.

228. Trokhimchuck P. P. Problems of reradiation and reabsorption in Nonlinear and Relaxed Optics.// IJARPS, Vol. 4, Is.2, 2017. – P.37-50

229. Trokhimchuck P. P. Radiation Physics of Status Solid. – Lutsk: Vezha, 2007. – 394 p. (In Ukrainian)

230. Trokhimchuck P. P. Recent Research and Development Satus of Relaxed Optics and Laser Technology: A Review.// Optics and Photonics Journal 11 (7), 2021. – P. 210-263

231. Trokhimchuck P. P. Relaxed Optics: Necessity of Creation and Problems of Development. // IJARPS. Vol. 2, Is. 3, 2015. – P. 22-33.

232. Trokhimchuck P. P. Relaxed Optics: Modelling and Discussions. – Saarbrukken: Lambert Academic Press, 2020. – 249 p. Trokhimchuck P. P. Relaxed Optics: Modelling and Discussions 2. – Saarbrukken-Cisinau: Lambert Academic Press, 2022. – 210 p.

233. Trokhimchuck P. P. Relaxed Optics: Modelling and Discussions 2. – New Delhi: AkiNik Publications, 2022. – 205 p.

234. Trokhimchuck P. P. Relaxed Optics: Realities and Perspectives. – Saarbrukken: Lambert Academic Publishing, 2016. – 260 p.

235. Trokhimchuck P. P. Role Physical-Chemical Processes in the Generation of Laser-Induced Structures. In: Research Trends in Chemical Sciences, ed. Ashok Kumar Acharya, Vol. 11, Ch.6. – New Delhi, AkiNik Publications, 2020. – P. 109-140.

236. Trokhimchuck P. P. Saturation of Excitation and Critical Processes in Nonlinear and Relaxed Optics./ Recent Review and Research in Physics. Ed. Jayminkumar Rajanikant Ray, S. S. Sharma, Vol. 1, Ch. 3. New Dehly: AkiNik Publications, 2022. – P. 69-98

237. Trokhimchuck P. P. Shock Electromagnetic Processes in Nonlinear and Relaxed Optics/Recent Review and Research in Physics. Ed. Jayminkumar Rajanikant Ray, S.S. Sharma, Vol. 4, ch.3. New Dehly: AkiNik Publications, 2023. – P. 23-52.

238. Trokhimchuck P. P. Some Electrodynamics Problems of Modelling the Nucleation and Crystallization // IJARPS. Vol. 10, Is. 3, 2023. – P. 19-34.

239. Trokhimchuck P. P. Some Problems of Modeling Laser-induced Filaments: Nonlinear and Relaxed Optical Aspects.// IJARPS. Vol.7, Is.2, 2020. – P. 1-15.

240. Trokhimchuck P. P. Some Problems of Modeling the Volume Processes of Relaxed Optics.// IJARPS. Vol. 5. Is. 11, 2018. – P. 1-14.

241. Trokhimchuck P. P. Some Problems of the Modeling the Optical Breakdown and Shock Processes in Nonlinear and Relaxed Optics.// IJARPS Vol. 7, Is.5, 2020. – P.17-30.

242. Trokhimchuck P. P. The main problems of modelling the nucleation and crystallization: electromagnetic aspects. /Recent Review and Research in Physics. Ed. Jayminkumar Rajanikant Ray, S.S. Sharma, vol. 5. New Dehly: AkiNik Publications, 2023. – 32 p. (must be published)

243. Trokhimchuck P. P. The main problems of modelling the nucleation and crystallization: thermodynamical aspects. /Recent Review and Research in Physics. Ed. Jayminkumar Rajanikant Ray, S.S. Sharma, vol. 5. New Dehly: AkiNik Publications, 2023. – 32 p. (must be published)

244. Trokhimchuck P. P. Theories of everything: Past, Present, Future. – Saarbrukken: Lambert Academic Publishing, 2021. – 260 p.

245. Tsukamoto M., Asuka K., Nakano N., Hashida M., Ratto M., Abe N., Fujita M. Period microstructures produced by femtosecond laser irradiation on titanium plate.// Vacuum, vol. 80, 2006. – P. 1346-1350.

246. Tyapkin A. A. Experimental instructions on the existance tachyons, obtained in the research Cherenkov radiation. Preprint JINR, Dubna, D1-99-292, 1999. – 7 p. (In Russian)

247. Tyapkin A.A. On induced emission caused by a charged relativistic particle in a gas below the Cherenkov threshold. // Brief communications JINR, No 3(60)-93, 1993. – P. 26-31. (In Russian)

248. Vaichaitis V. I., Ignavichyus M. V., Kudryashov V. A., Pimenov V. N. Observation of a Cherenkov type radiation during the propagation of picosecond light pulse in sodium vapor.// JETP Letters. Vol. 45, Is. 7, 1987. – P. 414-417.

249. Vanholsbeeck, F., Martín-López S., González-Herráez M., Coen S. The role of pump incoherence in continuouswave supercontinuum generation// Opt. Express. Vol. 13, 2005. – P. 6615– 6625.

250. Venables J. Introduction to Surface and Thin Film Processes. Cambridge: Cambridge University Press, 2000. – 392 p.

251. Veyko V. P., Libenson M. N., Chervyakov G. G., Yakovlev E. B. Interaction laser irradiation and matter. Force optics. – Moscow: Phyzmatlit, 2008. – 312 p (In Russian)

252. Volmer M., Weber A. Keimbildung in übersättigten Gebilden // Ztschr. Phys. Chem. Bd.119, 1926. – S.277-301.

253. von der Linde, D. Characterization of the noise in continuously operating mode-locked lasers.// Appl. Phys. B. Vol. 39, 1986. – P. 201–217.

254. Udem Th., Holzwarth R., Hänsch T. W. Optical frequency metrology.// Nature (London). Vol. 416, 2002. – P.233–237.

255. Wagner R., Gottman J. Sub-wavelength ripple formation on various materials induced by tightly focused fewmtosecond laser radiation.// Journal of Physics: Conference Series, vol. 59, 2007. – P. 333 – 337.

256. Wai, P. K. A., Menyuk C. R., Lee Y. C., Chen H. H. Nonlinear pulse propagation in the neighborhood of the zero-dispersion wavelength of monomode optical fibers.// Opt. Lett. Vol. 11, 1986. – P. 464–466.

257. Walton D. Nucleation of vapor deposits // The journal of chemical physics. Vol. 37, № 10, 1962. – P.2182-2188.

258. Wang Zhong-Yue. Generalized momentum equation of quantum mechanics.// Optical and Quantum Electronics. Vol.48, Is. 2, 2016. – 9 p.

259. Wautelet M., Faily-Lavato M., Laude L.D. Dangling bonds in Si and Ge during laser irradiation. // Physics C: Solid State Physics, v.13, 1980. – P.5505-5514.

260. von Weizsäcker C. F. Ausstrahlung bei Stößen sehr schneller Elektronen. Z.Phys. vol. 88, is. 9-10, 1934. – S. 612–625.

261. Werncke, W., Lau A., Pfeiffer M., Lenz K., Weigmann H.-J., Thuy C. D. An anomalous frequency broadening in water.// Opt. Commun. Vol. 4, 1972. – P.413-415.

262. Williams E. J. Nature of the High Energy Particles of Penetrating Radiation and Status of Ionization and Radiation Formulae.// Physical Review. Vol. 45, Is. 10, 1934. – P. 729-730.

263. Wimmel H. K. Tachyon and Cerenkov radiation. //Nature. Phys. Sci., vol. 236, 1972. – P.79-80.

264. Wu D.T. Nucleation theory // Solid State Physics Advance. Vol. 50, 1997. – P. 37-187.

265. Xing Q., Yoo K. M., Alfano R. R. Conical emission by four-photon parametric generation by using femtosecond laser pulses. Appl. Opt. Vol. 32, Is. 12, 1993. – P. 2087-2089.

266. Yablonovich E, Bloembergen N. Avalanche Ionization and the Limiting Diameter of Filament Induced by Light Pulses in Transparent Media. Phys. Rev. Lett. 1972;29(14): 907-910.

267. Yablonovich E. Optical Dielectric Srength of AlkaliHalide Crystalls Obtained by Laserinduced Breakdown.// Appl. Phys. Lett., vol.19, is.11, 1971. – P. 495-497.

268. Yablonovich E. Self-phase modulation and short-pulse generation from laser-breakdown plasmas.// Phys. Rev. A. Vol. 19, Is. 5, 1974. – P.1888-1895.

269. Yablonovich E. Self-phase Modulation of Light in a Laser-breakdown Plasma. //Phys. Rev. Lett. Vol. 32, Is. 10, 1974. – P.1101-1194.

270. You L., Mostowski J., Cooper J. Cone emission from laser-pumped two-level atoms. II. Analytical model studies.// Phys. Rev. A. Vol. 46, Is. 5, 1992. – P. 2925-2938.

271. Young F. R. Cavitation. – Oxford: McGraw Hills, 1989. – 444 p.

272. Zakharov V. E., Shabat A. B. Exact theory of two-dimensional self-focusing and one-dimensional selfmodulation of waves in nonlinear media.// Zh. Eksp. Teor. Fiz. Vol. 61, 1971. – P.118–134 (In Russian).

273. Zeldovich Ya. B. On the theory of the formation of a new phase. Cavitation // JETP. Vol. 12, Is. 1, 1942. – S. 525-536. (In Russian)

274. Zewail A. H. Femtochemistry: Recent progress in studiesand control of reactions and their transitions states. // J. Phys. Chem., vol. 100, No.31, 1996. – P. 12701 – 12704.

275. Zheleznyakov V.V., Kocharovskiy V.V., Kocharovskiy Vl.V. Polarization waves and superradiation in active media. // Progress of Physical sciences, vol. 159, No.2, 1989. – P.193-260. (In Russian)

276. Zheltikov, A. M., 2004, Nonlinear optics of microstructure fibers.// Usp. Fiz. Nauk. Vol. 147, Is. 1, 2004. – P.73-105. (In Russian)

277. Ziętek B. Optoelektronika. – Toruń: Wydawnictwo universytetu Nikolaja Kopernika, 2005. – 615s. (In Polish)

278. Zitter R. N., Koster D. F., Ringwelski A., Cantoni A. Pressure effects in the kinetics of cw laser induced reactions.// Appl. Phys. Vol. B30, 1983. – P. 19-21.

279. Zrelov V. P. Vavilov-Cherenkov radiation and its applications in high-energy physics. Vol.1. – Moscow: Atomizdat, 1968. – 276 p. (In Russian)

280. Zrelov V. P. Vavilov-Cherenkov radiation and its applications in high-energy physics. Vol. 2. – Moscow: Atomizdat, 1968. – 302 p. (In Russian)

Index

Besant problem
Bessel functions
β-particles
Bete
Bilanyuk
Bloembergen
Blokh
Bloch's formula
Bohr A.
Bohr N.
Bohrs hyperboloid
Bohr theory
Boltzmann
Boltzmann constant
Boltzmann distribution
Boltzmann principle
Bonch-Bruyevich V.
Bondarenko
Born-Haber circular process
Born-Lande formula
Boyraz
Bremsstrahlung radiation
Brewer
Bridgman-Stockbarger method
Brillouin scattering
Brodeur
bubble expansion
Buger-Lambert law
calibrated broad-band spectrometer
Cambridge Senate House Problems of 1847
carbon
carbon disulfide
cascade model of step-by-step excitation of chemical bonds in the regime of saturation

cascade theory of laser-induced optical breakdown
cavitations bubbles
Cheltsov V.
Cherenkov
Cherenkov angle
Cherenkov condition
Cherenkov detector
Cherenkov dipole
Cherenkov effect
Cherenkov emission
Cherenkov light
Cherenkov P.
Cherenkov's measurements
Cherenkov's observations
Cherenkov radiation
Cherenkov radiation of tachyons
Cherenkov relation
Cherenkov spectrum
Cherenkov threshold
Cherenkov-type emission process
Chiao
Chin
Chochralsky method
classical nucleation theory
classic theories of shock processes
Clausius
cluster
coherent photons
concept of coherent structures of Relaxed Optics
Como experiment
Compton electrons
conical emission
conical part of filament radiation
conical wavefronts

Cook S.
coordination numbers
Couette
Coulomb force
criterion of efficiency the using of laser radiation for generation proper structures
critical nucleus
crystal growth theories
crystal nucleation
crystallization
Curie M.
Damköhler number
Danos
Danyl’chenko P.
Dartmouth-Hitchcock's Norris Cotton Cancer Center
DeLong
density of laser irradiation
Dering
Descartes-Snell law
Deshpande
Di Trapani Paolo
Dianov
diffusive coefficient
diffusivity
Dicke
difference of electrical potentials
direct physical-chemical models of laser-induced optical breakdown
dispersionless point
dissociating medium
Doppler condition
Doppler effect
Dowty
drusen
Earth’s magnetic field
effect of shear and fluid micro-mixing on nucleation

eigenfrequency
electrical conductivity of dielectrical liquids
electrical currents
electrochemical formation of alloys
electrochemical nucleation
electrocrystallization
electromagnetic methods of modeling
electromagnetic nature of generation cavity bubbles
electromagnetic shock processes
elionic technologies
Eliseev P.
energy characteristics of laser-induced surface structures
Eulers constant
Fano profile
Faraday's constant
Feinberg
Fermi-Bohr microscopic concept
Fermi E.
Fermi theory
Fersman formula
filaments
Fischer
fluence threshold
formation of the nucleus
four-wave mixing
Fourier-Bessel transformations
Fourier-frequency component
Fourier integral
Fourier transform
Frank I.
Frank–Tamm formula
Frank-Tamm theory
Frank–van der Merwe mechanism
free-electron defocusing

growth times
Hall
Hansen
Harding
harmonic analysis
Hartman
Hasegawa
Hänsch
heat capacity
heat transfer
Heaviside O.
Henderson
Helmholtz free energy
heterogeneous nucleation
heterogeneous polarization
heterogeneous primary nucleation
Heyfets V.
Hincks
Holovatskiy V.
Holzwarth
homoogeneous nucleation
homogeneous polarization
Hugoniot adiabat
Huygens – Fresnel principle,
Huygens interference principle
Huygens' principle
Ice phasons in water
Il’ichev
indium antimonite
indium arsenide
interface kinetics
Islam
Jackson's theory
Jelly

Jones
Kachurin G.
Kant I.
Kapayev-Kopayev-Molotkov theory
Kapustinsky formulas
Keller–Miksis model
Kerr comb systems
Kerr media
Khaibullin I.
kinetic concept of Relaxed Optics
kinetic theory
Kiropoulos method
Kityk I.
Klimontovich Yu.
Knight
Kodama
Krastanov L.
Krylov
Kubota
Lambert Academic Publishing
Laplace equation
laser induced bubble in a sound field
laser-produced bubble in water
laser-induced critical phenomena
laser-induced optical breakdown
lattice energy
lead
Lebedev Institute
lightning
Lin
Linear Optics
Linde
liquid crystals
liquid-solid interface

liquid-vapor interface
Lofgren
longitudional modes
Lorentz invariance
Lorentz transformation
Loretzian fit
Lowell Radiation Laboratory
phase diagrams
photon crystals
plasma crystals
quantum dots
Mach cone
Mach number
macroscopic Golub model
macroscopic theory of homogeneous nucleation
Madelung constant
magmas
Mahabharata
Maidanovych-Sorensen L.
Makin V.
Makoviychuck M.
Mallet L.
Manassah
Markov
Marshall
material transport
Mayer
Maxwell J.C.
Maxwell's equations
McBirney
Medvid’ A.
Mehl
mesotron
methods of zonal crystallization

Michelson interferometer
microcolumn morphology
microscopic modified A. Bohr theory
microscopic theory of Cherenkov radiation
microstructures
Millar
Mitschke
mixing-induced supersaturation
mobility
mode-locked Kerr frequency comb
modified Rayleygh formula for solid
modified Rayleygh model
molecular-beam epitaxy
molecule of carbon C_2
Mollenauer
Morioka
multiple filamentation
Murase
Nakazawa
nanocavity
nanocolumns
nanoparticles
nanostructures
nanovoids
Newton’s rings
nonlinear ionization
nonlinear optical phenomena
nonlinear optical process
Nonlinear Optics
nonlinear Schrödinger equation
nonlinear Schrödinger model
nonlinear ultrafast optics
Nowak
nucleation

nucleation processes
nucleation rate
nucleation rate constants
number molecules in phason
olivine
optical breakdown
optoelectronic devices
optoelectronic systems
Parsons C.
Pauling L.
Perdok
Peretyatko V.
phase diagram
phase diagram of Si as function of coordination number
phasons
phasons of biological objects
phasons of carbons
photonic crystal fiber
photoproduction and pair annihilation processes
Physical Chemistry
pion
Planck constant
Poisson’s ratio
polarization
polarization effects
potassium chloride
polyphazons
Poynting vector
precipitate of arsenic
precision frequency metrology
pressure developed in a Liquid during the Collapse of a Spherical Cavity. Rayleygh concept
primary nucleation
Prinsloo-Lee experimental data

pyroxene
Pythagor
quartz
radiationless relaxation
Raman emission
Raman emission cone angles
Raman fibre laser
Raman-gain
Raman processes
Raman radiation
Raman scattering
Raman spectroscopy
Raman Stokes emission
Raman threshold
Ramayana
Ranka
Rayleygh concept
Raylegh formula
Rayleigh model
Rayleigh–Plesset model
Rayleygh ratio
Rayleigh's theory
Reeves
Relaxed, Nonlinear and Acoustic Processes and Materials
relative efficiency of using laser irradiation
Relaxed Optics
Reynolds
Rothenberg
Russell
Saikan
Satsuma
Schrödinger equation
Schütz
secondary nucleation

self-diffraction gratings
self-focusing
self-focusing length
self-guided pulse
self-trapped filament
self-trapped filament surface
self-trapping
Shabat
Shapiro
Shevchuk (Maidanovych) M.
Shimizu
shock mechanism
shock optical breakdown
shock processes
shock processes in Nonlinear and Relaxed Optics
shock wave
Shvalikovskiy D.
Shyrokovskiy V.
Silberberg
silicon
silicon carbide
size of phason
sizes of phasons of any materials
Slack
Smirnov
smut
Snell-Cherenkov effect
Snell’s law
sodium chloride,
sodium vapor
Sommerfeld A.
spatial coherence
spectra of Cherenkov radiation of tachyons
Spectra-Physics Tsunami and Spitfire

speed of light
speed of sound
spinodal decomposition
Stafeev V.
Stafeev phasons theory (model)
step of ellipsoidal forms
Stoicheff
Stokes-Einstein relation
Stokes side
Stokes spectrum
Stolen
Stoyanova I.
Stranski I.
Stranski-Krastanov mechanism
Stranski–Krastanov growth
Stranski-Krastanov theory
Sudarshan
Sugiyama's results
supercontinuum radiation
supersaturation
supersaturation ratio
supersonic flow
surface density of energy
surface diffusion
surface laser-induced structures
Svidzinskiy A.
synchrotron radiation
tachyons
Takuma
Tamura
Tamm I.
Tamman
Tappert
Taylor–Couette flows

Volmer-Weber-Becker-Dering theory
Volmer–Weber mechanism
volume atomic density
volume density of energy
volume laser-induced structures
Vorkman
Vorobyov S.
Udem
underwater nuclear reactor
Wai
Walton's microscopic theory of nucleation
water
water phasons in air
Weill Equation
Weisz
Wencke
white-light continuum spectra
Wyckoff
X-ray Cherenkov radiation
X-ray radiation
X-shape
X-waves
Yajima
Yukhymchuk V.
Young module
Zakharov
Zaitov F.
Zeits energy
Zel'dovich
Zheltikov